



HAL
open science

Optoelectronic, vibrational and transport properties of III-V/Si antiphase boundaries for photonics and solar energy harvesting

Lipin Chen

► **To cite this version:**

Lipin Chen. Optoelectronic, vibrational and transport properties of III-V/Si antiphase boundaries for photonics and solar energy harvesting. Materials Science [cond-mat.mtrl-sci]. INSA de Rennes, 2021. English. NNT : 2021ISAR0028 . tel-04465463

HAL Id: tel-04465463

<https://theses.hal.science/tel-04465463>

Submitted on 19 Feb 2024

HAL is a multi-disciplinary open access archive for the deposit and dissemination of scientific research documents, whether they are published or not. The documents may come from teaching and research institutions in France or abroad, or from public or private research centers.

L'archive ouverte pluridisciplinaire **HAL**, est destinée au dépôt et à la diffusion de documents scientifiques de niveau recherche, publiés ou non, émanant des établissements d'enseignement et de recherche français ou étrangers, des laboratoires publics ou privés.

THESE DE DOCTORAT DE

L'INSTITUT NATIONAL DES SCIENCES
APPLIQUEES RENNES

ECOLE DOCTORALE N° 596
Matière, Molécules, Matériaux
Spécialité: Physique, *Sciences des Matériaux*

Par

Lipin CHEN

Optoelectronic, vibrational and transport properties of III-V/Si antiphase boundaries for photonics and solar energy harvesting

Thèse présentée pour une soutenance à Rennes, le 15.06.2021
Unité de recherche : INSTITUT FOTON (UMR 6082 / CNRS)
Thèse N° : 21ISAR 16 / D21 - 16

Rapporteurs avant soutenance :

Magali BENOIT Directrice de recherche, CNRS CEMES Toulouse
Xavier MARIE Professeur, INSA Toulouse, LPCNO

Composition du Jury :

Antonio TEJEDA
Directeur de recherche, CNRS LPS-Orsay/ Examineur / Président
Magali BENOIT
Directrice de recherche, CNRS CEMES Toulouse/ Rapporteur
Xavier MARIE
Professeur, INSA Toulouse, LPCNO/ Rapporteur
Vincent ARTERO
Directeur de recherche, CEA Grenoble/ Examineur
Charles CORNET
Professeur, INSA Rennes, Institut FOTON/ Directeur de thèse
Christophe LEVALLOIS
Maître de conférences, INSA Rennes, Institut FOTON/ Co-encadrant
Rozenn PIRON
Maître de conférences, INSA Rennes, Institut FOTON/ Co-encadrant

Acknowledgements

Firstly, I would like to deeply acknowledge my supervisor Charles Cornet. Thank you for giving me the chances to study these interesting projects and for your continuous support and patience during my PhD studies. I learn a lot from you, not only on the research works but also on daily life. I also thank Christophe Levallois and Rozenn Piron sincerely for your instructions and helps.

Besides, there are many other FOTON members give me great helps, instructions and suggestions. I express my sincere gratitude to all of you, especially Yoan Léger, Jacky Even, Laurent Pedesseau, Antoine Létoublon, Julie Le Pouliquen, Tony Rohel, Nicolas Bertru, and Soline Boyer.

I thank all our collaborators, especially Gabriel Loget (ISCR), Rozenn Gautheron-Bernard (IPR), Oliver Skibitzki (IHP).

I also thank the committee members Magali Benoit, Xavier Marie, Antonio Tejeda, and Vincent Artero for your good comments, suggestions and questions for further improving the thesis.

Résumé

L'intégration de semi-conducteurs III-V sur silicium (Si) combinant les avantages du Si (abondance terrestre, faible coût et prévalence dans les industries électroniques et photovoltaïques) avec les excellentes propriétés optoélectroniques des III-V, est d'un grand intérêt dans les applications en photonique et récupération de l'énergie solaire [1,2]. Comme exposé dans le **Chapitre 1**, L'approche monolithique comme méthode d'intégration III-V/Si offre potentiellement d'énormes avantages, notamment des fonctionnalités polyvalentes, des coûts de production réduits sur de grandes surfaces de substrat et une intégration dense. Cependant, les différences fondamentales des propriétés physiques entre les matériaux III-V et Si, comme le paramètre de maille, le coefficient de dilatation thermique ou encore la polarité, introduisent une densité élevée de divers défauts lors de la croissance de semi-conducteurs III-V sur Si.

Parmi ces défauts, les parois d'antiphase (APB), constituées de liaisons chimiques accidentelles III-III ou V-V, sont particulièrement emblématiques de la croissance III-V/Si. Comme le montrent les **Fig.1a** et **b**, une APB dite « stœchiométrique » a un nombre égal de liaisons III-III et V-V (**Fig.1a**), alors qu'une APB « non stœchiométrique » n'est composée que de liaisons III-III ou de liaisons V-V (**Fig. 1b**). Des recherches récentes sur les mécanismes de génération, de propagation et d'enfouissement des APB [3,4] donnent des clés pour contrôler à volonté leur distribution dans les échantillons III-V/Si. Cependant, peu de travaux se sont concentrés spécifiquement sur l'étude de leurs propriétés physiques [5]. Cette thèse se concentre sur l'étude des propriétés optoélectroniques, vibrationnelles, et de transport des APB dans les matériaux III-V/Si, et leur utilisation pour les dispositifs de récupération d'énergie solaire, d'un point de vue théorique et expérimental. Les techniques de caractérisations structurales, optiques et de transport, ainsi que les méthodes de calcul par la théorie de la fonctionnelle de la densité (DFT) utilisées dans cette thèse sont exposées dans le **Chapitre 2**.

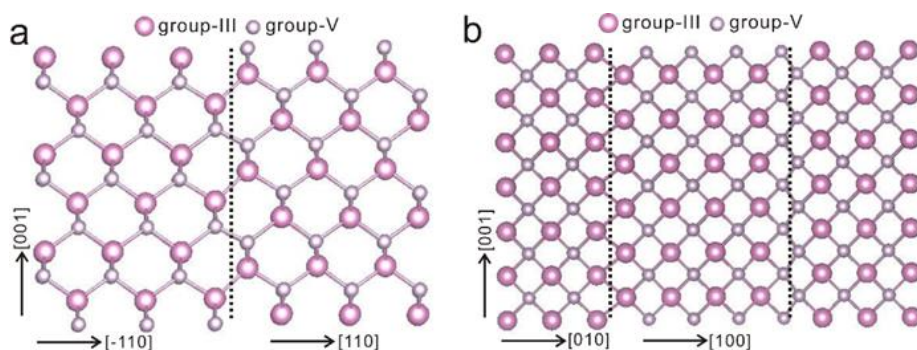


Figure 1 Configuration atomique de l'APB stœchiométrique (a) ou non stœchiométrique (b).

Au **Chapitre 3**, nous étudions les propriétés structurales, optiques et vibrationnelles d'un échantillon d'InGaP/SiGe/Si avec des APB stœchiométriques [6]. À partir des caractérisations structurales en diffraction des rayons X (XRD), microscopie électronique en transmission à balayage (STEM) et cartographie élémentaire par un système de rayons X à dispersion d'énergie (EDX), l'incorporation préférentielle d'atomes d'indium autour des APB est mise en évidence, formant ainsi des singularités homovalentes 2D verticales riches en In (**Figure 2**).

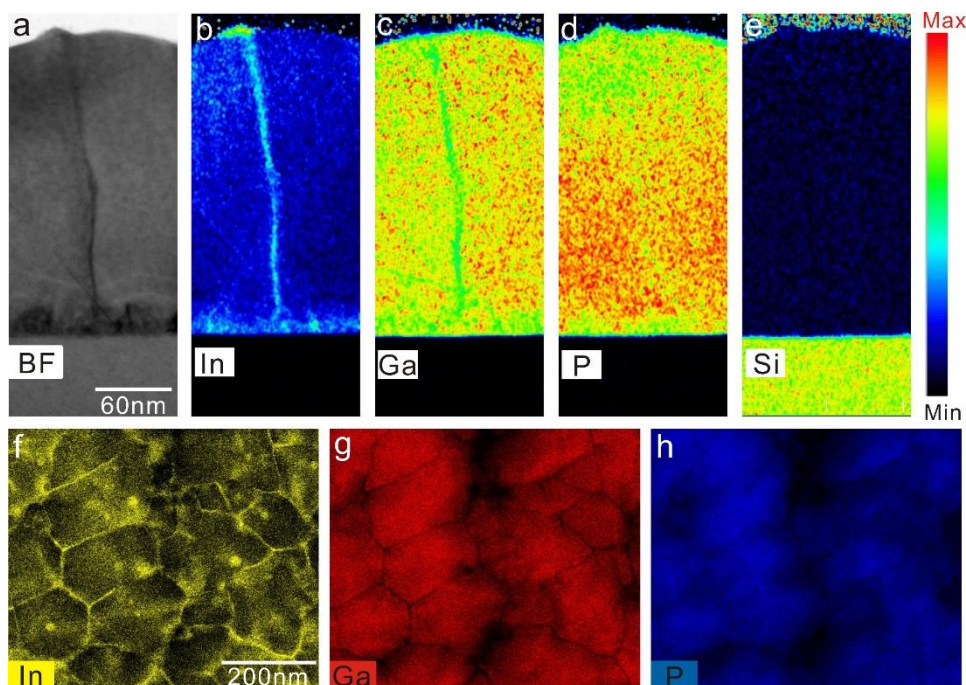


Figure 2 a, Image STEM en champ clair (BF) en coupe de la plate-forme InGaP/SiGe/Si. La ligne noire au milieu et la bosse sur la surface correspondent respectivement à l'APB et à la nanostructure de surface. b-e, Images de cartographie élémentaire EDX en coupe de l'indium (b), du gallium (c), du phosphore (d) et du silicium (e). f-h, cartographie élémentaire EDX en vue

plane de l'indium (f), du gallium (g) et du phosphore (h). On observe deux types de nanostructures riches en In: les nanostructures de surface en pur InP et les puits quantiques verticaux (QW) 2D riches en In entourant les singularités APB.

En outre, nous avons effectué des calculs de structure de bande et de phonons pour les APB stœchiométriques basés sur la théorie de la fonctionnelle de la densité (DFT). Nous constatons que les atomes au niveau des APB introduisent non seulement plusieurs états électroniques localisés sur le dessus de la bande de valence (**Fig.3a**), réalisant un confinement quantique des porteurs, mais introduisent également 5 modes de phonons localisés et plats dans la bande interdite de dispersion des phonons (**Fig.3b**), permettant le confinement des phonons.

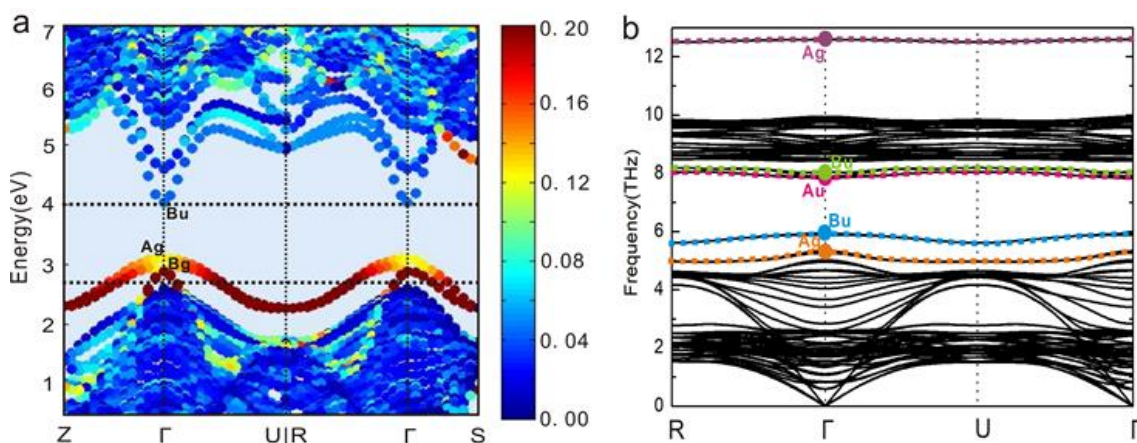


Figure 3 (a) Structure de bande électronique calculée d'une structure APB stœchiométrique, pondérée par la localisation spatiale des fonctions d'onde au voisinage de l'APB. (b) Structure de bande vibrationnelle (phonons) de la structure APB stœchiométrique. Les modes de phonon mis en évidence par des lignes pointillées orange, bleues, magenta, vertes et violettes correspondent à des modes localisés supplémentaires liés aux plans 2D d'APB.

L'impact de l'interaction électron-phonon sur les processus de photoluminescence est ensuite clarifié en combinant les résultats du calcul DFT avec des expériences de spectroscopie Raman et de photoluminescence. Le spectre de Photoluminescence (PL) contient plusieurs répliques de phonons et un facteur Huang-Rhys de 8 est finalement déterminé pour la raie d'émission liée aux APB (**Fig.4**), soulignant qu'un couplage électron-phonon important et inhabituellement fort peut être obtenu en raison du confinement simultané des porteurs de charge et des phonons au voisinage des structures

APB stœchiométriques 2D (**Fig.5**).

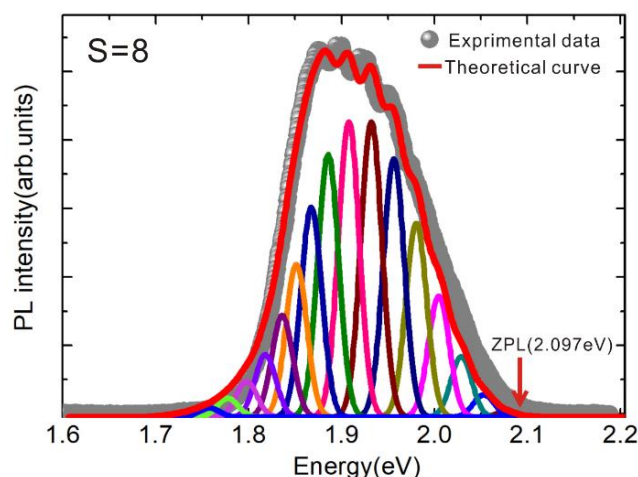


Figure 4 Données expérimentales (points gris) et ajustement théorique (ligne rouge) du large pic de PL basé sur le modèle de Franck-Condon. Les petits pics multicolores correspondent aux contributions distinctes des répliques de phonons.

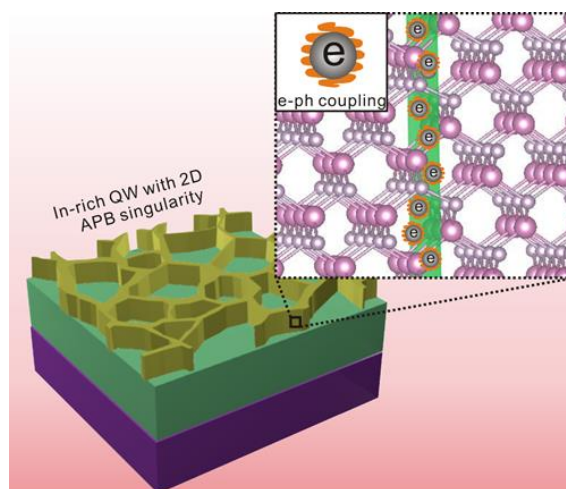


Figure 5 Diagramme schématique de la structure 2D verticale riche en indium, intégrant des plans APB avec une forte interaction électron-phonon.

Au **Chapitre 4**, une nouvelle association de matériaux en tandem GaPSb/Si (**Fig.6**) a été étudiée pour les applications en craquage photo-électro-chimique (PEC) de l'eau à partir de l'énergie solaire [7,8]. L'évolution de la structure de bande des alliages GaPSb est déterminée pour l'ensemble des compositions en Sb en combinant des mesures d'absorption avec des calculs de liaisons fortes, comme le montre la **Figure 7a**. Le croisement indirect (bande L) vers direct (bande Γ) se produit pour une composition en

Sb de 30%. En particulier, à 32% de Sb, l'alliage $\text{GaP}_{1-x}\text{Sb}_x$ atteint une configuration de gap direct souhaitée de 1.7 eV, permettant une absorption efficace de la lumière du soleil. En outre, l'alignement de bande de $\text{GaP}_{1-x}\text{Sb}_x/\text{Si}$ par rapport aux niveaux de potentiel redox de l'eau a été analysé (Fig.7b), ce qui montre que l'association 1.7eV/1.1eV GaPSb/Si est une combinaison intéressante à la fois pour les réactions de production d'hydrogène et de production d'oxygène.

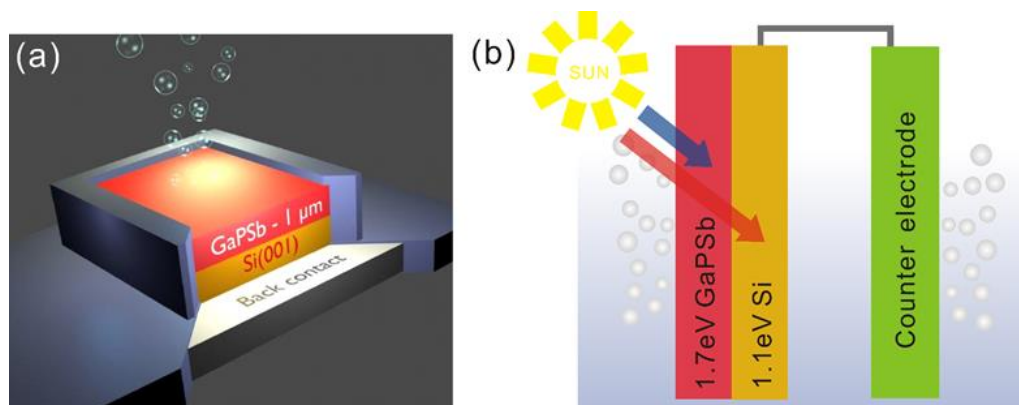


Figure 6 (a) Schéma du dispositif proposé en tandem $\text{GaP}_{1-x}\text{Sb}_x/\text{Si}$ pour le craquage PEC de l'eau. (b) Illustration montrant l'absorption de la lumière du soleil par le système tandem $\text{GaP}_{1-x}\text{Sb}_x/\text{Si}$ avec une combinaison de bande interdite d'environ 1.7/1.1eV pour le craquage de l'eau, qui permet une bonne absorption du spectre solaire.

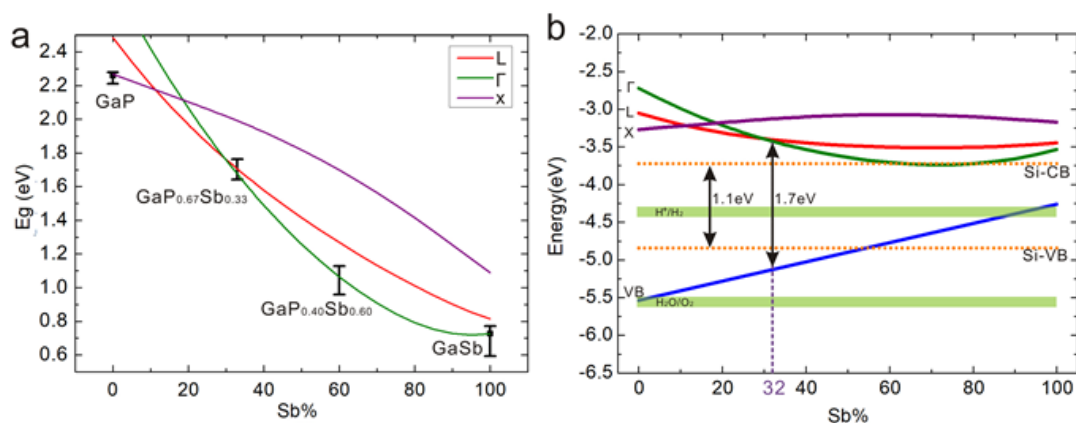


Figure 7 (a) Bandes interdites d'alliages $\text{GaP}_{1-x}\text{Sb}_x$ pour différentes compositions en Sb à température ambiante. Les lignes pleines vertes, rouges et violettes sont des courbes théoriques calculées par des calculs de liaisons fortes, correspondant respectivement aux vallées Γ , L et X. Les barres d'erreur séparées correspondent aux bandes interdites déterminées expérimentalement. (b) Alignement de bande des vallées Γ , L et X de $\text{GaP}_{1-x}\text{Sb}_x$ et bande interdite indirecte de Si par rapport aux potentiels d'oxydation et de réduction de l'eau.

En outre, une photoanode $\text{GaP}_{0.67}\text{Sb}_{0.33}/\text{Si}$ avec une combinaison de bande interdite très proche de l'optimum ($1.7\text{eV}/1.1\text{eV}$) a été étudiée pour le craquage PEC de l'eau par l'énergie solaire. Elle montre de bonnes performances en raison de la forte absorption de la lumière, notamment avec des couches de protection (TiO_2) et le co-catalyseur (Ni) (**Figure 8**), ce qui indique que ce matériau en configuration tandem est très prometteur pour le craquage de l'eau à haut rendement et à faible coût.

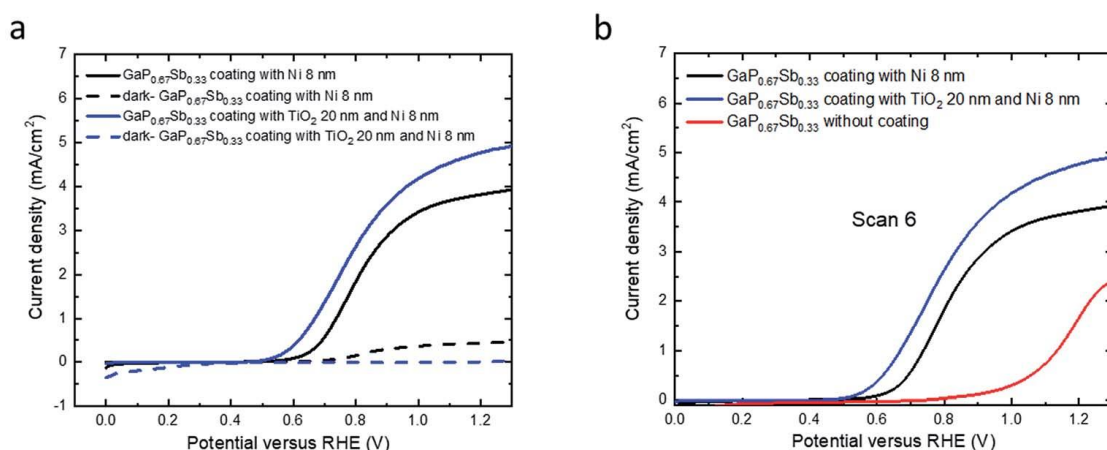


Figure 8 (a) Courbes de voltamétrie pour des photoanodes de $\text{GaP}_{0.67}\text{Sb}_{0.33}/\text{Si}$ recouverte de Ni 8nm et de $\text{GaP}_{0.67}\text{Sb}_{0.33}/\text{Si}$ recouverte par du TiO_2 (20 nm) et du Ni (8 nm) dans un électrolyte KOH 1,0 M sous illumination AM1.5 simulée en fonction de la tension appliquée par rapport à l'électrode hydrogène de référence. (b) Courbe de voltamétrie (scan numéro 6) pour le $\text{GaP}_{0.67}\text{Sb}_{0.33}/\text{Si}$ recouvert de Ni 8 nm ou recouvert de TiO_2 20 nm et Ni 8 nm. La courbe de voltamétrie rouge correspond au sixième balayage de la photoanode $\text{GaP}_{0.67}\text{Sb}_{0.33}/\text{Si}$ sans couche de protection.

Enfin, au **Chapitre 5**, les propriétés structurales, de transport et photo-électrochimiques de matériaux III-V/Si avec APB verticales et non stœchiométriques sont étudiées. En combinant les images AFM (microscopie à force atomique) et SEM (microscope électronique à balayage) avec l'analyse de la distribution spatiale des APB, nous avons prouvé que les échantillons III-V/Si contiennent à la fois des APB stœchiométriques et non stœchiométriques. Sur la base des expériences en C-AFM (AFM conducteur) et d'effet Hall, nous constatons que les APB montrent un bon transport. La **Figure 9** montre les images C-AFM d'un échantillon GaP/Si avec des APB émergents, à partir desquelles nous pouvons observer une intensité maximale claire du courant au niveau des APB.

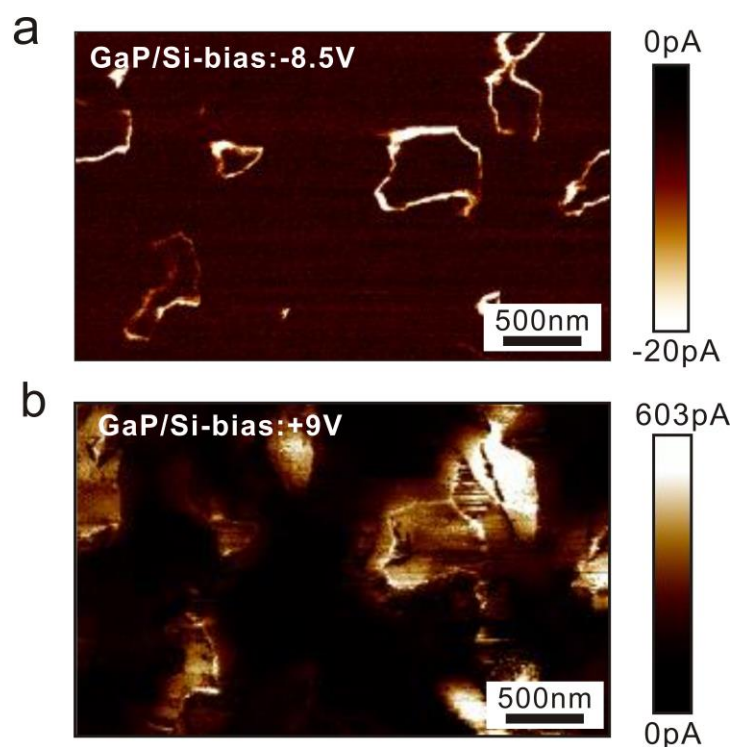


Figure 9 Images C-AFM de l'échantillon de GaP/Si bi-domaine sous tension négative (-8,5 V) (a) et tension positive (+ 9,0 V) (b).

En outre, diverses caractérisations PEC (y compris les courbes de voltamétrie à balayage linéaire (LSV), les spectres d'efficacité photon-courant incident (IPCE), la spectroscopie d'impédance électrochimique (EIS) et les tracés de Mott-Schottky (MS)) ont été effectuées pour les échantillons III-V/Si, qui présentent des comportements ambipolaires inhabituels et intéressants. Par exemple, les courbes de voltamétrie à balayage linéaire pour différents échantillons III-V/Si sont représentées sur la **Figure 10**, qui montre à la fois un photocourant cathodique et anodique.

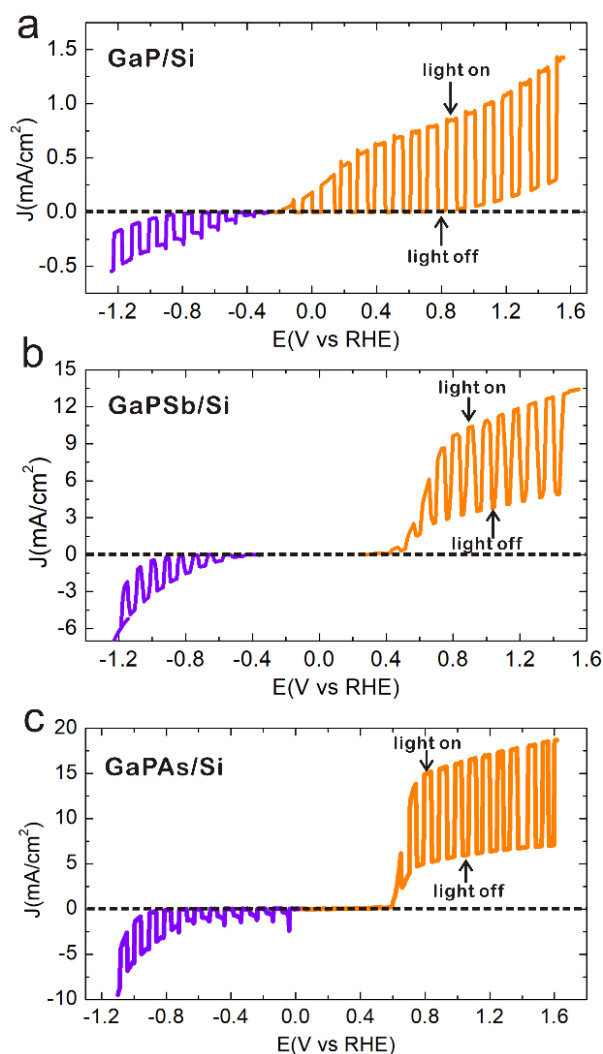


Figure 10 Courbes de voltamétrie à balayage linéaire à lumière intermittente du GaP/Si (a), GaPSb/Si (b), et GaPAs/Si (c), qui montre à la fois un photocourant anodique et cathodique.

Sur la base de calculs DFT, nous prouvons que les deux types d'APB non stœchiométriques III-III et V-V dans les couches III-V sont des inclusions semi-métalliques 2D. La **Figure 11** montre les structures de bande électronique des APB non stœchiométriques III-III et V-V de GaP, GaAs et GaSb, à partir desquelles on peut trouver les atomes d'APB introduisant des états métalliques dans la bande interdite, ce qui indique qu'ils sont une conséquence directe de la topologie 2D spécifique de l'APB.

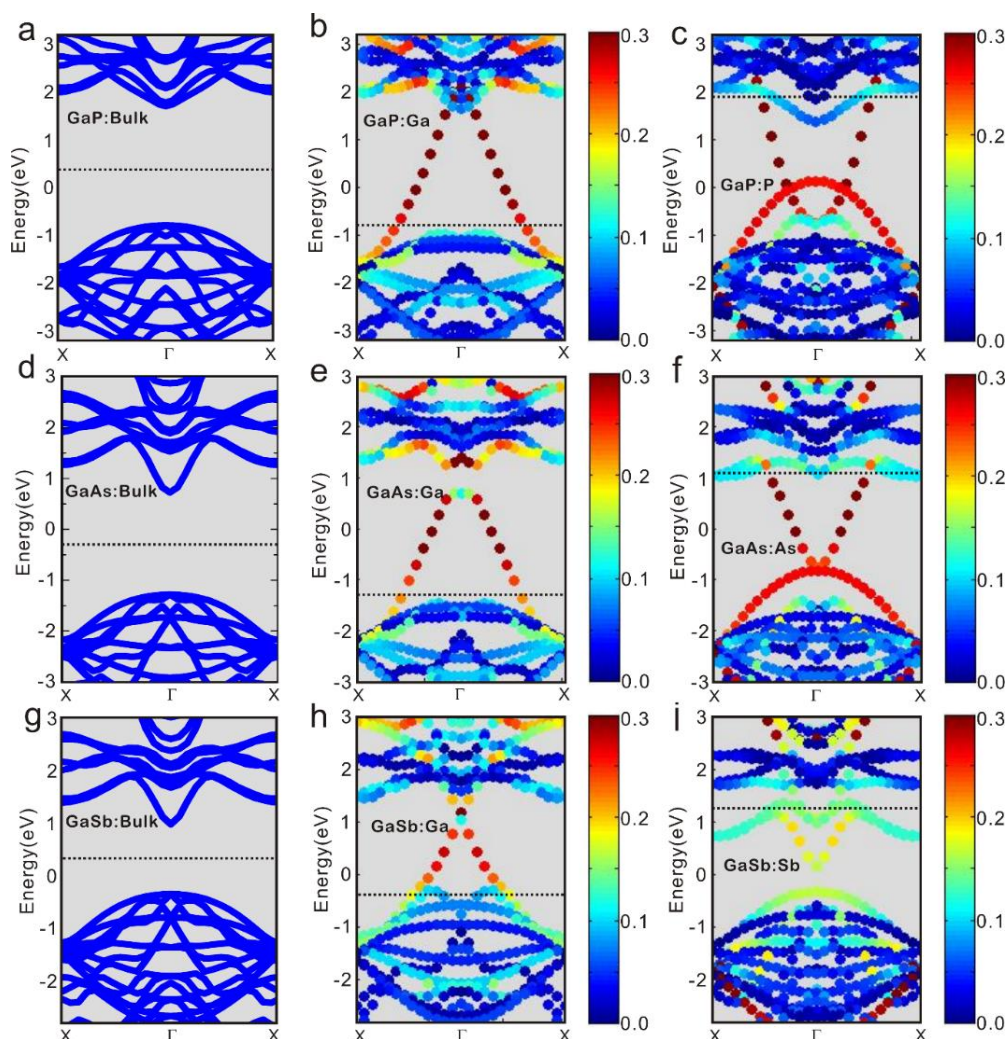


Figure 11 Structures de bandes électroniques calculées de structures zinc-blende, III-III APB et V-V APB pour GaP (a-c), GaAs (d-f) et GaSb (g-i). Les structures de bande APB (b, c, e, f, h, i) sont pondérées par la localisation spatiale des états à l'interface APB et la carte des couleurs du bleu au rouge souligne l'augmentation de l'effet de localisation des états à l'APB.

De plus, il a été démontré que les APB non stœchiométriques III-III (V-V) ont un niveau d'énergie de Fermi assez élevé (faible), respectivement, qui introduisent un fort champ électrique dans des régions à l'échelle nanométrique lorsqu'elles sont couplées avec les zones de semi-conducteur massif III-V. Le champ électrique intégré fournit une force motrice efficace pour une séparation efficace des porteurs de charge photo-générés (**Figure 12**). Nous montrons donc que les matériaux III-V/Si avec APB verticales non stœchiométriques sont des matériaux hybrides, composés de zones massives se comportant comme des semi-conducteurs photoactifs, avec des inclusions verticales semi-métalliques topologiques 2D. Nous montrons également que ces matériaux sont

capables dans la même couche d'absorber efficacement la lumière, de séparer latéralement les porteurs photo-générés, de les transférer vers les singularités semi-métalliques, et extraire les électrons et les trous verticalement, conduisant à une collecte efficace des porteurs et à des performances ambipolaires (comme illustré en **Figure 13**).

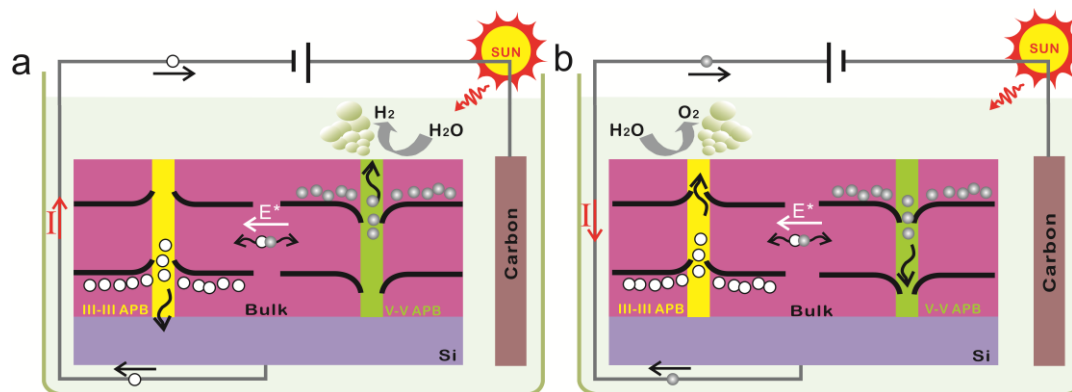


Figure 12 Diagramme schématique spatial du mécanisme de craquage de l'eau ambipolaire en tant que photocathode (a) et en tant que photoanode (b) à partir des singularités APB non stœchiométriques V-V et III-III. Les rectangles jaune et vert représentent respectivement les singularités III-III et V-V APB, et les lignes noires correspondent aux minima (maxima) de la bande de conduction (valence) du semi-conducteur III-V massif.

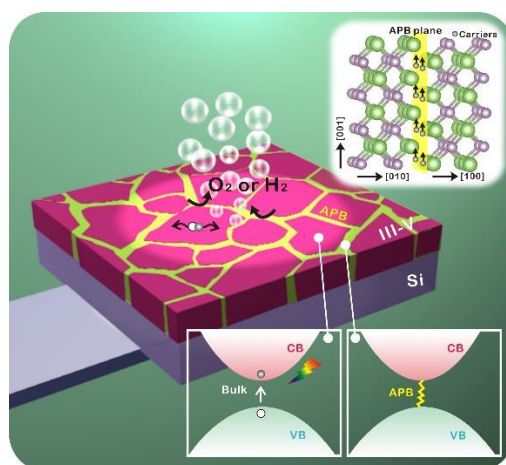


Figure 13 Illustration générale du matériau bi-domaine III-V/Si composé de zones de semi-conducteurs photoactifs avec des inclusions semi-métalliques APB 2D, qui permettent un bon transport et une séparation de charge efficace, réalisant le craquage PEC ambipolaire de l'eau.

En conclusion, les résultats de recherche présentés dans cette thèse démontrent que les parois d'antiphase III-V/Si ont des propriétés optoélectroniques, vibrationnelles et de

transport très spécifiques, qui ouvrent de nombreuses perspectives pour comprendre la physique de l'interaction électron-phonon et qui fournissent également de nouveaux paradigmes pour des applications en photonique, électronique, ou en récupération de l'énergie solaire.

References:

- [1] Fan, S. et al. Current-Matched III–V/Si Epitaxial Tandem Solar Cells with 25.0% Efficiency. *Cell Rep. Phys. Sci.* 1, 100208 (2020).
- [2] Tang, M. et al. Integration of III-V lasers on Si for Si photonics. *Prog. Quantum Electron.* 66, 1–18 (2019).
- [3] Lucci, I. et al. Universal description of III-V/Si epitaxial growth processes. *Phys. Rev. Mater.* 2, 060401 (2018).
- [4] Cornet, C. et al. Zinc-blende group III-V/group IV epitaxy: Importance of the miscut. *Phys. Rev. Mater.* 4, 053401 (2020).
- [5] Tea, E. et al. Theoretical study of optical properties of antiphase domains in GaP. *J. Appl. Phys.* 115, 063502 (2014).
- [6] Chen, L. et al. Strong Electron–Phonon Interaction in 2D Vertical Homovalent III–V Singularities. *ACS Nano* 14, 13127–13136 (2020).
- [7] Chen, L. et al. Assessment of GaPSb/Si tandem material association properties for photoelectrochemical cells. *Sol. Energy Mater. Sol. Cells* 221, 110888 (2021).
- [8] Alqahtani, M. et al. Photoelectrochemical water oxidation of $\text{GaP}_{1-x}\text{Sb}_x$ with a direct band gap of 1.65 eV for full spectrum solar energy harvesting. *Sustain. Energy Fuels* 3, 1720–1729 (2019).

Table of contents

General introduction	1
Chapter 1: Monolithic integration of III-V semiconductors on Si for photonics and energy harvesting applications	5
1.1 General properties of Si and III-V semiconductors.....	5
1.1.1 Silicon properties.....	5
1.1.2 III-V semiconductors properties.....	7
1.1.2.1 Atomic structure.....	7
1.1.2.2 Bandgap engineering through alloying.....	8
1.1.3 General interest of III-V and Si co-integration.....	9
1.1.3.1 Integrated photonics.....	9
1.1.3.2 Energy harvesting devices	10
1.1.3.3 III-V/Si integration methods.....	12
1.2 Monolithic integration of III-V on Si	13
1.2.1 Metamorphic integration	14
1.2.2 Pseudomorphic integration.....	17
1.3 Issues of monolithic integration of III-V semiconductors on Si.....	19
1.3.1 Lattice mismatch and thermal expansion coefficient	19
1.3.2 Polar on non-polar epitaxy	21
1.3.2.1 Stacking faults and microtwins.....	21
1.3.2.2 Antiphase domains and antiphase boundaries.....	22
1.4 Generation mechanism and properties of antiphase boundaries.....	23
1.4.1 Classification and formation energy of antiphase boundaries.....	23
1.4.2 Formation mechanism of antiphase boundaries	25
1.4.2.1 Historical approach.....	25
1.4.2.2 Generation, propagation and burying of antiphase domains: recent findings...27	
1.4.3 Optoelectronic properties of antiphase boundaries	29
1.5 Conclusions and objectives of the thesis	31
Chapter 2: Experiments and DFT calculations	33
2.1 Structural investigations and surface processes.....	33
2.1.1 Atomic force microscopy	33
2.1.2 Conductive atomic force microscopy.....	35
2.1.3 X-ray diffraction.....	36
2.1.4 Scanning transmission electron microscopy	40
2.1.5 Chemical mechanical polishing.....	40
2.2 Optical characterizations	42
2.2.1 Photoluminescence.....	42
2.2.2 Raman spectroscopy	43
2.2.3 Ellipsometry	45
2.3 Photoelectrochemical characterizations	46
2.3.1 Linear sweep voltammetry	48

2.3.2 Incident photon-to-current efficiency spectra.....	49
2.3.3 Electrochemical impedance spectroscopy.....	49
2.3.4 Mott-Schottky measurements.....	51
2.4 DFT calculations	52
2.4.1 Introduction to density functional theory	52
2.4.1.1 Hohenberg-Kohn theorems.....	53
2.4.1.2 Kohn-Sham approach	53
2.4.1.3 Local-Density approximation (LDA)	54
2.4.1.4 Generalized gradient approximation (GGA)	55
2.4.1.5 Heyd–Scuseria–Ernzerhof (HSE) hybrid functional.....	55
2.4.1.6 TB-mBJ potential.....	56
2.4.1.7 Self-Consistency and structure optimization	57
2.4.1.8 Computational codes	58
2.4.2 Electronic band structure calculation	60
2.4.3 Phonon calculation	61
2.4.4 Calculation of the electron-phonon interaction (EPI) matrix elements	62
2.4.5 Common DFT computational details	64
2.5 Summary	65

Chapter 3: Optoelectronic and vibrational properties of stoichiometric anti-phase boundaries

3.1 Introduction	67
3.2 Sample growth.....	68
3.3 Structural characterizations and post-growth processing	69
3.4 Optoelectronic and vibrational properties of stoichiometric APBs studied by DFT	77
3.4.1 Definition and properties of the supercell	77
3.4.2 Bandstructure calculations	79
3.4.3 Vibrational properties calculations	82
3.5 Optical characterizations	86
3.5.1 Raman measurement	86
3.5.2 Ellipsometry Measurements	88
3.5.3 Photoluminescence measurements	89
3.6 Proposed mechanism for the PL with multi-phonon replicas.....	93
3.7 Fitting of the PL spectrum with multi-phonon replicas.....	95
3.8 Electron-phonon interaction calculation.....	97
3.9 Discussion on the possible microscopic origins of the strong EPI.....	98
3.10 Summary	100

Chapter 4: Development of GaPSb/Si photoelectrodes for solar water splitting..

4.1 Introduction	101
4.2 GaPSb/Si material growth and targeted device design for solar water splitting	103
4.3 Structural properties of GaPSb/Si epilayers	104
4.4 Bandgap evaluation of GaPSb alloys	108
4.4.1 Ellipsometry measurements	108
4.4.2 Tight Binding calculations.....	112

4.5 Band alignment of GaPSb/Si with water redox levels	114
4.6 Discussion and assessment of GaPSb/Si for water splitting.....	115
4.7 Photo-Electro-Chemical characterizations	116
4.8 Summary	124
Chapter 5: Epitaxial III-V/Si vertical heterostructures with hybrid 2D semimetal/semiconductor ambipolar and photoactive properties	127
5.1 Introduction	127
5.2 Sample growth.....	129
5.3 Structural analysis of III-V/Si materials with emerging APBs.....	129
5.4 Transport characterizations of III-V/Si with emerging APBs.....	133
5.4.1 Hall measurements	133
5.4.2 Conductive atomic force microscopy (C-AFM) measurements.....	135
5.5 PEC characterizations of III-V/Si with emerging APBs.....	137
5.5.1 Linear sweep voltammetry (LSV).....	137
5.5.2 Incident photon-to-current efficiency (IPCE) spectra	140
5.5.3 Electrochemical impedance spectroscopy (EIS)	141
5.5.4 Mott-Schottky (MS) plots	142
5.6 DFT calculations for non-stoichiometric APB structures.....	143
5.6.1 Construction of non-stoichiometric APB supercells	143
5.6.2 Band structure and charge density distribution of non-stoichiometric APBs....	144
5.6.3 3D band structure and density of states	147
5.6.4 Enlarged band structure and Fermi energy calculations.....	150
5.7 Band structure of stoichiometric APB in GaP and GaSb	156
5.8 General description of III-V/Si photoelectrodes operation	156
5.8.1 General picture for the ambipolar III-V/Si photoelectrode	156
5.8.2 Influence of Si substrate doping on PEC performances	159
5.8.3 Contribution of the Si substrate to the PEC response.....	162
5.8.4 Synthetic view	164
5.9 Summary	164
Conclusions and perspectives	167
Appendices	171
Molecular beam epitaxy and ultra-high vacuum chemical vapor deposition	171
List of publications/conferences	175
Bibliography.....	179

General introduction

Integration of III-V semiconductors on silicon (Si), combining the excellent optoelectronic properties of III-V semiconductor with the benefits of silicon (such as low cost, abundance, maturity of manufacturing technologies), is of great interest for integrated photonics and energy harvesting (including solar cells and solar water splitting) applications [1,2]. Especially the monolithic integration of III-V semiconductors on Si offers great potential advantages, including versatile functionalities, low-cost and large-area production, and dense integration. However, the material dissimilarities between III-V and Si, such as lattice constant, thermal expansion coefficient, and polarity, introduces a high density of various crystal irregularities during the growth of III-V on Si, that were considered for years as detrimental defects, without a clear assessment of their physical properties. However, for the development of highly-integrated devices, the specific impacts of these crystal irregularities on the optoelectronic properties of III-V/Si have to be clarified.

Especially, very specific crystal defects, known as AntiPhase Boundaries (APBs), are very specific to the III-V/Si monolithic integration and have been considered as “device killers” for a long time. The recent researches on the generation, propagation and burying mechanisms of APBs [3,4] gave keys to tune at will their distribution in III-V/Si samples. Nevertheless, only few works studied specifically the optoelectronic properties of APBs. This thesis not only demonstrates that APBs are nanostructures with unique physical properties, but also shows how it can be used for energy harvesting applications. Therefore, this work, combining experiments and theory, focuses on the study of the specific optoelectronic, vibrational and transport properties of APBs in III-V/Si materials, and their use for energy harvesting devices.

Dissertation overview:

Chapter 1 introduces the research background of the monolithic integration of III-V semiconductors on Si. A brief state-of-the-art of the different III-V/Si integration

approaches for photonics and solar energy harvesting is presented. Then, a focus is given on the issues raised during the crystal growth of III-V semiconductors on silicon substrate. Finally, a summary of the recent research developments about the generation, propagation and burying mechanisms of APBs, and their known properties is proposed, where it can be seen that their physical properties were almost not explored in previous works.

Chapter 2 presents the experimental and theoretical supports of this work. The different experimental setups (structural, optical or photo-electro-chemical (PEC) characterizations) are described, with the related mechanisms, techniques and parameters settings used in this thesis. For the theoretical calculations, we firstly give a brief introduction to the basic concepts of the DFT, then the calculation steps and parameter settings for the determination of electronic band structure, and of the vibrational and electron-phonon coupling properties are presented.

Chapter 3 focuses on the study of the electron-phonon coupling around stoichiometric APBs in an InGaP/SiGe/Si sample. 2D vertical In-rich stoichiometric APB singularities are investigated firstly with X-Ray Diffraction (XRD), scanning transmission electron microscopy (STEM) and energy-dispersive x-ray spectroscopy (EDX) structural characterizations. The impact of the electron-phonon interaction on the photoluminescence processes is then clarified by combining Raman and photoluminescence experiments with electronic band and phonon DFT calculations. The strength and origin of the observed coupling is then deeply discussed, with regards to the APB symmetry properties.

Chapter 4 aims to assess the potential of a novel GaPSb/Si tandem materials association for high-efficient low-cost solar water splitting, based on bandgap engineering. Thus, the quality of samples is investigated firstly based on X-ray diffraction (XRD), scanning electron microscopy (SEM), and atomic force microscopy (AFM) structural characterizations. Then, the bandgap of GaPSb alloys is determined on the whole Sb range by absorption measurements and tight-binding calculations. Based on the bandgap and band alignments determined, the potential of GaPSb/Si material for water splitting is then discussed. Finally, the PEC performances of a $\text{GaP}_{0.67}\text{Sb}_{0.33}/\text{Si}$ photoanode are

investigated and discussed in terms of solar spectrum absorption, while transport properties in these photoanodes are questioned.

Chapter 5 demonstrates that epitaxial III-V/Si samples with vertical non-stoichiometric APBs are hybrid materials composed of bulk semiconductors and 2D topological semi metallic inclusions. Based on structural, transport, PEC experiments and theoretical calculations, the photo-activity, ambipolar transport and PEC performances are investigated for the epitaxial III-V/Si samples with non-stoichiometric APBs.

Chapter 1: Monolithic integration of III-V semiconductors on Si for photonics and energy harvesting applications

1.1 General properties of Si and III-V semiconductors

1.1.1 Silicon properties

Silicon was named by Thomas Thomson in 1817 [5] and was first isolated by Swedish chemist Berzelius in 1825 [6]. Pure silicon is a dark gray solid with the same crystalline structure as diamond, which consists of two face-centered cubic (fcc) sub-lattices with one sub-lattice shifted one quarter of the body-diagonal with respect to the other sub-lattice (as shown in **Fig. 1.1**), called "two interpenetrating face-centered cubic" primitive lattices by Ashcroft and Mermin [7].

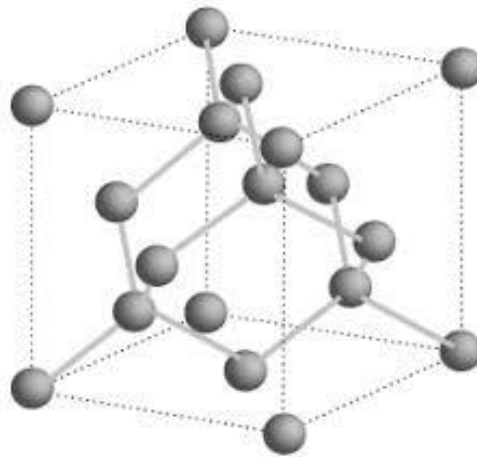


Figure 1.1 Crystal structure of silicon. Courtesy of [7]

Silicon has several great advantages. It is the seventh-most abundant element in the universe and the second-most abundant element on earth, after the oxygen. Silicon is naturally found in the form of compounds with oxygen, aluminum and magnesium but can easily be synthesized with a high purity at a low cost. Silicon has also a high thermal

conductivity, which is important for electronic devices, because as the current density and working time increase, more heat is generated, causing device operating temperature to rise and thus leading potentially to device degradation. Moreover, the electrical properties of silicon can be finely tuned by implantation processes, widely used during the doping steps within the fabrication of MOS (metal–oxide–semiconductor) transistors. For these reasons, silicon is today the ruling material in micro-electronics and photovoltaics (PV).

On the other hand, optical properties of silicon remain fundamentally limited. Indeed, Si has an indirect bandgap, with the minimum of the conduction band in the X valley of the reciprocal space and the maximum of the valence band in the Γ valley (see **Fig. 1.2**) [8]. Thus, a radiative recombination between an electron and a hole requires a phonon-assisted transition in order to satisfy the momentum conservation. The poor light emission efficiency of Si is thus directly related to the low probability of an electron to meet a phonon before it meets a non-radiative center. Besides, for photovoltaic applications, crystalline silicon is also not the most efficient material due to its indirect bandgap and consequently to slow recombinations, long charge carrier lifetimes and low absorption properties. It is usually compensated by using thick Si absorbers.

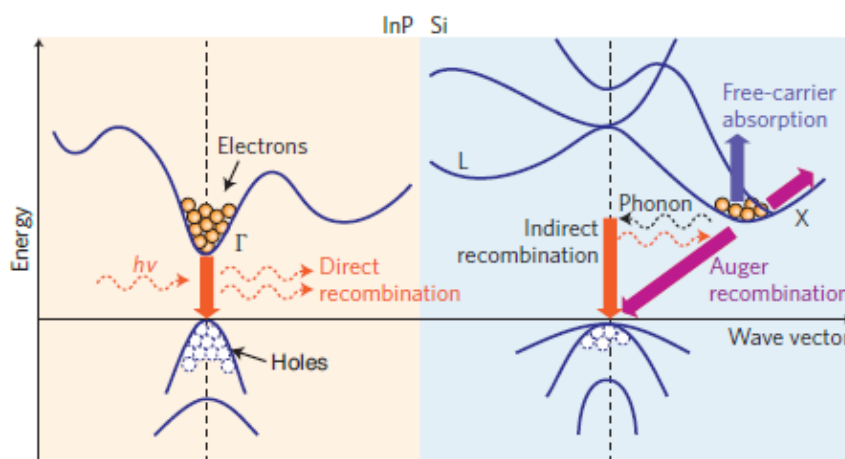


Figure 1.2 Energy band diagram and main carrier transition processes in bulk InP and bulk Si.

Courtesy of [8]

1.1.2 III-V semiconductors properties

1.1.2.1 Atomic structure

The crystal structure of most III-V semiconductors consists in two face-centered cubic (fcc) sub-lattices, composed of two different atoms: one sub-lattice is occupied by Group-III atoms, while the other one is occupied by Group-V atoms, leading to the so-called Zinc-Blende structure (as shown in **Fig. 1.3**). Consequently, III-V materials are polar semiconductors, while Si is a non-polar semiconductor [9].

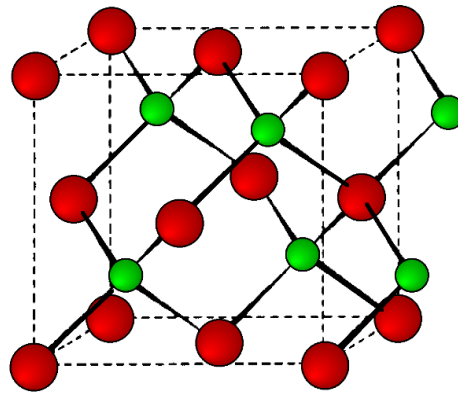


Figure 1.3 Zinc-Blende structure of a III-V semiconductor. Courtesy of [10]

Most of the III-V semiconductors present a direct bandgap (**Fig. 1.2** left) and are thus naturally suited for applications in photonics or energy harvesting [11]. They typically provide efficient light emission and high photon absorption because of their direct bandgaps (e.g. for InP, GaAs, InAs or GaSb), high electron mobilities (e.g. for InAs, InP and GaAs). They can also be alloyed, which gives the opportunities to tune at will their bandgaps and bandlineups, from the infrared range to the ultraviolet one (this will be discussed in the next section). On the other hand, the largest disadvantage of III-V semiconductors is their high cost. Unlike silicon wafers, which are produced at a large scale worldwide, with extraordinary purity over very large wafers, III-V crystals are produced in much smaller volumes and are far more expensive. 200 mm III-V wafers can cost as much as \$5,000 (This also depends on the type of III-V used) while 300 mm silicon wafers cost less than \$100 [12]. Historically, cost has been one of the major barriers

against the massive development of III-Vs.

1.1.2.2 Bandgap engineering through alloying

Bandgap engineering is the process of controlling or altering the band gap of a material. This is typically done with semiconductors by controlling the composition of alloys or constructing layered materials with alternated compositions [13]. Bandgap engineering of III–V semiconductors materials started 30 years ago and today many existing commercial devices (including LEDs, lasers and so on) use this approach. Based on bandgap engineering, both the bandgap and band type of III-V semiconductors can be adjusted by adding other elements (one or two typically) to achieve ternary or quaternary alloys (pentanary alloys are most of the time too difficult to control to be implemented in devices).

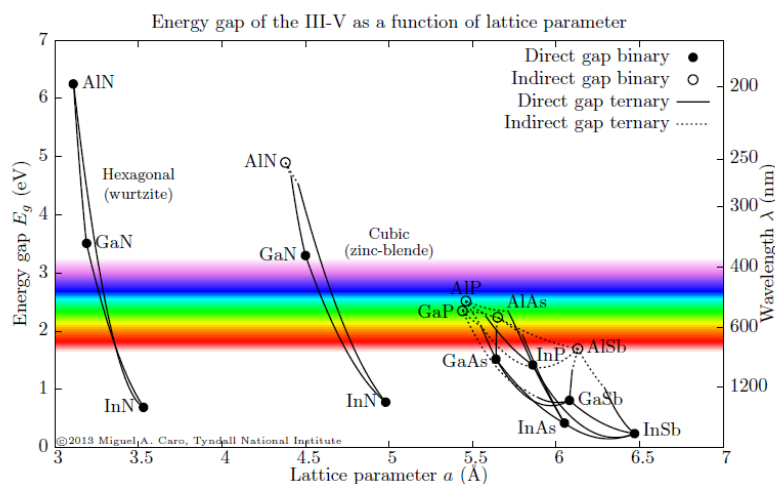


Figure 1.4 Bandgap energy versus lattice constant of the most common III-V semiconductors. Solid circles indicate a direct bandgap binary material while empty circles indicate an indirect bandgap binary material. The curves show the band gap for some of the ternary alloys, where solid lines indicate direct bandgaps and dashed lines indicate indirect bandgaps. Courtesy of [14]

In many semiconductor alloys, a linear interpolation between the respective lattice parameters at the two end points may be used to determine the lattice parameter of the alloy. It is a function of the composition, often referred as the Vegard's law. However, the bandgap of most of the semiconductors does not vary linearly with the composition and

a deviation is observed, which is known as the bandgap bowing [15]. To account for this deviation, a correction term known as bowing parameter b is added. This bowing parameter b is needed to determine the bandgap of semiconductor alloys [16]. The composition dependence of bandgaps of ternary alloys $A_xB_{1-x}C$ with two kinds of cations (or CA_xB_{1-x} with two kinds of anions) at room temperature can be determined by using the standard formula [17]:

$$E_g(x) = E_g(AC) * x + E_g(BC) * (1 - x) - b * x(1 - x) \quad (1-1)$$

Where E_g is bandgap of the ternary alloy $A_xB_{1-x}C$ (or CA_xB_{1-x}), $E_g(AC)$ is the bandgap of the binary alloy AC, $E_g(BC)$ is the bandgap of the binary alloy BC, b is the bowing parameter, x is the concentration of the A element and $(1-x)$ is the concentration of the B element.

Bandgap engineering was investigated for many ternary or quaternary III-V alloys. **Figure 1.4** shows the bandgap of some important binary and ternary III-V semiconductors as a function of the lattice parameter. The bandgaps of the ternaries are given at their minimum, which can correspond to the gaps at the Γ , X or L valleys, from the respective band gap bowing parameters provided in ref. [18,19], based on **Eq.1-1**.

1.1.3 General interest of III-V and Si co-integration

1.1.3.1 Integrated photonics

The Si-based complementary metal-oxide-semiconductor (CMOS) technology is the fundamental building block of the contemporary electronics [20,21]. However, the electrons travelling through copper wires is now a bandwidth limitation for the most advanced MOS transistors. In contrast, photons move at light speed and avoid the bottleneck of metallic connections. Besides, electronic current generates non-negligible heat through the Joule effect, which is harmful to electronic devices. Photons can transmit great amounts of information, releasing only a fraction of the energy they carry [22].

Therefore, Si photonics integrating optical systems at the inter-chip or even intra-chip scale, has emerged as a highly attractive research area for ultra-fast and low-cost optical data transmission on the Si-on-insulator (SOI) platform compatible both with the CMOS process [21] and photonic architectures requirements.

However, as mentioned above, the bulk Si material has only limited optical properties. Although Si-based light-emitting devices, like Si Raman laser [23] and p-n junction emitter [24,25] were developed, their performances are still far from the one of III-V devices [2,21]. Indeed, III-V semiconductors have been widely used in light-emitting/absorbing devices, including light-emitting diodes (LEDs), lasers, detectors due to their superior optoelectronic properties. Thus, integration of III-V on Si leveraging the benefits of both Si and III-V semiconductors has brought great deal of interest and excitement for integrated photonics (**Fig. 1.5**).

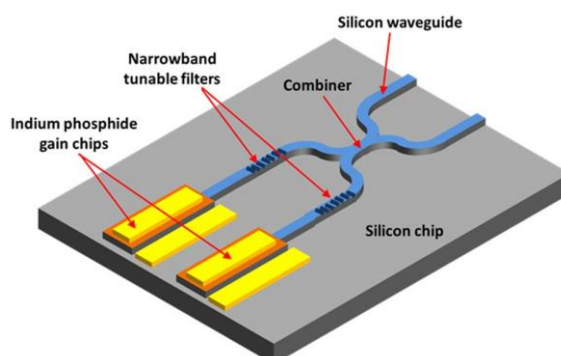


Figure 1.5 Integration of III-V on Si chip for integrated photonics. Courtesy of [26]

1.1.3.2 Energy harvesting devices

(a) solar cell

III-V compound semiconductor based multijunction solar cells have been the most successful technology with the highest photovoltaic conversion efficiency for space power applications [27]. III-V solar cells have steadily shown performance improvement

at ~1% increase in efficiency every year. The recent world record efficiency of 44.7% at 297 suns for a four-junction III–V solar cell was achieved [28]. Nevertheless, their expensive cost is the biggest impediment in their large-scale deployment for terrestrial applications. On the other hand, Si has been one of the dominant prime materials for photovoltaic technology since the 1950s [29]. But the performance of single-junction Si solar cells has almost saturated at around 25%. The domination of silicon solar cells is now facing the strong competition of other efficient technologies, such as perovskites solar cells [30].

The cost of the substrate significantly contributes to the high cost of III–V solar cells. Typically, GaAs or Ge substrates used for III–V multijunction solar cell growth are not only smaller in diameter but are also greatly more expensive than Si [27]. Besides, Si also offers higher thermal conductivity and superior mechanical strength in comparison to GaAs or Ge substrates [27]. Integration of III–V multijunction solar cell on Si substrate, where the Si can potentially be used as an active bottom sub-cell or just as an inactive low cost starting template, provides a promising path for low-cost and high-efficiency photovoltaic devices [1].

(b) solar water splitting

Solar water splitting converting solar energy to hydrogen through photoelectrochemical (PEC) cell, provides a promising path for scalable and sustainable carbon-free hydrogen production [31,32]. It is one significant milestone on the road to a sustainable energy future, especially under the current background of global energy and environmental crisis. The development of the PEC water splitting technology (as shown in **Fig.1.6**), where the sunlight falling on an immersed semiconductor photoelectrode, turns the liquid water into gaseous storable hydrogen that can be reused on demand for heat or electricity production, has driven many researches in the past years.

Within the same way as for photovoltaic applications, the development of efficient

semiconductor photoelectrodes for solar water splitting not only requires excellent optical properties to enable high light absorption but also the use of low-cost materials for large-scale deployment and development. Besides, with the flexibility offered by bandgap engineering strategies with III-V semiconductors, not only the bandgap can be adjusted to obtain high light absorption, but also the band alignment with water redox potential levels can be optimized. Therefore, the III-V/Si heterogeneous association of materials is also highly attractive and interesting for low-cost high efficiency solar water splitting applications. At the beginning of this work (2017), the only existing III-V/Si photoelectrodes were made of III-V Nano-wires, with complex designs and/or limited performances. We will see later (**Chapter 4**) that the two first monolithic III-V/Si photoelectrodes were demonstrated in 2019 simultaneously by our laboratory (with P-based photoelectrodes) [33] and the one of Pr. Nötzel (with N-based photoelectrodes) [34].

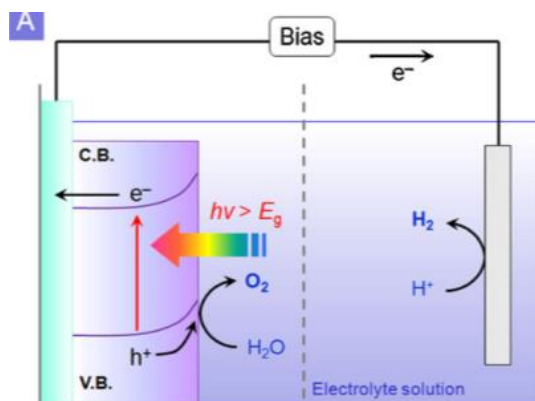


Figure 1.6 Working principle of a PEC cell with a n-doped semiconductor. Courtesy of [35]

1.1.3.3 III-V/Si integration methods

Plenty of strategies have been tried to co-integrate III-V semiconductors and silicon for optoelectronic applications [36]. Two main integration methods can be considered: hybrid integration and monolithic integration, as shown in **Fig. 1.7**. The hybrid one includes “sticking” or “bonding” of optical layers or devices directly on the silicon chip. The bonding process can be achieved by direct bonding (molecular-assisted), adhesive

bonding (polymer-assisted) or metal-assisted bonding [37]. The monolithic integration consists in growing the III-V semiconductors directly on the Si substrate. This approach has different advantages with respect to the hybrid one, such as low fabrication costs and time. It should also ease the very large-scale integration of III-V devices on Si, which can hardly be achieved through the hybrid integration. In the following sections, more information about the monolithic integration method will be provided.

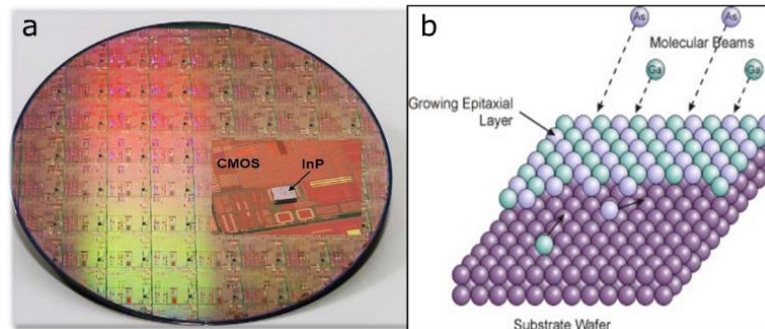


Figure 1.7 Hybrid integration (a) and monolithic integration (b) of III-V semiconductors on the Si substrate. Courtesy of [38,39]

1.2 Monolithic integration of III-V on Si

As discussed above, the monolithic integration approach offers many promises. Nevertheless, its primary challenge is to reach a high III-V/Si interface crystal quality and manage the crystal defects which may propagate in the volume of the device and degrade its performances and stability.

The lattice mismatch between the III-V and Si is one main parameter determining the quality of the epitaxial III-V/Si materials. **Fig. 1.4** displays the bandgap energies of different III-Vs as a function of their lattice parameter. On the one hand, it reveals that some III-V semiconductors (such as GaAs, GaSb or InP) have a direct bandgap but a large lattice mismatch with the silicon. This will cause the formation of defects (e.g. misfit dislocations) and decrease the photonic devices efficiency. On the other hand, III-Vs such as AlP or GaP are quasi-lattice-matched to the silicon but, they have an indirect bandgap which can limit as well the device performances. When growing lattice mismatched III-

Vs on Si substrate, the integration is called metamorphic, otherwise it is called pseudomorphic. The approaches and the strategies, which were used for overcoming the related growth issues, will be presented in the following parts.

1.2.1 Metamorphic integration

For most applications, the main advantages of III-V semiconductors are their direct bandgap, such as GaAs or InP. However, they also present a large lattice mismatch to the silicon. As a result, the misfit dislocations formation is unavoidable. Crystal defects are usually considered as non-radiative recombination centers in the materials (we will see afterwards that it is not always the case). Depending on the targeted application, the density of these defects has to be reduced at a given value to ensure both efficient transport and adapted optical properties. For instance, considering laser devices, it is commonly accepted that the density of emerging dislocations should lie below 10^6 cm^{-2} to guarantee reasonable laser performances and stability, and should even reach 10^4 cm^{-2} for high performances III-V lasers. **Fig. 1.8** shows the propagation of dislocations in a GaAs on Si epilayer [40]. A large number of approaches have been tried to grow high quality III-V epitaxial layers on Si substrate with low density of dislocations to improve the device performances.

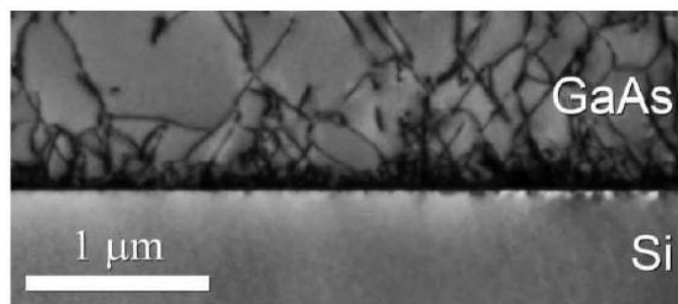


Figure 1.8 Cross-sectional transmission electron microscopy (TEM) image of dislocations propagating through the GaAs grown on Si substrate. Courtesy of [40]

One can for instance benefit from the specific crystal relaxation processes of Sb-based alloys which have a very large lattice mismatch with Si (e.g. 12% for GaSb and 13% for AlSb). The strain energy due to the large mismatch could be relieved into the III-V epilayer through the formation of self-organized interfacial misfit dislocations (IMD) arrays [41,42]. As shown in **Fig. 1.9**, the formation of planar array of 90° misfit dislocations which are partly confined at the interface, could be induced when AlSb is grown on Si substrate. The low threading dislocation density obtained with this approach highlights the potential of this strategy for the monolithic integration. Kim *et al.* [43] and Akahane *et al.* [44] improved the quality of the GaSb/Si crystal interface via an AlSb nucleation layer. GaSb-based devices have also been realized in the literatures [45-49].

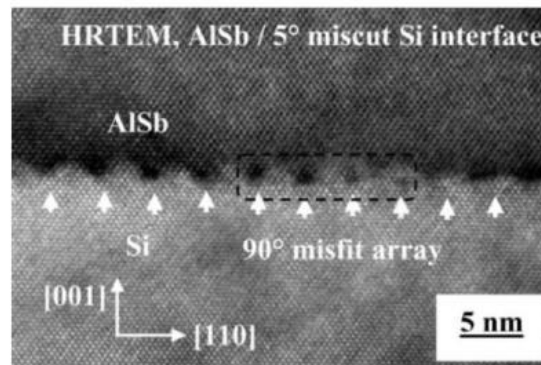


Figure 1.9 Cross-sectional TEM image of a two-dimensional dislocation network confined at the AlSb/Si interface. Courtesy of [41]

Another effective strategy to reduce the threading dislocations is the use of strained layer superlattice (SLS) and short period superlattice (SPL) [36]. This approach has been presented by growing high quality InGaAs quantum-dots (QDs) on Si substrate and by growing InP-on-Si heterostructures [40,50]. An example is shown in **Fig. 1.10**.



Figure 1.10 Cross-sectional TEM images, displaying the suppression of threading dislocations through the growth of strained superlattice (SPS) and short period superlattices (SPL). Courtesy of [40]

The adaptation of the lattice parameter by compositionally graded buffers is also a widely investigated approach, for instance $\text{Si}_x\text{Ge}_{(1-x)}/\text{Si}$ pseudo substrate [51] to reduce the dislocation density at the GaAs/Si interface. High performance GaAs-based solar cells [52] and laser structures [53] have been realized. TEM cross-section micrograph of the GaAs/AlGaAs laser structure on Si substrate with relaxed graded SiGe buffer layers is shown in **Fig.1.11**, where the dislocations are suppressed effectively. This strategy was also used to grow lattice mismatched $\text{GaAs}_{0.7}\text{P}_{0.3}$ solar cells on Si substrate [54].

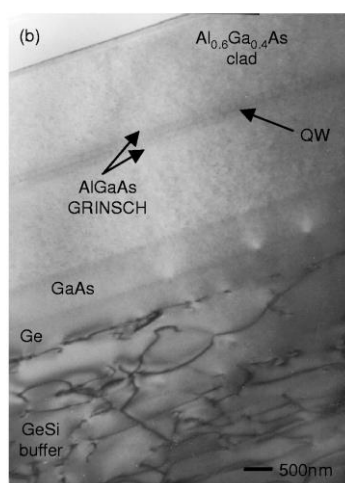


Figure 1.11 TEM cross-section micrograph of the GaAs/AlGaAs laser structure on Si substrate with relaxed graded GeSi buffer layers. Courtesy of [53]

Besides, the growth of III-V nanowires on Si is another widely used strategy to mitigate the appearance of defects [55]. It includes growing III-V core-shell nanowires through catalyst-assisted (for instance with the help of Au nanoparticles) or catalyst-free processes [56,57]. **Fig. 1.12** shows monolithic GaAs/InGaP nanowires light emitting diodes on silicon with Au nanoparticle catalyst.

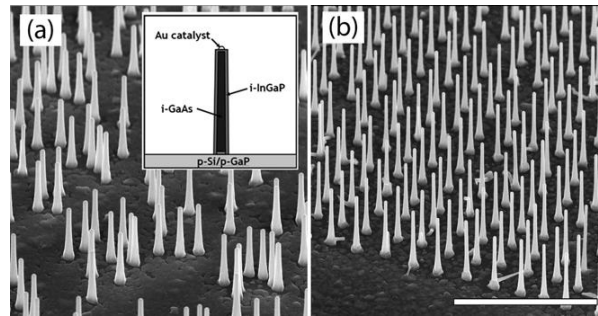


Figure 1.12 Core-shell GaAs/InGaP nanowires grown on Si (111). The epi-structure is shown in the inset. Courtesy of [55]

1.2.2 Pseudomorphic integration

The pseudomorphic integration consists in growing III-V semiconductors lattice matched to the Si substrate, to avoid the formation of misfit dislocations. The low lattice mismatch allows avoiding the formation of misfit dislocations between GaP or AlP and the silicon surface until a critical thickness of around 100 nm. The GaP is one of the best candidates for this approach. Indeed, the lattice mismatch of GaP and Si is only 0.37% at room temperature. Thus, the epitaxial growth of quasi-lattice matched GaP on silicon is considered to be an efficient platform for the subsequent integration of low defect or defect-free III-V based heterostructures. **Fig. 1.13** shows good atoms alignments [58] due to its very low lattice mismatch to the Si. It is possible to avoid defects formation such as microtwins (MTs) and to annihilate antiphase domains [59] by choosing the good growth conditions. As shown in **Fig. 1.14**, most of the antiphase boundaries (APBs) could be annihilated within 10 nm from the GaP/Si interface. Takagi *et al.* [60] reported that it is possible to reduce the defects formation and improve the surface roughness through migration enhanced epitaxy (MEE). Volz *et al.* [61] were able to grow a defect-free

GaP/Si(001) after almost 50 nm GaP layer thickness. A two-step growth process was developed by Grassman *et al.* by using low temperature MEE, and then followed by molecular beam epitaxy (MBE) [62]. In this way, a very smooth and defect-free GaP/Si interface was realized. However, the indirect nature of its bandgap has imposed severe limitations on the performances of GaP-based laser devices. Based on bandgap engineering, lasing on silicon was even demonstrated with GaAsPN quantum wells [63]. With the incorporation of Nitrogen (N), the GaP indirect bandgap can be converted into a pseudo direct one for overcoming the indirect band structure issue. Also, some GaP/Si-based photovoltaic devices were achieved, either considering GaP/Si heterostructures or by developing tandem-like architectures [64]. More recently, our group developed high quality phase-controlled GaP/Si micro-resonator for non-linear integrated photonics [65].

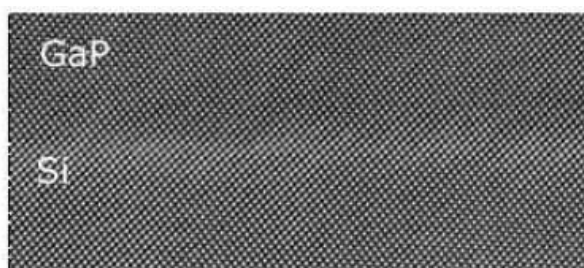


Figure 1.13 Cross-section HRSTEM-HAADF image of GaP grown on Si, showing the good atoms alignment at the interface. Courtesy of [58]



Figure 1.14 STEM-BF images showing the annihilation of most of the APDs at 10nm from the interface. Courtesy of [59]

1.3 Issues of monolithic integration of III-V semiconductors on Si

The quality of III-V/Si materials is crucial for the performances of the developed devices. In the monolithic integration context, in order to obtain a high crystal quality III-V/Si interface and III-V layers, different materials growth challenges have to be taken into account, including the Si surface preparation, the lattice mismatch and thermal expansion coefficient, the 3D-growth or the issues related to the polar on non-polar epitaxy [37]. In the following, main issues related to the III-V/Si monolithic integration directly connected to this work, are briefly exposed.

1.3.1 Lattice mismatch and thermal expansion coefficient

The lattice mismatch and thermal expansion coefficient strongly influence the quality of the monolithic integration of III-V semiconductors on Si. The lattice mismatch is often used to quantify the difference of lattice parameters between the epitaxial layers deposited and the substrate. The lattice mismatch f is defined by the following equation [66]:

$$f = \frac{a_s - a_f}{a_s} \quad (1-2)$$

Where a_f and a_s are the lattice parameters of the semiconductor epitaxial film and substrate, respectively.

The generated strain can be accommodated either through elasticity or through plasticity. In the first case (usually associated to small lattice mismatch, and thin epilayers), the elastic energy is mostly stored through a biaxial strain of the epilayer to match the in-plane lattice constant of the substrate, as shown in **Fig. 1.15a**. The deposited material is coherently strained to the substrate which means that the lattices planes are continuous at the interface. In this case, the epitaxial film is compressively strained if its lattice constant is larger than that of the substrate, otherwise it is tensily strained. On the other hand, the plastic relaxation occurs for larger mismatches or thicker epitaxial films

(Fig. 1.15b). In this case, if the epitaxial film thickness is above a given “critical thickness”, elastic energy will be released through the creation of the so-called misfit dislocations. The critical thickness was investigated in many materials systems by scientists. In the case of GaP/Si, Soga *et al.* [67] reported a critical thickness less than 90 nm, and Takagi *et al.* [68] and Skibitzki *et al.* [69] gave further estimation around 45-95 nm and 64 nm, respectively. In the case of GaSb/Si, the mismatch is so high that dislocations appear almost instantaneously (the critical thickness is very small). In this case, the formation of a regular network of misfit dislocations have been observed with Sb-based materials [3,41].

In addition, the lattice parameter also depends on the temperature. Therefore, the thermal expansion coefficient has a main impact on lattice mismatch issues. This effect can be very different from one semiconductor to another [70]. When the temperature varies from room temperature to growth temperature (in the range of 350°C to 1000°C), microcracks can be induced, due to the different thermal expansion coefficients of the substrate and the epilayer. In the case of III-V/Si epitaxy, the III-V epilayer may undergo a large tensile or compressive stress. For instance, the thermal expansion coefficient of GaP is almost twice the one of the silicon ($\alpha_{\text{GaP}}=4.65 \times 10^{-6}/\text{K}$ and $\alpha_{\text{Si}}=2.4 \times 10^{-6}/\text{K}$), which means that the GaP layer will be more compressively strained at growth temperature. In fact, the lattice mismatch is 0.52% at typical GaP/Si MBE growth temperature (580°C). However, it will become 0.36% at room temperature.

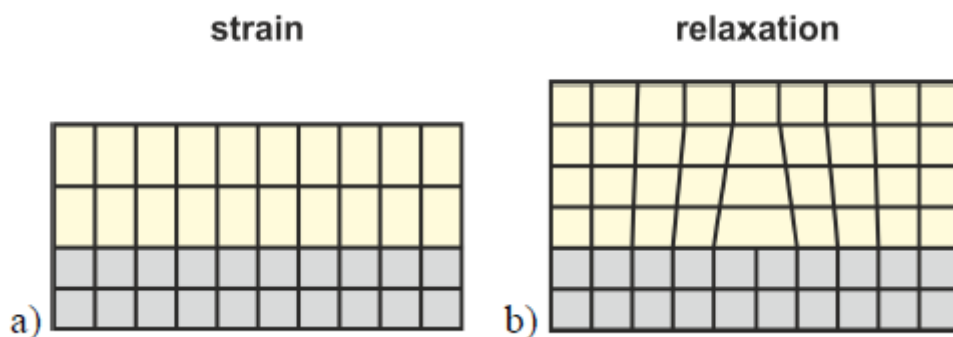


Figure 1.15 A 2D schematic representation of (a) elastic strain and (b) plastic relaxation at the interface of a heteroepitaxial thin layer grown on a lattice mismatched substrate. Courtesy of [71]

1.3.2 Polar on non-polar epitaxy

While the management of misfit dislocations and strain is a general concept in epitaxy, other defects are more specifically related to III-V/Si heterogeneous epitaxy. This is the case of stacking faults (SFs), microtwins (MTs) and antiphase domains (APDs). These defects are attributed to the difference of the two crystal symmetries and surface energies, and are specifically observed when a polar semiconductor (e.g. a III-V compound) is heteroepitaxially deposited on a non-polar one (e.g. the silicon).

1.3.2.1 Stacking faults and microtwins

The stacking faults are planar defects which alter the crystallographic plane order. They are found in close-packed structures where atomic layers are arranged in a certain stacking order. Most of the III-V semiconductors are formed in the zinc-blende structure, which includes two face centered cubic (fcc) sublattices. The crystallographic order in the (111) plane can be expressed as a ABCABCABC ordering atomic sequence. Stacking faults are formed when the sequence is altered and it is modified as ABCACABC or ABCAABCABC which are called respectively intrinsic or extrinsic stacking faults (as shown in **Fig. 1.16**).

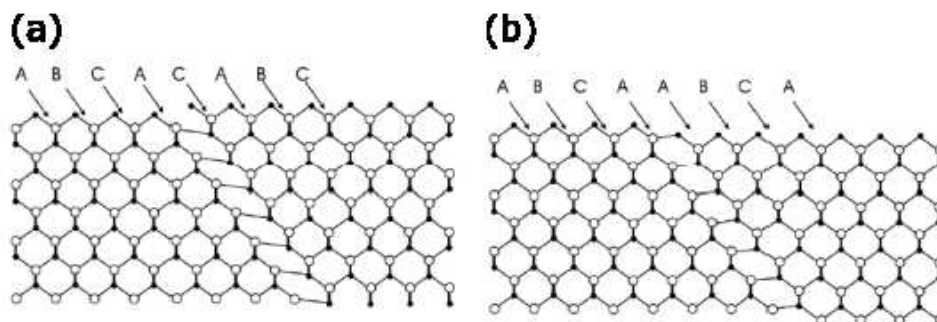


Figure 1.16 Representation of (a) intrinsic (b) extrinsic stacking faults. Courtesy of [72]

In addition, a stacking fault is bounded by two partial dislocations given by the dissociation of a perfect dislocation (which has a higher energy). If the crystallographic order is changed so that the atoms arrange in a mirror symmetric-like order, the stacking fault formed is called microtwin. The microtwins can be described as a 60° or 180° crystal rotation with respect to the $\langle 111 \rangle$ (Fig. 1.17). This is commonly observed in the case of Zinc-Blende III-V/Si epitaxy. It should be noted that to our knowledge, the precise origin and description of their formation (chemical preparation of the silicon, influence of silicon steps, growth temperature, surface energy) was not yet clarified in the literature up to now.

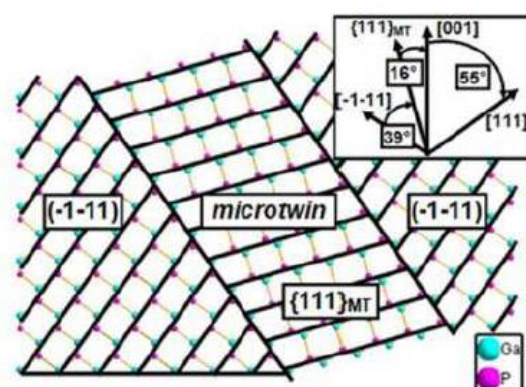


Figure 1.17 Schematic representation of a microtwin model in a zinc-blende GaP structure.
Courtesy of [69]

1.3.2.2 Antiphase domains and antiphase boundaries

As mentioned previously, the III-V Zinc-Blende material structure is a material with polar bonds where each group-III atom is bounded to four group-V atoms. The Si diamond crystal structure is however non-polar, and each Si atom is bounded to other four Si atoms. During the epitaxial growth of III-V semiconductors on Si, antiphase domains can be formed, which are bounded by the so-called antiphase boundaries (APBs). APBs are highlighted by the reversal of the III-V bond polarity. A sketch of a vertical stoichiometric APB at the atomic scale is shown in Fig. 1.18. More details about APBs will be given in the following.

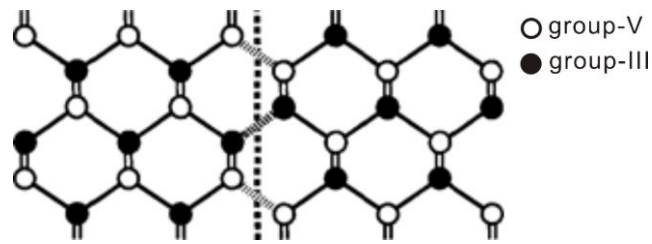


Figure 1.18 Sketch of the Antiphase boundaries with wrong V-V or III-III bonds marked by the dashed line. Courtesy of [73]

1.4 Generation mechanism and properties of antiphase boundaries

For years, APBs were considered as the most important issue to be understood during III-V/Si epitaxy, as their presence strongly modify electrical and optical properties of the III-V/Si devices, as well as the surface roughness of samples. Its generation mechanism and properties were thus widely investigated since the 80's for the different applications of III-V/Si materials.

1.4.1 Classification and formation energy of antiphase boundaries

An AntiPhase Domain (APD) is a domain composed of bulk semiconductor, bounded by APBs. APBs are planar defects consisting of anti-site (“wrong”) bonds, i.e. III-III and/or V-V bonds. The existence of APBs was first proposed by Aminoff & Broome in 1931 [74]. APBs can be classified as stoichiometric ones or non-stoichiometric ones, depending on the total density of each type of wrong bonds. The stoichiometric ones have equal numbers of III-III and V-V bonds within the same APB as shown in **Fig. 1.19a**. On the other hand, non-stoichiometric ones do not have the same number of III-III and V-V bonds. An extreme case can be found when considering APBs composed only of III-III bonds or V-V bonds, which are supposed to be highly charged, as shown in **Fig. 1.19b**. In the different chapters of this thesis, we will sometimes consider only this extreme case as representative of non-stoichiometric APBs for the sake of simplicity. The formation energies of stoichiometric and nonstoichiometric APBs lying along different

crystallographic plane (including $\{110\}$, $\{111\}$, $\{112\}$, and $\{113\}$) of GaAs and GaP were studied theoretically using a full-potential linearized augmented plane-wave density-functional approach and described in the pioneering works of Rubel *et al.* [75]. The corresponding results are shown in **Fig. 1.20**. They found that the formation energy of APB's in GaP is about 20% higher than that in GaAs. Besides, it reveals that the nonstoichiometric $\{111\}$ APB has the highest formation energy, while the stoichiometric $\{110\}$ APB has the lowest energy due to charge compensation effect. Both $\{112\}$ and $\{113\}$ APB's have an intermediate value of the formation energy. On this basis, many papers in the literature considered that the generation of stoichiometric APBs should be the dominant process during III-V/Si heteroepitaxy. We will show in next chapters that it is not the case.

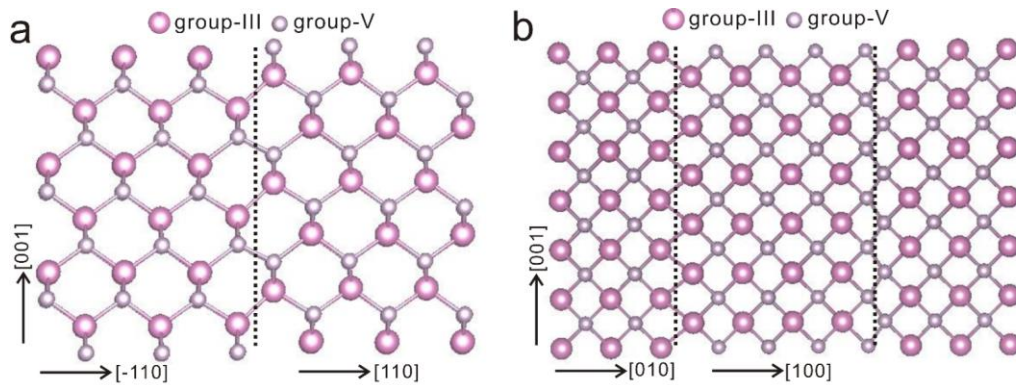


Figure 1.19 Atomic configuration of stoichiometric (a) or non-stoichiometric APB (b).

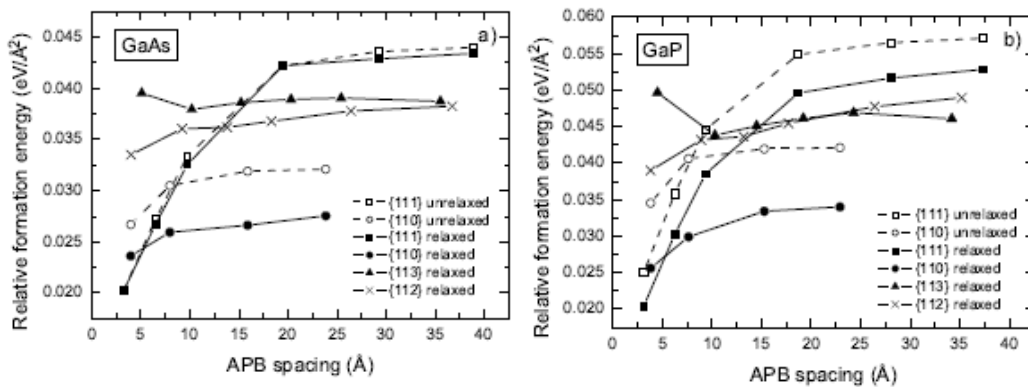


Figure 1.20 Specific formation energy of the $\{110\}$, $\{111\}$, $\{112\}$, and $\{113\}$ APB's in GaAs (a) and GaP (b). “Relaxed” and “unrelaxed” refer to calculations that include or exclude relaxation of atomic coordinates within the supercell. Courtesy of [75]

1.4.2 Formation mechanism of antiphase boundaries

1.4.2.1 Historical approach

At the beginning of my thesis, the formation mechanism of APBs, and the role of the starting Si surface, was mostly understood through the historical models proposed in the 80's. In 1987, two different mechanisms for the generation of APBs were firstly proposed by Kroemer [73]. In this seminal work, it was considered that if neither group-III nor group-V elements have a preferential probability of bonding to the substrate surface, APBs could be induced at the interface between the III-V semiconductors and the Si substrate, as shown in **Fig. 1.21a**. In order to simplify the process, it has been widely accepted that the deposition of III-V materials on Si (001) always starts with the same kind of atom in the literature, as shown in **Fig. 1.21b-d**.

In addition, Kroemer also proposed a strong correlation between the APBs and the kind of steps present on the Si (001) surface. If the III-V layer deposition nucleates always with the same atom on the Si, a Si surface populated only with D-steps does not lead to the formation of APBs, as shown in **Fig. 1.21b**. However, when the step height corresponds to an odd number of atomic planes, the III-V material grows with inverse polarities on each side of the step generating an APB, as shown in **Fig. 1.21c** and **Fig. 1.21d** [73,76].

The idea above rapidly became the main motivation for using substrates with a miscut, in order to form biatomic steps (**Fig. 1.21b**) at the Si surface and avoid theoretically the generation of APBs in the subsequent III-V growth process. Based on this model, K. Volz *et al.* explained their remarkable achievements about high quality epitaxial GaP/Si by considering a 2D III-V growth mode on the substrate [73]. The recent studies in our group and in this thesis strongly challenge this view, which will be discussed in the following parts. Besides, based on the index planes and types of APBs, researchers discussed the propagation or annihilation of APBs [77]. It was considered that the stoichiometric APBs with lower formation energies usually form perpendicularly to

the interface. In this case, the stoichiometric APB will propagate easily and cross the whole III-V layer, emerging at the surface. For the non-stoichiometric APBs with higher formation energy, they were considered to form in higher index planes with an inclined angle with respect to the substrate. In this case, it may lead to cross another APB, and thus allowing the so-called annihilation of these defects. In the present work, we will also challenge this view.

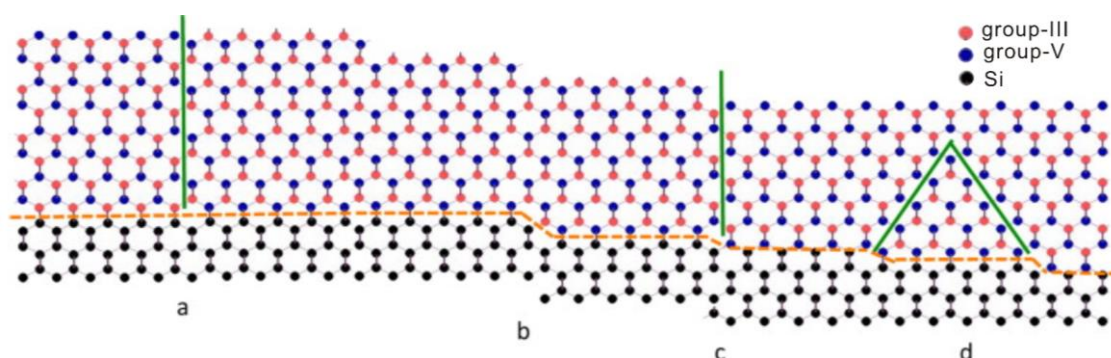


Figure 1.21 (a) A III-V material grown on a Si (001) substrate in cross-sectional view, where the Si, Group-V and Group-III atoms are depicted in black, blue and red, respectively. APBs are highlighted by green lines. According to Kroemer's description, APBs can be generated by mixed nucleation on the same terrace (a), or it can be the consequence of silicon monoatomic steps (b, c&d). For simplicity, it is considered in (b), (c) and (d) that the nucleation of the III-V layer on Si starts always with the same type of atom. In this configuration, D-steps do not generate APBs. (c) and (d) show APBs generated by S-steps on the Si surface. (c) APB generated in the $\{110\}$ plane perpendicular to the interface and (d) APBs self-annihilation model base on generation of APBs along $\{111\}$. Courtesy of [78]

For years, researchers have been widely adopting the above model for the description of APBs generation, and as an explanation for the needs of using a miscut to achieve good quality III-V/Si epilayers [76]. Indeed, this model provides an easy representation about APBs generation and propagation, but also faces fundamental inconsistencies with the experimental data published during these last 40 years. Together with French academic partners (IES, IPR, C2N, CEMES and CRHEA), our laboratory revisited this model in 2018 [3] and in 2020 [4], which will be explained in the next section.

1.4.2.2 Generation, propagation and burying of antiphase domains: recent findings

In 2018, I. Lucci *et al.* proposed a more comprehensive picture: an alternative model [3] based on Density Functional Theory calculation and the extensive in-depth atomic-scale characterization of a variety of GaP/Si, AlSb/Si and AlN/Si samples. Conclusions of this study can be summarized as follows. Firstly, there is always a partial wetting between III-V semiconductors and Si, thus leading to the formation of pure 3D Volmer-Weber growth mode, irrespective of the lattice mismatch (**Fig. 1.22**). As an example, they provided the energy-dispersive x-ray spectroscopy (EDX) image displayed in **Fig. 1.22a**, which shows that AlSb nucleation on Si generates 3D islands. This growth mode is also experimentally confirmed by some other studies [79,80]. Therefore, the 2D nucleation growth mode of III-V semiconductor layer on Si substrate in the historical approach shown in **Fig. 1.21** simply cannot happen. Secondly, they demonstrated that APBs are generated during the coalescence of 3D islands having different phases, which was briefly suggested in pioneering works on III-V/Ge [81]. They also proved that the size of individual monodomain islands can be much larger than the distance between steps (the terrace width), suggesting that the step itself cannot be the main cause for the APDs generation, which also contradicts the historical Kroemer's model. Thirdly, they showed that the elastic energy does not have a significant impact on the island morphology at the coalescence growth step for most III-V/Si materials systems (and therefore does not impact the APD distribution), as most of the islands are already plastically relaxed (even for GaAs/Si [82]) at this stage (or quasi-unstrained in the particular case of the quasi-lattice-matched GaP/Si system). In addition, they made the hypothesis that the epitaxial relationship is defined locally at the nucleation site which further governs the phase distribution.

In 2020, this work was further developed, generalized and completed by our group [4]. We investigated comprehensively the effect of the Si substrate miscut on III-V epitaxy on Si and proposed two regimes that determine the initial APB distribution. At very low

miscut angles, several islands of the same domain can nucleate on a terrace. The APB distribution is then expected to follow the step distribution on the surface. This is the so-called terrace-driven regime (**Fig. 1.23a**). At higher miscut angles, monodomain islands nucleate randomly, and as explained above, the size of these islands is larger than the terraces width. Therefore, the APB distribution is no longer correlated to the step distribution. This is the so-called nucleation-driven regime (**Figure 1.23b**). We also demonstrated that for the majority of III-V semiconductors grown on Group-IV substrates, the critical miscut angle at which the regime evolves from terrace-driven to nucleation-driven is in the range of $[0.1-1]^\circ$. In this thesis, most of the Si substrates used for the deposition of III-V layers have an intentional or residual miscut larger than 0.1° [76]. Therefore, in most cases the formation of the two different polar-domains will be considered as governed by the nucleation-driven regime. Besides, through introducing the growth rate imbalance coefficient $C_{\alpha/\beta}$ (which is a simple ratio between the growth rate of two adjacent phases α and β), we discussed the growth conditions requirements needed for the propagation or burying of APBs. When the $C_{\alpha/\beta}$ is lower or larger than unity, the β phase or α phase will grow faster than the other one. Like this, only one phase will become dominant, and therefore the APDs will be buried. When the $C_{\alpha/\beta}$ equals to one, the growth rates are the same and APBs will propagate to the surface. Moreover, we demonstrated how the growth rate imbalance is closely related to the growth temperature and V/III ratio chosen during the III-V/Si growth. As a general conclusion of these recent experimental and theoretical developments, one can keep in mind that these works give the keys to ultimately control the lateral and vertical extents of APBs and APDs [65,83].

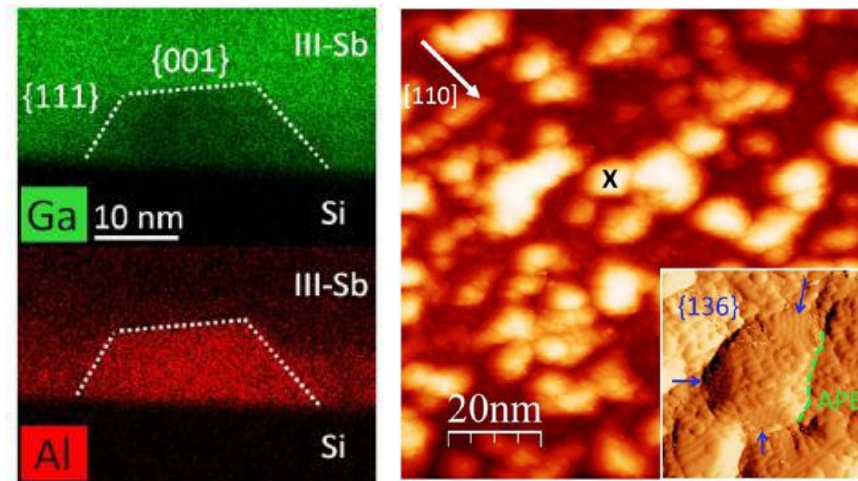


Figure 1.22 3D islands in various III-V on Si material systems. STEM-EDX image of GaSb/AlSb layers grown on 6° miscut Si, showing the Ga and Al concentration (a). Plan view STM imaging of a 3 nm-thick GaP deposition on 6° miscut Si. The $20 \text{ nm} \times 20 \text{ nm}$ inset shows the atomically resolved morphology of the individual island marked in black. APB is highlighted in green (b). Courtesy of [3]

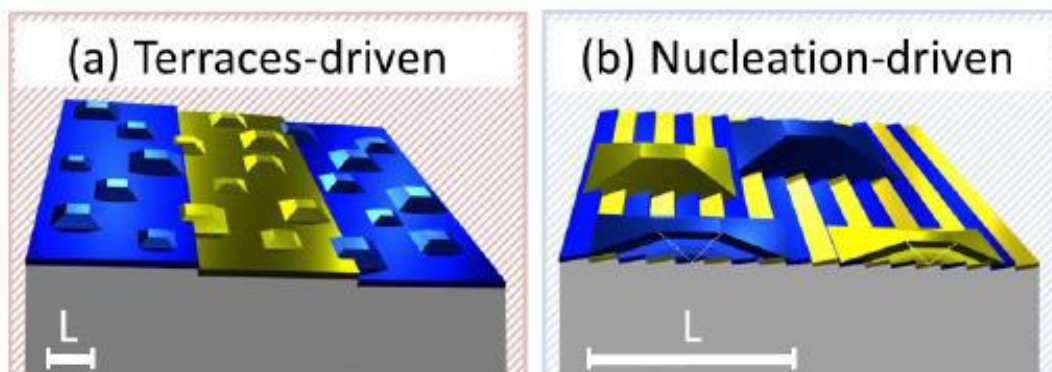


Figure 1.23 Terrace-driven regime (a) and nucleation-driven regime (b) phase distribution in III-V monodomain islands grown on low and large miscut group IV substrates, respectively. Courtesy of [4]

1.4.3 Optoelectronic properties of antiphase boundaries

Many works in the broad literature on the subject of III-V/Si monolithic integration made reference to APBs as detrimental defects for photonic or energy harvesting devices [84,85], without providing explanation of this observation. Of course, this statement is based on the common observation of scientists that any laser or photovoltaic device

simply cannot work if APBs are not buried in the structure. To explain this behavior, scientists have claimed for decades that APBs are non-radiative recombination centers. But, as we are going to explain in this thesis, this is far from the real situation. Indeed, when looking carefully at the atomic scale structure of one antiphase boundary, the topology observed is fundamentally different as compared with e.g. grain boundaries in other polycrystalline materials, as they do not contain any dangling bonds, and respect the lattice ordering. Surprisingly, at the beginning of this thesis, only a few works focused specifically on the study of antiphase boundaries optoelectronic properties.

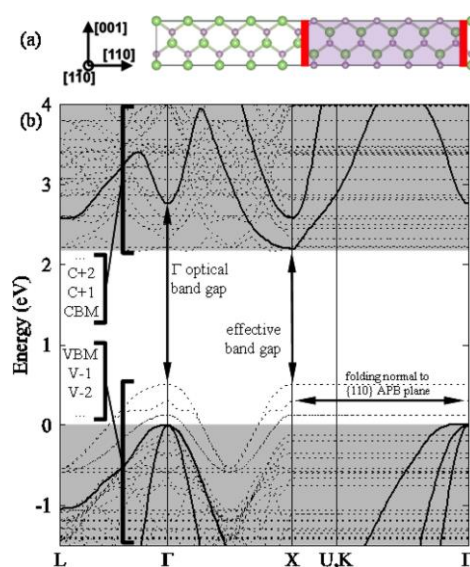


Figure 1.24 (a) Sketch of a $\{110\}$ supercell containing APBs. APBs are indicated by thick vertical lines. (b) Band structures for irreducible GaP unit cell (thick solid lines), and APB spacing supercell (dots). Shaded areas correspond to energy space occupied by bulk states. Courtesy of [86]

Tea *et al.* studied the optical properties of stoichiometric APB in GaP by electronic band structure and absorption calculations [86]. The band structure (**Fig.1.24**) shows that APBs introduce several new localized states at the top of the valence band, shifting the VBM (valence band maximum) upward (by roughly 0.5 eV) and thus reducing the band gap. Besides, the imaginary part of the calculated dielectric function for direct optical transitions was extracted versus the energy, as shown in **Fig.1.25**, which reveals that the absorption onset appears at lower photon energies for the APB structure (≈ 1.7 eV) compared to the bulk one (≈ 2.8 eV) due to the reduction of the bandgap.

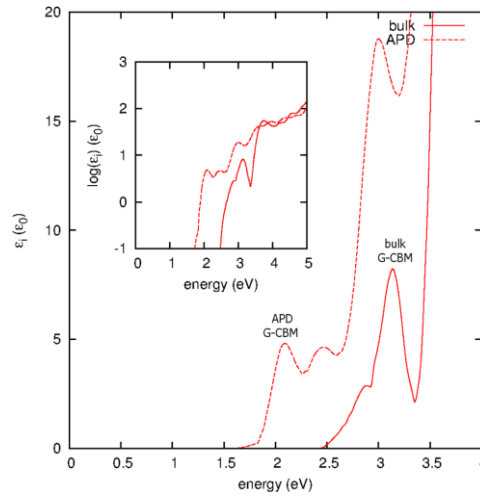


Figure 1.25 Imaginary part of the calculated dielectric function for direct optical transitions $\epsilon_i(q \rightarrow 0, \omega)$. Results for bulk and APB structure are drawn with solid and dashed lines, respectively. The inset shows the same data on a log scale. Courtesy of [86]

1.5 Conclusions and objectives of the thesis

In summary, the integration of III-V semiconductors on Si combining the advantages of Si (earth abundance, low cost and prevalence in the electronics and PV industries) with the excellent optoelectronic properties of III-V, is of great interest in photonics and energy harvesting applications. The different III-V/Si integration approaches and the specific issues related to the monolithic integration were presented in this chapter. Among the different crystal defects generated at the III-V/Si interface and propagating in the materials and devices, the recent researches about the antiphase domain and boundaries generation, propagation and burying were reviewed, giving keys to tune at will their distribution in III-V/Si samples.

At the beginning of my thesis, the main objective was to clarify and assess optoelectronic properties of III-V (GaP-based)/Si samples and devices. Rapidly, from the results obtained, we jointly decided to refocus the thesis objectives on the theoretical and experimental study (**Chapter 2**) of the specific optoelectronic properties of APBs, and its use for energy harvesting devices. This led to the following main results:

- First demonstration of the strong electron-phonon coupling arising in stoichiometric

III-V/Si APBs and clarification of optoelectronic properties (**Chapter 3**).

-First demonstration of a bulk III-V/Si photoelectrode for solar water splitting applications, with assessment of III-V/Si bandgaps and bandlineups, and promising PEC performances (**Chapter 4**).

-First evidence of the hybrid 2D-semimetal/semiconductor ambipolar and photoactive properties of epitaxial III-V/Si samples with non-stoichiometric APBs (**Chapter 5**).

Chapter 2: Experiments and DFT calculations

In this chapter, the experimental and theoretical tools supporting this work are presented. All the samples used in this work were grown by Molecular Beam Epitaxy (MBE), except when bare substrates were used as a reference. The basic principle of MBE sample growth in our lab is shown in appendices and the specific growth parameters will be given when needed in the following chapters. Here, the different experimental characterizations setups are first described, with the related physical mechanisms, and parameters settings used in this thesis. The DFT calculations are then introduced, with a brief introduction to the basic concepts of the DFT, followed by the calculation steps and parameter settings for the determination of electronic band structure, and of the vibrational and electron-phonon coupling properties.

2.1 Structural investigations and surface processes

2.1.1 Atomic force microscopy

Atomic Force Microscopy (AFM) is a characterization technique used to obtain the topography of the surface of a sample. This technique is easy to use because no special treatment of the sample is needed before measurement, and it is a technique that can be used for a large variety of materials, including soft or non-metallic materials. The AFM used in this thesis is a Veeco di Innova setup, presented in **Fig. 2.1**, allowing producing $100 \times 100 \mu\text{m}^2$ images with a lateral resolution of 15 nm and a vertical resolution of 0.2 nm in standard conditions.

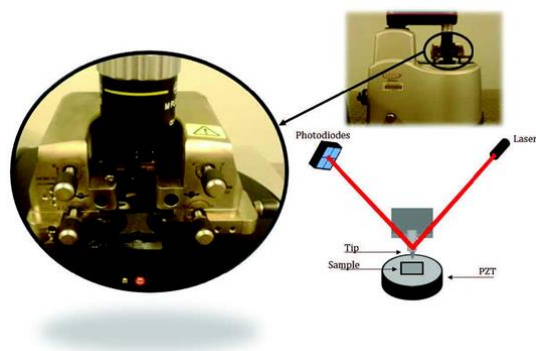


Figure 2.1 Veeco di Innova setup of the FOTON institute at INSA Rennes [87].

The operating principle of the AFM is to use a fixed tip (typically made by Si_3N_4 or Si) on a deformable cantilever to probe the surface of the sample through the tip/surface interaction. Depending on the type of sample analyzed, the interaction can occur through different types of forces: Van Der Waals force, capillarity force, electrostatic force or magnetic force. The deviation of the cantilever Z is proportional to the interaction force F : $F = -kZ$. The radius of the tip used is typically around few nanometers, allowing an accurate surface characterization of the sample at a nanometer scale. A red laser source is focalized on the top of the cantilever and reflected to a four-quadrant photodiode to record the spatial variation of laser intensity due to the cantilever's deviation (X, Y and Z directions), and the cantilever's torque. Meanwhile, the substrate is moved to keep a constant interaction between the tip and substrate surface. The movement is realized by a cylinder-shaped piezoelectric (PZT) tube, whose shrinkage and expansion will lead to a movement in three dimensions. Through a loop system, the Z-movement of the piezoelectric tube is indirectly controlled by the signal received from the photodiode.

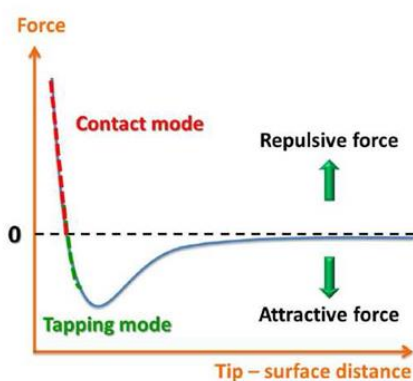


Figure 2.2 Force profile when the distance between the tip and the surface changes [88].

AFM measurements can be performed in two basic working modes (see **Fig. 2.2**): contact mode and non-contact mode ("tapping" mode). In the contact mode, the type of force is repulsive and the tip scans over the surface maintaining the cantilever vertical deviation at a constant level. Before starting the measurement, the laser is adjusted at the end of the cantilever and the reflected spot is positioned as a reference at the center of the photodiode. During the scanning, the deflection is recorded by the optical system and is compared by a DC feedback loop to the set-point level. The resulting error signal from the amplifier is used to actuate the PZT, moving the sample in order to maintain constant the tip/sample interaction by applying the required voltage. The tapping mode alternatively uses both the attractive and repulsive forces. The cantilever vibrates at high frequency. Therefore, the detected signal on the photodiode alternates. The amplitude of the vibration is sensitive to the force between tip and sample surface, which changes with the distance between them. In this situation, the feedback loop aims to maintain a constant oscillation amplitude keeping constant the average distance between the cantilever and the surface. As compared to the contact mode, tapping mode shows some advantages: samples with soft surfaces will be less damaged and the tip will be less contaminated. In this thesis, all the AFM measurements were performed in tapping mode with the cantilever tuned around 293 kHz.

2.1.2 Conductive atomic force microscopy

In order to characterize the transport properties of APBs of III-V/Si samples, Conductive Atomic Force Microscopy (C-AFM) measurements were performed, in close collaboration with IPR (Institut de Physique de Rennes).

C-AFM is a measurement technique that derives from atomic force microscopy, where a conductive tip scans the sample surface and a voltage is applied between the tip and the sample to generate an image related to the current measured. A topographic image is also generated simultaneously. Both the current and the topographic images are taken from the same area of the sample, which allows the identification of features on the

surface conducting more or less the current, as shown in **Fig.2.3**, and allowing the identification of possible current artefacts that could simply be due to the morphology. The main advantage of C-AFM over standard electrical measurement techniques is the high spatial resolution. On the other hand, a meaningful quantitative evaluation of the local current is hard to achieve, and most of the time, qualitative analysis is only proposed. In this work, we will use only qualitative comparisons between the different parts of the samples.

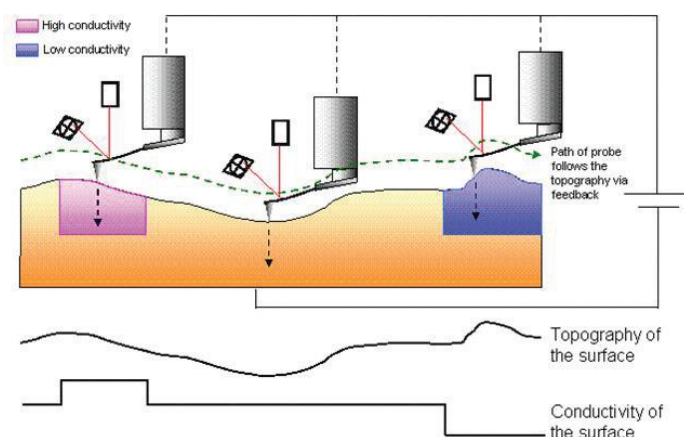


Figure 2.3 Schematic diagram of Conductive AFM system [89].

In this thesis, the C-AFM measurements are carried out on a Bruker Multimode AFM with a Pt/Ir coated Sb doped silicon cantilever (spring constant of 0.1 N/m, and resonant frequency of 10 kHz). Before measurements, the sample surface was exposed to a HF-5% solution for 1 minute (to remove the surface oxide), then the samples were rinsed in deionized water and then quickly transferred to the C-AFM set-up. Measurements were performed under dry nitrogen gas to limit humidity. Then different biases were applied to the III-V/Si samples at 0.3 Hz in contact mode. All current mapping images were obtained with the cantilever moving across the thin film surface.

2.1.3 X-ray diffraction

X-ray diffraction (XRD) is a powerful nondestructive technique for characterizing

crystalline materials. It provides information on structures, phases, preferred crystal orientations (texture), and other structural parameters, such as crystallinity, strain, and crystal defects [90]. X-ray diffraction is based on Bragg's law ($n\lambda=2d\sin\theta$). A monochromatic beam of X-rays is sent to the sample, and reflected X-rays are detected by a detector, as shown in Fig. 2.4.

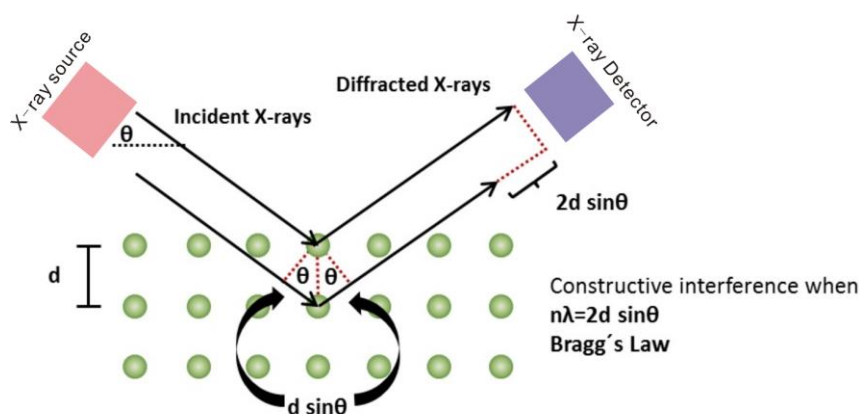


Figure 2.4 Schematic representation of the X-ray diffraction technique [91].

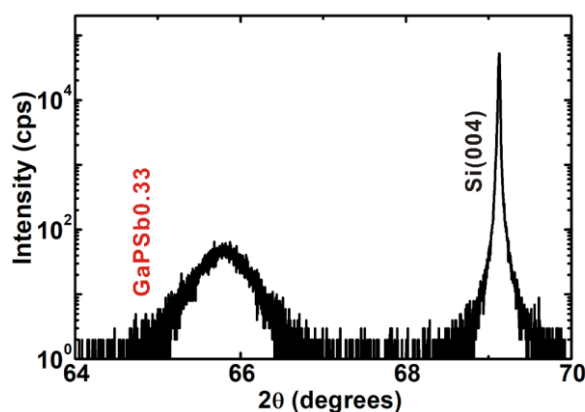


Figure 2.5 XRD pattern for one $\text{GaP}_{0.67}\text{Sb}_{0.33}/\text{Si}$ sample.

In this thesis, the compositions of different III-V/Si samples are determined with the XRD technique. For example, Figure 2.5 shows the XRD patterns for one $\text{GaP}_{1-x}\text{Sb}_x/\text{Si}$ sample by using a $\omega/2\theta$ scan. Assuming that the $\text{GaP}_{1-x}\text{Sb}_x$ epitaxial layer is fully plastically relaxed on the Si substrate, the free-of-strain cubic lattice constant of GaP_{1-x}

$x\text{Sb}_x$ (a_{fos}) can be obtained based on the equation:

$$a_{fos} = \frac{n\lambda}{2 \sin \theta} \sqrt{h^2 + k^2 + l^2} \quad (2-1)$$

Where n is equal to 1 for the first order diffraction maximum, λ is the wavelength of the X-ray source (Cu target was used in this thesis), θ can be obtained in the $\omega/2\theta$ scan, and the (h, k, l) are the Miller indices.

Then the Sb content in $\text{GaP}_{1-x}\text{Sb}_x$ can be calculated from the Vegard's law:

$$x = \frac{a_{fos} - a_{GaP}}{a_{GaSb} - a_{GaP}} \quad (2-2)$$

Where a_{GaP} and a_{GaSb} are the lattice constant of GaP and GaSb. Based on the equations above, the Sb content for the studied sample is 33% here.

However, if the relaxation and strain state of the epitaxial layer is unknown or not certain, then reciprocal space mappings (RSM) will be needed to determine the relaxation degree (R) and calculate the composition. **Fig 2.6** shows the RSM around the (224) Bragg peak for the $\text{GaP}_{0.67}\text{Sb}_{0.33}/\text{Si}$ sample (S_x and S_z are the projected coordinates in the right handed Cartesian, with z axis parallel to the surface normal).

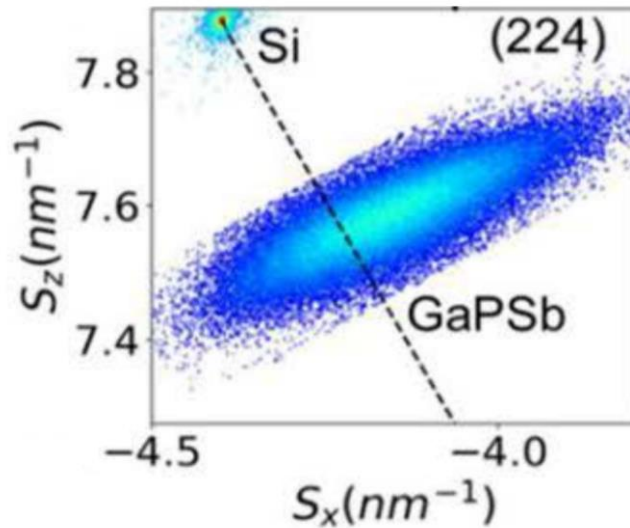


Figure 2.6 The RSM around (224) for the $\text{GaP}_{0.67}\text{Sb}_{0.33}/\text{Si}$ sample (S_x and S_z are the projected coordinates in the right handed Cartesian, with z axis parallel to the surface normal) [92]. The black dot line the represents the full relaxation line.

Lattice constants in the in-plane and out-of-plane directions can be directly deduced from the RSM [88]:

$$a_L^{//} = a_S \frac{S_{sub}^{//}}{S_L^{//}} \quad (2-3)$$

$$a_L^{\perp} = a_S \frac{S_{sub}^{\perp}}{S_L^{\perp}} \quad (2-4)$$

Where $a_L^{//}$ and a_L^{\perp} are the lattice constant of the epitaxial layer in the directions parallel and perpendicular to the surface (in-plane and out-of-plane), a_S is the lattice constant of the substrate, $S_L^{//}$, S_L^{\perp} , $S_{sub}^{//}$ and S_{sub}^{\perp} are the positions of the layer and the substrate diffraction spots in the RSM in the directions parallel (corresponding to S_x) and perpendicular (corresponding to S_z) to the surface. The free of strain cubic lattice constant of the GaPSb layer (a_L^{fos}) is then given by:

$$a_L^{fos} = \frac{a_L^{\perp} - \alpha a_L^{//}}{1 - \alpha} = \frac{a_L^{\perp} + 2 \frac{C_{12}}{C_{11}} a_L^{//}}{1 + 2 \frac{C_{12}}{C_{11}}} \quad (2-5)$$

Where $\alpha = \frac{e_{zz}}{e_{xx}} = -2 \frac{C_{12}}{C_{11}}$ and the C_{12}, C_{11} are the elastic constants of GaPSb. The Sb content x is then deduced based on the Vegard's law.

The relaxation degree (R) can also be determined by using:

$$R = \frac{a_L^{//} - a_S}{a_L^{fos} - a_S} \quad (2-7)$$

In **Fig.2.6**, the black dotted line represents the full relaxation line, which goes through the center of Si RSM signal and the origin point ($S_z=S_x=0$). In this case, the signal of GaPSb appears around the full relaxation line, indicating that the GaPSb alloy is almost fully plastically relaxed. In this thesis, the full relaxation lines will be given in all the RSM for the samples studied. If the peak of the epitaxial layer is vertically aligned on the substrate peak, then the layer will be considered as fully biaxially strained ($R=0$). If the peak of the layer is located around the full relaxation line, then the layer will be considered as fully relaxed ($R=1$). In between, the samples will be considered as partially relaxed.

The XRD characterizations in this thesis are performed on a 4 circles Bruker D8 Diffractometer. A Bartels asymmetric Ge (220) monochromator was used for both line scans and reciprocal space maps. The detection is ensured by a LynxeyeTM, 1 dimensional position sensitive detector (PSD) allowing a collection angle of 2.6° over 2θ .

2.1.4 Scanning transmission electron microscopy

The scanning transmission electron microscope (STEM) has become one of the prominent structural analysis tools for high spatial resolution imaging and spectroscopy of materials, most notably at atomic resolution [93]. A highly-focused electron probe is raster-scanned across the material, and the various types of electron scattered are then collected and analyzed as a function of the position. The sample needs to be thinned to guarantee transmission of electrons, and limit the volume of the probed layer. The transmitted electrons at high scattering angle can be collected to form high-resolution, chemically sensitive, atomic number contrast images. The X-rays generated can be collected using an energy-dispersive X-ray spectroscopy (EDX) detector and further used to form high spatial resolution compositional maps.

The STEM measurements in this thesis were performed by our German partner (IHP-microelectronics). The STEM high-resolution imaging and Energy Dispersive X-Spectroscopy (EDX) (presented in **Chapter 3**) were obtained by a FEI Tecnai Osiris TEM tool, operating at 200 kV with implemented energy-dispersive x-ray (EDX) detector. TEM lamellas were prepared by milling and undercutting processes using a Zeiss NVision 40 focused ion beam operating at up to 30 kV.

2.1.5 Chemical mechanical polishing

Chemical mechanical polishing (CMP) is a process of smoothing surfaces with the combination of chemical and mechanical forces [94]. The process uses an abrasive and

corrosive chemical slurry in conjunction with a polishing pad and retaining ring, typically of a greater diameter than the wafer. The pad and wafer are pressed together by a dynamic polishing head and held in place by a plastic retaining ring. The dynamic polishing head is rotated with different axes of rotation (not concentric). This removes material and tends to even out any irregular topography, making the wafer flat or planar. The schematic diagram of functional principle of CMP is shown in **Fig.2.7**.

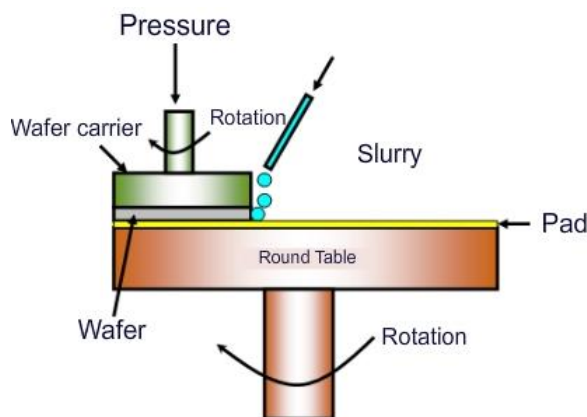


Figure 2.7 Functional principle of CMP [95].

In this thesis, to improve the surface quality, III-V/Si samples were polished applying CMP on the surface with 1% H_3PO_4 . **Figure 2.8** shows the SEM images of one III-V/Si sample before and after CMP, from which we can find that the surface of the sample becomes much smoother than the as-grown one (before CMP). Besides, during this thesis, this technique was further improved by J. Le Pouliquen and Y. Léger to highlight the APBs emerging at the surface of III-V/Si samples, by combining CMP and additional etching [65].

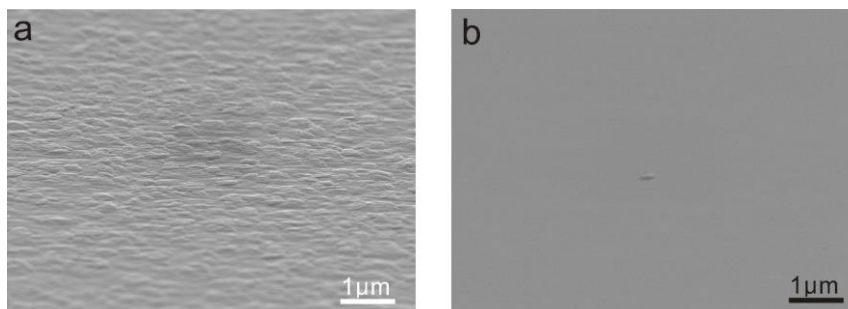


Figure 2.8 SEM image of a III-V/Si sample before (a) and after (b) CMP.

2.2 Optical characterizations

2.2.1 Photoluminescence

Figure 2.9 shows the principle of the photoluminescence (PL) experiment. Under light illumination, the electrons of the semiconductor on ground states (in valence band or on some trap states) are excited to higher energy states by absorbing photons of the pumping laser beam. The electrons photo-generated remain in the excited state for a very short time (around 10^{-12} s). Then, the electrons relax to lower states (the bottom of the conduction band or some localized states) mostly by phonon emission. Finally, the electrons will go back to the ground states (recombine with holes) and at the same time give rise to photoluminescence.

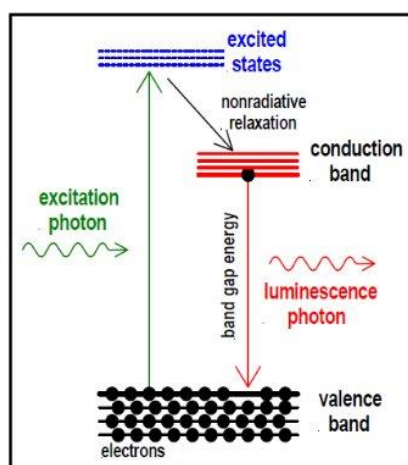


Figure 2.9 Principle of photoluminescence (PL) spectroscopy [96].

The setups used for PL experiments at room temperature and low temperature are described in **Fig. 2.10**. The laser beam mainly used during this thesis was a 405 nm laser diode. The laser beam goes through different plane mirrors and illuminates on the sample surface, which is positioned horizontally in the ambient air for room temperature PL, and vertically in a cryostat for low temperature PL. The photoluminescence emitted by the sample is then collected by spherical mirrors and sent to a Si detector, through a monochromator (iHR320 Horiba). In order to study the evolution of the PL signal with

the temperature variations, we have used a helium bath closed cycle cryostat to control the temperature and study the PL properties from 15 K to 300 K.

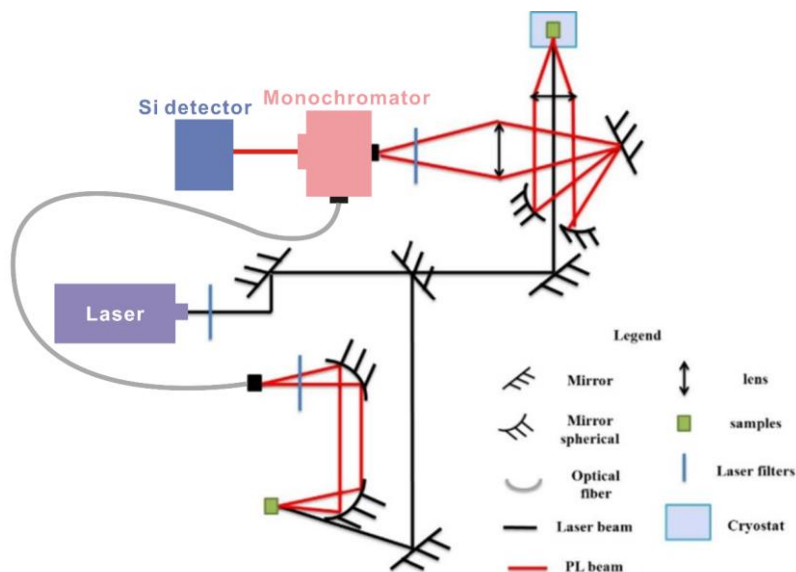


Figure 2.10 FOTON experimental setup at room (lower part) and low temperature (upper part) [97].

Besides, with the helium bath closed cycle cryostat, low temperature time-resolved PL of some III-V/Si samples (the results are shown in **Chapter 3**) was also measured at 15 K by using a Q-switched 355 nm pulse laser at an excitation density of 560 mW/cm^2 (pulse duration: 7 ns, repetition rate: 5 kHz). The signals were filtered by two different bandpass filters of 600 and 800 nm. The fluorescence lifetime was determined by time-correlation single photon counting based on Single Photon Detector driver with integrated correlator (SPD-TDC) setup. The SPD-TDC is provided with a time to digital converter, placed at two avalanche photodiode electrical output. It's possible to acquire directly via the graphical user interface, the photons arrival time relative to the trigger input or between two photons arrival time named time correlation single photon counting.

2.2.2 Raman spectroscopy

Raman spectroscopy is a spectroscopic technique typically used to determine vibrational modes of molecules. Raman spectroscopy is based on inelastic scattering of

photons, known as Raman scattering. Typically, for Raman measurement, the samples are illuminated by a monochromatic laser source and the scattered light is then collected in a spectrometer.

When the samples are illuminated by a monochromatic laser source, most of the scattering that takes place is elastic, with no loss of energy, and therefore no frequency change. This is known as Rayleigh scattering (**Fig.2.11** red line), which needs to be filtered out and discarded during the Raman measurement. Raman scattering, on the other hand, is due to inelastic scattering. The incident photons are scattered by the vibrational or rotational modes of molecules/dimers/bonds in the sample, which causes a change in the energy and frequency of the scattered light as compared to the incident light. During the scattering process, the incident photon may release energy to the lattice (or to some molecules) through vibrations/rotations, and thus the photon is scattered with a redshifted frequency; this is the so-called Stokes shift (**Fig. 2.11**). On the contrary, during the scattering, transfer of vibrational or rotational energy from the lattice (or from the molecule) to the scattered photon may occur. The light output will have a blue-shifted frequency, which is called as anti-Stokes shift (**Fig. 2.11**). In most cases, the photons collected and analyzed during the Raman scattering experiments are corresponding to the Stokes photons (referred to as Stokes lines), which corresponds to the most probable process, thus leading to larger light intensity.

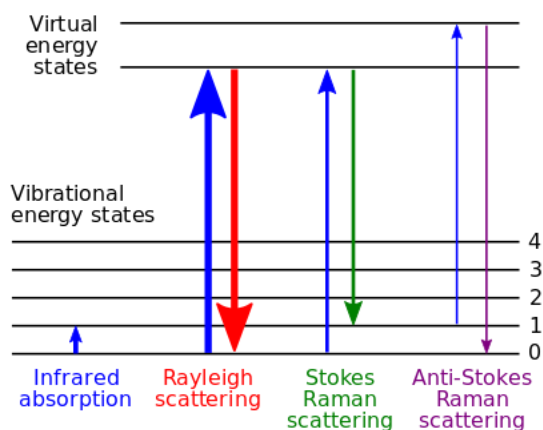


Figure 2.11 Energy-level diagram showing the states involved in Raman spectra [98].

In this thesis, the Raman measurements were performed in collaboration with both IPR (Institut de Physique de Rennes) and IHP microelectronics (Germany). At IPR, the Raman image was obtained with a HR800 micro-Raman spectrometer (HORIBA Scientific). The HR800 system is a high-resolution spectrometer fitted with a confocal microscopy system coupled to different lasers. Our experiments were performed in "confocal mode" with a 532 nm laser diode for excitation and, to avoid sample heating, an optical density filter was used.

2.2.3 Ellipsometry

Ellipsometry is traditionally used to determine the complex refractive index of thin film materials ($n' = n + ik$) and their thickness. It is a non-destructive technique, currently used for determining the dielectric functions of thin films and substrates [99]. In this thesis, we mainly focused on the determination of the complex part (k) of the refractive index to deduce the absorption coefficient (α) of the III-V layers grown on Si substrate by applying the well-known formula:

$$\alpha = \frac{4\pi k}{\lambda} \quad (2-8)$$

Ellipsometry principle is based on the measurement of a change in polarization as light reflects or transmits from/through a material (see schematic image in **Fig. 2.12**). The polarization change is represented as an amplitude ratio, Ψ , and the phase difference, Δ , according to the following relation:

$$\frac{r_p}{r_s} = \tan \Psi \cdot \exp\{i\Delta\} \quad (2-9)$$

Where r_p and r_s are respectively the complex reflection coefficient for p and s polarization. Our experimental setup (Horiba UVSEL 2) comprises two detectors for a spectral range from UV light (6 eV) until infrared wavelengths (0.5 eV). This equipment mainly consists in two optical arms and a sample-holder (as shown in **Fig. 2.12**). The first arm comprises a Polarization State Generator (PSG) coupled to a light source. In every case, the PSG includes a linear polarizer set at an azimuth P with respect to the plane of

incidence. The second arm is used to determine the polarization and intensity of the outgoing beam. It is composed of a Polarization State Analyser (PSA) and a detector.

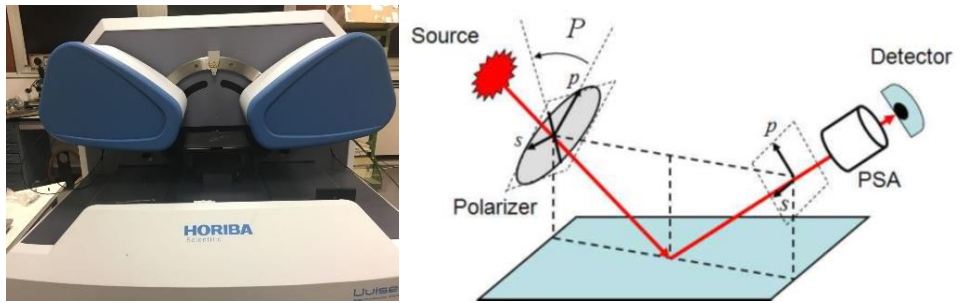


Figure 2.12 Real and schematic [100] images of the ellipsometry setup.

From the two values Ψ and Δ , the ratio (ρ) between r_s and r_p can be deduced. For a bulk material (a substrate), by taking into account the angle of incidence (θ), the so-called “pseudo” dielectric function can be easily obtained with the equation below:

$$\langle \epsilon \rangle = \epsilon_r + i\epsilon_i = \sin^2\theta \left[1 + \tan^2\theta \left(\frac{1-\rho}{1+\rho} \right)^2 \right] \quad (2-10)$$

However, for thin film deposited on a substrate, no direct formula can be applied, but the use of a model allows the measurement to be fitted. Thus, extraction of the absorption coefficient of a given single layer, or even of a layer in a multiple-stack structure can be done.

2.3 Photoelectrochemical characterizations

Photoelectrochemical (PEC) water splitting allows turning the liquid water into hydrogen and oxygen gases, based on semiconducting photoelectrodes under sunlight and a given voltage [101].

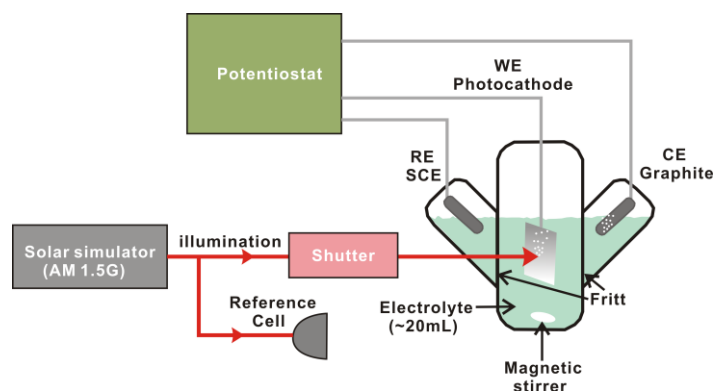


Figure 2.13 Schematic diagram of 3-electrodes photoelectrochemical measurements.

The photoelectrochemical characterizations for solar water splitting applications presented in **Chapter 4** and **Chapter 5** were first performed in collaboration with University College London (UCL), and were rapidly developed as well in collaboration with ISCR (Institut des Sciences Chimiques de Rennes). For the sake of simplicity, I will emphasize hereafter on the experimental tools I used during my thesis available at ISCR. It is mainly composed of one solar simulator (LS0106, LOT Quantum Design) equipped with an AM 1.5G filter, a Zennium potentiostat (Zahner) and a standard three-electrode configuration with a graphite rod as the counter-electrode and SCE (Saturated Calomel Electrode-Hg/Hg₂Cl₂) as the reference electrode (as shown schematically in **Fig.2.13**). The measured potentials vs. the reference electrode were converted to the standard Reversible Hydrogen Electrode (RHE) potential using the following equation:

$$E_{\text{RHE}} = E_{\text{SCE}} + 0.24 + 0.059 \cdot \text{pH} \quad (2-11)$$

For the specific results obtained at UCL and presented in **Chapter 4**, the reference electrode used in the standard three-electrode configuration was Ag/AgCl. In this case, the standard RHE potential was inferred using the following equation:

$$E_{\text{RHE}} = E_{\text{Ag/AgCl}} + 0.059 + 0.059 \cdot \text{pH} \quad (2-12)$$

Based on this PEC characterization setup, different measurements were performed in this thesis, including linear sweep voltammetry (LSV), Incident photon-to-current efficiency (IPCE), Electrochemical impedance spectroscopy (EIS) and Mott-Schottky

(MS) measurements.

2.3.1 Linear sweep voltammetry

Linear sweep voltammetry (LSV) is a voltammetric method where the current at a working electrode is measured while the potential between the working electrode and a reference electrode is swept linearly in time [102]. Normally, the LSV can be measured under three different conditions: in the dark, under light and in chopped light mode (dark and light states shown alternatively).

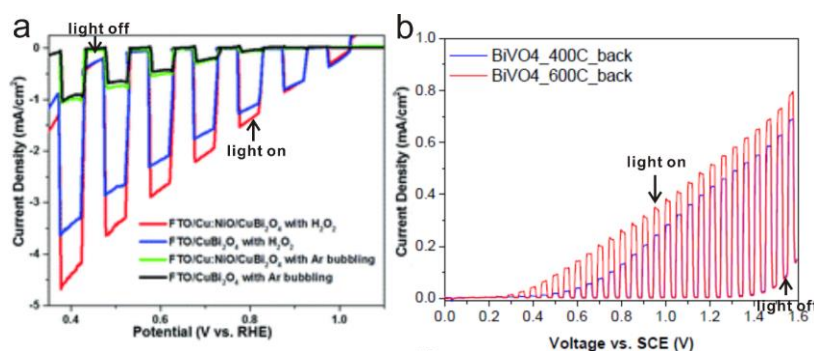


Figure 1.14 Chopped light LSV curves of semiconductor working as photocathode(a) [103] and photoanode(b) [104] given for illustration.

Figure 1.14a and **b** show the chopped light LSV curve of some semiconductors working as photocathode and photoanode, respectively. The current under light-off state corresponds to the dark current and the current under light-on state contains both photocurrent and dark current. From these two figures, we can find that for all the curves, both the photo- and dark currents improve with the increase of applied voltage. Corrosion is one common phenomenon for many semiconductor photoelectrodes, which can be reflected in cyclic voltammetry curves. If the current of voltammetry curve evolves toward lower values with time, it may be the signature that corrosion occurs during the PEC reactions.

2.3.2 Incident photon-to-current efficiency spectra

The incident photon-to-current efficiency (IPCE) is a measure of the ratio of the photocurrent (converted to an electron transfer rate) versus the rate of incident photons (converted from the calibrated power of a light source) as a function of wavelength [105].

The IPCE measurements were performed with a CIMPS-QE IPCE 3 workstation (Zahner) comprising a TLS03 tunable light source controlled by a PP211 potentiostat in the same cell as the one used for classical electrochemical experiments. The applied potentials were set to -0.74 V and 1.26 V vs RHE for the IPCE results presented in **Chapter 5**. The light modulation frequency was 1 Hz, the settling time was 5 s and the number of counts was 25. The Thales software provides the spectra in photocurrent efficiency (A W^{-1}) or in IPCE (%). In order to check the validity of the IPCE measurements, the photocurrent integration is performed from the photocurrent density spectrum (in A W^{-1}) and using the AM 1.5G reference solar spectrum obtained from the ASTM (American Society for Testing Materials) [106]. The result is compared to the one determined by LSV.

2.3.3 Electrochemical impedance spectroscopy

Electrochemical impedance spectroscopy (EIS) uses the application of a small, sinusoidal, alternating current (AC) or voltage to the sample under investigation. The AC perturbation (either voltage or current) is applied over a range of frequencies, and the electrical response of the system is measured and analyzed over this range of frequencies.

In this case, the impedance can be represented as a complex function [107]:

$$Z = \frac{V_t}{I_t} = \frac{V_0 e^{j\omega t}}{I_0 e^{j\omega t - j\varphi}} = Z_0 e^{j\varphi} \quad (2-13)$$

Where Z is the impedance, V is the voltage, I is the current. V and I have a phase difference of φ . j is the imaginary component and ω is the angular frequency.

Then the impedance can be expressed as:

$$Z = Z_0(\cos(\varphi) + j\sin(\varphi)) \quad (2-14)$$

real and imaginary parts of the impedance can thus be written:

$$Z_{real} = Z' = Z_0 \cos(\varphi) \quad (2-15)$$

$$Z_{img} = Z'' = Z_0 \sin(\varphi) \quad (2-16)$$

With a phase angle

$$\varphi = \tan^{-1} \frac{Z''}{Z'} \quad (2-17)$$

And a modulus

$$|Z| = [(Z')^2 + (Z'')^2]^{1/2} \quad (2-18)$$

Based on the formulas above, different parameters can be obtained by EIS measurements. Therefore, the data can be presented in different ways. For instance, real and imaginary parts of the impedance can be plotted against one another, which is called Nyquist plots (**Fig.2.15(left)**). Another representation used is the Bode plot (**Fig.2.15(right)**), where the impedance and phase angle are plotted against frequency, which can be helpful to find capacitive or inductive effects of electrochemical systems. In this thesis, we will use the Nyquist representation. One has to keep in mind that, with this representation, any change of the semi-circle radius corresponds to an evolution of the impedance, for different samples or different experimental conditions.

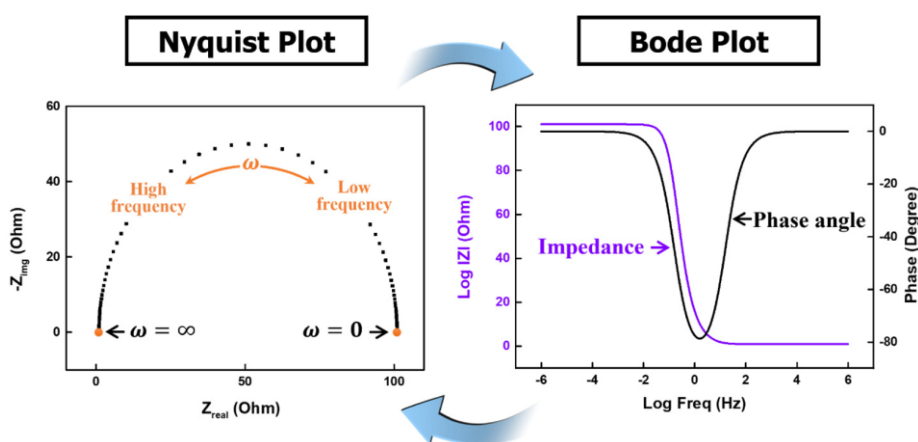


Figure 2.15 Electrochemical Impedance Spectroscopy representation by the Nyquist plot (left) and the Bode plot (right) [108].

2.3.4 Mott-Schottky measurements

From the EIS measurements, reciprocal of the square of capacitance versus the potential difference can also be represented, which is called Mott-Schottky (MS) plot. **Figure 2.16** a and b show the Mott-Schottky curves of p-doped [109] and n-doped [110] semiconductor photoelectrodes, respectively.

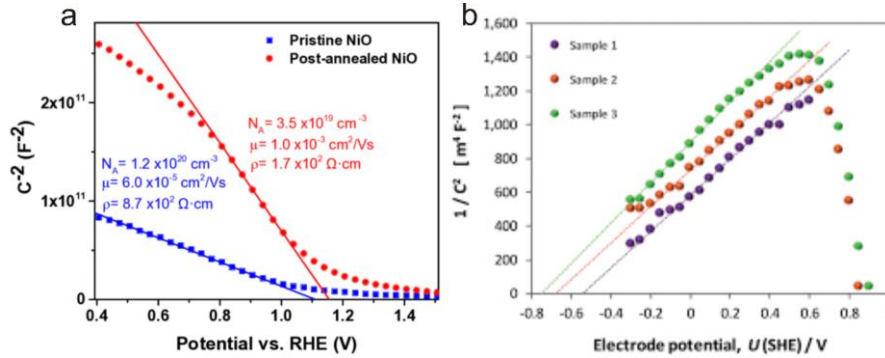


Figure 2.16 Mott-Schottky curve of a p-doped (a) [109] and a n-doped (b) [110] semiconductor photoelectrode.

The Mott-Schottky curve is often used to determine the flat band potential or doping density of the system. The Mott-Schottky equation makes the link between the capacitance C and the applied potential E across a semiconductor-electrolyte junction following:

$$\frac{1}{C^2} = \frac{2}{eN_{Dopant}A^2\varepsilon_0\varepsilon_r} \left(E - E_{fb} - \frac{kT}{e} \right) \quad (2-19)$$

Where, ε_r is the relative permittivity of the semiconductor, ε_0 is the permittivity in vacuum, A is the surface area, e is the charge of an electron, N_{Dopant} is the free carrier density, k is Boltzmann constant and T is the temperature. E_{fb} corresponds to the flatband potential which can be extracted from the x-intercept of the linear portion of the MS curve. For the p-doped and n-doped semiconductors, the MS curve will show negative or positive slop respectively, as shown in **Fig. 2.16**.

2.4 DFT calculations

2.4.1 Introduction to density functional theory

Density functional theory (DFT) is one of the most widely used *ab initio* methods for the determination of electronic properties of atoms, molecules, crystals, surfaces, and their interactions [111]. It is considered as the most successful quantum mechanical approach for describing the electronic structure of matter. In the quantum mechanics theory, the system's wave function contains all the information of a given system, which can be obtained by solving the Schrödinger equation:

$$\hat{H}\Psi = E\Psi \quad (2-20)$$

Where \hat{H} is the Hamiltonian operator, Ψ is the wave function and E is the energy. The exact solution of this equation for a many-body system (which contains $3N$ variables; N being the number of electrons) is analytically impossible. Therefore, a series of approximations and numerical methods are introduced to solve this problem.

D. Hartree introduced one of the first procedures to calculate approximately wave functions and energies [112,113] to various atoms and ions (He, R^+ , Na^+ and Cl^-), in which the electrons are considered independent and interact only by the average static field with the other electrons. Therefore, the $3N$ dimensional many body Schrödinger equation is transformed to a set of single particle equations. However, due to the mandatory antisymmetric property of the wavefunction, this method is incompatible with the Pauli Exclusion Principle [114,115]. In order to overcome this problem, the Slater determinant [114,116] was considered by Hartree and Fock in 1930 [115].

In parallel of the Hartree method, Thomas [117] and Fermi [118] proposed another approach, which was further improved by Dirac [119]. In this pioneer approach, a many-body system is not described by its wave function but by its electronic density. This is the cornerstone of the development of density functional theory, simplifying the N -body system problem by decreasing the degrees of freedom from $3N$ to only 3 variables. The

question was then to know if the electronic density was sufficient or not to describe the electronic structure of a system. In 1964, Hohenberg and Kohn tackled this problem and solved it by proposing 2 new theorems [120]. One year later, a practical method to calculate the electronic density was proposed by Kohn and Sham [121]. At this stage, DFT simulations became thus consistent and feasible. Despite all the approximations proposed to simplify the calculation method, Hohenberg-Kohn and Kohn-Sham theorems are still considered as the major breakthroughs [122], which led to the formulation of the density functional theory used today.

2.4.1.1 Hohenberg-Kohn theorems

In 1964, Hohenberg and Kohn demonstrated that the ground state of a many particles system is a unique functional of the electron density $\rho(\mathbf{r})$. They proposed to replace all the various interactions in the system by an external potential and formulate the ground state energy of the system as a functional of the electronic density for further simplification. Therefore, the total energy of a system can be expressed as:

$$E[\rho] = T[\rho] + V_{EE}[\rho] + V_{N-e}[\rho] = F_{HK}[\rho] + \int dr^3 \rho(\mathbf{r}) V_{N-e}(\mathbf{r}) \quad (2-21)$$

Where, $F_{HK}[\rho]$ is a universal functional related to the functional of the kinetic energy coming from the interacting electrons $T[\rho]$ and the functional of the electron-electron interactions $V_{EE}[\rho]$. The potential $V_{N-e}[\rho]$ corresponds to the total external potential due to the nuclei which are considered as clamped.

2.4.1.2 Kohn-Sham approach

The energy functional above contains a kinetic energy term. There is no known expression for this term, and thus the functional cannot be evaluated as it stands in the Hohenberg-Kohn formulation.

In order to overcome this, Kohn and Sham replaced the system with a fictitious non-interacting system that generates the same ground state electron density than the real

system of interacting electrons. The $F_{HK}[\rho]$ was redefined by introducing the following functional $E_{XC}[\rho]$:

$$F_{KS}[\rho] = T_S[\rho] + V_H[\rho] + E_{XC}[\rho] \quad (2-22)$$

Where $T_S[\rho]$ is the kinetic energy functional of non-interacting electrons, $V_H[\rho]$ is the Hartree potential functional and $E_{XC}[\rho]$ is the exchange and correlation energy. The associated potential to the latter is:

$$V_{xc}(\mathbf{r}) = \left. \frac{\delta E_{xc}[\rho]}{\delta \rho} \right|_{\rho(\mathbf{r})} \quad (2-23)$$

So, the equation changes to:

$$\left[\frac{1}{2} \nabla^2 + V_{N-e}(\mathbf{r}) + V_H(\mathbf{r}) + V_{xc}(\mathbf{r}) \right] \varphi_i(\mathbf{r}) = \epsilon_i \varphi_i(\mathbf{r}) \quad (2-24)$$

This is known as the Kohn-Sham (KS) equation, where all the terms are known except $V_{xc}(\mathbf{r})$. We thus need to introduce an approximate exchange-correlation functional. The accuracy of the electronic density of the system investigated will depend on the choice of this functional and how close it comes to the exact value [123]. The most common approximations are the local-density approximation (LDA) [121] and the generalized gradient approximation (GGA) [124,125], which are described below.

2.4.1.3 Local-Density approximation (LDA)

The local density approximation (LDA) is one of the simplest approximations. In the local-density approximation, the density is considered locally uniform [126]. The exchange-correlation energy at every position is considered to be the same as it would be for a homogeneous electron gas having the same density. Thus, the total exchange correlation energy of the system can be written as:

$$E_{xc}^{LDA}[\rho] = \int \rho(\mathbf{r}) \epsilon_{xc}[\rho(\mathbf{r})] d\mathbf{r} \quad (2-25)$$

Where $\epsilon_{xc}[\rho(\mathbf{r})]$ is the exchange-correlation energy per particle for a uniform gas density $\rho(\mathbf{r})$.

2.4.1.4 Generalized gradient approximation (GGA)

The Generalized Gradient Approximation (GGA) is an improved form based on the LDA functional. In the generalized gradient approximation, the non-homogeneity of the local density is taken into account by including the gradient of the electron density through a general function f depending on $\rho(\mathbf{r})$ and $\nabla\rho(\mathbf{r})$ [124].

$$E_{XC}^{GGA}[\rho] = \int f(\rho(\mathbf{r}), \nabla\rho(\mathbf{r})) d\mathbf{r} \quad (2-26)$$

In this work, the GGA in the Perdue-Burke-Ernzerhof (PBE) approach [124] was used for the structure optimization and phonon calculations. For electronic band structure calculations, the conventional functionals such as LDA and GGA always underestimate electronic band gaps. In order to overcome this issue and at a lower cost of simulation (compare to GW “many-body” corrections), the Heyd–Scuseria–Ernzerhof (HSE) hybrid functional and TB-mBJ (Tran-Blaha modified Becke-Johnson) potential were chosen for the band structure calculations.

2.4.1.5 Heyd–Scuseria–Ernzerhof (HSE) hybrid functional

GGA functional makes DFT a useful tool in computational physics and chemistry, and hybrid density functionals improve the GGA results by taking into account a given fraction of Hartree-Fock (HF) exchange. However, the expensive computation cost remains an issue. In order to improve computational efficiency, Heyd, Scuseria, and Ernzerhof (HSE) proposed an accurate and efficient screened hybrid functional-HSE hybrid functional based on the PBE functional, which uses an error-function-screened Coulomb potential to calculate the exchange portion of the energy [127].

As the Coulomb operator can be separated into long-range (LR) and short-range (SR) parts, all the terms of the PBE exchange energy can be splitted into SR and LR components. The LR components of the HF exchange have only very small contributions to this functional and it can be compensated at some point by the description of the exchange energy in the PBE approach [127]. Therefore, the HSE functional is finally

expressed as:

$$E_{xc}^{\omega PBEh} = aE_x^{HF,SR}(\omega) + (1 - a)E_x^{PBE,SR}(\omega) + E_x^{PBE,LR}(\omega) + E_c^{PBE} \quad (2-27)$$

Where a is the mixing parameter, and ω is an adjustable parameter for controlling the short-range interaction. $E_x^{HF,SR}(\omega)$ is the short-range Hartree-Fock exact exchange functional, $E_x^{PBE,SR}(\omega)$ and $E_x^{PBE,LR}(\omega)$ are the short- and long-range components of the PBE exchange functional, and $E_c^{PBE}(\omega)$ is the PBE correlation functional.

In this work, we used HSE functional to study the electronic band structure of III-V materials. Firstly, the band structure of simple zinc-blende III-V binary semiconductors unit cells (including InP, GaP, GaSb and GaAs) were calculated by HSE with different ω . From the comparison with bandgaps determined experimentally, the ω was fixed, and then used for further band structure calculations of more complex structures.

2.4.1.6 TB-mBJ potential

Even if the HSE functional gives similar results that the traditional HF calculations, the calculation is much faster. But still, for large structures with dense k points, the HSE calculation remains quite expensive (in terms of computational cost) and time-consuming. Therefore, for the calculations of large structures with dense k points, HSE functional is not a good choice. On the other hand, as mentioned above, the calculations with GGA and LDA functionals are fast and economical but greatly underestimate the bandgaps for many semiconductors. In order to improve the calculation accuracy of the bandgaps in DFT, an alternative system was proposed by Tran and Blaha [128] by modifying the Becke-Johnson (BJ) potential. The Becke-Johnson potential is expressed as [129]:

$$V_x^{BJ}(\mathbf{r}) = V_x^{BR}(\mathbf{r}) + \frac{1}{\pi} \sqrt{\frac{5}{6}} \sqrt{\frac{t(\mathbf{r})}{\rho(\mathbf{r})}} \quad (2-28)$$

Where $t(\mathbf{r})$ is the density of the kinetic energy:

$$t(\mathbf{r}) = \frac{1}{2} \sum_{i=1}^N \nabla \phi_i^*(\mathbf{r}) \nabla \phi_i(\mathbf{r}) \quad (2-29)$$

$V_x^{BR}(\mathbf{r})$ is the Becke-Roussel (BR) potential [130]:

$$V_x^{BR}(\mathbf{r}) = -\frac{1}{b(\mathbf{r})} \left(1 - e^{-x(\mathbf{r})} - \frac{1}{2} x(\mathbf{r}) e^{-x(\mathbf{r})}\right) \quad (2-30)$$

$$b(\mathbf{r}) = \left[\frac{x^3(\mathbf{r}) e^{-x(\mathbf{r})}}{8\pi\rho(\mathbf{r})} \right]^{\frac{1}{3}} \quad (2-31)$$

Tran and Blaha introduced a parameter "c" to modify the relative weights of the two terms of the BJ potential and the modified potential (TB-mBJ) are shown as [128]:

$$V_x^{TB-mBJ}(\mathbf{r}) = cV_x^{BR}(\mathbf{r}) + (3c - 2) \frac{1}{\pi} \sqrt{\frac{5}{6}} \sqrt{\frac{t(\mathbf{r})}{\rho(\mathbf{r})}} \quad (2-32)$$

TB-mBJ potential was proved to reach similar accuracy than computationally more expensive functionals, such as HSE. This approach is only slightly more expensive than conventional LDA and GGA calculations. Therefore, it is a suitable method for the DFT calculations performed over large systems or with very dense k points.

2.4.1.7 Self-Consistency and structure optimization

The Self-Consistency loop is shown in the **Fig.2.17** (right part). Firstly, an initial guess for electron density $\rho^{in}(\mathbf{r})$ is needed to calculate Hartree potential $V_H(\mathbf{r})$ and exchange-correlation potential $V_{xc}(\mathbf{r})$, which will be further used to solve KS Equation. Once a new set of wave functions $\varphi_i^{out}(\mathbf{r})$ is obtained by solving the non-interaction electron problem in the external potential V_{ext} , a new electron density can be constructed as $\rho^{out}(\mathbf{r}) = \sum_{i=1}^N |\varphi_i^{out}(\mathbf{r})|^2$. The self-consistency is reached if $\rho^{out}(\mathbf{r}) = \rho^{in}(\mathbf{r})$. If this is not the case, the procedure will be iterated with a new guess for electron density constructed from $\rho^{out}(\mathbf{r})$. For the structure optimization, the self-consistent calculation is done for each new atomic position. The algorithm of relaxation will stop at specific force criteria (as shown in the left part of **Fig.2.17**). This method is used for system such as bulk material or slabs for surfaces and interfaces studies. In this thesis, for structure optimization, the structures were considered as relaxed until the Hellmann-Feynman forces on the atoms were less than 10^{-4} eV/Å before any other subsequent calculations.

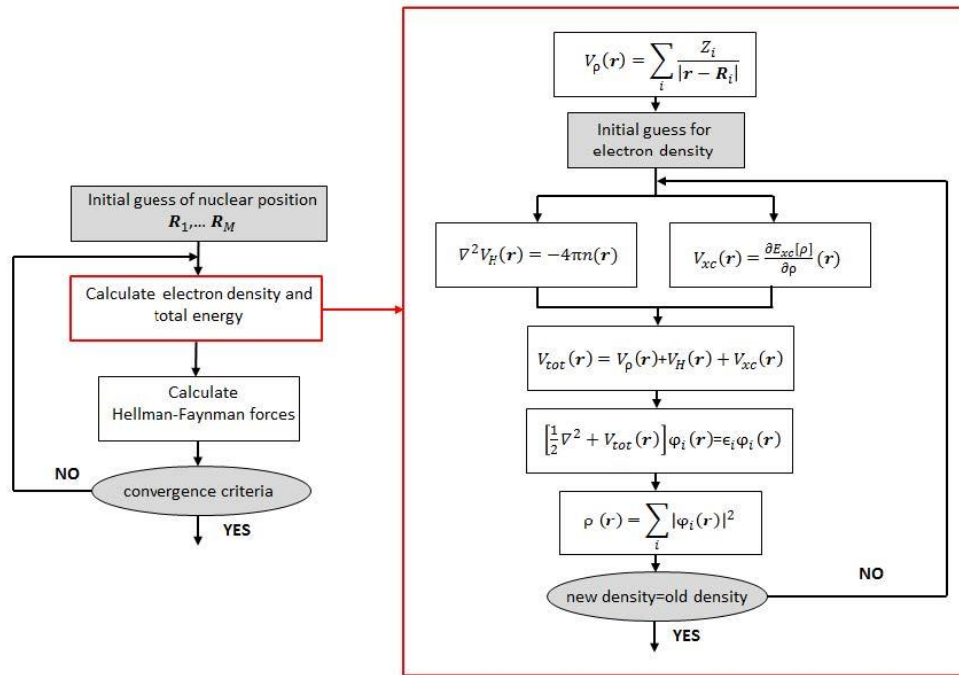


Figure 2.17 Flow chart of the iteration scheme. The scheme on the left corresponds to DFT self-consistent calculation for relaxation and structure optimization. The scheme on the right, in the red frame, is the self-consistent total energy calculation [37].

2.4.1.8 Computational codes

The density functional theory has been implemented in various computational codes. In this thesis, most DFT calculations (including electronic band structure and phonon calculations) were performed with the Vienna Ab-initio Simulation Package (VASP) code [131]. The VASP code is by far one of the most popular computational codes for calculations of infinite systems such as solid-state materials and condensed matter.

The self-consistency cycles and choices of numerical methods used to calculate the electronic Kohn-Sham ground state in VASP are quite efficient and robust. VASP code uses plane wave basis set rather than localized basis set. The disadvantage of using plane waves is that it requires rapid oscillation of the wave function near the core region. For the core electrons, it is necessary to use a large number of plane waves and a large plane wave cut off. For reducing the computational workload, in VASP code, pseudopotentials or the Projector Augmented-Wave (PAW) method [132] are used to describe the

interaction between ions and non-valence electrons so that the size of the basis set can be reduced. The main idea of the pseudopotential method is that the core electrons are not considered and therefore the rapid oscillations of the valence wave functions around the nucleus, which causes extremely large basis set, are avoided. Indeed, the core electrons are often considered as chemically inert and chemical bondings mostly involve the valence electrons. For the PAW method, the potentials can be defined as the frozen core all-electron potentials, which unifies all-electron and pseudopotential approaches. In order to improve the accuracy, the PAW method also takes the core wave functions into account. It divides the wavefunction in two parts, with a partial wave in a sphere around the atom called the augmentation region and outside the sphere called the interstitial region. Inside the augmentation region, the all-electron wave function can be expanded. These two terms are then added and the overlapping part is subtracted to obtain a wave function close to the all-electron wave function.

Periodic Boundary Conditions (PBCs), in all spatial directions, are imposed in the VASP code to treat infinite number of atoms. The Bloch functions are used to take into account the system periodicity:

$$\varphi_{\mathbf{k}}(\mathbf{r}) = e^{i\mathbf{k}\cdot\mathbf{r}}u_{\mathbf{k}}(\mathbf{r}) \quad (2-33)$$

Where $u_{\mathbf{k}}(\mathbf{r})$ is a function with the lattice periodicity $u_{\mathbf{k}}(\mathbf{r}) = u_{\mathbf{k}}(\mathbf{r} + \mathbf{R})$, so that:

$$\varphi_{\mathbf{k}}(\mathbf{r} + \mathbf{R}) = e^{i\mathbf{k}\cdot\mathbf{R}}u_{\mathbf{k}}(\mathbf{r}) \quad (2-34)$$

Where \mathbf{k} is the reciprocal lattice vector in the Brillouin zone and \mathbf{R} is the translation vector of the lattice. During the computation, only the atoms within one periodic cell are optimized and computed taking into account their interactions with atoms in the neighboring cells.

The package also includes the Monkhorst-Pack [133] to sample the Brillouin zone. The VASP offers support for a large variety of platforms. Besides, high performance computation (parallel computing) was used in this work.

In addition, the band symmetry properties and electron-phonon interaction were

studied by using Quantum ESPRESSO (QE). QE is an open-source software [134]. Similar to VASP, QE also uses planewave basis sets combined with pseudopotentials or the PAW method to achieve DFT electronic band structure calculations. Periodic boundary conditions are also imposed in this code to treat infinite number of atoms. As compared to VASP, the calculations by QE need longer time generally. Besides, implementation of the hybrid functionals (HSE, in particular) is easier with VASP than with QE. But QE also has its specific advantages. For instance, detailed symmetry information of electronic states can be extracted from the band structure calculations and it also has advanced modules for electron-phonon interaction calculations.

2.4.2 Electronic band structure calculation

The band structure calculations in this work were performed with the PAW method. The calculations contain three main steps. Firstly, self-consistent field (SCF) calculation (as shown in **Fig.2.17**) is needed to obtain a self-consistent electron density using a uniform k-point mesh. Secondly, based on the electron density obtained above, the eigenvalues along high symmetry k-point paths are determined. Finally, the band structures (eigenvalues versus k point) can be plotted in 2D along a specific k direction (**Fig. 2.18a**) or in 3D in a given k plane (**Fig. 2.18b**).

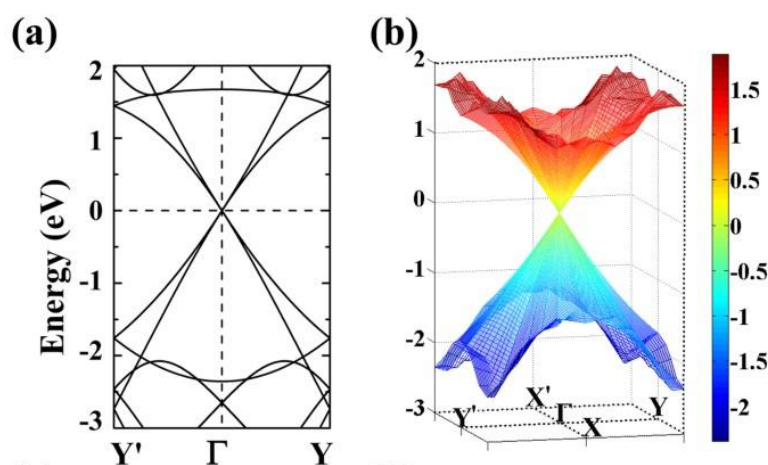


Figure 2.18 The electronic band structure along one 2D k-path in reciprocal space (a) and the 3D plotting in a k plane (b) [135].

Besides, the band folding effect will occur in band structures for the supercell [136]. **Figure 2.19** shows the principle of band folding effect. **Figure 2.19a** and **b** show the band structures of a polymer obtained with a supercell (two atoms per unit cell) and with a unit cell (one atom per unit cell), respectively. We can see the band folding effect in **Fig.2.19a** which is produced by folding the band structure in **Fig.2.19b** and the corresponding folding process is described in **Fig.2.19c**.

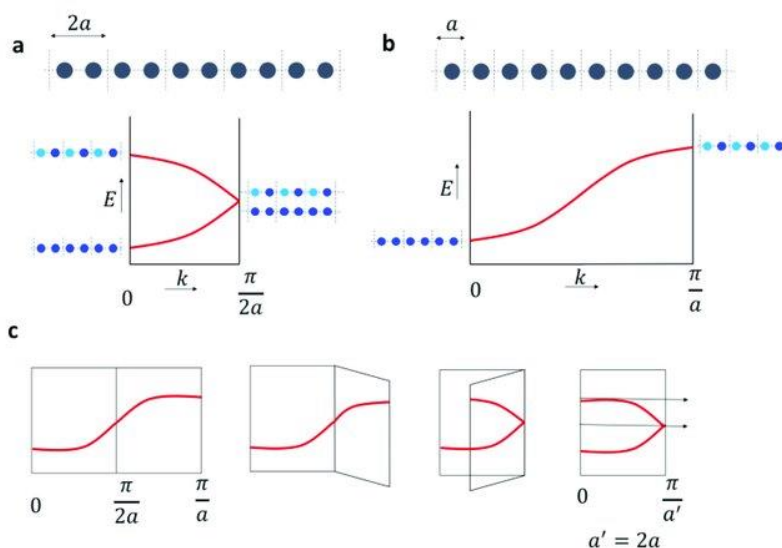


Figure 2.19 Band folding in one-dimensional polymers [136]. (a) Band structure of a polymer in which there are two atoms per unit cell. The two branches intersect at $k = \pi/(2a)$. (b) Band structure of a polymer in which there is one atom per unit cell. The Brillouin zone is doubled because the unit cell is one half as it is in (a). (c) Production of band structure in (a) by folding band structure in (b).

2.4.3 Phonon calculation

There are two main methods for phonon dispersion calculations: Finite displacement method and Linear Response method. In this work, we chose the Finite displacement method to do phonon calculations (the results are shown in **Chapter 3**) combining VASP and PHONOPY software [137].

One way to implement the theory of crystal vibrations for realistic structures is to explicitly calculate the forces between every atom in the crystal and construct the force constant matrix of the crystal. This force constant matrix then allows us to calculate the

normal modes at any specific wavevector, \mathbf{q} . In order to calculate the forces caused by the displacement of an atom i , one can shift this atom i , and then use DFT to calculate the forces on every other atoms using the Hellman-Feynman theorem [138]. This method of calculating the force constant matrix by explicitly displacing atoms is called the Finite displacement method. This method is generally quicker and computationally cheaper than the Linear Response method [139], which uses density functional perturbation theory to calculate forces.

The phonon calculations by Finite displacement method use the following steps:

1. Creation of supercell structures with (or without) displacements from a unit cell.
2. Calculation of sets of forces.
3. Calculation of Force constants from the sets of forces.
4. Building of Dynamical matrix from the force constants.
5. Determination of phonon frequencies and eigenvectors from the dynamical matrices with specified \mathbf{q} -points.

2.4.4 Calculation of the electron-phonon interaction (EPI) matrix elements

In the classic Fröhlich analytical model, the electron phonon coupling matrix element is evaluated in the case of an isotropic interaction of an electron in a parabolic band with a single dispersionless LO phonon mode [140]:

$$g_{\mathbf{q}} = \frac{i}{|\mathbf{q}|} \left[\frac{e^2}{4\pi\epsilon_0} \frac{4\pi}{N\Omega} \frac{\hbar\omega_{LO}}{2} \left(\frac{1}{\epsilon_{\infty}} - \frac{1}{\epsilon_0} \right) \right]^{1/2} \quad (2-35)$$

Where \mathbf{q} is the phonon wave vector, Ω the unit cell volume, N the number of unit cells in the Born-von Kármán supercell, and e , ϵ_0 , ϵ_{∞} and \hbar are the electron charge, static and high-frequency dielectric constants, and reduced Planck constant, respectively. As shown by Eq.2-35, the Fröhlich coupling constant $g_{\mathbf{q}}$ diverges at long wavelengths ($\mathbf{q} \rightarrow 0$) following a simple $1/\mathbf{q}$ variation.

In the context of DFT, EPI matrix elements ($g_{m\nu\nu}(k, q)$) can be calculated using a state-of-the-art numerical implementation of the general microscopic theory [141-143]. This theory generalizes the classic Fröhlich approach to anisotropic materials and multiple phonon branches by separating the short- (S) and long-range (L) contributions to the matrix elements [142]:

$$g_{m\nu\nu}(k, q) = \langle \Psi_{mk+q} | \Delta_{qv} V | \Psi_{nk} \rangle = g_{m\nu\nu}^S(k, q) + g_{m\nu\nu}^L(k, q) \quad (2-36)$$

Where the two electronic states Ψ_{nk} and Ψ_{mk+q} are defined by the m and n indices for the electronic dispersion curves, as well as the wavevectors k+q and k. The phonon branch is defined by ν and q is the phonon wavevector.

The EPI matrix element has the meaning of a probability amplitude for the scattering between the initial electronic state $|\Psi_{nk}\rangle$ and the final state $\langle \Psi_{mk+q}|$ via the perturbation $\Delta_{qv}V$. The long-range (L) matrix element $g_{m\nu\nu}^L(k, q)$ represents the generalization of the Fröhlich vertex for *ab initio* calculations [142].

$$\begin{aligned} g_{m\nu\nu}^L(k, q) &= i \frac{4\pi}{\Omega} \frac{e^2}{4\pi\epsilon_0} \sum_k \left(\frac{\hbar}{2NM_k\omega_{qv}} \right)^{(1/2)} \\ &\times \sum_{G \neq -q} \frac{(q+G) \cdot Z_k^* \cdot e_{kv}(q)}{(q+G) \cdot \epsilon^\infty \cdot (q+G)} \\ &\times \langle \Psi_{mk+q} | e^{i(q+G) \cdot r} | \Psi_{nk} \rangle \end{aligned} \quad (2-37)$$

Where the angular brackets have to be evaluated within the Born–von Kármán supercell. This formula shows that the increase of this contribution at long wavelengths, $q \rightarrow 0$, is more complex than in the case of the classic Fröhlich analytical model [142].

In this thesis, the EPI matrix element was calculated based on QW code and the results are shown in **Chapter 3**.

2.4.5 Common DFT computational details

In this work, the DFT calculations mainly contain two parts. The first one involves the electronic band structure, phonon and electron-phonon coupling calculations for InP-based stoichiometric APB structures and the corresponding results are shown in **Chapter 3**. The other one is mainly about the band structure calculations of nonstoichiometric APB structures with GaP, GaAs and GaSb materials and the corresponding results are shown in **Chapter 5**.

For the DFT calculations of InP-based stoichiometric APB structures (**Chapter 3**), a Monkhorst-Pack 4x1x6 grid of k points was used for the geometry optimization step and the structures were relaxed until the Hellmann-Feynman forces on the atoms were less than 10^{-4} eV/Å. Band structure and phonon calculations were performed with the density functional theory by combining the VASP and PHONOPY package codes. DFT calculations were performed using the plane-wave projector augmented wave (PAW) method as implemented in the VASP code. The standard generalized gradient approximation (GGA) parameterized by Perdew-Burke-Ernzerhof (PBE) was used for structure optimization and phonon calculation, and the Heyd-Scuseria-Ernzerhof (HSE) hybrid functional was chosen for the band structure calculation, with energy cutoff of 500eV. Besides, the symmetry information and simulated Raman spectrum of the localized phonons around APB were extracted through the phono3py [144] package codes. The symmetry properties of electronic states and electron-phonon interaction matrix elements were calculated and extracted by using metaGGA (TB-mBJ) potentials and LDA exchange-correlation functional, respectively, using the QE package code.

For the DFT calculations of nonstoichiometric APB structures, III-III and V-V nonstoichiometric APB structures with GaP, GaAs and GaSb materials were constructed. In order to investigate separately the III-III and V-V APB singularities, slab structures were constructed by adding vacuum on both sides and the surfaces were passivated with fictitious hydrogen atoms to avoid contribution of localized surface states. Two kinds of nonstoichiometric APB structures with relatively short and long lengths were constructed

for the DFT calculations, which are presented in **Chapter 5**. Around 20 Å and 30 Å vacuum were added on the short and long structures, respectively, which is thick enough to avoid any interaction between slab surfaces. The structures were optimized with Hellmann-Feynman forces criterion less than 10^{-4} eV/Å, and based on a Monkhorst-Pack 6x6x1 grid of k points. The DFT band structure calculations were performed by using HSE hybrid functional and metaGGA (TB-mBJ) potential, based on the VASP code, with an energy cutoff of 500 eV. Besides, in order to study the topological properties, the topological related (including band structures and Berry phase) calculations were carried out by generating ab initio tight-binding Hamiltonians from the maximally localized Wannier functions within HSE potential [145] as implemented in Wannier Tools package [146]. The Bloch wave functions are projected onto the s, p, d atomic orbitals of Ga and s, p atomic orbitals of P, As and Sb. The symmetry properties of the electronic states were analyzed starting from the irreducible representations provided by Quantum Espresso package codes.

2.5 Summary

In this chapter, firstly, the different experimental characterization techniques involving structural (AFM, C-AFM, XRD, STEM, CMP), optical (PL, Raman, ellipsometry) and PEC characterizations have been presented with the related physical mechanisms, experimental setups and parameter settings used in this thesis. Then DFT calculations have been described with a brief introduction to the basic concepts of the DFT, followed by the calculation steps and parameter settings for the determination of electronic, vibrational and electron-phonon coupling properties.

Chapter 3: Optoelectronic and vibrational properties of stoichiometric anti-phase boundaries

The initial objective of my thesis was to explore the optoelectronic properties of III-V/Si epilayers. The preliminary observations of unusual PL features on III-V/Si samples rapidly showed the need for a deep understanding of optoelectronic and vibrational properties of these samples, which, as we understood, could only be driven by the presence of some stoichiometric antiphase boundaries. This led to the demonstration of a strong electron-phonon coupling in these 2D nano-objects, published in 2020 in ref. [147]. The results presented hereafter have been obtained with the participation of many members of the OHM research team. In addition, group IV sample growth and STEM/EDX measurements have been performed in collaboration with IHP microelectronics (Germany). The Raman measurements were achieved in collaboration with both IHP microelectronics and IPR (Institut de Physique de Rennes).

3.1 Introduction

The electron-phonon interaction has a strong impact on electrical, optical and thermal properties of solids [148,149]. Especially, strong electron-phonon interactions were recently investigated for materials and devices developments as well as for understanding of fundamental physical processes, such as phonon lasing [150], superconductivity [151] or colossal magnetoresistance [152]. The strength of this interaction and the formation of a polaron however highly depends on the polarizability of the chemical bonds composing the material [153]. Therefore, strong electron-phonon interaction was preferentially studied in highly polar materials, such as alkali halides [153], oxides [152,154] or perovskites [155]. The strength of this interaction is commonly quantified with the so-called Huang-Rhys factor S , whose maximum value may reach 100

with alkali halides [156]. On the other hand, group-II-VI, III-V or IV semiconductors, have been widely used in photoelectric device applications due to their excellent optical and/or transport properties. When these bulk materials are pure and undoped, the electron-phonon interaction remains generally weak, reflected by quite low Huang-Rhys (S) factor (e.g. 0.0033 for InAs [157] and 0.035 for CdSe [158]), as the chemical bonds are either covalent (group IV) or slightly polar (group III-V or II-VI). Effective enhancement of the electron-phonon interaction was successfully obtained by using spatial confinement or carrier localization effects [159]. A. Alkauskas *et al.* comprehensively and deeply discussed the electron-phonon interaction in III-V semiconductors defects [160]. Especially, punctual antisite defects were found to greatly enhance the electron-phonon interaction [161]. M. Kang *et al.* discovered Holstein polaron in surface-doped layered MoS₂ semiconductor [162]. Electron-phonon coupling was also investigated in many different localized systems such as nanoscale core-shell structures [148], graphene and InAs double quantum dot (DQD) systems [163], WSe₂/hBN heterostructure [149] or graphene/Monolayer h-BN structure [164].

In this chapter, we demonstrate strong electron-phonon interactions in 2D vertical In-rich Indium gallium phosphide ((In,Ga)P) stoichiometric APB, where the homovalent bonds drastically change the local polarity and charge distribution in the crystal, leading to efficient phonon confinement and localized holes wavefunctions. It is furthermore surrounded by a Ga-rich (In,Ga)P barrier enabling the quantum confinement of carriers. The unprecedented electron-phonon coupling strength measured in these buried and non-oxidized III-V vertical singularities opens many perspectives to understand the physics of the electron-phonon interaction in semiconductors.

3.2 Sample growth

The preparation of the studied In_{0.3}GaP on SiGe/Si sample contains two main steps. The first step is the growth of a relaxed SiGe buffer layer on Si substrate [165], performed by our German partner (IHP-microelectronics). A 760nm Si_{0.433}Ge_{0.567} layer was grown

at 550°C and 80 Torr reactor pressure on one clean Si (001) wafer misoriented by 4° towards the [110] direction with a reduced pressure chemical vapor deposition (RPCVD) system. Then SiGe was annealed in-situ at 1000°C for 5 mins under H₂ flow for relaxation. The second step is the regrowth of In_{0.3}GaP on SiGe/Si pseudo-substrate by our lab, which contains two growth modes: Migration Enhanced Epitaxy (MEE) and traditional Molecular Beam Epitaxy (MBE). The first 10nm InGaP layer was grown with the MEE growth mode. One MEE cycle consists in a first 0.63 ML (MonoLayer) Ga deposition at a growth rate of 0.1 ML/s, followed by a 0.27 ML In deposition at the same growth rate (0.1 ML/s), and then by a 4s growth interruption. Finally, a 200nm-thick In_{0.3}GaP layer is grown at 500°C in the conventional continuous MBE growth mode and at a growth rate of 0.14 ML/s on the top of the MEE layer.

3.3 Structural characterizations and post-growth processing

As discussed in **Chapter 1**, APBs are commonly formed during the epitaxy of Zinc-Blende III-V semiconductors on a group IV substrate in the diamond phase (e.g. silicon (Si) or Germanium (Ge)). It originates from the two different ways for the III-V crystal to fit the group IV substrate orientation [3]. As a consequence, two domains with different phases may grow on the same substrate, separated by wrong III-III or V-V bonds, inside the III-V matrix, as illustrated in **Fig. 3.1**. This leads to the insertion of a local translational symmetry breaking. III-III (V-V) bond also adds 2 free holes (2 free electrons) in the semiconductor. However, unlike doping, APBs extend in the form of vertical 2D planes (at least locally), that can emerge at the sample surface. From this description, APB can thus be considered as 2D homovalent singularities in a III-V bulk matrix. As described in **Chapter 1**, theoretically, the APB composition may range from a pure vertical III-III APB to a pure V-V APB, resulting in these two extreme cases to a large excess of charges released in the lattice. But stoichiometric APBs (with equal numbers of III-III and V-V bonds within the same APB), depicted in **Fig. 3.1**, have been mostly considered, due to their relatively low formation energy resulting from the charge compensation effect [75].

We will see in **Chapter 5** that it is also the only configuration that leads to the presence of a semiconducting bandgap, and thus the only possible additional contribution to the optical properties of the layer studied.

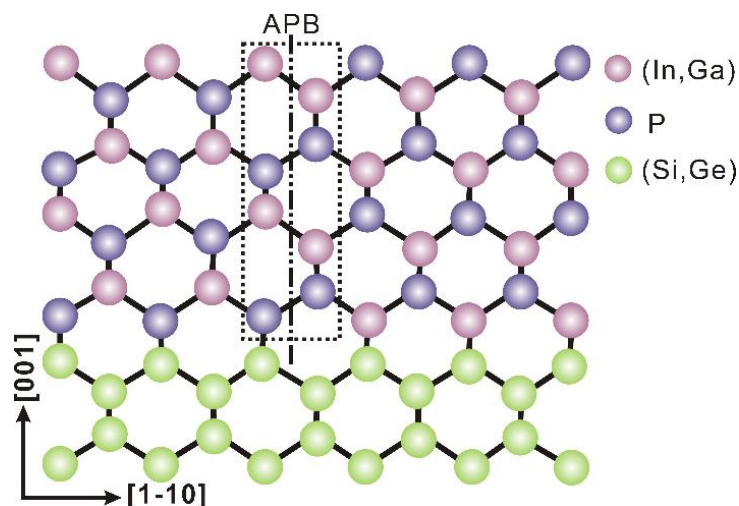


Figure 3.1 Sketch representing the atoms arrangement in a stoichiometric APB.

Figure 3.2a is a schematic representation of the InGaP/SiGe/Si sample's structure. Experimental scanning transmission electron microscopy (STEM) plan-view and cross-sectional images are shown in **Fig. 3.2b** and **Fig. 3.2c**, respectively. The sample is composed of three main layers: a Si substrate, a 760 nm-thick $\text{Si}_{0.433}\text{Ge}_{0.567}$ buffer layer and a 210 nm-thick InGaP III-V layer (**Fig. 3.2a**) with a nominal In content of 30%. The last epitaxial layer was grown at relatively high growth temperature (500°C) and low growth rate, to enhance non-equilibrium kinetic effects during the growth of the metastable (In,Ga)P alloy. Especially, In atoms are well-known for their ability to efficiently migrate at the surface of InGaP semiconductors during the growth, due to their low binding energy to the surface at high temperature. In this sample, APBs in InGaP are propagating almost vertically until the surface (boundary between dark grey and clear grey in **Fig. 3.3c**), giving rise to 2D vertical homovalent singularities. We note here that, even if the TEM images are not presented here with a high resolution or may seem a bit blurry, our laboratory has a strong experience in studying these samples and can guarantee that the observed contrast can be attributed unambiguously to APBs. The 2D vertical

homovalent singularities thus form a random honeycomb-like lattice at the surface (black lines in **Fig. 3.2b**), and separate the different domains, as illustrated in **Fig. 3.2a**.

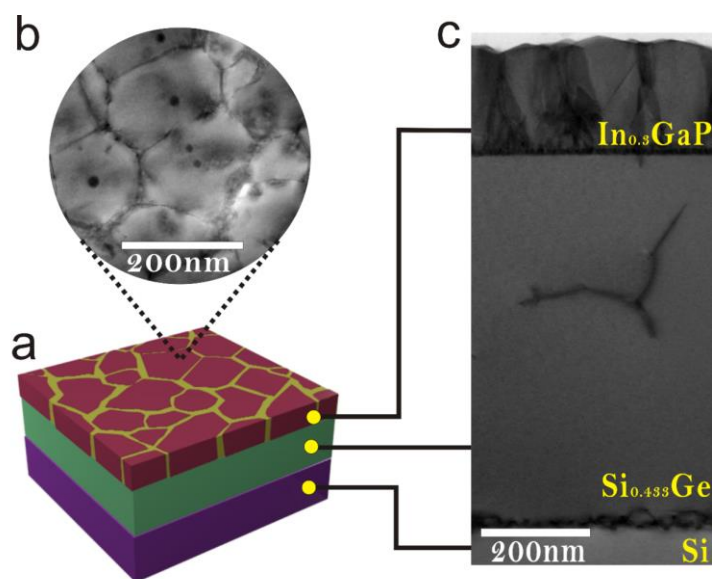


Figure 3.2 Schematic image (a) as well as plan view (b) and cross-sectional (c) STEM images of the studied InGaP/SiGe/Si sample.

Elemental mapping by an energy-dispersive X-ray (EDX) system in a scanning transmission electron microscope (STEM) was employed to analyze local chemical composition in the sample. **Fig. 3.3a** presents the cross-sectional bright field image of the sample along the [110] direction. The black line in the middle represents one APB. **Fig. 3.3b-e** show the corresponding EDX mapping images of elemental indium (**Fig. 3.3b**), gallium (**Fig. 3.3c**), phosphorus (**Fig. 3.3d**), and silicon (**Fig. 3.3e**) contents. **Figure 3.3f-h** show the plan view EDX mapping images of indium (**Fig. 3.3f**), gallium (**Fig. 3.3g**), and phosphorus (**Fig. 3.3h**). Additional STEM and EDX images are shown in **Fig. 3.4** and **Fig. 3.5**. First, a preferential incorporation of In in the close vicinity of the antiphase boundary singularity is observed, together with an In-rich phase at the surface where the singularity emerges. Second, almost pure InP surface quantum dots (QDs) are evidenced in **Fig. 3.2b** (black circular areas) and in **Fig. 3.3f**, arising from demixing due to the non-equilibrium growth conditions used [166]. Removal of these surface QDs will be discussed hereafter.

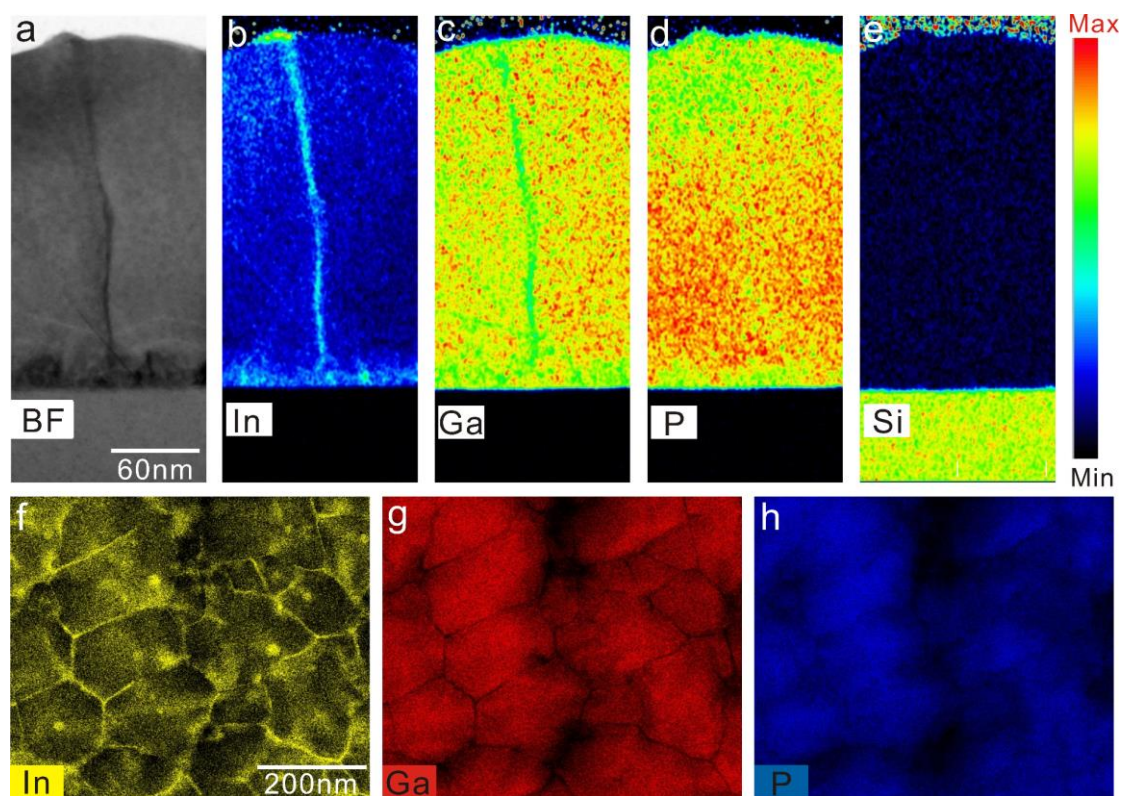


Figure 3.3 a, Cross-sectional bright-field (BF) STEM image of the InGaP/SiGe/Si sample. The black line in the middle and the hump on the surface corresponds to the APB and surface nanostructure, respectively. b-e, Cross-sectional EDX elemental mapping images of indium (b), gallium (c), phosphorus (d) and silicon (e). f-h, Plan-view EDX mapping images of indium (f), gallium (g), phosphorus (h). Two kinds of In-rich nanostructures are observed: pure InP surface nanostructures and 2D In-rich vertical quantum wells (QWs) surrounding the APB singularities.

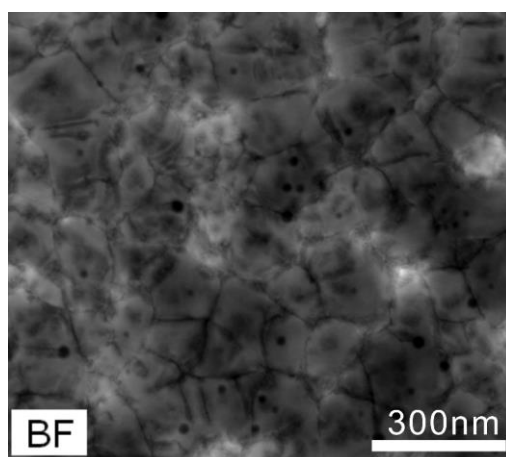


Figure 3.4 Plan-view bright field image of the (In,Ga)P/SiGe/Si sample.

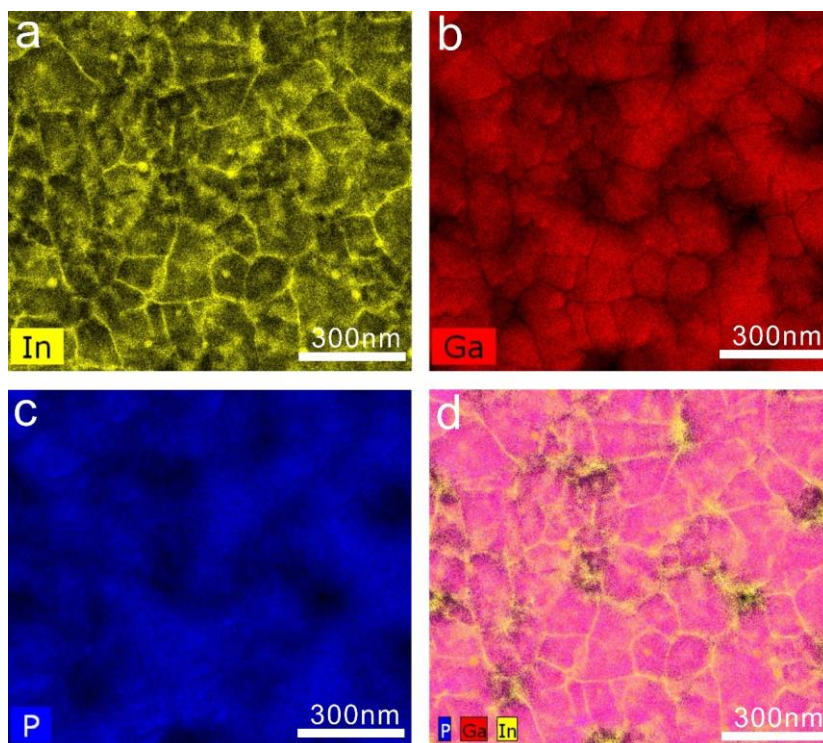


Figure 3.5 Plan-view elemental mapping images of indium (a), gallium (b), phosphorus (c) and indium-gallium-phosphorus integration (d), corresponding to **Fig. 3.4**.

In order to study the property of the 2D In-rich APB structures independently of other In-rich nano-objects, we developed a procedure to carefully remove them. Thus, a chemical mechanical polishing (CMP) process was used to remove the surface nanostructures. The scanning electron microscope (SEM) images of the as-grown sample and the sample after CMP are shown in **Fig. 3.6a** and **Fig. 3.6b**, respectively. By comparison, it is observed that the surface of the sample was polished in an effective way.

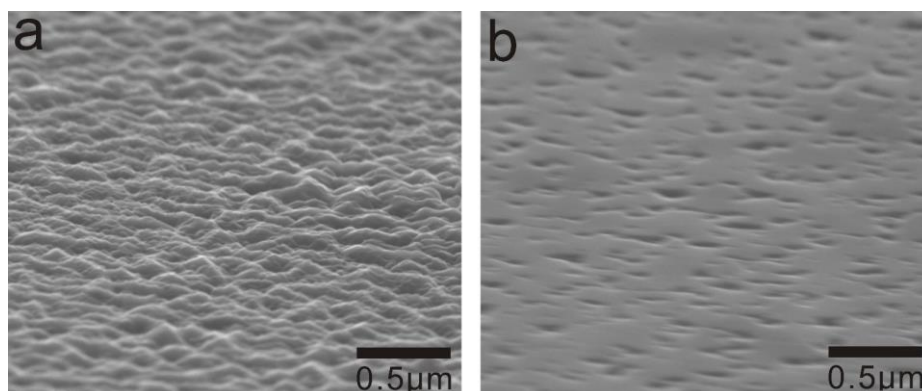


Figure 3.6 Scanning electron microscopy (SEM) plan-view images of the sample before (a) and after (b) CMP.

Figure 3.7 shows the Photoluminescence (PL) of the sample before(a) and after(b) CMP. After CMP, the low PL energy peak disappears which indicates that the low energy PL peak comes from the surface nanostructures, which were effectively removed by the CMP process.

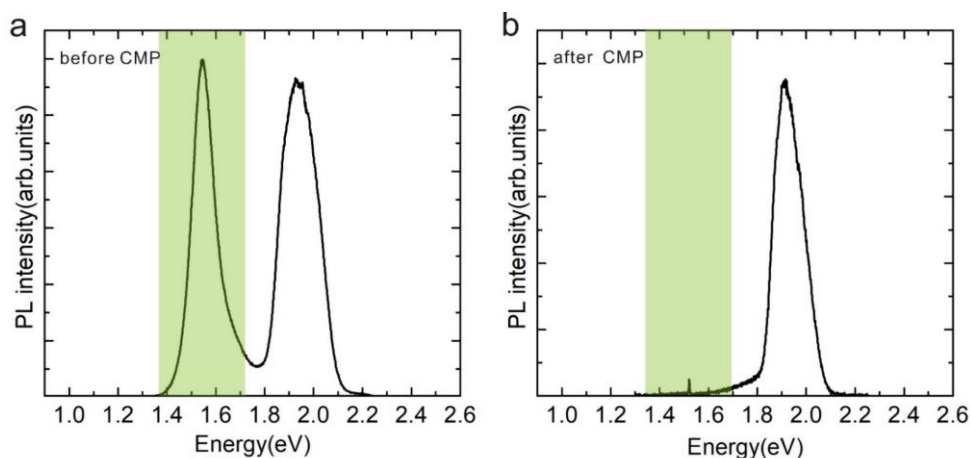


Figure 3.7 Photoluminescence of the sample before (a) and after (b) CMP.

X-ray diffraction profile of the reported as-grown InGaP/SiGe/Si sample (before CMP) is shown in **Fig. 3.8** and the X-Ray diffraction Reciprocal Space Maps (RSM) around the (224) and (004) reflections on the sample before and after CMP are displayed in **Fig. 3.9**. In **Fig. 3.8**, the strong peaks 1 and 3 originate from Si and SiGe. Comparing the RSM of the sample before (**Fig. 3.9a,b**) and after (**Fig. 3.9c,d**) CMP, we can find that the peak 5 disappears after CMP, indicating that it corresponds to the surface nanostructures. Their In composition is found to be around 100%, assuming a full plastic relaxation of the crystal. This is in good agreement with the EDX images presented above. The peak 4 is attributed to a layer fully strained to the SiGe buffer layer and does not change after CMP. It is therefore attributed to the MEE InGaP layer next to the SiGe buffer layer. The relatively strong peak 2 coming from the main In-poor phase, corresponds to a layer totally plastically relaxed, as shown in **Fig. 3.8**. The lattice parameters of the main In-poor (In, Ga)P phase were extracted from both RSM (**Fig. 3.9**) and $\omega/2\theta$ scans (**Fig. 3.8**) [92], leading to very similar values, confirming the full plastic relaxation state and giving mean lattice parameters of 0.55258 ± 0.0004 nm and thus corresponding to an In composition lying between 17 and 19%. On the contrary, it is hard

to determine precisely the In content of the In-rich (In,Ga)P alloy close to the antiphase boundary singularity due to the small size of the nanostructure. But from EDX contrast, we deduce that the local content is larger than 60%, suggesting that the APB structures at the atomic scale are closer to InP-based APB rather than GaP-based APB. Finally, the In-rich phase observed at the top of the APB (where it emerges) is composed of pure InP.

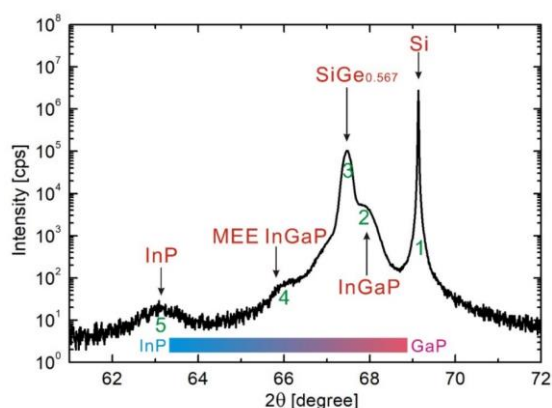


Figure 3.8 X-ray diffraction (XRD) patterns of the reported as-grown InGaP/SiGe/Si sample (before polishing).

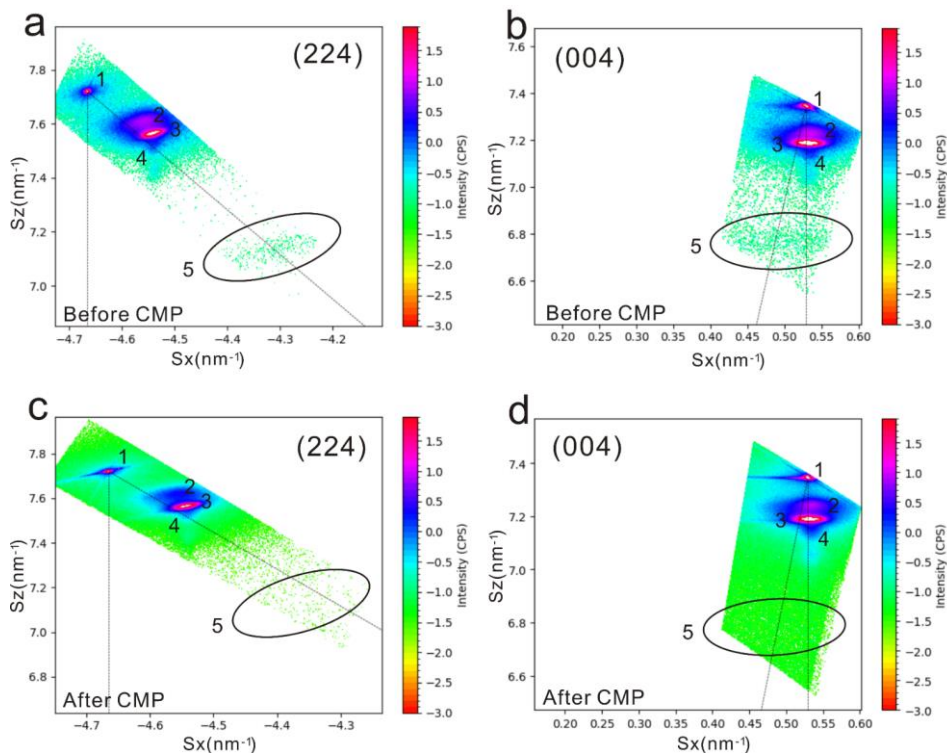


Figure 3.9 X-Ray diffraction reciprocal space mappings around (224) and (004) reflection on the sample before and after CMP. The black dotted vertical and inclined lines represent respectively the full strain lines and full relaxation lines.

At the III-V/Si interface, intermixing is not observed. The origin of In accumulation at the APB level rather than Ga is therefore generally connected to the formation of an InP nanostructure at the surface where it emerges, to feed progressively the APB during the growth. In accumulation and InP nanostructure formation are the consequences of stress and electrostatic interactions induced at the surface where the APB emerges, and the favored migration of In atoms. A sketch of a possible growth mechanism consistent with these experimental observations is indicated in **Fig. 3.10**. Overall, this preferential indium incorporation leads to the presence of a quantum confinement for carriers around the 2D homovalent singularities.

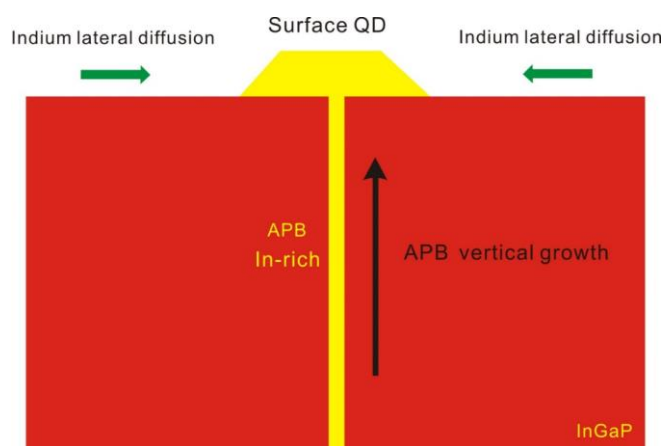


Figure 3.10 Schematic image of a possible APB growth mechanism explaining the preferential In incorporation.

We demonstrate in the following, that the 2D homovalent APB singularities are new interesting nano-objects with original optical, vibrational or electronic properties due to their unique atomistic structure and the quantum confinement effects afforded by the surrounding In-rich local environment. The next section is dedicated specifically to the determination of optoelectronic and vibrational properties of stoichiometric APBs, in order to support further experimental findings.

3.4 Optoelectronic and vibrational properties of stoichiometric APBs studied by DFT

3.4.1 Definition and properties of the supercell

As described previously, APBs are composed of III-III or V-V bonds [75,86], which induce a lack or excess of electrons, as compared to the surrounding matrix. Therefore, it is expected to behave as acceptor or donor-like centers [75]. One of the first consequences of the intrinsic APB structure is that inversion symmetry, which is absent in the bulk III-V zinc-blende lattice is restored locally. An InP supercell containing two stoichiometric APB planes (called hereafter APB-supercell) with 32 atoms ($n=32$) is shown in **Fig. 3.11**. For comparison, a reference InP supercell structure ($n=32$) without APB (called hereafter bulk-supercell) was also constructed as shown in **Fig. 3.12**.

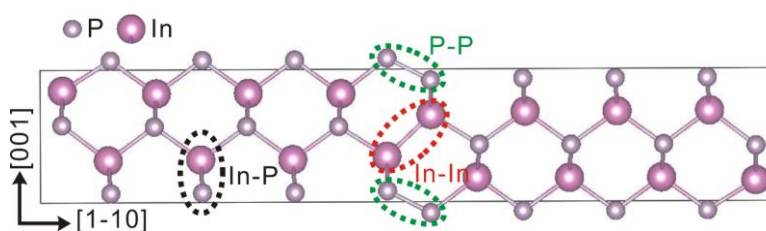


Figure 3.11 The 32 atoms APB-supercell (APB in an InP matrix) used for DFT band structure and phonon calculations.

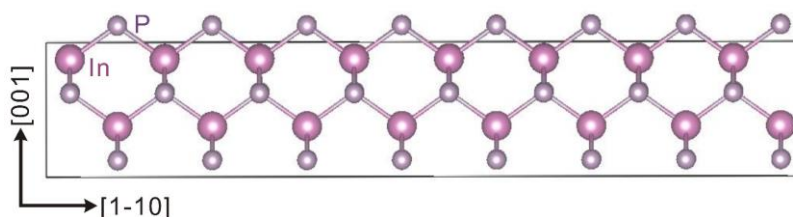


Figure 3.12 Model 32 atoms bulk-supercell structure of InP used for DFT calculations.

An APB locally exhibits an inversion symmetry, contrary to the surrounding zinc-blende lattice. This unusual property appears more clearly when considering an APB supercell with maximized Pnm (space group no 58) symmetry, or the layer group symmetry $p2/m11$ no14 for an isolated APB. The logical connection between the layer and the space groups is performed by considering the space group $P2/m$ (no10) as an intermediate (as shown in Fig. 3.13).

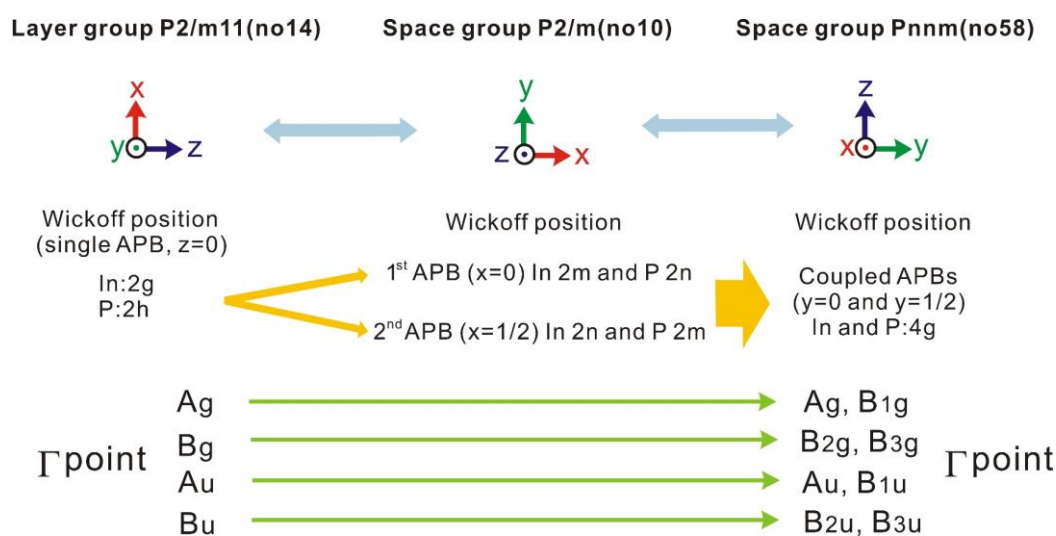


Figure 3.13 Illustration of the connection between the layer and the space groups. The wickoff positions for In and P atoms are given. The connection between the irreducible representations at the Γ point in both cases is also indicated. The axis perpendicular to the layer is z and y respectively for the standard settings of layer and Pnm space groups.

In order to better understand and analyze the vibrational and electronic properties in the system, phonon and band structures need to be clarified. Electronic band structure and phonon calculations were performed using Density Functional Theory (DFT) for InP APB-supercell and bulk-supercell. The corresponding results and discussions will be shown in the following paragraphs.

3.4.2 Bandstructure calculations

Electronic bands were calculated along different k-paths ($Z(0,0,0.5)$)- $\Gamma(0,0,0)$ - $U(0.5,0,0.5)$; $R(0.5,0.5,0.5)$ - $\Gamma(0,0,0)$ - $S(0.5,0,0.5)$), where the axis x, y, z of the reciprocal space correspond to the $[001], [1-10], [110]$ crystallographic directions, based on the Heyd–Scuseria–Ernzerhof (HSE) hybrid functional. The band structure plot for the APB-structure is shown in **Fig. 3.14**, where the states are weighted by their spatial localization at the APB plane. The color map from blue to red underlines the increase of localization effect of the states considered around the APB. **Figure 3.15** shows the band structure of the reference bulk supercell with a direct bandgap of 1.40eV. For a clear comparison, the Valence Band Maximum (VBM) and the Conduction Band Minimum (CBM) of the bulk-supercell were marked in **Fig. 3.14**, shown as horizontal black dotted lines. Both supercell structures show band folding effects due to the construction of the supercell. As compared to the bulk, the APB structure does not affect much the nature of the CBM, while it introduces two localized states at the top of the VB, shifting the VBM upward (by roughly 0.5eV) and thus reducing the bandgap.

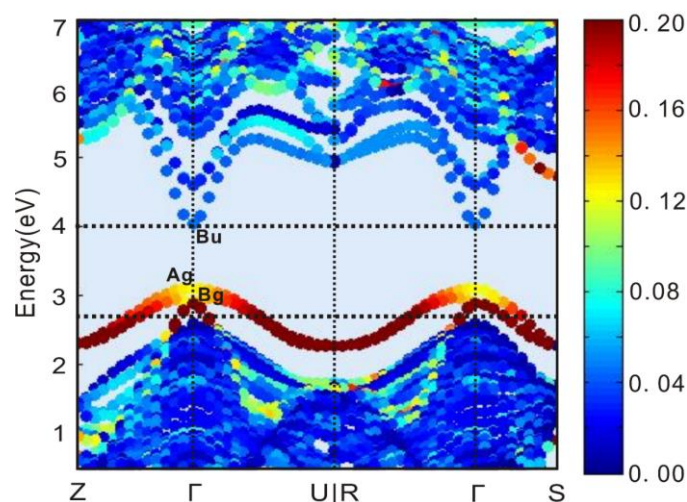


Figure 3.14 Calculated bandstructure of a 48 atoms APB-structure, weighted by the spatial localization of the wave functions at the APB interface. Layer group IRs at Γ point are given.

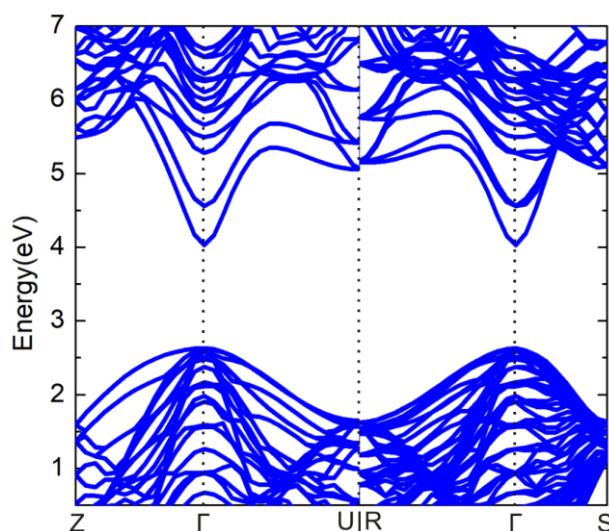


Figure 3.15 Bandstructures of bulk InP for the supercell (48 atoms) computed by DFT using the HSE functional.

In order to identify the electronic states strictly related to the isolated APB, calculations were performed on APB supercells with $n=32/48/64$ atoms (with increasing number of atoms only along the $[1-10]$ direction, leading to longer distance between the nearby APBs) based on metaGGA (TB-mBJ) [128] potential by Quantum Espresso package codes to obtain the symmetry properties of electronic states and get rid of finite size effects which lead to artificial electronic coupling between the APBs. **Fig. 3.16** gives the energies of the various electronic states labelled according to the IRs of the $Pnmm$ space group. As indicated in **Fig. 3.16**, the energy splittings of pairs of states are expected to vanish for large APB separations and thus large n values. Therefore, according to the labelling of the layer space group, the top of the VB is related to the A_g IR. It is also clearly identified as a localized state for a single APB according to its electronic density profile in the APB supercell. The second VB state is also localized on the APB and corresponds to B_g layer group symmetry. The VB states which appear next about 0.5eV below the top of the VB are not located anymore on the APB and correspond to InP bulk VB states (**Fig. 3.14**). From these simulations, we conclude that a single APB yields two VB states located into the band gap of the surrounding InP matrix. On the other hand, the first electronic states at the bottom of the CB appear to be located into the InP matrix and correspond to a B_u layer group symmetry. Overall, the bandgap of the APB-structure is equal to about 0.93 eV (**Fig. 3.14**). Therefore, we notice that the energy difference

between the bottom of the CB and the first bulk InP-like VB states amounts to about 1.43eV in nice agreement with the electronic band gap of bulk supercell InP (1.40 eV, **Fig. 3.15**) at the same level of theory. To summarize, the overall picture emerging from this analysis, is that a type II band alignment between the APB and the surrounding InP matrix is shown, yielding two APB localized VB states. These 2D VB electronic states belong to Ag and Bg IR in a layer group representation, which are marked in **Fig. 3.14** together with the layer group representation Bu of first electronic states at the bottom of the CB.

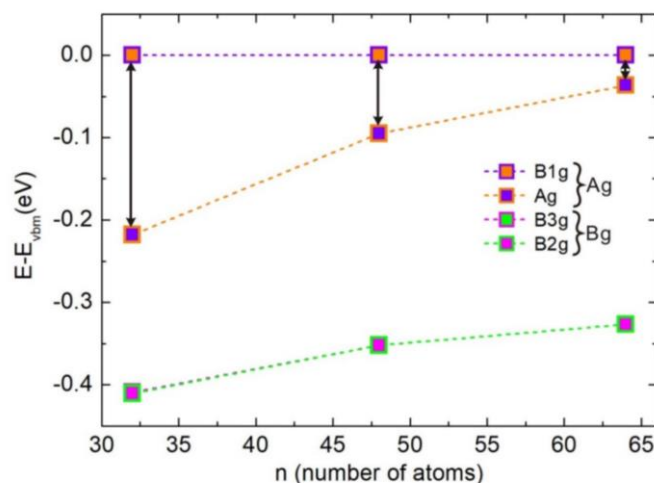


Figure 3.16 The energies of the VB localized electronic states on APB labelled according to the IRs of the Pnmm space group at Γ point vs the APB supercells size ($n=32/48/64$ atoms). The electronic states with B3g and B2g symmetries almost overlap.

In addition, **Figure 3.17** shows the planar averages of the partial charge densities of the VBM and CBM integrated parallel to the APB. The VBM partial charge density clearly reveals localization of carriers on the APB plane and the density drops between APBs, in good agreement with the weighted bandstructure represented in **Fig. 3.14**. Conversely, the charge density of CBM slightly decreases at the APB level, which indicates the type-II band alignment between the APB singularity and the bulk (schematically shown in **Fig. 3.29**), in good agreement with the results and analysis of electronic band calculations given above.

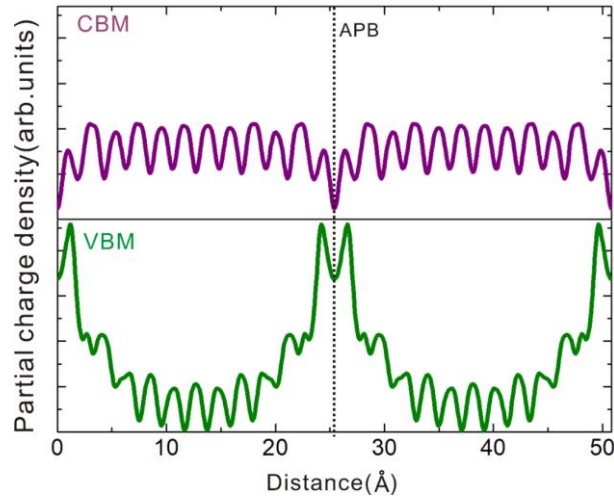


Figure 3.17 Partial charge density of the VBM and CBM at the Γ point for a 48 atoms supercell, integrated in the planes parallel to APBs. The dotted line corresponds to the APB plane.

3.4.3 Vibrational properties calculations

Phonon dispersions of the APB-supercell and the reference bulk-supercell (InP) are then computed and shown in **Fig. 3.18** and **Fig. 3.19**, respectively, where $R(0.5,0.5,0.5)$, $\Gamma(0,0,0)$ and $U(0.5,0,0.5)$ are the high symmetry points of the first Brillouin zone. In both cases, the phonon dispersion also shows band folding effects due to the construction of the supercell. From the known bulk phonon dispersions, we can identify the contributions of underlying InP acoustic (low frequency) and optical (high frequency) phonon branches. We may notice that the computed bulk phonon frequencies are a little smaller than the experimental ones [167], which is an expected consequence of the generalized gradient approximation (GGA) that overestimates lattice constants and underestimates the energies of vibrational modes [168].

Comparing the phonon dispersions of the bulk (**Fig. 3.19**) and APB-structure (**Fig. 3.18**), it can be clearly observed that the APB-supercell introduces several new flat phonon branches in the phonon dispersion gap, positioned at around 5.3 THz, 5.9 THz, 7.8 THz, 8.0 THz, 12.6 THz, marked by orange, blue, magenta, green and purple dotted lines, respectively (**Fig. 3.18**). These phonons correspond at the Γ point, respectively, to the Ag, Bu, Au, Bu, Ag irreducible representations of the layer group for a single APB.

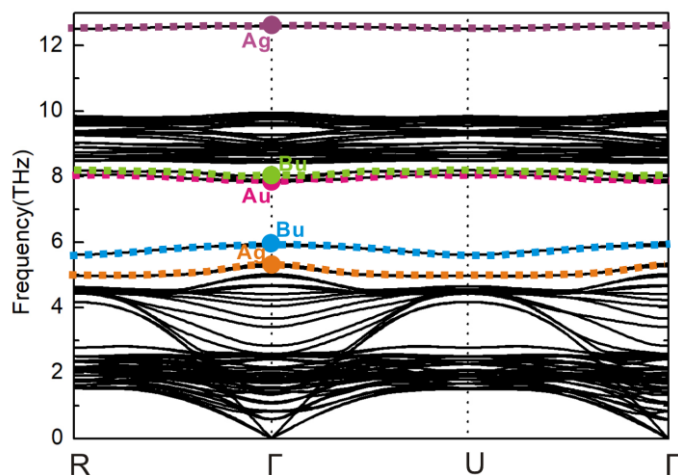


Figure 3.18 Phonon dispersion of the 32 atoms APB-structure. The phonon modes highlighted by orange, blue, magenta, green and purple dotted lines correspond to additional localized modes related to APB planes. They are labelled according to layer group IRs at Γ point.

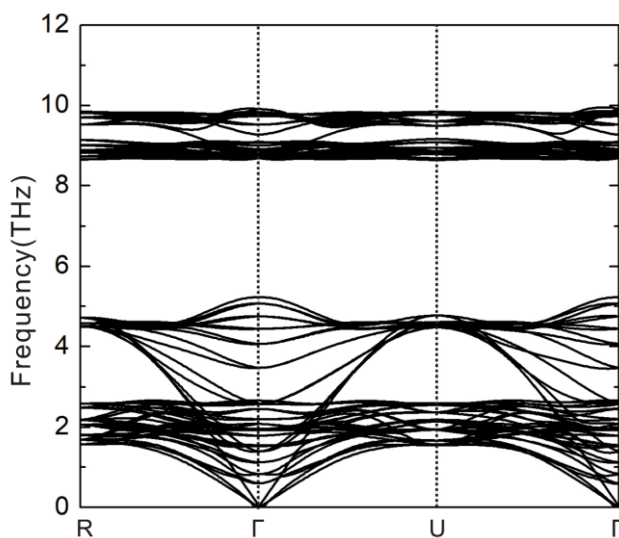


Figure 3.19 Phonon dispersion of bulk InP for the supercell (32 atoms)

The symmetry properties were investigated for these additional phonon modes based on an APB supercell of 32 atoms at the DFT-GGA level (**Table 3.1**). The phonon modes are all grouped by pairs since the supercell contains 2 APBs, but the phonons can be labelled as well, according to the IR of the layer group, which are relevant for a single APB (**Fig. 3.13**). The small splitting for each pair of phonons is related to the mechanical coupling between APBs that should vanish for an infinite supercell. Therefore, the five new phonons characteristic of a single APB are identified with frequencies equal to about

5.30, 5.92, 7.84, 7.96, 12.6 THz and well-defined symmetries (**Table 3.1**). Each two phonons grouped by pairs have almost the same vibration behavior. The IR of the layer group of the new phonon modes are marked in the **Fig. 3.18**.

Table 3.1. Space group IR and layer group IR of the five new phonon modes (all grouped by pairs) in order to evidence the phonon modes characteristic of a single APB.

Phonon mode order	Frequency(THz)	Pnnm space group IR (Γ G)	p2/m11 layer group IR (Γ)
47 /48	5.269 / 5.337	Ag /B1g	Ag
49 /50	5.891 /5.952	B2u/B3u	Bu
51/52	7.836/7.837	B1u/Au	Au
53/54	7.881/8.037	B2u/B3u	Bu
95/96	12.610/12.616	B1g/Ag	Ag

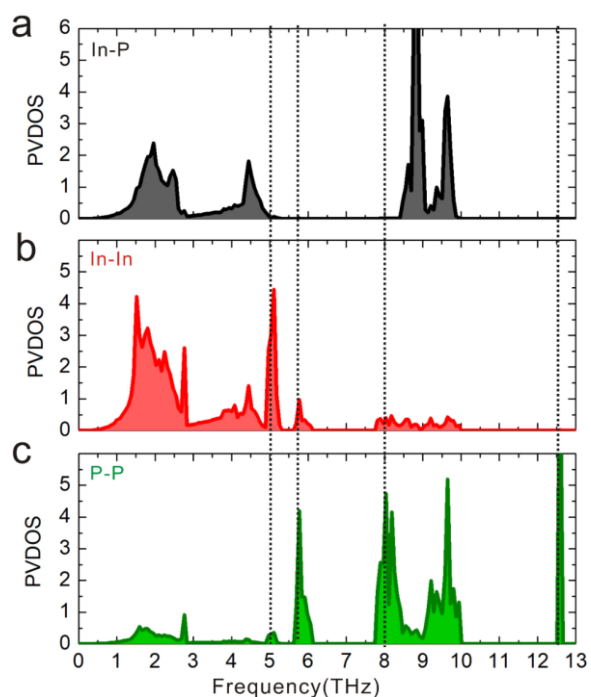


Figure 3.20 Partial vibrational (phonon) density of states of the middle InP atoms (a), In-In APB atoms (b) and P-P APB atoms (c), corresponding to the atoms encircled by the black, red and green dotted lines respectively in **Figure 3.11**.

Figure 3.20a-c show the partial vibrational density of states (PVDOS) of the “bulk-like” In-P bond, In-In APB bond and P-P APB bond (encircled by black, red and green dotted lines in **Fig. 3.11**), respectively, which reveals that the new flat phonon branches mainly result from the APB singularity. Moreover, the localized phonon with relatively low frequency (around 5.3 THz) mainly comes from the vibration of the In-In APB bonds and the other localized phonons mainly correspond to the vibration of the P-P APB bonds. The vibration behavior of the five localized phonon modes at the Γ point (corresponding to the orange, blue, magenta, green and purple dots in **Figure 3.18**) were extracted. The schematic images are shown in **Fig. 3.21**, where the arrows represent the vibration directions and amplitudes of the main atoms involved. We can see that the five new phonon modes are mainly localized at the APB plane singularity, which is consistent with the vibrational PVDOS calculated before.

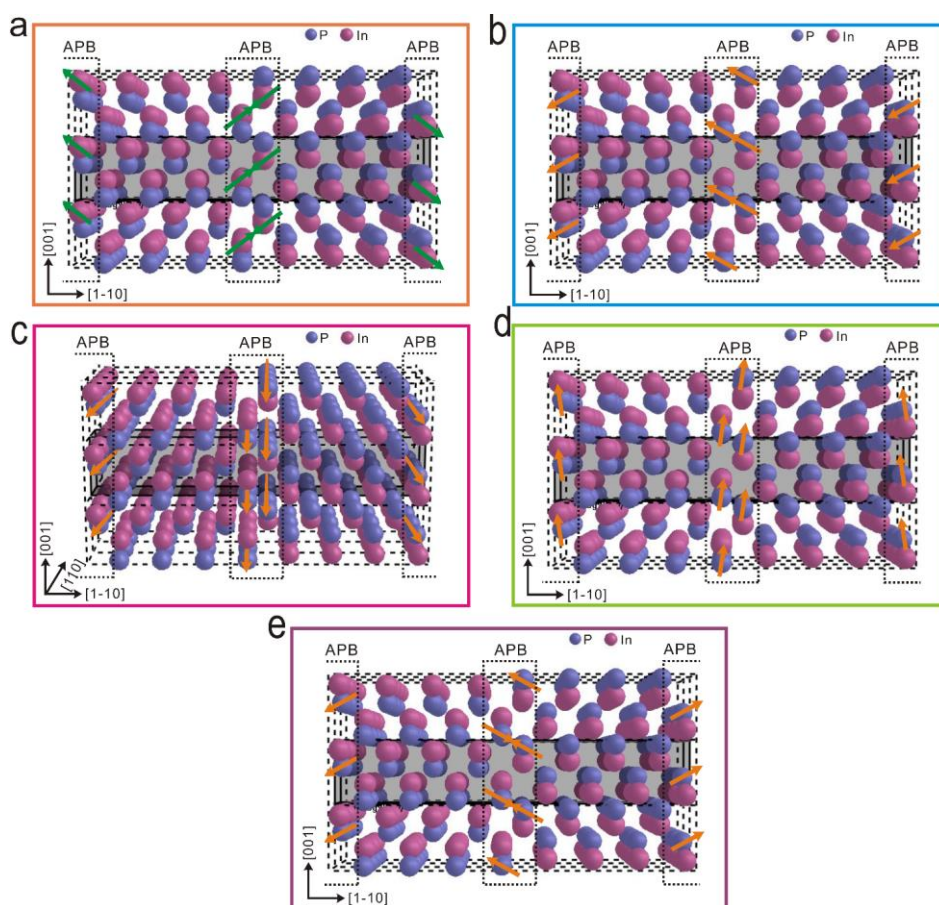


Figure 3.21 Schematic images of vibration behaviors of the five APB localized phonon modes at Γ point: 5.3 THz-Ag(a); 5.9 THz-Bu(b); 7.8 THz-Au(c); 8.0 THz-Bu(d); 12.6 THz-Ag(e).

In order to further estimate the contribution of the five localized phonons to the Raman signal, the Raman spectrum of the five localized phonons at Γ point was calculated and extracted, as shown in **Fig. 3.22**. We thus confirm numerically that only the A_g localized phonons with frequencies around 5.3 and 12.6 THz may significantly contribute to the Raman spectrum.

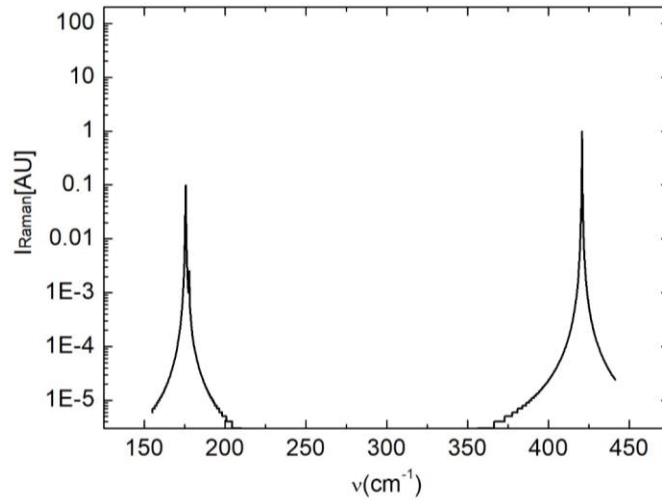


Figure 3.22 Simulated Raman spectrum of the five localized phonons at the Γ point, from DFT.

3.5 Optical characterizations

3.5.1 Raman measurement

Spatially- and spectrally-resolved Raman measurements were performed on the sample after CMP and the results are shown in **Fig. 3.23**. The Raman peaks 2, 3, 4, 5, 6, 7, correspond respectively to Ge-Ge bonds [169], GaP transverse optical (TO) phonons [170], InP longitudinal optical (LO) phonons [170], GaP LO phonons [170], Ge-Si bonds [169] and Si-Si bonds [170], and the InP TO phonons [170] should give some contribution to the signal around 303 cm^{-1} . The Raman peak 1 is relatively broad and weak, but its central frequency (around 200 cm^{-1} , i.e. 6 THz) shows a reasonable agreement with the A_g Raman active mode with frequency around 5.3 THz localized at the APB calculated previously. Therefore, the Raman peak 1 in the experimental data is attributed to the A_g localized vibration with theoretical frequency around 5.3 THz. The Raman signal of the

experimental data in the range of $400\text{-}500\text{ cm}^{-1}$ should contain the contribution from the second Ag APB localized phonon with a theoretical frequency around 12.6 THz, but it is most probably hidden by the contributions related to the other parts of the sample. The hyperspectral mapping in the inset displays the spatial distribution of the Raman peak 3 of GaP TO (green area) and Raman peak 1 (red area) vibration modes. The clear observation of remaining red and green area in the spatial superposition of the two vibrational modes indicate that the two phonon vibrations do not originate from the same region. Based on the EDX images, we know that there are two main structures in the InGaP layer (after CMP): the main In-poor phase (InGaP with around 18% In) and the In-rich phase located around the 2D APB singularities. Therefore, we attribute peak 3 observed in the Raman spectrum to lattice vibrations inside the In-poor domains away from the APB, while peak 1 comes from phonons localized in the APB homovalent singularities. The signature of the localized phonons (peak 1) in Raman experiments is relatively weak because of the small volume fraction of APBs. But this does not entail a low oscillator strength. From the structural investigations, the band structure and phonon dispersion calculations and from Raman measurements, we can conclude that the 2D APB singularities simultaneously bring in both carrier and phonon localization in the same region of the sample, which are the basic ingredients to create uncommon carrier-phonon interaction effects. The existence of an unexpected low-frequency localized Raman-active vibrational mode at about 6 THz is in particular consistent with first-principles predictions.

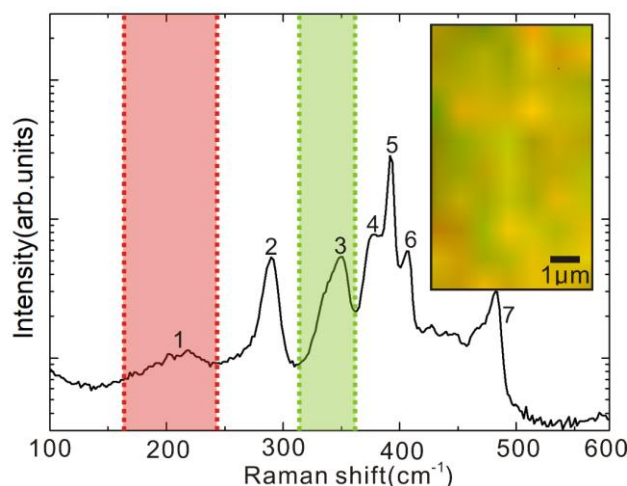


Figure 3.23 Experimental Raman spectrum. The Raman peaks 2, 3, 4, 5, 6, 7, correspond respectively to Ge-Ge bonds, GaP transverse optical (TO) phonons, InP longitudinal optical (LO) phonons, GaP LO phonons, Ge-Si bonds and Si-Si bonds. The Raman peak 1 shows a good corresponding to the 5.3 THz phonon localized in the APB, calculated previously. The inset shows the plan-view spatial distribution on the sample of the Raman peaks 1 (around 200 cm^{-1} , i.e. 6 THz) and 3 (GaP TO).

3.5.2 Ellipsometry Measurements

The optical constants of the InGaP/SiGe/Si sample were measured by spectroscopic ellipsometry (VASE) at room temperature in the 1.5–5 eV photon energy region. A Tauc-Lorentz model with 2 oscillators was used to fit the ellipsometry data. The measurements performed by ellipsometry are in colored dots and the fits are plotted in black continuous lines in **Fig. 3.24a**. These curves give the real and imaginary parts of the so-called “pseudo” dielectric function which can be obtained from **Eq. 2-9** and **Eq. 2-10**.

From the fitting model, the refractive index (n) and extinction coefficient (k) were extracted, as shown in **Fig. 3.24b**. From the imaginary part, absorption spectrum for the InGaP layer has been deduced, as shown in **Fig. 3.24c**.

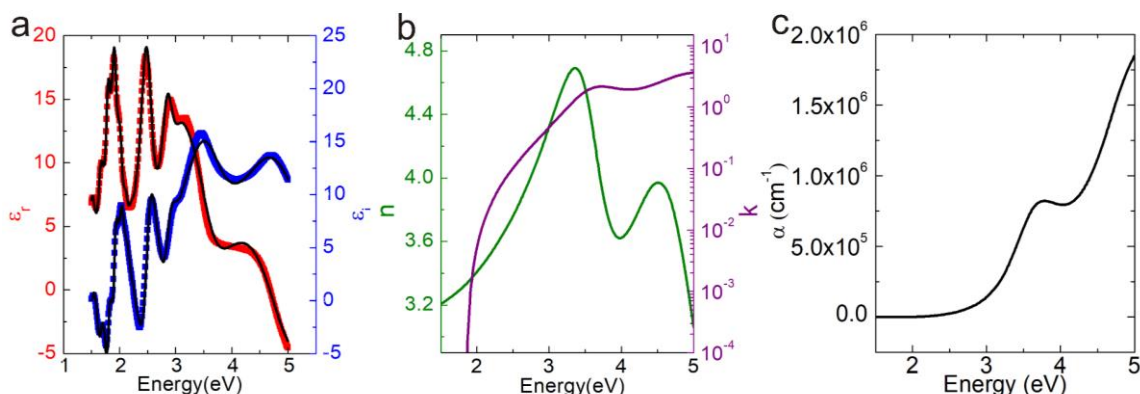


Figure 3.24 a, Experimental ellipsometry spectra of ϵ_r and ϵ_i (red and blue lines) and comparison with theoretical curves by using a 2-oscillators Tauc-Lorentz model (black lines). b, n (optical index real part) and k (optical index imaginary part) optical constants extracted from the fitting model. c, Absorption spectrum deduced.

3.5.3 Photoluminescence measurements

Low temperature (15 K) PL experiments were performed for the sample after CMP, as shown in **Fig. 3.25**. In order to analyze the PL and absorption spectra comprehensively, the absorption spectrum (**Fig. 3.24c**) was shifted at higher energy by 66 meV to account for the Varshni temperature dependence of the bandgap [171] and put together with the low temperature PL spectrum (**Fig. 3.25**). In the PL spectrum, one broad PL peak is observed between 1.8 and 2.1 eV. In the absorption spectrum, one peak between 3.5 and 4.0 eV can be observed, with a similar shape than the one usually reported for GaP [172], indicating that the absorption spectrum mainly comes from the In-poor phase. But the absorption curve starts from the high energy side of the PL around 2.1 eV, which is smaller than the expected bandgap of the In-poor phase $\text{In}_{0.18}\text{GaP}$ at low temperature (which should be around 2.32 eV) [173]. This absorption tail can result from the alloy fluctuation of the InGaP matrix or another part of the material with a lower bandgap (i.e. the In-rich phase with the APB singularity).

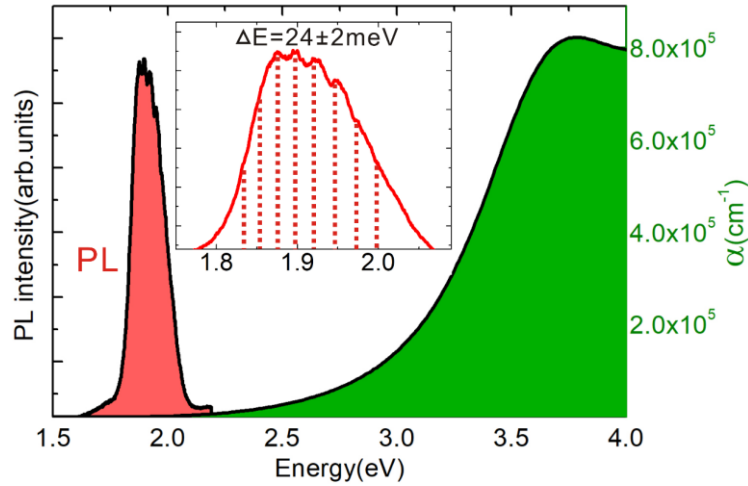


Figure 3.25 Photoluminescence and absorption spectra at low temperature (15 K). The inset corresponds to the PL spectrum in high magnification.

Another important feature of the PL spectrum is the presence of several small peaks on the top (inset of **Fig. 3.25**), separated by approximately the same energy (24 ± 2 meV, 5.8 ± 0.5 THz, 193.6 ± 16.1 cm^{-1}), which shows the contribution of phonons in the PL process. The small peaks are referred to as phonon replicas. In fact, a phonon energy around 24 meV is much smaller than the optical phonons of both GaP and InP, while it is in fair agreement with the energy of phonons localized around APB planes, predicted theoretically and observed in Raman spectroscopy. The observation of these phonon replicas further shows that a specific PL signal results from the APB singularity region. Besides, the APB-localized phonons dispersion curves of **Fig. 3.18** are very flat, which can facilitate phonon-assisted emission.

Figure 3.26a displays the power-dependent PL spectra, from which it can be observed that the whole spectrum (including small peaks and the broad contribution) remains proportionally unchanged with increasing pumping power, which further indicates the broad PL peak contains and only contains multi-phonon replicas. **Figure 3.26b** displays the logarithm plot of the integrated PL intensity versus excitation power. The k refers to the exponent of the power law equation $I_{\text{PL}} \sim I_{\text{ex}}^k$, where I_{PL} is the integrated photoluminescence intensity and I_{ex} is the excitation laser power [174]. It is found that at low pumping power it shows a super-linear power-dependency ($k=1.3$). With the increase

of the power, the k value decreases and finally turns to linear dependency ($k=0.96$). This behavior is a typical characteristic of the emissions involving saturation effect of trap centers (acceptors or donors) [175,176].

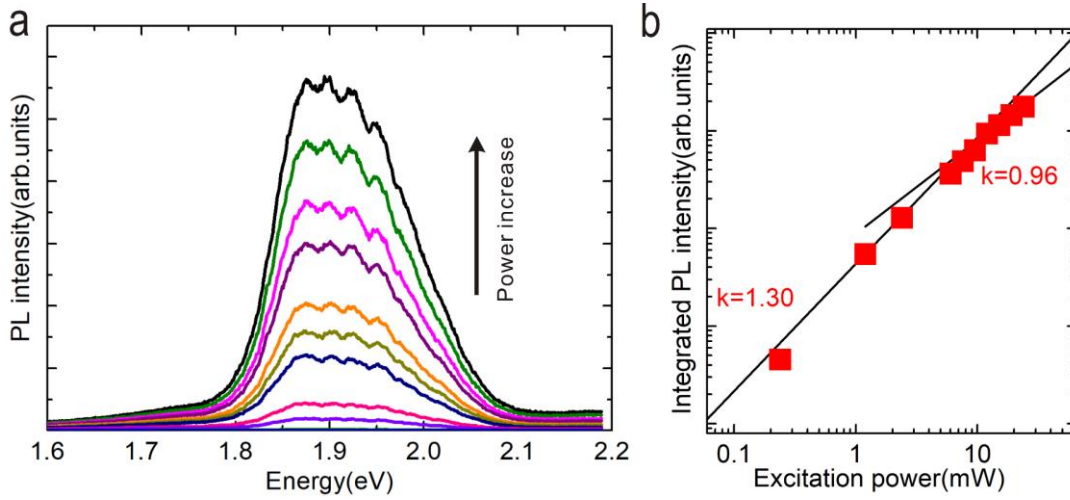


Figure 3.26 (a) Power-dependent Photoluminescence spectrum at 15 K. (b) Logarithm plot of the integrated PL intensity versus excitation power.

Temperature-dependent photoluminescence (PL) measurements were also performed on the sample after CMP, as shown in **Fig. 3.27**. The inset shows the corresponding Arrhenius plot of the integrated PL intensity, which mainly shows three temperature regimes. Three activation energies of 5 meV ($a_1= 6.6$), 38 meV ($a_2= 1124$) and 200 meV ($a_3= 8E^{10}$) were deduced, based on the equation [177]:

$$I_A(T) = \frac{I_0}{1+a_1 e^{-E_1/k_B T}} + \frac{I_0}{1+a_2 e^{-E_2/k_B T}} + \frac{I_0}{1+a_3 e^{-E_3/k_B T}} \quad (3-1)$$

Here, I_0 corresponds to the initial integrated PL intensity at the lowest temperature $T=15$ K, a_1 , a_2 , a_3 are dimensionless temperature-independent constants, and k_B refers to the Boltzmann constant.

The first activation energy is attributed to alloy disorder [33], while the two others may represent the detrapping of localized carriers (electrons or holes) to other localized states or extended states. Following the results obtained by DFT, the 200 meV activation energy is considered to be related to the detrapping of the localized holes in the APB

states to extended states of the In-rich phase.

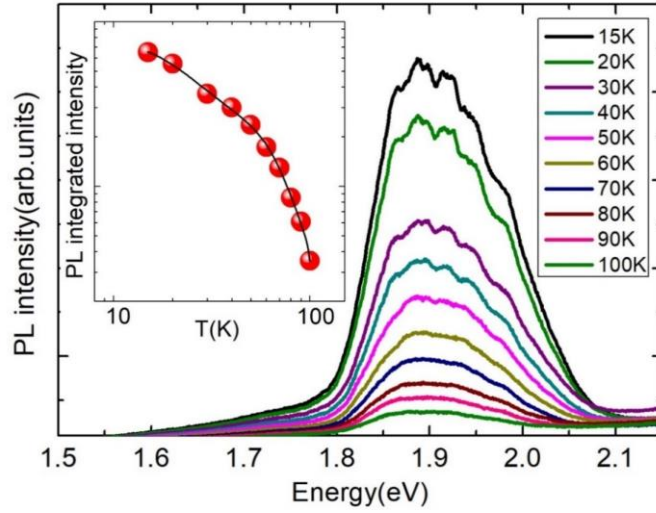


Figure 3.27 Temperature-dependent PL. The inset shows the corresponding Arrhenius plot of the integrated PL intensity.

In addition, time-resolved PL was measured. **Figure 3.28** shows the PL decay curve at 15 K, excited by a 355 nm pulse laser at a 560 mW/cm² excitation density. The PL decay curve was fitted by a power decay model designed for type II system [178]:

$$I(t) = \frac{\gamma n_0^2}{(1 + \gamma n_0 t)^{3/2}} \quad (3-2)$$

Where n_0 corresponds to the carrier density n at $t = 0$ and γ is a constant that gives the recombination rate $\Gamma = \Gamma(n) = \gamma n$. The fitting curve is shown as the red curve in **Figure 3.28** and the parameters $\gamma = 0.0004$ & $n_0 = 1800$ were obtained. The lifetime corresponding to the half of the maximum intensity (I_0) is 1.4 μ s. The good fitting and the observed long lifetime (within the μ s order of magnitude) are consistent with the theoretical picture of a type II band alignment. It indicates that confined holes in the APB play a major role in the enhancement of the electron-phonon interaction.

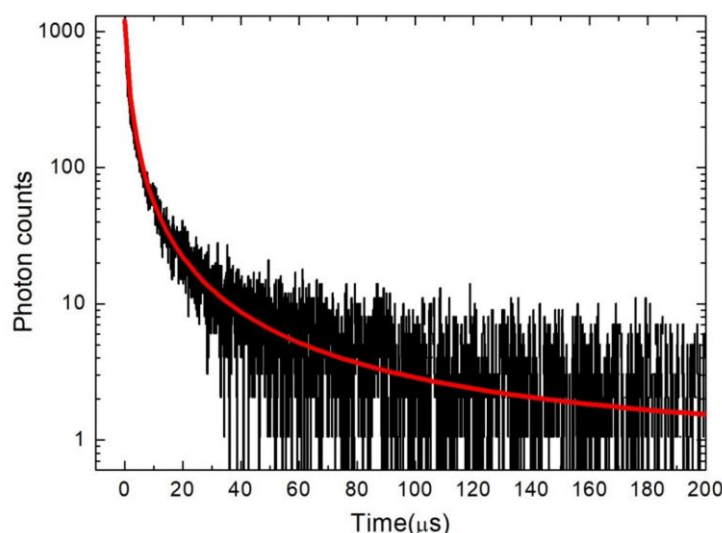


Figure 3.28 Time-resolved photoluminescence decay of the polished InGaP/SiGe/Si sample.

3.6 Proposed mechanism for the PL with multi-phonon replicas

Based on the DFT calculations and experimental results above, the general mechanism of the PL resulting from the 2D homovalent singularity is schematically represented in **Fig. 3.29a**. After illumination, the excited electrons in the conduction band recombine with the holes localized in the APB plane and it leads to PL emission. The mechanisms of electron-phonon interaction leading to the phonon replicas in the PL spectrum are analyzed first following the simplified Franck-Condon approach (**Fig. 3.29b**). The configuration coordinate diagram is used to show the potential well vs the normal mode coordinate (Q). Configuration coordinate diagram is the best way to describe the change of the defect geometry associated with the change of its electronic state [179], which in our simple picture is proportional to the bond length [160]. The dotted horizontal lines represent oscillator states and in this illustration, the potential well is ideally considered as harmonic so that the energy difference between two nearby oscillator states are the same and equal to the phonon energy.

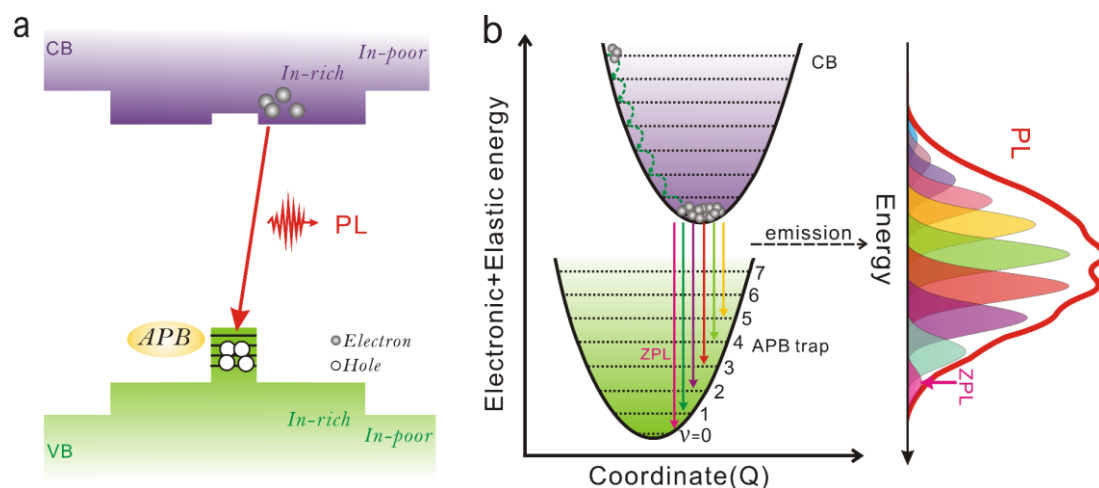


Figure 3.29 Mechanism of the Photoluminescence with a spatial representation (a) or within the electron-phonon interaction configuration coordinate point of view (b).

Beyond the localization effect related to the 2D homovalent singularity itself, the APB is embedded in an In-rich region surrounded by In-poor regions, which further brings an additional quantum confinement effect. Therefore, we expect a large number of localized electrons at the vicinity of the singularity. During absorption of the laser pump, the incoming photons can excite the electrons into the conduction band (CB) and change the filling of the APB states. Based on the classical Franck-Condon approximation [179,180], this optical transition takes place instantaneously. Meanwhile, the ions are slow, and their position does not change when the electronic state changes. After losing the electrons, the lattice near the nanostructure relaxes to a new equilibrium position, through which the electrons relax to the bottom of the potential well of the conduction band of the 2D structure [160] (the dotted green curves in **Fig. 3.29b**). Then the excited electrons will recombine with the holes in different localized vibration states ($v=0,1,2\dots$), giving the photoluminescence, shown as the multicolor emission lines in **Fig. 3.29b**, which correspond to the phonon replicas. The interaction between the electrons and phonons has usually to be strong to exhibit such quantum effects, which is consistent with the co-confinement of the electrons and phonons in the same region. The magenta emission line from the bottom of the conduction band potential well to the ground vibration state ($v=0$) corresponds to the zero phonon line (ZPL). At low temperature, the photoluminescence

intensity I_n of the n -th emission line follows the Poisson distribution [181]:

$$I_n = \frac{S^n e^{-S}}{n!} \quad (3-3)$$

where S is the Huang-Rhys factor which describes the magnitude of the electron-phonon coupling, and n the number of phonons generated in the transition. Moreover, the luminescence phonon wing is characterized by the relation: $E_n = E_{ZPL} - nE_{ph}$ (E_{ZPL} and E_{ph} corresponding to the energy position of the zero phonon emission line and the energy of phonons, respectively).

3.7 Fitting of the PL spectrum with multi-phonon replicas

The broad PL was fitted based on the **Eq. 3-3**. The phonon replicas were fitted by Gaussian functions with full width at half maximum (FWHM) of 26.5 meV and a phonon energy of around 24 meV was used. Note that Lorentzian functions did not allow fitting the phonon replicas correctly. The Gaussian broadening observed is mainly considered as the consequence of the inhomogeneous broadening effect due to the composition inhomogeneity or the different distances between the APBs [160]. The broadening effect due to acoustic phonons shall amount only to a few meV range [182], which can be neglected in the present study. In addition, the energy difference between two nearby phonon lines in the low energy part of the spectrum becomes a bit smaller gradually, indicating that the potential well is slightly anharmonic. Anyway, this observation doesn't impact the conclusions given here. **Figure 3.30** shows the experimental data and the theoretical fitting achieved by the Franck-Condon principle. Accurate fitting of the experimental curve was only obtained with a S parameter of 8 and a ZPL positioned at 2.097 eV.

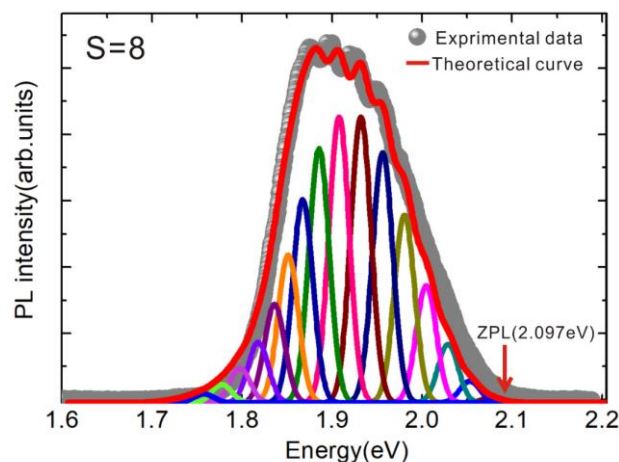


Figure 3.30 Experimental data (grey dots) and theoretical fitting (red line) of the broad PL peak based on the Franck-Condon model. The small multicolored peaks correspond to the distinct phonon replicas contributions.

To our knowledge, a Huang-Rhys factor of 8 is considerably larger than those found usually for undoped bulk III-V and II-VI semiconductors, even with confinement of carriers such as in QDs or QWs (0.015 for InAs/GaAs QD [157]; 0.3 for InGaN/GaN QW [183]; 0.36-0.7 for CdSe QDs [184]; 1.25 for InP/GaInP QD [185]). It indicates the presence of unusual strong electron-phonon interaction in the 2D In-rich vertical singularity due to (i) the double quantum confinement by the vertical quantum well, and (ii) the simultaneous confinement of electrons and phonons in the same region (as shown in **Fig. 3.31**).

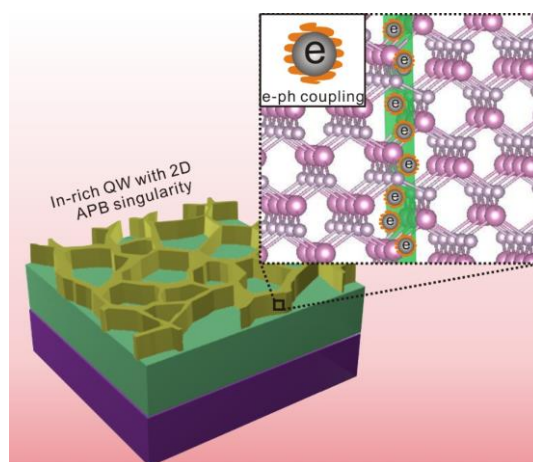


Figure 3.31 Schematic plot of the 2D vertical In-rich structure, embedding APB planes with strong electron-phonon interactions.

3.8 Electron-phonon interaction calculation

To further confirm the strong electron-phonon coupling induced by the new localized phonon modes around the APB structure, we calculated electron-phonon interaction (EPI) matrix elements ($g_{mnv}(k, q)$) for both polar and non-polar-localized modes using state of the art DFT-based microscopic theory.

Table 3.2 Electron phonon interaction matrix element $|g_{m,n,v}(k, g)|$ related to the A_g phonon non-polar modes for the bottom of the conduction band ($m=n=CBM$) and the top of the valence band ($m=n=VBM$) at the Γ point.

	5.4THz A_g Localized phonon	13.4THz A_g Localized phonon
CBM, CBM	5.212669	4.219345
VBM, VBM	2.327812	8.652394

Table 3.2 lists the electron phonon interaction matrix elements $|g_{mnv}(k, q)|$ related to the coupling at the Γ point between the A_g localized non-polar phonon modes and, the bottom of the conduction band ($m=n=CBM$) or the top of the valence band ($m=n=VBM$). We can find that the EPI matrix elements are large and consistent with the large S parameter. On the other hand, **Figure 3.32** shows the variation of the EPI matrix element for the polar-localized phonon modes as a function of q coupled to the same electronic states. As described in **Section 2.4.4**, the matrix elements vanish at the Γ point ($q=0$). They may exhibit an increase at long wavelengths, $q \rightarrow 0$ (**Fig. 3.32a**), although these variations exhibit as well significant deviations from the classic analytical Fröhlich model [140] (**Fig. 3.32b-d**).

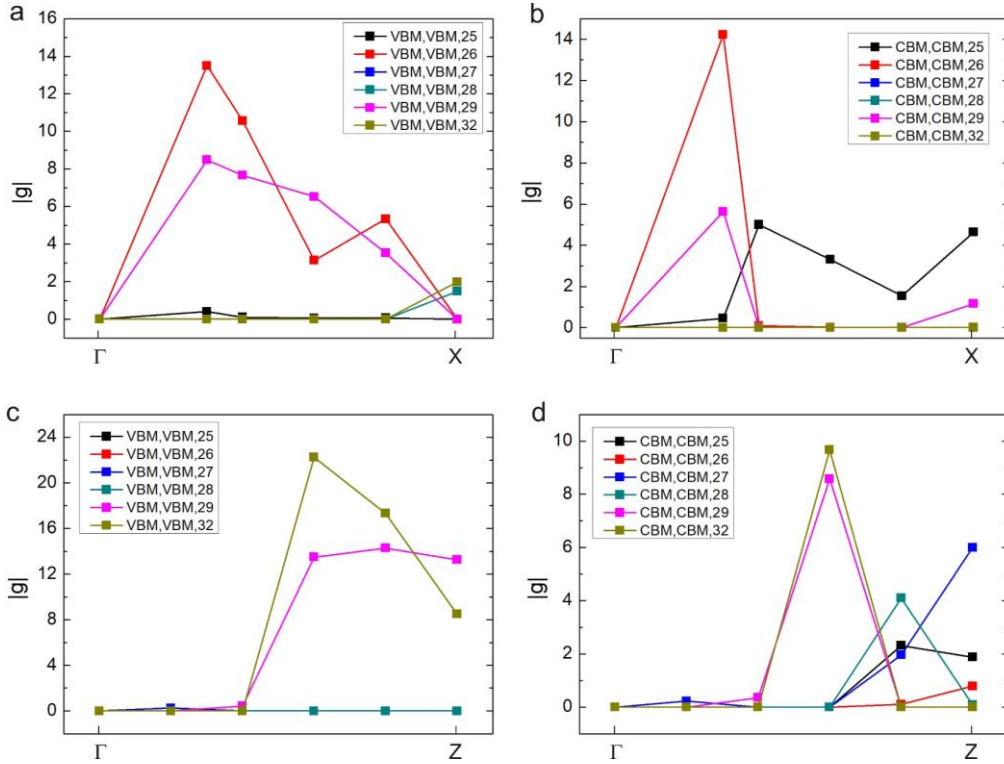


Figure 3.32 EPI matrix elements for the phonon branches corresponding to the localized polar phonon modes at the Γ point as a function of q for (a),(c) the top of the valence band ($m=n$ =VBM) and (b),(d) the bottom of the conduction band ($m=n$ =CBM) along the X and Z in-plane directions of the APB (The Γ -X and Γ -Z paths corresponding to the [001] and [110] crystallographic directions, Fig. 3.11).

3.9 Discussion on the possible microscopic origins of the strong EPI

Finally, we shall discuss the possible microscopic origins of the observed strong coupling regime between localized carriers and phonons. Raman scattering measurements coupled with PL replica characterization and localized phonon simulations point toward a mechanism involving both 2D Ag even localized phonon modes and APB localized VB electronic states. Therefore, a specific optical deformation potential mechanism is the most probable process to explain the experimental observations [178]. The observation of phonon replica is a signature of a strong electron-phonon interaction, which is consistent with the microscopic computation of a large electron phonon coupling matrix elements for the first localized non-polar Ag mode (**Table 3.2**). However, the second localized Ag mode is also predicted to exhibit a strong coupling to the same confined

valence state, despite the absence of corresponding discrete signatures on top of the PL envelope. Therefore, other aspects beyond our theoretical description and simplified APB model structure are likely to be important as well, including phonon-phonon interactions or lattice disorder. The Raman scattering experiment (**Fig. 3.23**) indeed shows that the first low-frequency localized mode already exhibits a broader signature than extended lattice modes. We may thus infer that such broadening is even more important for the other localized modes, leading only to shallow contributions to the envelope of the PL spectrum.

In addition, another classical electron-phonon coupling mechanism should be also considered for odd (polar) modes, that is the Fröhlich interaction. The theoretical study predicts that the APB polar phonon modes shall be located at a sizable energy above the lowest APB Ag even phonon mode, and therefore shall not be good candidates to explain the observed phonon replica. These localized polar modes are nevertheless likely to be coupled to localized VB electronic states. The matrix elements correspond to sizeable numerical values (**Fig. 3.32**) on the same order as the ones for non-polar modes at the Γ point (**Table 3.2**), thereby suggesting that the coupling to the localized polar modes is important for optoelectronic properties, and also playing a role for hole transport. This can shed some light on the recent experimental observation of APBs benefiting to carrier transport at room temperature [33,64]. Indeed, APBs are planar structures, not point defects and therefore, vertical transport in the APB planes can take place. In the present work, APBs can be assimilated to effective quantum wells forming planar conduction channels for carriers. We will however see in **Chapter 5** that other mechanisms involving non-stoichiometric APBs have also to be considered to explain the observed transport properties in III-V/Si samples. Anyway, considering the recent researches that allow controlling both lateral and vertical extensions of APDs [3,83], more investigations are needed to characterize the nature and the strength of the electron-phonon interaction processes in such homovalent singularities.

3.10 Summary

In this chapter, we demonstrated the simultaneous confinement of charge carriers and phonons at the vicinity of 2D vertical homovalent singularities (stoichiometric APBs) in an (In, Ga)P/SiGe/Si sample. The impact of the electron-phonon interaction on the photoluminescence processes was clarified, by combining transmission electron microscopy, X-ray diffraction, *ab initio* calculations, Raman spectroscopy and photoluminescence experiments. 2D localization and layer group symmetry properties of homovalent electronic states and phonons were studied by first principles methods, leading to the prediction of a type II band alignment between the APB and the surrounding semiconductor matrix. A Huang-Rhys factor of 8 was finally experimentally determined from the APB emission line, underlining that a large and unusually strong electron-phonon coupling can be achieved by 2D vertical quantum confinement in an undoped III-V semiconductor. This work extends the concept of electron-phonon interaction to 2D vertically buried III-V homovalent nanoobjects and therefore provides different approaches for material designs, vertical carrier transport, heterostructure design on silicon and device applications with weakly polar semiconductors.

Chapter 4: Development of GaPSb/Si photoelectrodes for solar water splitting

In 2018, at the end of I. Lucci's PhD thesis, the OHM research team at the FOTON Institute realized the advantages of using III-V/Si materials for green hydrogen production, through the development of photoelectrodes [186]. The results presented in this chapter were obtained in the framework of a collaboration initiated in 2019 with the department of Chemistry from UCL (University College London) for the characterizations of photo-electrodes. This led to the assessment of GaPSb/Si materials for photoelectrode developments, published in ref. [187], and the first demonstration of an operating bulk III-V/Si photoelectrode, published in ref. [33].

4.1 Introduction

As described in **Chapter 1**, solar water splitting technology producing clean and green hydrogen is of great interest for solving the environment and energy issues under the current global warming background.

However, numbers of challenges remain for the development of this technology, in terms of efficiency, profitability and sustainability. At the heart of the Photo-Electro-Chemical (PEC) conversion process is the choice of an appropriate photoelectrode material with both good bandgap and good band alignment to harvest the largest portion of the solar spectrum and provide sufficient voltage to accomplish the water splitting reactions [188]. Due to the broadness of the solar spectrum, from infrared to ultra-violet light, the needs for combining monolithically different materials with different bandgaps and thus absorbing different wavelengths, is considered today as the main pathway to reach high solar-to-hydrogen (STH) conversion efficiency [189,190]. In the tandem

association of two materials, the optimum combination of bandgaps has been widely discussed for different device configurations [191]. Especially, the combination of a 1.7 eV top absorber bandgap with a 1.1 eV bottom absorber is recognized as one of the best tandem materials configuration and gives rise to a theoretical maximum STH efficiency η_{STH} , larger than 26% [192]. Different device demonstrations were proposed with a III-V/III-V materials design, mostly based on the Ga(In)As/GaInP association, reaching η_{STH} larger than 15% [192-195]. In these works, high quality materials are achieved, thanks to the lattice-matching of these alloys on the expensive GaAs substrate. A way to reduce the cost of tandem materials association is to monolithically integrate a III-V top absorber (1.7 eV bandgap) on the silicon substrate (because of its approximate 1.1 eV band gap, earth abundance, low cost and prevalence in the electronics and PV industries) [191]. But by now there are only very few reports on Si-based tandem systems for water splitting, mainly due to the difficulty in growing high quality III-V epilayers on Si. The recent progresses in the understanding of III-V/Si epitaxial processes and devices developments give new hopes for the development of high efficiency III-V/Si PEC devices on the low-cost Si substrate [3,196]. Following this approach, pioneering works were performed on the development of bipolar configured 1.6 eV AlGaAs on 1.1 eV Si tandem association. Water splitting at a 18.3% conversion efficiency was reported [197]. Very recently, a single InGaN absorber photoanode monolithically integrated on silicon (where the Si (111) substrate is used as a back contact) was proposed with an applied-bias photo-to-current efficiency of 4.1% [34]. GaP-based materials were also proposed as an ideal tandem association with Si for water splitting [186]. However, as discussed in **Chapter 1**, this approach suffers from the indirect and large bandgap (2.26 eV) nature of GaP. Therefore, alloying GaP with other group III-V atoms is needed to achieve a direct bandgap at 1.7 eV through bandgap engineering. Doscher H. *et al.* theoretically proposed GaPN/Si and GaPNAs/Si tandem lattice-matched materials for water splitting based on GaP/Si-based photoelectrochemistry experiments and GaPN/Si epitaxial growth results [198]. But the N-including lattice-matched materials face the issue of excitons localization effects, which hamper easy charge carrier transportation in the developed devices. On the other hand, metamorphic III-V integration on Si is known to generate dislocations that are

usually detrimental for solar devices. The epitaxial growth of Sb-based III-V compounds on Si is particularly interesting in this regard, as it allows relaxation of the crystal stress through a near-perfect misfit dislocation network localized at the III-V/Si interface [3] leading to efficient and stable photonic device demonstrations [199]. Recent work proposed the use of freestanding GaPSb as a photoelectrode for water splitting [200]. However, the crystal growth and properties of this novel alloy was not yet deeply investigated.

In the next sections, we assess the potential of a new monolithic III-V/Si tandem materials association ($\text{GaP}_{1-x}\text{Sb}_x/\text{Si}$) for solar water splitting. The $\text{GaP}_{1-x}\text{Sb}_x$ was directly grown on Si substrate by molecular beam epitaxy (MBE), with the aim to keep the greatest merit of the tandem system, i.e. an efficient light absorption at 1.7 eV on the top of the 1.1 eV silicon bandgap. The bandgaps and band alignments of the $\text{GaP}_{1-x}\text{Sb}_x$ alloys are carefully and comprehensively studied over the whole Sb range, by combining the experimental data with tight binding (TB) theoretical calculations, and its possible use as a photoelectrode is discussed.

4.2 GaPSb/Si material growth and targeted device design for solar water splitting

Three $\text{GaP}_{1-x}\text{Sb}_x/\text{Si}$ samples (referred to as GaPSb-1, GaPSb-2 and GaPSb-3, with increasing Sb amounts) were grown by Molecular Beam Epitaxy (MBE) on HF-chemically prepared n-doped (around 10^{17} cm^{-3}) Si (001) substrates, with a 6° miscut toward the [110] direction. The substrates were heated at 800°C for 10 minutes to remove hydrogen at the surface. $1\mu\text{m}$ -thick $\text{GaP}_{1-x}\text{Sb}_x$ layers were then grown at 500°C in a conventional continuous MBE growth mode, and at a growth rate of 0.24 ML/s, with a Beam Equivalent Pressure V/III ratio of 5. The whole epilayer was undoped, and epitaxial strategies to annihilate antiphase boundaries [201] were not used, leading to emerging APBs.

The schematic diagrams of the proposed GaP_{1-x}Sb_x/Si tandem device for water splitting and the light absorption of the GaP_{1-x}Sb_x/Si tandem system with around 1.7/1.1eV bandgap combination are shown in **Fig. 4.1a** and **Fig. 4.1b**. The sun light should first enter the top cell (1.7 eV-bandgap targeted) GaP_{1-x}Sb_x layer, in which high-energy photons are absorbed and low-energy photons are transmitted and harvested by the Si substrate or bottom cell, leading potentially to very large light absorption of the sunlight (as shown in **Fig. 4.1b**). Then the photo-induced charges (electrons and holes) are generated in both layers, and, depending on the doping, one kind of charges flows toward the illuminated surface (the top surface of GaPSb layer) to generate H₂ or O₂ and the other one flow toward the back contact which is connected to the Si substrate (as shown in **Fig. 4.1a**) and is further extracted to feed the counter-electrode.

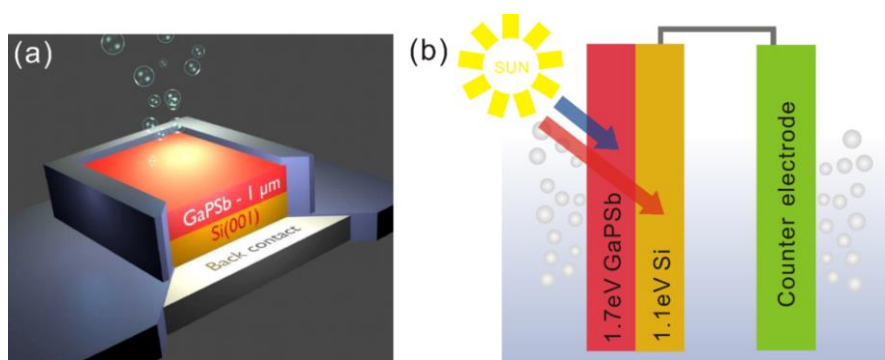


Figure 4.1 (a) Schematic of the proposed GaP_{1-x}Sb_x/Si tandem device for PEC water splitting. (b) Sunlight absorption illustration of GaP_{1-x}Sb_x/Si tandem system with a 1.7/1.1eV bandgap combination for water splitting which guarantees large light absorption.

4.3 Structural properties of GaPSb/Si epilayers

Figure 4.2 shows the X-ray diffraction (XRD) $\omega/2\theta$ profiles for the three samples. A miscut of around 6° toward the [110] direction is inferred for the three samples from the positions of Si Bragg peaks, which is in agreement with the substrate specifications. The $\omega/2\theta$ scans exhibit well-defined GaP_{1-x}Sb_x Bragg peaks for the three samples. Reciprocal space maps (RSM) carried out on either (004) or (115) (**Fig. 4.3**) reflections show a full plastic relaxation of the GaP_{1-x}Sb_x layers for the three samples. GaP_{1-x}Sb_x

lattice parameters were extracted from both reciprocal space maps and $\omega/2\theta$ scans, leading to very similar values for each sample, confirming the full plastic relaxation rates and giving mean lattice parameters of 0.5665 nm, 0.5835 nm, 0.6093 nm, for the samples GaPSb-1, GaPSb-2, GaPSb-3, respectively. The Sb contents of 0.33, 0.60, and >0.99 are then inferred [92]. Sample GaPSb-3 is almost pure GaSb. These RSM images also exhibit an important Bragg peak broadening due to a relatively large crystal defect density, in low Sb content samples. Furthermore, the XRD analysis does not give any evidence of a phase separation that could occur between GaP and GaSb in the $\text{GaP}_{1-x}\text{Sb}_x$ alloys in these growth conditions.

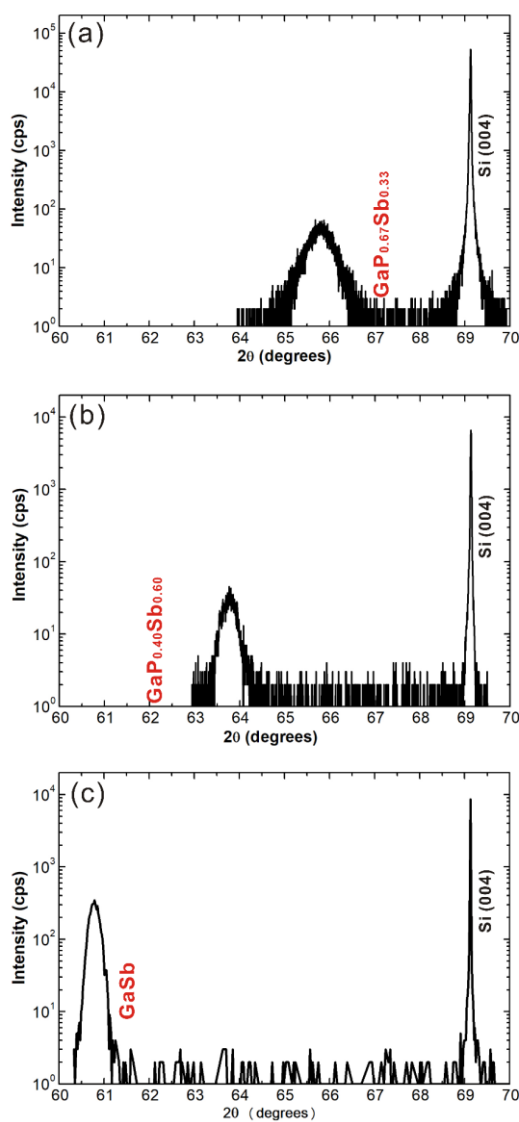


Figure 4.2 X-Ray Diffraction profiles for the three MBE-grown $\text{GaP}_{1-x}\text{Sb}_x/\text{Si}$ samples with different Sb contents: GaPSb-1 (i.e. $\text{GaP}_{0.67}\text{Sb}_{0.33}$) (a), GaPSb-2 (i.e. $\text{GaP}_{0.40}\text{Sb}_{0.60}$) (b) and GaPSb-3 (i.e. GaSb) (c).

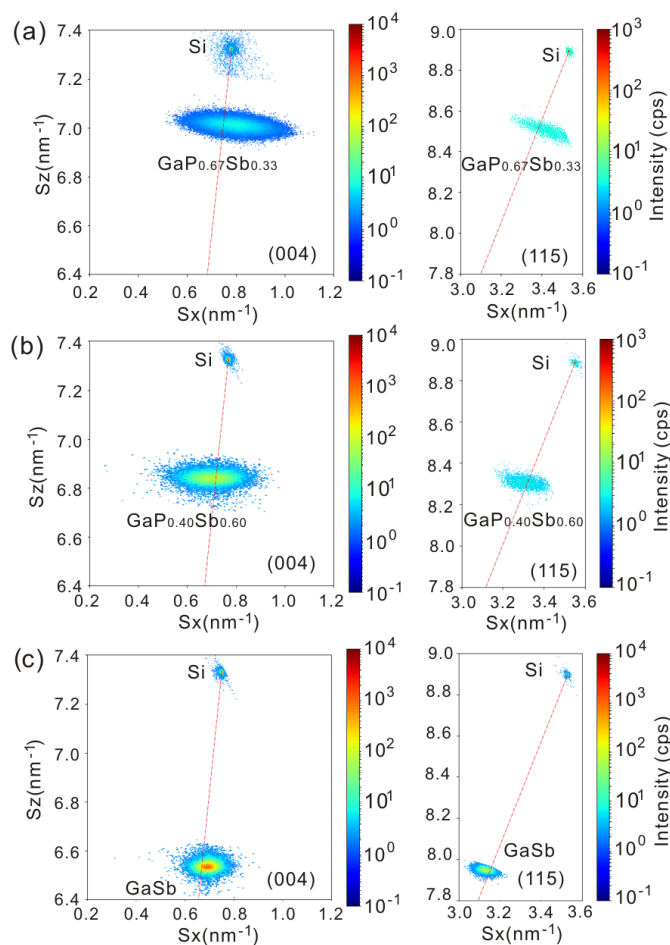


Figure 4.3 X-Ray diffraction reciprocal space maps around (004) and (115) for the three samples, correspondingly (S_x and S_z are the projected coordinates in the right handed Cartesian, with z axis parallel to the surface normal) [92]. The red lines represent the full relaxation lines.

Figure 4.4 shows the scanning electron microscopy (SEM) images of the three $\text{GaP}_{0.67}\text{Sb}_{0.33}/\text{Si}$, $\text{GaP}_{0.40}\text{Sb}_{0.60}/\text{Si}$, GaSb/Si samples on plan-view (**Fig.4.4** a, c, e) and cross-sectional view (**Fig.4.4** b, d, f). From these images, it can be observed that the samples $\text{GaP}_{0.40}\text{Sb}_{0.60}/\text{Si}$ and GaSb/Si exhibit relatively smooth surfaces as compared with the other $\text{GaP}_{0.67}\text{Sb}_{0.33}/\text{Si}$ sample. The roughness observed is attributed to both emergence of some crystal defects such as residual dislocations or antiphase boundaries and residual stress in the sample. The corresponding atomic force microscopy (AFM) images are given in the **Fig. 4.5** and the RMS (root-mean-square) roughnesses of the surfaces were found to be 22.80 nm for $\text{GaP}_{0.67}\text{Sb}_{0.33}$, 9.32 nm for $\text{GaP}_{0.40}\text{Sb}_{0.60}$ and 7.91 nm for GaSb . It suggests an improvement of the crystal quality with increasing Sb content. This is also confirmed by a very significant Bragg peak sharpening observed on reciprocal space

maps (RSM) (**Fig. 4.3**). Nevertheless, the crystal quality of the GaPSb alloy grown on Si has been significantly improved compared with the one obtained in previous work with different crystal growth techniques [200].

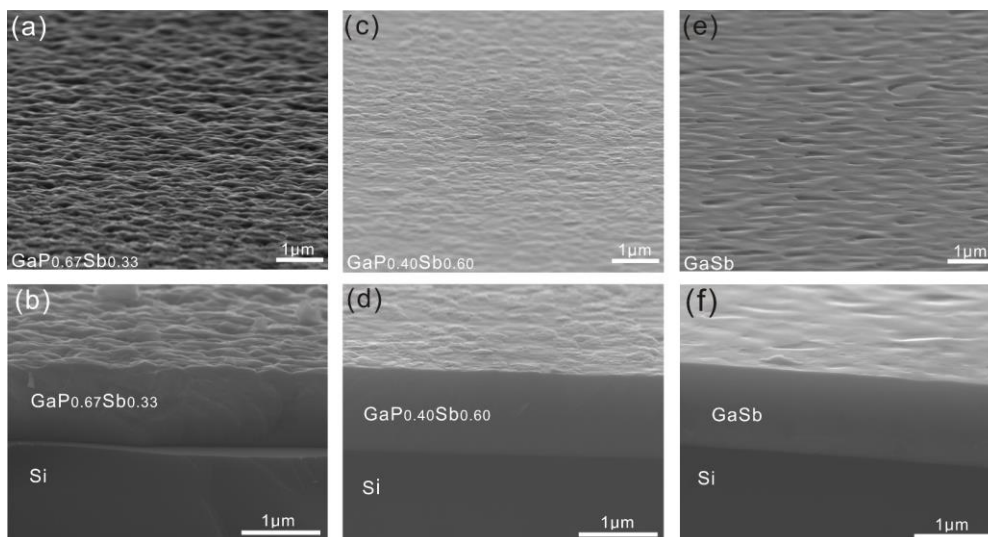


Figure 4.4 Scanning electron microscopy (SEM) images of the $\text{GaP}_{0.67}\text{Sb}_{0.33}$, $\text{GaP}_{0.40}\text{Sb}_{0.60}$, GaSb samples before CMP on plan view (a),(c),(e) and cross-sectional view (b),(d),(f).

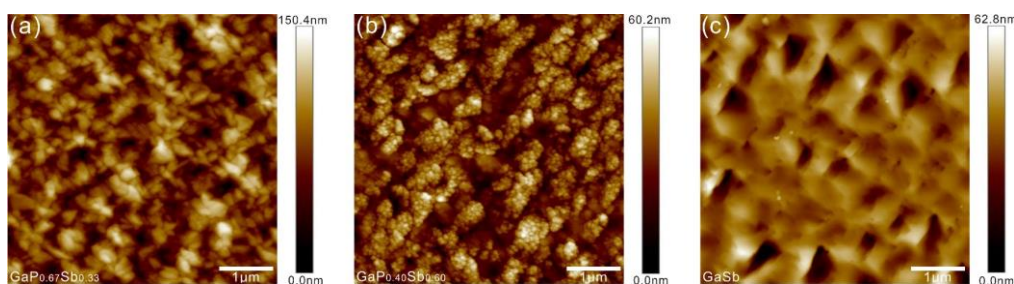


Figure 4.5 Atomic force microscopy (AFM) images of the $\text{GaP}_{0.67}\text{Sb}_{0.33}$ (a), $\text{GaP}_{0.40}\text{Sb}_{0.60}$ (b), and GaSb (c) samples before CMP.

In order to obtain smoother surfaces and avoid distortion on ellipsometry measurements, Chemical Mechanical Polishing (CMP) was performed on the three GaPSb/Si samples. **Fig. 4.6** shows the plan-view SEM images of the $\text{GaP}_{0.67}\text{Sb}_{0.33}/\text{Si}$, $\text{GaP}_{0.40}\text{Sb}_{0.60}/\text{Si}$, GaSb/Si samples after CMP, from which we can find that the surface smoothness of the three samples was much improved. Besides, **Figure 4.7** displays the AFM images of the three samples after CMP and the resulting surface RMS roughnesses of the three samples after CMP are 0.33 nm ($\text{GaP}_{0.67}\text{Sb}_{0.33}$), 0.28 nm ($\text{GaP}_{0.40}\text{Sb}_{0.60}$) and

0.56 nm (GaSb), indicating that the surfaces of the three samples become very smooth after CMP processes.

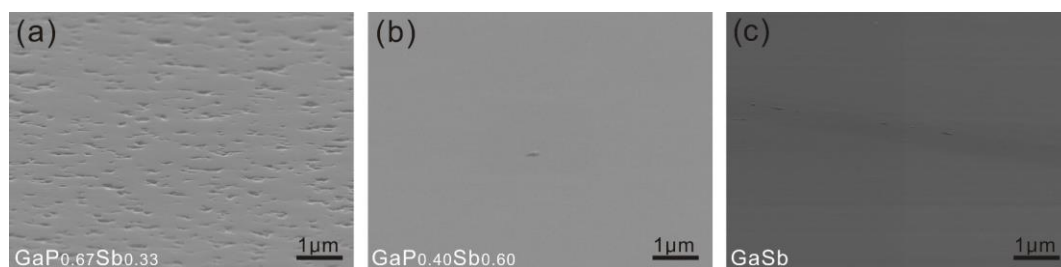


Figure 4.6 Scanning electron microscopy (SEM) plan view images of the GaP_{0.67}Sb_{0.33} (a), GaP_{0.40}Sb_{0.60} (b) and GaSb (c) samples after CMP.

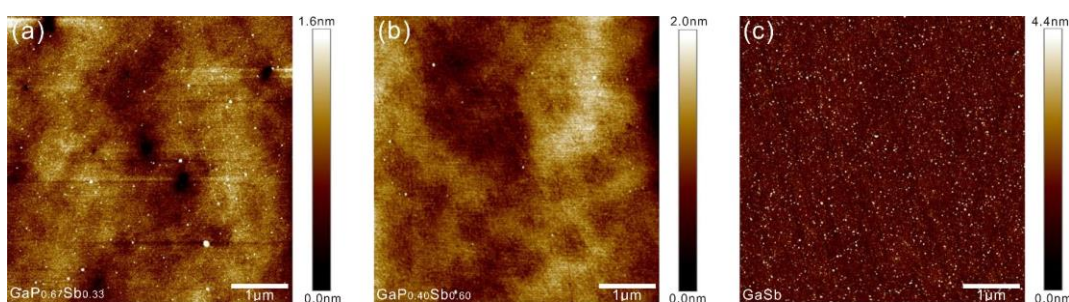


Figure 4.7 Atomic force microscopy (AFM) images of the GaP_{0.67}Sb_{0.33} (a), GaP_{0.40}Sb_{0.60} (b) and GaSb (c) samples after CMP.

Overall, from these measurements, we can conclude that the GaPSb epilayers grown on the Si substrates are monocrystalline, but defective, and are almost fully relaxed (strain effects won't be included in bandgap energy calculations). We will also consider that, when CMP is used, roughness of the samples cannot impact significantly the measured optical properties.

4.4 Bandgap evaluation of GaPSb alloys

4.4.1 Ellipsometry measurements

In order to evaluate the bandgap of the GaPSb/Si samples, ellipsometry measurements were performed. This technique has the advantage to extract the optical constants of the grown layer, independently of the Si substrate. The optical constants of

the $\text{GaP}_{0.67}\text{Sb}_{0.33}$, $\text{GaP}_{0.40}\text{Sb}_{0.60}$ and GaSb samples were measured by variable angle spectroscopic ellipsometry (VASE) at room temperature in the 0.58–5 eV photon energy region. The angles of incidence were set to 60° and 70° . A Tauc-Lorentz model with 2 oscillators was used to fit the ellipsometry data and extract the absorption coefficient value. **Fig.4.8** shows the fitting results for the $\text{GaP}_{0.67}\text{Sb}_{0.33}$, $\text{GaP}_{0.40}\text{Sb}_{0.60}$, GaSb samples, respectively. The red and blue lines correspond to experimental spectra where I_s and I_c parameters are represented. I_s and I_c are related to the well-known ellipsometry variables ψ (amplitude component) and Δ (phase difference) through the following relations: $I_s = \sin(2\psi) \cdot \sin(\Delta)$, $I_c = \sin(2\psi) \cdot \cos(\Delta)$. The black lines correspond to the theoretical curves after adjusting the parameters of the Tauc-Lorentz model. From this model, the refractive index (n), extinction coefficient (k) and absorption curves were extracted, as shown in **Fig. 4.9** and **Fig.4.10** (red curves).

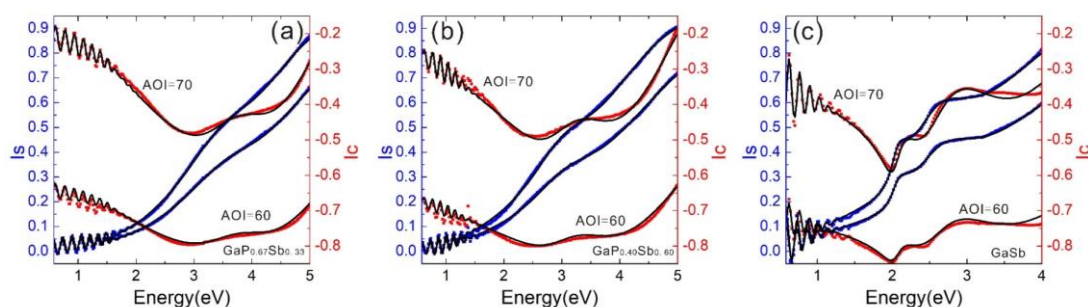


Figure 4.8 Experimental ellipsometry spectra of I_s and I_c (red and blue lines) for two incidence angles and comparison with theoretical curves by using a 2-oscillators Tauc-Lorentz model (black lines) for the $\text{GaP}_{0.67}\text{Sb}_{0.33}$ (a), $\text{GaP}_{0.40}\text{Sb}_{0.60}$ (b) and GaSb (c) samples, respectively.

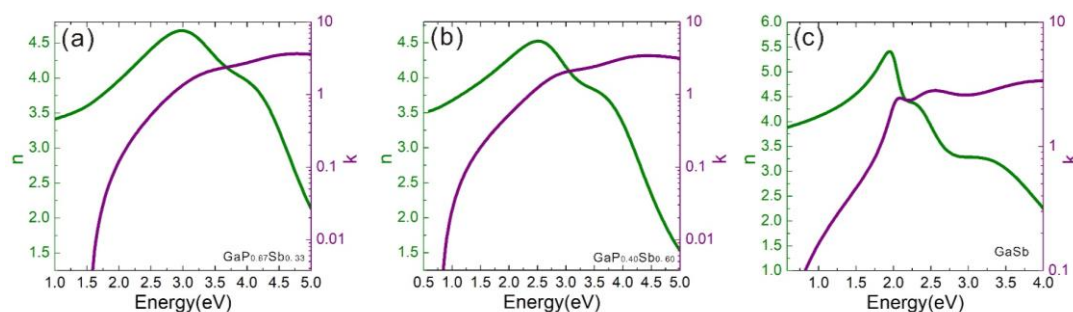


Figure 4.9 n (optical index real part) and k (optical index imaginary part) optical constants of $\text{GaP}_{0.67}\text{Sb}_{0.33}$ (a), $\text{GaP}_{0.40}\text{Sb}_{0.60}$ (b) and GaSb (c) extracted from the fitting of **Fig.4.8** (a), (b), (c), respectively.

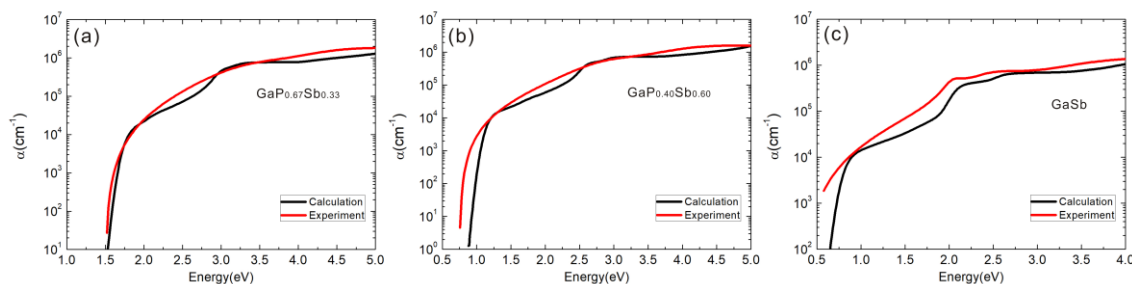


Figure 4.10 Optical absorption spectra of the GaP_{0.67}Sb_{0.33} (a), GaP_{0.40}Sb_{0.60} (b) and GaSb (c) semiconductors. The red lines were deduced from ellipsometry measurement and the black lines were obtained from TB calculations.

Additionally, ellipsometry measurement (with incidence angle 70°) was also performed on one GaP/Si sample for reference, and the corresponding optical constants extracted by using the Tauc-Lorentz model are shown in **Fig. 4.11**. The deduced absorption curves of GaP in GaP/Si and GaSb in GaSb/Si as measured by ellipsometry were compared with the experimental and theoretical data in the reference [202] (**Fig. 4.12**), and show good agreement.

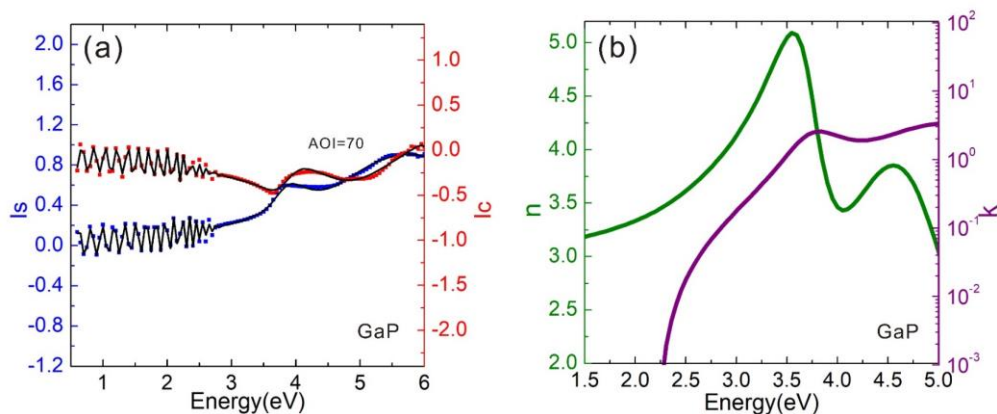


Figure 4.11 (a) Experimental ellipsometry spectra of I_s and I_c (red and blue lines) and comparison with fitting curves obtained with the Tauc-Lorentz model (black lines) for GaP. (b) n (optical index real part) and k (optical index imaginary part) optical constants of GaP extracted from the fitting of (a).

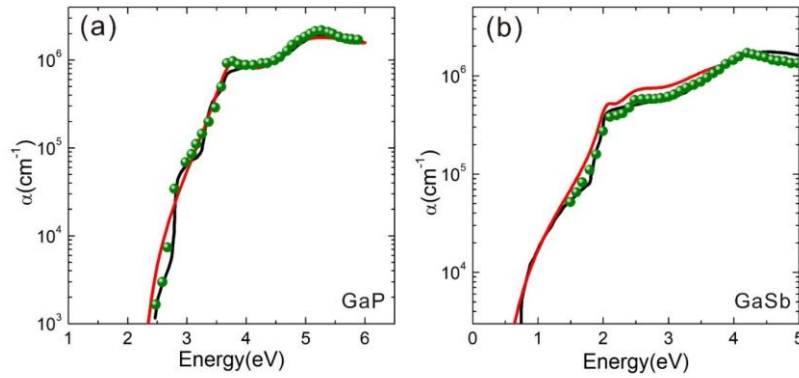


Figure 4.12 Optical absorption spectra of GaP (a) and GaSb (b). The red lines were deduced from ellipsometry measurements performed on our GaP/Si and GaSb/Si samples. The experimental data (green dots) and the theoretical ones (black lines) are obtained from the literature [202].

The absorption spectra were employed to plot the Tauc's curve ($(\alpha h\nu)^k$ vs $h\nu$) for the four GaPSb samples (**Fig. 4.13**) based on the Tauc's law:

$$(\alpha h\nu)^k = C(h\nu - E_g) \quad (4-1)$$

Where: $k=1/2$ for the GaP indirect bandgap and $k=2$ for the direct bandgap $\text{GaP}_{0.67}\text{Sb}_{0.33}$, $\text{GaP}_{0.40}\text{Sb}_{0.60}$ and GaSb (this assumption will be further confirmed by the tight binding calculations in the following part), α the absorption coefficient, h the Planck constant, ν the photon frequency and C a constant. An absorption coefficient range between 3000 and 10000 cm^{-1} was used for bandgap evaluation of the direct bandgap $\text{GaP}_{0.67}\text{Sb}_{0.33}$, $\text{GaP}_{0.40}\text{Sb}_{0.60}$ and GaSb samples. While for GaP, with its indirect bandgap, the absorption coefficient corresponding to the bandgap is smaller and the absorption coefficient range was chosen between 100 and 5000 cm^{-1} . The optical band gap can be obtained by linear extrapolation of the straight-line portion to $\alpha=0$. Finally, the bandgaps of the four samples were estimated: $E_g=2.25\pm 0.04$ eV for GaP; $E_g=1.70\pm 0.06$ eV for $\text{GaP}_{0.67}\text{Sb}_{0.33}$; $E_g=1.04\pm 0.08$ eV for $\text{GaP}_{0.40}\text{Sb}_{0.60}$, and $E_g=0.68\pm 0.09$ eV for GaSb (as shown in **Fig. 4.15**), which are consistent with bandgaps reported in pioneering works for the metamorphic growth of GaPSb on InP substrate [203]. In this study, we neglect the possible impact of alloy fluctuations and Sb ordering on the bandgap determination. Further experiments would be needed to assess quantitatively the influence of such effects.

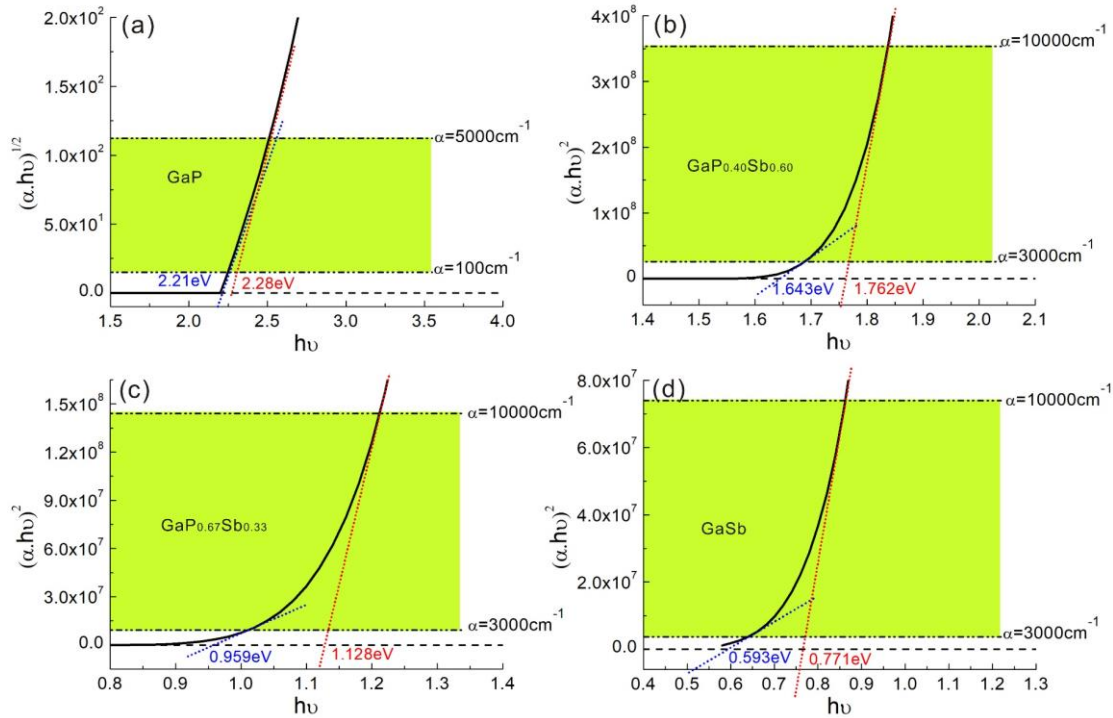


Figure 4.13 Tauc plot of $(\alpha h\nu)^k$ versus photon energy ($h\nu$) for GaP (a), GaP_{0.67}Sb_{0.33} (b), GaP_{0.40}Sb_{0.60} (c) and GaSb (d) epilayers grown on silicon.

4.4.2 Tight Binding calculations

The band structures of the unstrained GaP_{1-x}Sb_x alloys in the whole Sb compositional range have then been calculated by tight-binding calculations, using an extended basis sp³d⁵s* tight binding Hamiltonian [204]. This technique has been used for years to predict the bandgap evolution of III-V ternary alloys, as it provides a good accuracy for the bandgap calculations on simple alloys, while keeping a reasonable computing time. These calculations were made by S. Boyer from Institut FOTON. From the tight binding parameters of GaP and GaSb binary compounds [204], a virtual crystal approximation is performed to obtain the band structures of the different GaP_{1-x}Sb_x alloys at 0K as a function of the Sb content. Then the energies were shifted to take into account the influence of the temperature, in order to get room temperature band structures [171]. The calculated band structures of GaP, GaP_{0.67}Sb_{0.33}, GaP_{0.40}Sb_{0.60}, and GaSb semiconductors are given in the **Fig. 4.14**.

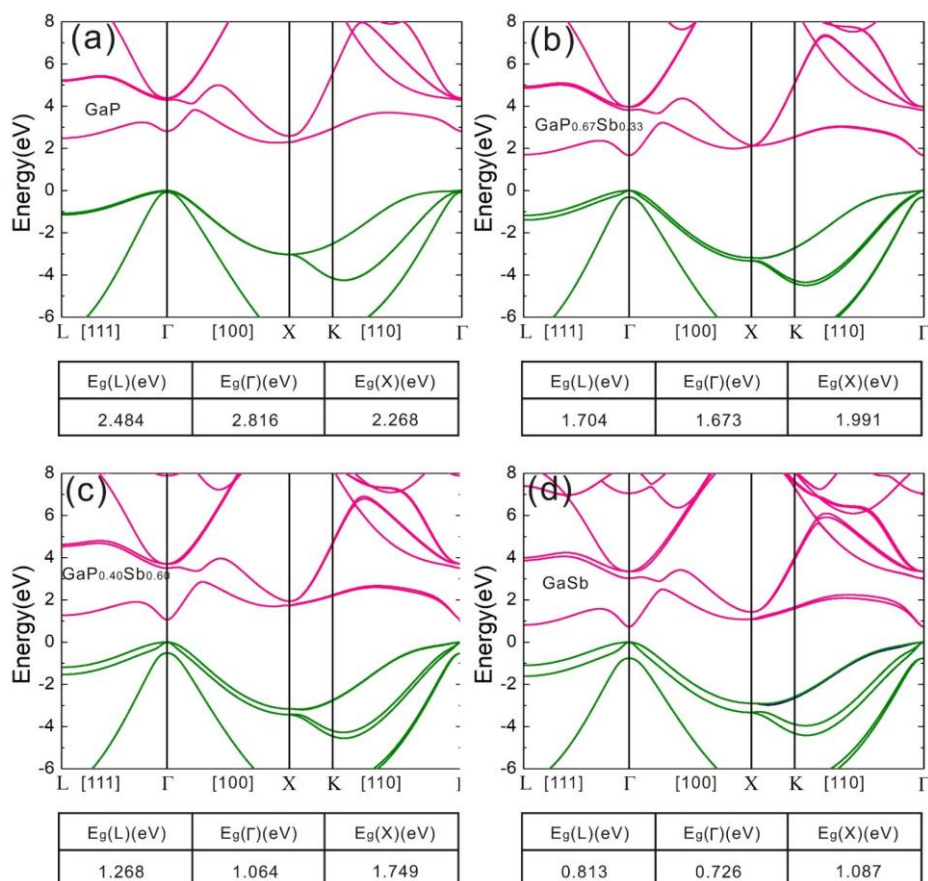


Figure 4.14 Room temperature band structures of the bulk unstrained GaP (a), GaP_{0.67}Sb_{0.33} (b), GaP_{0.40}Sb_{0.60} (c) and GaSb (d) obtained by TB calculations.

The bandgap evolutions obtained in the Γ , L and X valleys of the GaP_{1-x}Sb_x alloy for the whole Sb content range are presented in **Fig. 4.15**, from which we can find both the band gap value and the band gap type (direct or indirect). For the GaP, GaP_{0.67}Sb_{0.33}, GaP_{0.40}Sb_{0.60}, and GaSb semiconductors, TB calculations are in good agreement with the experimental absorption measurements. The theoretical absorption curves of GaP_{0.67}Sb_{0.33}, GaP_{0.40}Sb_{0.60} and GaSb semiconductors (corresponding to the three MBE grown samples) determined with TB calculations are shown as black lines in **Fig. 4.10**, which also shows good consistency with the ellipsometry experimental results (the red curves in **Fig. 4.10**). From this analysis, we deduce that the Sb content at which a 1.7 eV direct bandgap needed for tandem materials association can be reached, is obtained at 32%.

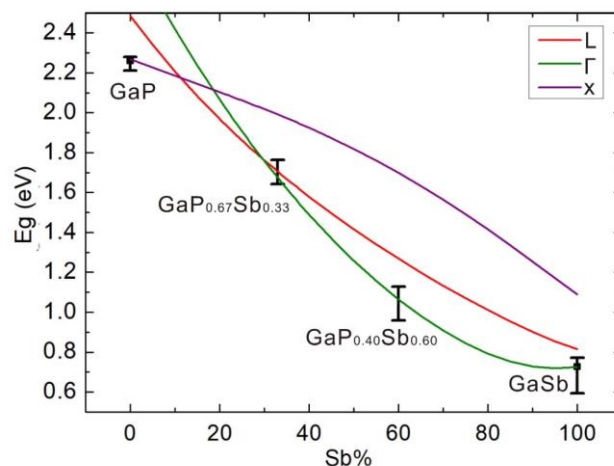


Figure 4.15 Room temperature bandgaps of $\text{GaP}_{1-x}\text{Sb}_x$ alloys with different Sb contents. The green, red and purple solid lines are theoretical curves computed by tight-binding calculations, corresponding to Γ , L and X valleys, respectively. The separated error bar lines correspond to the bandgaps determined experimentally. The black square dots correspond to the bandgaps of GaP and GaSb given in ref. [205,206].

4.5 Band alignment of GaPSb/Si with water redox levels

For efficient photoelectrochemical water splitting, another important aspect is to estimate the band edge location with respect to the redox potentials of water. The band alignment (no external electric field applied) of the $\text{GaP}_{1-x}\text{Sb}_x/\text{Si}$ tandem architecture for water splitting is presented in **Fig. 4.16** as a function of the Sb content. The VBM (valence band maximum) energy (E_v) of the $\text{GaP}_{1-x}\text{Sb}_x$ alloy over the whole Sb content range was obtained based on the absolute bandlineup between VBM energy of GaP and GaSb [207], which follows the linear formula $E_v(\text{GaP}_{1-x}\text{Sb}_x) = xE_v(\text{GaSb}) + (1-x)E_v(\text{GaP})$ [208]. In a first approximation, the evolution of the surface acidity with Sb content was neglected. The CBM (conduction band minimum) energy of the $\text{GaP}_{1-x}\text{Sb}_x$ alloy was obtained by using the results from TB calculations presented in **Fig. 4.15**.

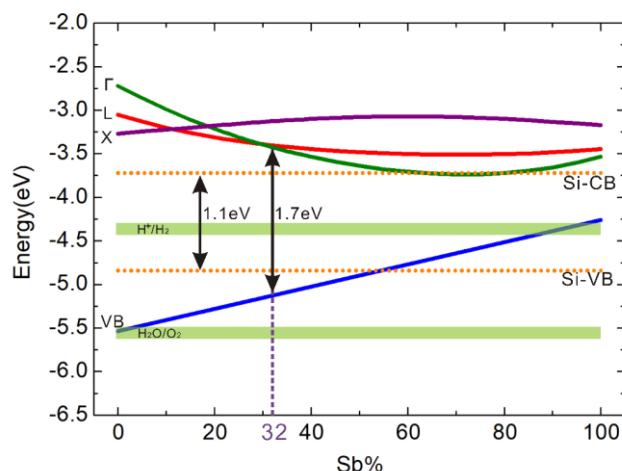


Figure 4.16 Band alignments of Γ , L and X valleys of $\text{GaP}_{1-x}\text{Sb}_x$ and indirect bandgap of Si with respect to water oxidation and reduction potentials. The relative position of redox potentials of water are shown as green bars at $\text{pH}=0$.

For this alloy, the minimum of the conduction band is located in the X-valley between 0% and 11%. It then moves to the L valley for Sb contents between 11% and 30%. It finally reaches a direct bandgap configuration (minimum of the CB in the Γ valley) beyond 30% of Sb incorporation. While the precise value predicted by the calculations for the L to Γ valley crossover seems hard to confirm experimentally in this work, calculations clearly demonstrate that in any cases, an indirect to direct cross-over is expected for this alloy at around 30% Sb. The VBM energy of bulk GaP is very close to the oxidation potential of water, which has been verified by many reports [207,209-211]. So, here we position the redox levels of water from the VBM position of GaP [207] and the energy differences between the water redox levels and GaP VBM reported in previous works [207,209-211], with error bars to analyze potential water splitting reactions more accurately and comprehensively (**Fig. 4.16**).

4.6 Discussion and assessment of GaPSb/Si for water splitting

From the **Fig.4.15** and **Fig.4.16**, it can be observed first that, in order to benefit from a direct GaPSb bandgap larger than the one of the silicon (to absorb higher energy solar radiations), the Sb content should lie between 30% (indirect to direct cross-over) and 54%

(bandgap equal to the Si one). In this Sb content range, it is also noticed that the band lineup is of type I, promoting the charge carrier extraction in the silicon under zero bias conditions. Now looking at the band lineups between GaPSb and the water redox potentials in the 30%-54% Sb content range, it is seen that GaPSb has a strong reduction ability due to its relatively higher CBM (around 0.9 eV higher than H^+/H_2 potential at 32% Sb content). On the other hand, the VBM is higher than the O_2/H_2O potential in the 30%-54% Sb content range, and due to the linear increase of VBM with the Sb content, the GaPSb with low Sb content (around 30%) is thus more suitable for oxygen evolution reactions (about 0.43 and 0.46 eV higher than O_2/H_2O potential at 30% and 32% Sb content). Overall, addition of Sb in GaP will therefore ease photocathode operation, although large current densities can be obtained with a GaPSb/Si photoanode (this will be shown in the following part and the explanation for this given in **Chapter 5**) due to a strong direct bandgap absorption. Of course, the picture given here is a simplified one, as many other parameters should be taken into account, and especially the physics & chemistry of the Helmholtz layer. However, the band lineups calculated in this work give a basis for further device analysis, where the precise determination of Nernstian shifts and band bending will be needed in future works.

4.7 Photo-Electro-Chemical characterizations

In order to further check the potential of GaPSb/Si tandem materials for solar water splitting applications, photoelectrochemical performances were investigated at UCL (London) for the $GaP_{0.67}Sb_{0.33}/Si$ sample which is very close to the optimal bandgap combination.

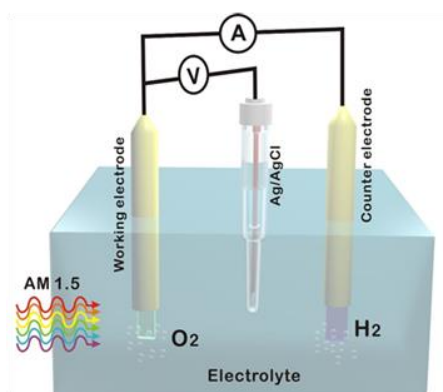


Figure 4.17 The experimental setup using a three-electrode system for the photoelectrochemical measurements.

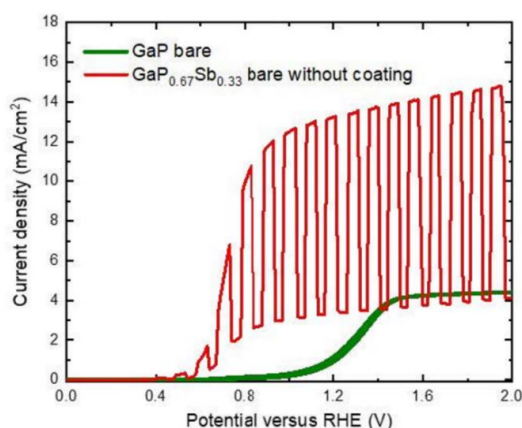


Figure 4.18 Voltammetry curve of GaP_{0.67}Sb_{0.33}/Si photoanode without coating (red line) and GaP wafer (green line) in 1.0 M KOH (pH=14) electrolyte under simulated AM1.5 illumination versus RHE.

The PEC properties of GaP_{0.67}Sb_{0.33}/Si photoanodes were investigated using a standard three-electrode configuration, consisting of a working electrode (GaP_{0.67}Sb_{0.33}/Si), a reference electrode (Ag/AgCl), and a counter electrode (platinum coil) in 1.0 M KOH electrolyte (pH=14) under one sun illumination, as shown in **Fig. 4.17**. The voltammetry curve for the GaP_{0.67}Sb_{0.33}/Si photoanode without a protection layer is shown in **Fig. 4.18**. Under AM 1.5G simulated one sun illumination, it shows an onset potential (where the visible increase of current density starts in the voltammetry curve) for the GaP_{0.67}Sb_{0.33}/Si photoanode of around 0.4 V versus RHE. The saturated photocurrent density is 13.26 mA/cm² at 1.23 V vs RHE. For comparison, PEC measurements of GaP reference photoanodes were also taken and the corresponding voltammetry curve is shown as the green curve in **Fig. 4.18**. We can find that, as compared to the GaP photoelectrode, the GaPSb/Si photoelectrode shows much higher photocurrent

which should, in a first approach, result from the better light absorption. Surprisingly, we note that a relatively high photo-current is observed, despite the absence of any intentional doping, and despite the numerous crystal defects that were evidenced previously (the full relaxation of the crystal implies a large density of dislocations generated during the metamorphic growth). This is very unusual, as conventional III-V photoelectrodes usually require n- or p-doping to ensure efficient transfer and transport of charge carriers to the electrolyte. We will demonstrate in **Chapter 5** that emerging APBs strongly impact the operation of these photoelectrodes. STEM measurements performed on the $\text{GaP}_{0.67}\text{Sb}_{0.33}/\text{Si}$ photoelectrode, provides evidence that APBs were not buried in this sample, and that they emerge at the sample surface (**Fig. 4.19a**). Besides, **Fig. 4.19b** shows the temperature-dependent PL of the $\text{GaP}_{0.67}\text{Sb}_{0.33}/\text{Si}$ sample. As shown in the previous part, the bandgap of this sample is around 1.7eV, while its maximum PL peak is around 1.35 eV. There is therefore a strong Stokes-shift, which is necessarily a consequence of deep carrier localization in the $\text{GaP}_{0.67}\text{Sb}_{0.33}$ layer. Three activation energies 8 meV, 30 meV and 130 meV are extracted. The first one is attributed to a small alloy disorder [33], while the two others represent the detrapping of localized carriers to extended states. Even if the detailed analysis of local PL signatures or phonon replica was not performed on this sample, these PL properties are very similar to the ones of In-rich APB structures discussed in details in **Chapter 3**, linked to the strong electron-phonon coupling, further confirming the presence of APBs in the $\text{GaP}_{0.67}\text{Sb}_{0.33}/\text{Si}$ photoelectrode.

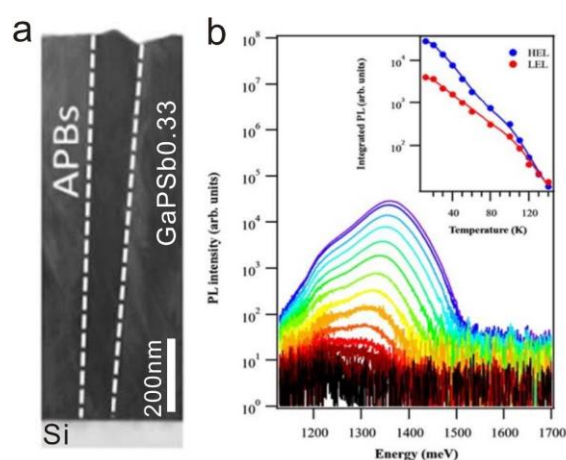


Figure 4.19 a. The cross-sectional high-resolution STEM images of the $\text{GaP}_{0.67}\text{Sb}_{0.33}/\text{Si}$ photoelectrode. b. Temperature-dependent photoluminescence spectra between 15 K (purple) and 150 K (dark red). The inset corresponds to the Arrhenius plot for the two transitions, being Low

Energy Line (LEL), and High Energy Line (HEL).

The large photo-current obtained with the III-V/Si photoelectrode and presented in **Fig. 4.18** should however be considered carefully. Indeed, the voltammetry curves presented also show a significant current under dark conditions, which confirms that corrosion occurs significantly during the photoelectrode operation. In addition, one can expect that photo-corrosion also occurs during the photoelectrode operation. This is also confirmed by the very short life-time of the developed bare GaPSb/Si photo-electrode. Indeed, under the considered pH=14 conditions, the bare photoelectrodes were able to work during less than 10 J(V) scans.

Thus, following the strategy developed in 2014 by Lewis and co-workers [212], a 20 nm-thick ALD-TiO₂ was deposited directly onto the surface of the GaP_{0.67}Sb_{0.33}/Si photoanode as a protection layer from (photo-) corrosion. Then, an 8 nm-thick metallic nickel (Ni) layer was deposited onto the surface of the TiO₂/GaP_{0.67}Sb_{0.33}/Si photoanode as a catalyst by a thermal evaporator, as shown schematically in **Fig. 4.20**.

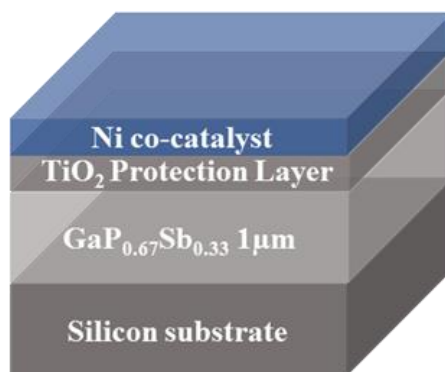


Figure 4.20 Structure of the coated GaP_{0.67}Sb_{0.33}/Si photoanode with protection layer (TiO₂) and catalyst (Ni).

Figure 4.21a presents the voltammetry curves for GaP_{0.67}Sb_{0.33}/Si coated with TiO₂ and Ni and GaP_{0.67}Sb_{0.33}/Si coated with Ni photoanodes in 1.0 M KOH (pH=14) electrolyte under one sun illumination. The GaP_{0.67}Sb_{0.33}/Si coated with Ni (8 nm) shows an onset potential of 0.37 V and a saturated current density of 3.84 mA/cm² at 1.23 V versus RHE. In contrast, the GaP_{0.67}Sb_{0.33}/Si coated with both TiO₂ (20 nm) and Ni (8 nm)

shows significant improvement with the increase of the photocurrent and a small anodic shift of the onset potential, as compared to that of the GaP_{0.67}Sb_{0.33}/Si coated with Ni (8 nm). The onset potential is shifted to 0.35 V and the current density is increased to 4.82 mA/cm² at 1.23 V versus RHE. In the absence of light, the dark current falls down to zero, contrary to what is observed for the GaP_{0.67}Sb_{0.33}/Si without coating and the GaP_{0.67}Sb_{0.33} coated with Ni (8 nm) photoanodes. This is attributed to the efficiency of the protection layer formed by the TiO₂ with the Ni catalyst. Obviously, it shows that the TiO₂ and Ni coatings improve the (photo-) stability of the photoanode. On the other hand, the voltammetry curves for the three photoelectrodes which are GaP_{0.67}Sb_{0.33}/Si without coating, GaP_{0.67}Sb_{0.33}/Si coated with Ni (8 nm), and GaP_{0.67}Sb_{0.33}/Si coated with TiO₂ (20 nm) and Ni (8 nm) after six voltage sweeping scans are shown in **Fig. 4.21b**. We can find that the GaP_{0.67}Sb_{0.33}/Si photoelectrode without coating exhibits a drastic reduction of the photocurrent due to the (photo-) corrosion. In contrast, the GaP_{0.67}Sb_{0.33}/Si coated with Ni and GaP_{0.67}Sb_{0.33}/Si coated with TiO₂ and Ni photoelectrodes do not lead to an apparent degradation of the current versus potential behavior under the same conditions which traduces again the good protection of the TiO₂ and Ni layers against corrosion [213,214].

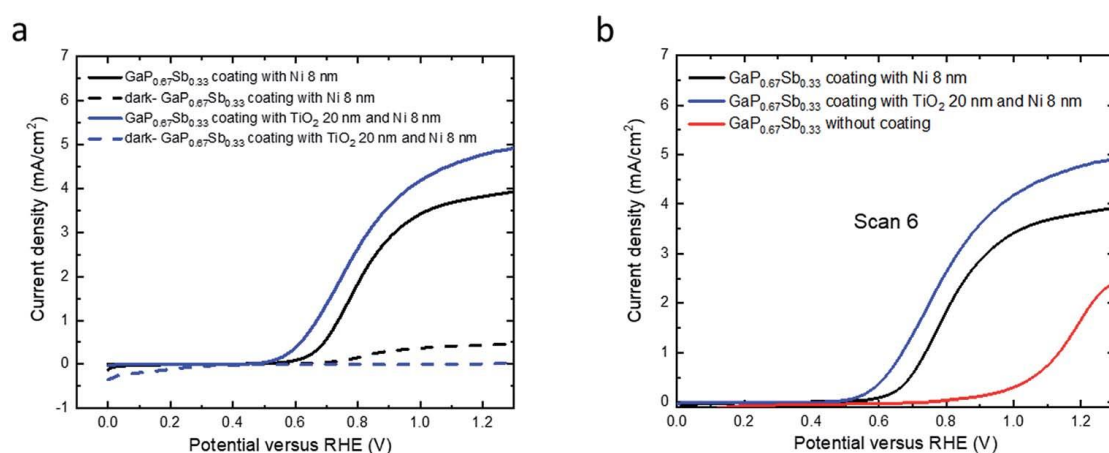


Figure 4.21 (a) Voltammetry curves of GaP_{0.67}Sb_{0.33}/Si coated with Ni 8nm and of GaP_{0.67}Sb_{0.33}/Si coated with TiO₂ 20 nm and Ni 8 nm photoanodes in 1.0 M KOH electrolyte under simulated AM1.5 illumination versus RHE. (b) Voltammetry curve (scan number 6) for the GaP_{0.67}Sb_{0.33}/Si coated with Ni 8nm and coated with TiO₂ 20 nm and Ni 8 nm photoanodes. The red voltammetry curve corresponds to the sixth scan of the GaP_{0.67}Sb_{0.33}/Si photoanode without coating.

The incident photon-to-current conversion efficiency (IPCE) as a function of the wavelength of the incident light for the GaP_{0.67}Sb_{0.33}/Si without coating, and reference GaP photoanodes were further investigated at an applied bias of 1.23 V versus RHE in a 1.0 M KOH electrolyte (pH=14). **Figure 4.22** shows the IPCE curves of GaP_{0.67}Sb_{0.33}/Si without coating and GaP photoanodes. The narrow bandgap of GaP_{0.67}Sb_{0.33} photoanode shows enhanced photo-response over the visible light range from 400 nm to 700 nm, which leads to higher photocurrent density. This observation shows the benefit of the incorporation of Sb. For the GaP_{0.67}Sb_{0.33}/Si photoanode without coating, the maximum of IPCE was 58.5% at 400 nm and decreases rapidly to 18.6% at 550 nm. The poor performance is attributed to the oxidation/corrosion of the electrode, which is in agreement with the significantly reduced photocurrent as shown in the sixth measurement of the voltammetry (**Fig. 4.21b**). In comparison, the maximum IPCE value for the GaP photoanode (see **Fig. 4.22**) was ~53.2% at 400 nm and decreases towards longer wavelengths (> 550 nm). This is due to the large and indirect bandgap of GaP [212].

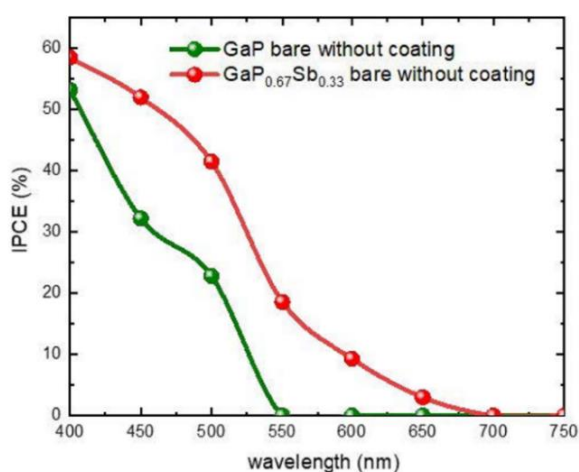


Figure 4.22 Incident photon-to-current conversion efficiency (IPCE) of the GaP wafer and GaP_{0.67}Sb_{0.33}/Si without coating in 1.0 M KOH electrolyte at 1.23 V versus RHE.

By depositing 8 nm of Ni as a catalyst, significant improvement was noticed as shown in **Fig. 4.23**. A maximum IPCE of 63% is achieved for the GaP_{0.67}Sb_{0.33}/Si electrode coated with 8 nm Ni at 400 nm and it gradually decreases to 53.4% at 550 nm. The IPCE of the GaP_{0.67}Sb_{0.33}/Si photoanode coated with Ni (8 nm) is equal or larger than

51.16% over the visible light region from 400 nm to 550 nm, due to the catalytic behavior of Ni for oxygen evolution reaction [215-217]. In contrast, the GaP_{0.67}Sb_{0.33}/Si photoanode coated with TiO₂ (20 nm) and Ni (8 nm) reaches a high IPCE of 76.4% at 400 nm and at least 67.1% between 400 nm and 650 nm, which indicates efficient and fast charge transfer to the semiconductor/electrolyte interface (**Fig. 4.23**). The IPCE falls and tends to zero around 750 nm in agreement with the energy bandgap (1.70±0.06eV) deduced previously from the measured GaP_{0.67}Sb_{0.33} absorption spectrum. From IPCE measurements, we note here that the Si substrate does not contribute to the PEC response. This is an important observation that will be widely discussed in **Chapter 5**, where we will show how one can promote photo-response of the III-V or of the Si material.

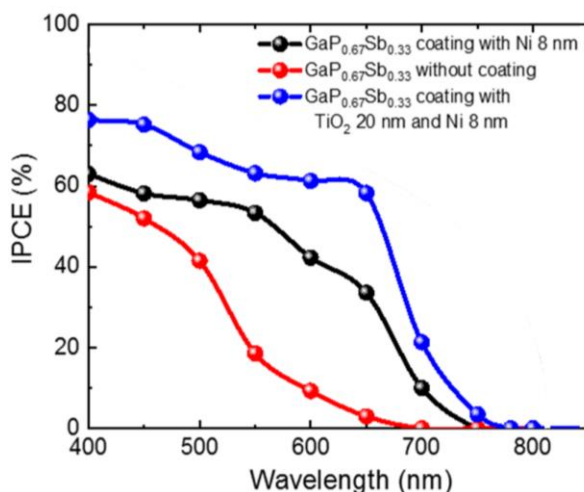


Figure 4.23 Incident photon-to-current conversion efficiency (IPCE) of the GaP_{0.67}Sb_{0.33}/Si without coating, GaP_{0.67}Sb_{0.33}/Si coating with Ni 8 nm, and GaP_{0.67}Sb_{0.33}/Si coating with TiO₂ 20 nm and Ni 8 nm in 1.0 M KOH electrolyte at 1.23 V versus RHE.

The stability of III-V semiconductors is a critical challenge in aqueous solution [212]. To assess the stability of the GaP_{0.67}Sb_{0.33}/Si photoanodes, the photocurrent density versus the time (J-t) characteristics of electrodes were investigated at a constant potential of 1 V versus RHE in a corrosive solution of 1.0 M KOH (pH=14) as shown in **Fig. 4.24** and **Fig. 4.25**. The photocurrent of the GaP_{0.67}Sb_{0.33} photoelectrode without coating decreases very rapidly, which is attributed to (photo-) corrosion. However, after the modification of the GaP_{0.67}Sb_{0.33} surface by the deposition of Ni (8 nm) as a catalyst, the current was maintained for around 1.30 h with a small decay in the current density and decreased

sharply after that. Clearly, depositing Ni onto the surface of $\text{GaP}_{0.67}\text{Sb}_{0.33}$ photoanode ($\text{GaP}_{0.67}\text{Sb}_{0.33}/\text{Si}$ coated with Ni 8 nm) reduced the (photo-) corrosion of the electrode. In contrast, using the corrosion resistant TiO_2 (20 nm) layer and Ni catalyst (8 nm) gave drastic improvement in the stability of the electrode ($\text{GaP}_{0.67}\text{Sb}_{0.33}/\text{Si}$ coated with TiO_2 (20 nm) and Ni (8 nm)) as shown in **Fig. 4.25**. The photocurrent of the $\text{GaP}_{0.67}\text{Sb}_{0.33}/\text{Si}$ photoelectrode coated with TiO_2 (20 nm) and Ni (8 nm) remained stable for 5h without degradation whereas the $\text{GaP}_{0.67}\text{Sb}_{0.33}/\text{Si}$ without the protective TiO_2 layer failed within 1.30 h. These results are attributed to the well-known corrosion resistance of TiO_2 in combination with the highly active Ni catalyst, which is consistent with previous reports [218].

While these PEC results are very promising (both in terms of performances and stability), numbers of experimental observations cannot be explained with a simple bandgap engineering and band lineups approach. As discussed above, the GaPSb layer was not intentionally doped, and thus neither good carriers transport properties nor high photocurrents would normally be expected with such sample. Therefore, a deep understanding of the III-V/Si photoelectrode operating principle will be needed. It will be proposed in **Chapter 5**, which will give new and general insights of the involved photo-electro-chemical mechanisms.

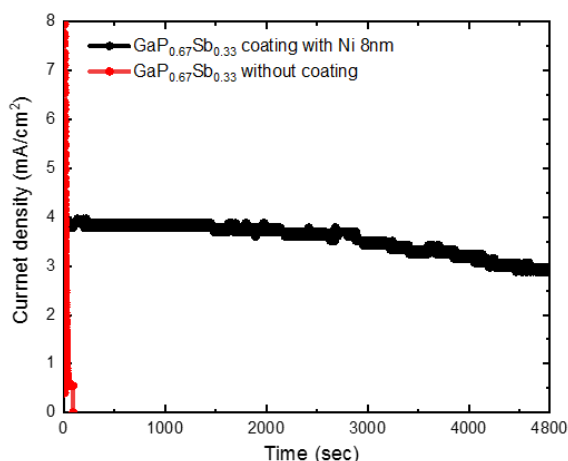


Figure 4.24 Photocurrent density versus time ($J-t$) for $\text{GaP}_{0.67}\text{Sb}_{0.33}/\text{Si}$ without coating and $\text{GaP}_{0.67}\text{Sb}_{0.33}/\text{Si}$ coated with Ni 8 nm photoanodes in a 1.0 KOH (pH=14) aqueous solution under one sun illumination.

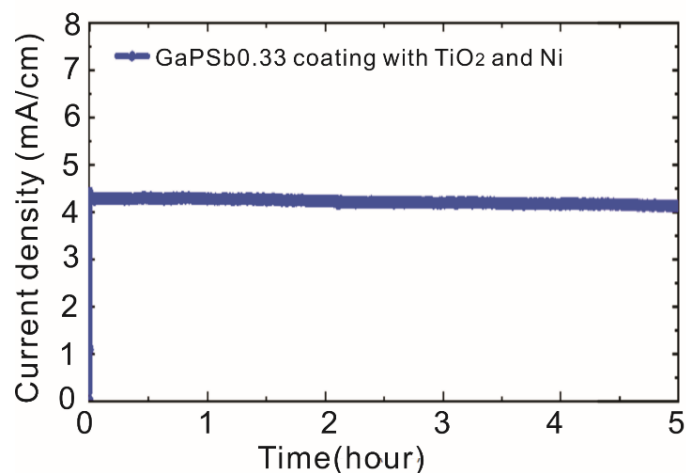


Figure 4.25 Photocurrent density versus time (J-t) for $\text{GaP}_{0.67}\text{Sb}_{0.33}/\text{Si}$ coated with TiO_2 20 nm and Ni 8 nm photoanode in a 1.0 KOH (pH=14) aqueous solution under one sun illumination.

4.8 Summary

In this chapter, we studied the novel $\text{GaP}_{1-x}\text{Sb}_x/\text{Si}$ tandem materials association for solar water splitting. The bandgaps and band structures of GaPSb alloys were determined over the whole Sb range, by combining experimental absorption measurements with tight binding theoretical calculations. The indirect (X-band) to direct (Γ -band) cross-over was found to occur at 30% Sb content. Especially, at a Sb content of 32%, the $\text{GaP}_{1-x}\text{Sb}_x$ alloy reached the desired 1.7 eV direct bandgap, enabling efficient sunlight absorption. Moreover, the band alignment of $\text{GaP}_{1-x}\text{Sb}_x$ alloys and Si with respect to water redox potential levels have been analyzed, which shows the 1.7eV/1.1eV GaPSb/Si association is an interesting combination both for the hydrogen evolution and oxygen evolution reactions. At last, a $\text{GaP}_{0.67}\text{Sb}_{0.33}/\text{Si}$ photoanode with a bandgap configuration very close to the optimal bandgap combination (1.7eV/1.1eV) was investigated for PEC characterizations and promising PEC performances were obtained due to the reduced direct bandgap of $\text{GaP}_{0.67}\text{Sb}_{0.33}$. Besides, it was proved that the stability of the $\text{GaP}_{0.67}\text{Sb}_{0.33}/\text{Si}$ photoanode can be much improved with TiO_2 and Ni coating layers. These results further demonstrate the promises of the $\text{GaP}_{1-x}\text{Sb}_x/\text{Si}$ tandem system for low-cost high-efficiency solar water splitting. But it also raises many opened questions. For instance, how can we get a high current in these PEC devices, despite the high density

of defects, and without the need of any intentional doping? Could it become possible to tune at will the properties of the photoelectrodes by using bandgap engineering of III-V semiconductors? Could the Si become photoactive in these photoelectrodes? **Chapter 5** will try to answer some of the numerous questions arising from results shown in this chapter.

Chapter 5: Epitaxial III-V/Si vertical heterostructures with hybrid 2D-semimetal/semiconductor ambipolar and photoactive properties

Building on the demonstrations of photoelectrodes presented in **Chapter 4**, we initiated in 2020 a collaboration with the research team of B. Fabre and G. Loget, from Institut des Sciences Chimiques de Rennes (ISCR). Before any optimization of the III-V/Si photoelectrodes, our research efforts focused on the understanding of the possible involved mechanisms to explain their performances. The presence of non-stoichiometric Antiphase Boundaries in III-V/Si samples was rapidly considered as the most credible explanation to interpret the unusual transport properties observed. This chapter gives a detailed analysis of the novel physical properties of non-stoichiometric APBs, describes how it can be used for the development of III-V/Si photoelectrodes, but also for other applications in photonics, electronics/computing or energy harvesting. Contrary to **Chapter 4**, I was actively involved in the photoelectrochemical (PEC) measurements in collaboration with ISCR. The Hall effect and C-AFM experiments were performed in collaboration with Institut de Physique de Rennes (IPR). The results presented here were just submitted for publication.

5.1 Introduction

Hybrid materials and devices have driven many researches recently, addressing the most advanced issues in today's energy harvesting [219], photonic [220], sensing [221] or computing [222] technologies. Among the various challenges raised, the simultaneous and ultimate control of carrier transport and optical properties in the same material remains usually tricky. On the one hand, the bandgap of semiconducting materials provides a path for electron-hole generation through light absorption, or electron-hole

recombination through light emission, especially with direct bandgap semiconductors, such as III-V, II-VI, CuInGaSe or perovskites [223]. The price to pay is the necessity to adjust carefully the internal electric field and the potential profile of stacked materials needed for carrier injection or extraction, thanks to the so-called p-type/n-type architecture or using electron and hole transporting layers. Only organic devices successfully manage to combine in the same material both photo-generation/light emission and carriers extraction or injection using bulk heterojunctions, but with limited yields, and lifetime issues [224]. On the other hand, the absence of a bandgap in metals, semimetals or Dirac materials make them highly interesting for transport, but can hardly be employed as photonic or energy harvesting materials [225].

Most of the classical semiconductor devices developed in the previous century were based on the combination of single usage unipolar layers, where the predominant conductive charges are holes for p-type and electrons for n-type, in dedicated architectures and applications. In the last past years, different researches pointed out the prospects offered by ambipolar devices, where simultaneous transport of electrons and holes can be achieved, thus promoting simultaneously n- and p-type characteristics. This led to recent ground-breaking demonstrations in the field of memory or logic devices [226,227], neuromorphic computing [228], sensing [229], light emitting devices [230,231], photovoltaics [232] or photo-electrochemical cells [233].

In this chapter, we demonstrate experimentally and theoretically that epitaxial III-V/Si materials with emerging non-stoichiometric APBs are hybrid structures, composed of bulk semiconductors, with 2D topological semi metallic inclusions, enabling simultaneously photo-activity, charge separation and ambipolar transport. A proof-of-concept is given through the demonstration of various operating III-V/Si ambipolar photoelectrodes. The unusual topological properties of the 2D semimetallic inclusions are also discussed. The unique physical properties of these heterostructures open new paradigms for energy harvesting, photonics, electronics or computing devices, combining high efficiency and predictable properties of inorganic materials and nano-scale charge carriers transport management flexibility usually offered by organic materials.

5.2 Sample growth

In this chapter, the III-V samples (GaP, GaPSb and GaAsP are considered in this study) were grown by Molecular Beam Epitaxy (MBE) on HF-chemically prepared n-doped ($5 \times 10^{14-18} \text{ cm}^{-3}$), p-doped ($2.6 \times 10^{15} - 1.4 \times 10^{16} \text{ cm}^{-3}$) or high resistivity ($>5000 \text{ } \Omega \cdot \text{cm}$) Si (001) substrates. As described in **Chapter 4**, the substrates were heated at 800°C for 10 minutes to remove hydrogen at the surface. $1 \mu\text{m}$ -thick III-V layers were then grown at 500°C in a conventional continuous MBE growth mode, and at a growth rate of 0.24 ML/s , with a Beam Equivalent Pressure V/III ratio of 5. The whole epilayer was undoped, and epitaxial strategies to annihilate antiphase boundaries [201] were not used here, leading to emerging APBs.

5.3 Structural analysis of III-V/Si materials with emerging APBs

As discussed in the previous chapters, the APBs are commonly formed during the epitaxy of Zinc-Blende III-V semiconductors on a group IV substrate in the diamond phase (e.g. silicon or germanium). It originates from the two different ways for the III-V crystal to fit the group IV substrate orientation [3]. As a consequence, two domains with different phases may grow on the same substrate (called bi-domain hereafter), separated by non-polar III-III or V-V bonds, inside the III-V matrix. The physical properties of the specific stoichiometric APBs (with equal numbers of III-III and V-V bonds within the same APB, as shown in **Fig. 3.1**) have been clarified in **Chapter 3**. It was demonstrated that the electronic band gap is reduced by 2D electronic localization, and that, a specific and strong electron-phonon coupling arises in stoichiometric APBs and impact the photoluminescence properties. Therefore, APBs should no longer be considered as non-radiative recombination centers, but as a 2D homovalent singularity in a bulk semiconducting matrix. Due to the insertion of a local translational symmetry breaking, III-III (V-V) bond also adds 2 free holes (2 free electrons) in the semiconductor. While different experimental works highlighted the strong influence of APBs on transport

properties [64,234], the physical properties of non-stoichiometric APBs were not yet explored. Indeed, as already mentioned previously, the APB composition may range from a pure vertical III-III APB to a pure V-V APB, resulting in these two extreme cases to a large excess of charges released in the lattice, as shown in **Fig. 5.1**, which describes the atomic structure of two non-stoichiometric APBs along [001].

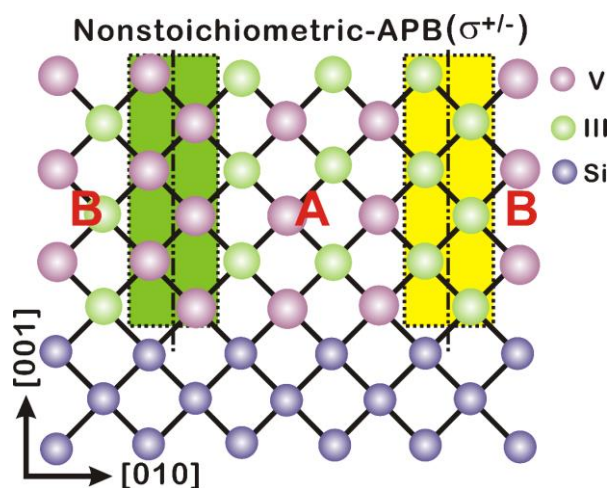


Figure 5.1 Schematic of non-stoichiometric APB atomic configuration. The APBs result from the coalescence of two domains marked by A and B (referred to as bi-domain) with different phases.

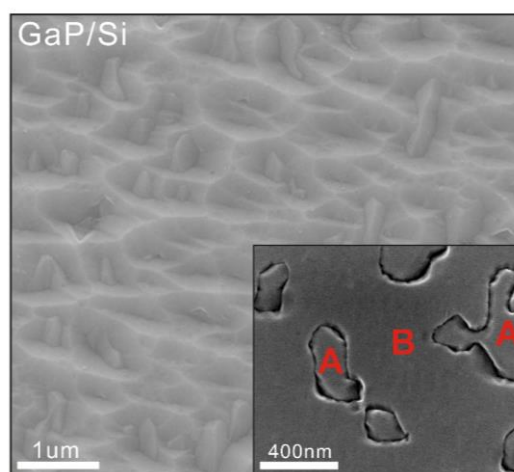


Figure 5.2 Top-view SEM images of one GaP/Si sample with emerging antiphase domains. The inset corresponds to the same sample after APB developing treatment on the surface.

Figure 5.2 shows the plan-view scanning electron microscopy (SEM) image of one as-grown GaP/Si sample. The surface appears rough, with visible inclusions of anti-phase materials in the main phase matrix. To further identify and study the local properties of the singularities, independently of the roughness and faceting induced by emerging APBs [186], an APB developing treatment (combining chemical mechanical polishing (CMP) and etching processes [65]) was used. A typical SEM image of the same sample after APB developing treatment is given in the inset of **Fig. 5.2**, showing the nice improvement of the surface smoothness in individual single-phase domains (below 3 nm root-mean-square roughness), and the clear identification of emerging APBs distribution. The same procedure was applied to the different samples. For illustration, the plan-view SEM images after APB developing treatment of one GaPSb/Si sample (Sb content around 30%) is presented in **Fig. 5.3**, where the APBs emerging at the surface are shown with a denser and random honeycomb-like lattice. For comparison, the top-view SEM image of an n-doped GaP substrate is shown in **Fig. 5.4**, from which a clean surface without APBs can be observed expectedly.

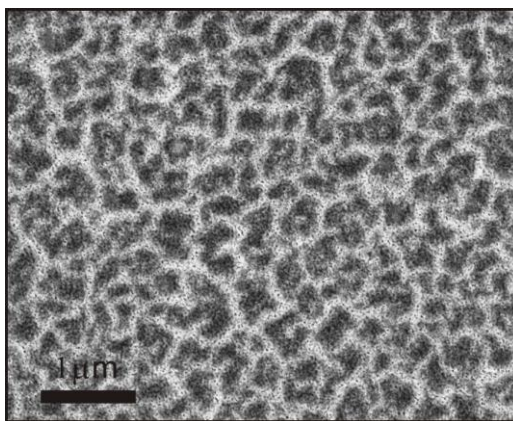


Figure 5.3 Plan-view SEM image of one GaPSb/Si sample with emerging antiphase domains after APB developing treatment on surface. The white lines correspond to APBs, due to the faster chemical etching of APBs.

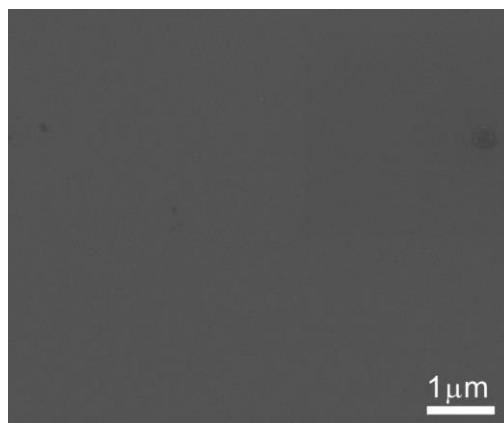


Figure 5.4 Plan-view SEM image of n-doped GaP wafer.

The spatial distribution of the singularities is of great importance, as it directly defines their nature. Indeed, considering a perfect vertical propagation of APBs along the [001] direction, APBs lying along the [110] or [-110] directions will be perfectly stoichiometric, while APBs lying along [100] or [010] directions will be perfectly non-stoichiometric (i.e. with only III-III or V-V bonds). In all the other cases, this will lead to intermediate charge states. A schematic diagram of in-plane charge distribution is given in **Fig. 5.5**, where stoichiometric APBs lying along [110] or [-110] correspond to the neutral configuration σ° in blue, and non-stoichiometric APBs lying along [100] or [010] correspond to the perfectly charged configuration $\sigma^{+/-}$ in red. The positive or negative nature of the charge cannot be determined here, but will be discussed in details later in this work.

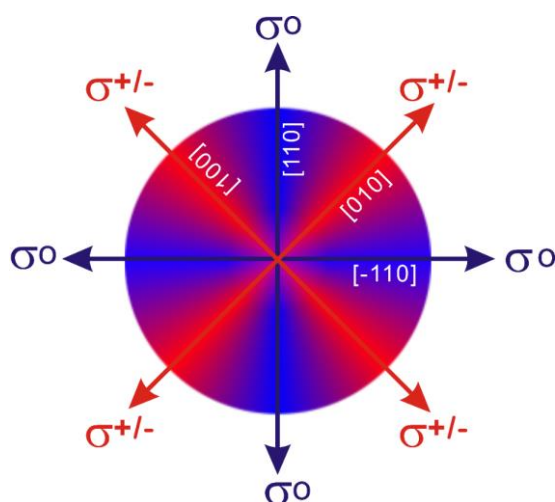


Figure 5.5 Schematic diagram of in-plane charge distribution. Red (blue) color corresponds to directions, along which vertical APBs are overall charged (neutral).

Figure 5.6 shows the AFM image of the bi-domain GaP/Si sample after APB developing treatment. While some APBs follow the $[110]$ or $[-110]$ directions (blue lines), and are thus expected to follow the σ° charge configuration, numerous other APBs are lying along other directions (red lines), and are thus expected to follow the $\sigma^{+/-}$ charge configuration or intermediate ones. This is in good agreement with the atomically-resolved observations performed in previous works [186] and is not fully surprising as the APBs naturally result from the coalescence of monodomain islands [3]. The simplified picture given here does not take into account the possible charge compensation effects which could occur during the growth [235], but nevertheless, it clearly evidences that the III-V/Si samples are not composed only of σ° -like APBs, but also of $\sigma^{+/-}$ -like ones. This excess of charges is expected to impact significantly transport properties, which are studied in the following.

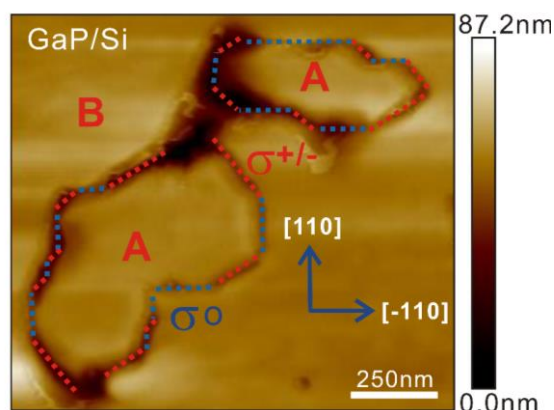


Figure 5.6 AFM image of the GaP/Si sample after the APB developing treatment on the surface revealing that APBs follow different local crystallographic directions.

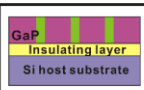
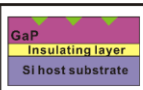
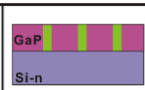
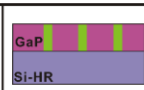
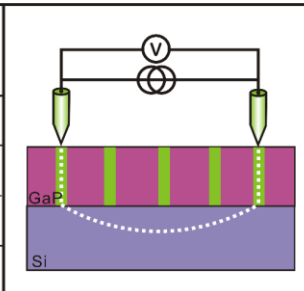
5.4 Transport characterizations of III-V/Si with emerging APBs

5.4.1 Hall measurements

To probe the electrical conductivity and charge carrier density, and identify the specific contribution of APBs to transport properties, 1 μm -thick GaP samples were grown on different Si substrates (6° -off or nominal ones, n-doped or with a high resistivity

(HR)) with either buried APDs [83] or emerging APBs (such as in **Fig. 5.2**). Importantly, all these III-V layers were not intentionally doped. For some measurements, the silicon substrate was etched, and standalone GaP membranes were bonded onto a thermally oxidized silicon host wafer with an insulating adhesive polymer (benzocyclobutene) layer, to better separate the transport properties of the III-V layer from the Si substrates. Hall effect measurements were carried out on these samples and the results are summarized in **Table 5.1**. For the GaP membranes with emerging or buried APBs on insulating layer, transport physical parameters could not be determined, because of their very large electrical resistance exceeding experimental capabilities. Note that a high resistance was also previously measured for a GaP layer with buried APBs on a n-doped Si substrate [64]. This result would be typically expected for the large bandgap non-intentionally doped GaP bulk material. However, charge carriers are easily injected into GaP layers with emerging APBs on Si substrates as demonstrated by Hall effect measurements.

Table 5.1: Schematic illustration of Hall effect measurements and the relevant results (resistivity, doping concentration and mobility) of four different samples: bi-domain GaP membrane on insulating layer with emerging APBs; mono-domain GaP membrane on insulating layer with buried APBs; bi-domain GaP layer with emerging APBs on a n-doped Si substrate; bi-domain GaP layer with emerging APBs on a highly resistive Si substrate. The green color represents the APBs in the schematic diagrams of the different samples. The results demonstrate that the current flows vertically through the III-V APBs and laterally through the silicon.

					
Type			N	N	
Sheet resistance [Ω/\square]			170	78×10^3	
Charge carrier sheet density [cm^{-2}]	Resistance $> 10\text{G}\Omega$	Resistance $> 10\text{G}\Omega$	3.5×10^{13}	8×10^{10}	
Mobility [$\text{cm}^2/\text{V}\cdot\text{s}$]			1450	950	

For both GaP/Si-n and GaP/Si-HR samples with emerging APBs, values of the measured mobility are about one order of magnitude higher than those reported in the literature for GaP/Si [236] or even for bulk GaP [237,238]. More precisely, we observed that the measured mobility is very close to that expected for Si. This result indicates that

most of the in-plane current flows within the underlying Si substrate. For the Si substrate, the measured sheet resistance of $170 \text{ } \Omega/\text{sq}$ gives a resistivity of $5.95 \text{ } \Omega\cdot\text{cm}$ and the carrier sheet density of $3.5 \times 10^{13} \text{ cm}^{-2}$ leads to a bulk carrier density of $1 \times 10^{15} \text{ cm}^{-3}$. These values of resistivity and mobility are exactly those expected for Si with a doping concentration giving an electron density equal to the measured one [239]. All these results combined together unambiguously demonstrate that carriers transport in bi-domain III-V semiconductors occurs mostly vertically, and that the current path is related to APBs. This current path is due to a great contrast between the in-plane APB resistivity and the out-of-plane APB resistivity. From our measurements, we estimate that the former is at least 10^3 times larger than the latter.

5.4.2 Conductive atomic force microscopy (C-AFM) measurements

To get more local information about transport, the nano-electronic properties of the epitaxial bi-domain GaP/Si:n sample was evaluated by conductive atomic force microscope (C-AFM). The surface current mapping images under negative and positive bias are shown in **Fig. 5.7b** and **Fig. 5.7c**, respectively. For both biases, a clear maximum intensity is observed where the APBs emerge, further confirming the prominent role of APBs in the charge carrier transport (this is also confirmed by C-AFM measurements performed on another bi-domain GaPSb/Si:n sample (**Fig. 5.8**)). Basically, the observation of a current at the APB level under both positive and negative biases highlights the bidirectional conduction ability of the singularities. We note that the maximum intensity measured for both biases cannot be quantitatively compared here due to the influence of the substrate doping.

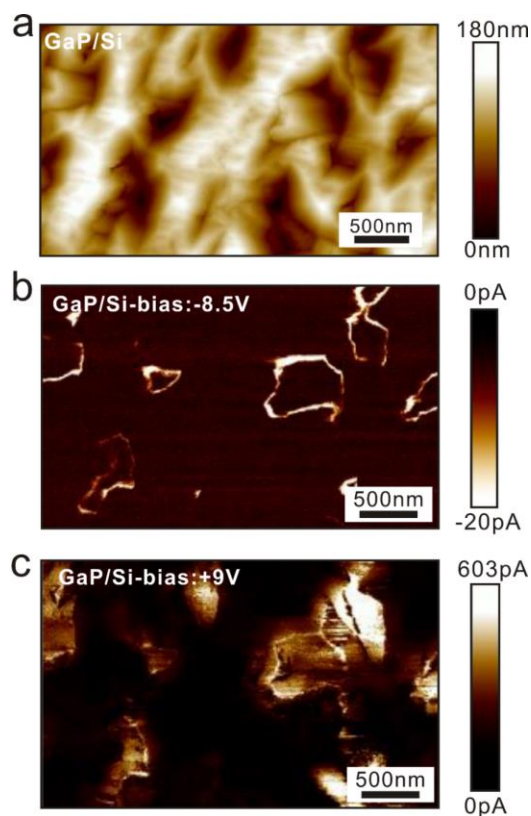


Figure 5.7 Topography (a) and current distribution C-AFM images of the bi-domain GaP/Si sample under negative voltage (-8.5V) (b) and positive voltage (+9.0V) (c).

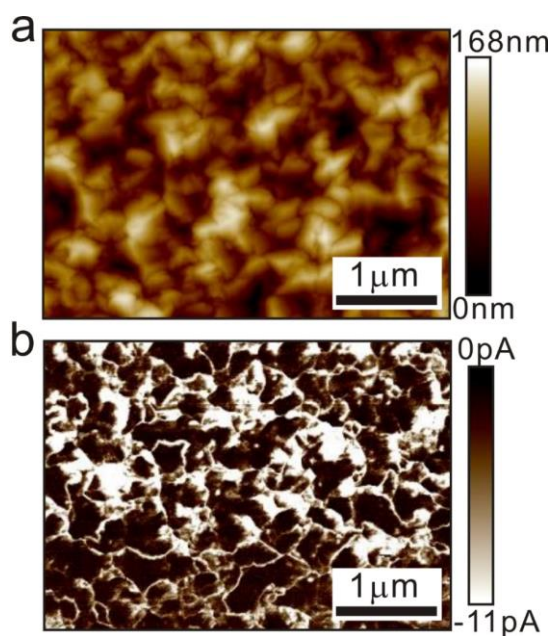


Figure 5.8 Topography (a) and current distribution (b) C-AFM images (DC bias = -7.5V) of the bi-domain GaPSb/Si sample.

5.5 PEC characterizations of III-V/Si with emerging APBs

The III-V/Si samples with emerging APBs are thus composed of vertical singularities that can ensure the anisotropic transport of both electrons and holes, but are also composed in between the singularities of monodomain bulk semiconductor grains, whose photo-activity should remain preserved (for absorption or emission). The demonstration of an efficient photoelectric device with emerging APBs is therefore conditioned to the ability to transfer the carriers between the bulk semiconducting grains and the APB singularities and vice versa. In the following, we study the possible use of the III-V/Si materials with emerging APBs to develop efficient photoelectrodes for photoelectrolysis (i.e. solar water splitting), taking advantage of the attractive properties of this material. Indeed, as introduced in **Chapter 1**, solar water splitting allows converting solar energy to hydrogen through a photoelectrochemical (PEC) cell, in which occurs the cathodic hydrogen evolution reaction (HER) and the anodic oxygen evolution reaction (OER), and provides a promising path for scalable and sustainable carbon-free energy production and storage [31]. HER and OER reactions occur through the transfer of photogenerated minority carriers at the solid-liquid phase, thus, for traditional semiconductors, photoanodes (photocathodes) are usually associated to n-type (p-type) materials.

PEC characterizations were carried out at ISCR in a three-electrode cell in 1M H₂SO₄ electrolyte (measured pH=0.3) under simulated (AM 1.5G, 100 mWcm⁻²) sunlight illumination for various bare and non-intentionally doped III-V/Si materials with emerging APBs. The linear sweep voltammetry (LSV), incident photon-to-current efficiency (IPCE) spectra, electrochemical impedance spectroscopy (EIS) and Mott-Schottky (MS) results are presented below.

5.5.1 Linear sweep voltammetry (LSV)

The chopped-light linear sweep voltammetry (LSV) curve of the bidomain GaP/Si:n

sample is displayed in **Fig. 5.9a**. Interestingly, it shows both anodic and cathodic photocurrents. This unusual ambipolar behavior is of great interest for the development of fully integrated PEC cells, as it may allow the use of a single material to be used for both photoelectrodes. The measured anodic photocurrent is higher than the cathodic one, in good agreement with the C-AFM results presented above. For comparison, the same curve is given for a single GaP:n wafer (**Fig. 5.9b**), which shows, as expected, only a photoanodic behavior.

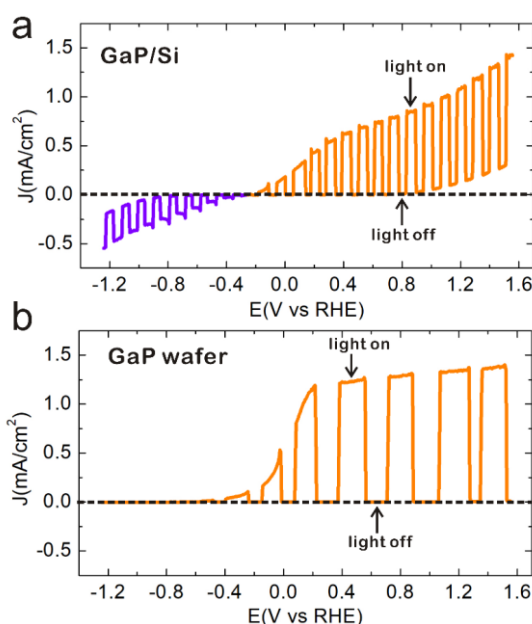


Figure 5.9 Chopped-light linear sweep voltammetry curves (scan rate = 50 mV/s) of the GaP/Si (a) and GaP wafer (b).

The voltammetry curves of bi-domain GaPSb/Si:n and GaPAs/Si:n samples with emerging APBs are also given in **Fig.5.10a** and **Fig.5.10b** and reveal similar behaviors, demonstrating that ambipolar transport is not only a specific property of GaP/Si, but a general trend for all III-V/Si systems. Besides, it is found that the onset potential values for cathodic photocurrent and anodic photocurrent of GaP/Si:n sample are very close and around -0.3 V vs Reversible Hydrogen Electrode (RHE) (**Figure 5.9a**). This suggests an unusual distribution of carriers in bulk GaP where both electrons and holes are available almost simultaneously for the oxidation and the reduction reactions. Since our surfaces are not coated with a protective layer, the photocurrents are not only representative of HER and OER but are rather the result of a kinetic competition between photocorrosion

and the latter reactions [240-242]. Despite the corrosion process, the reached maximum photocurrent is relatively high, and not far from that measured with bare III-V substrates, indicating that the photogeneration and transport are overall efficient in these devices. For stable water photoelectrolysis, the corrosion issue is expected to be tackled effectively in a short-term perspective by using catalytic and/or protection layers, as widely demonstrated on numerous unstable semiconductors [33,212,243].

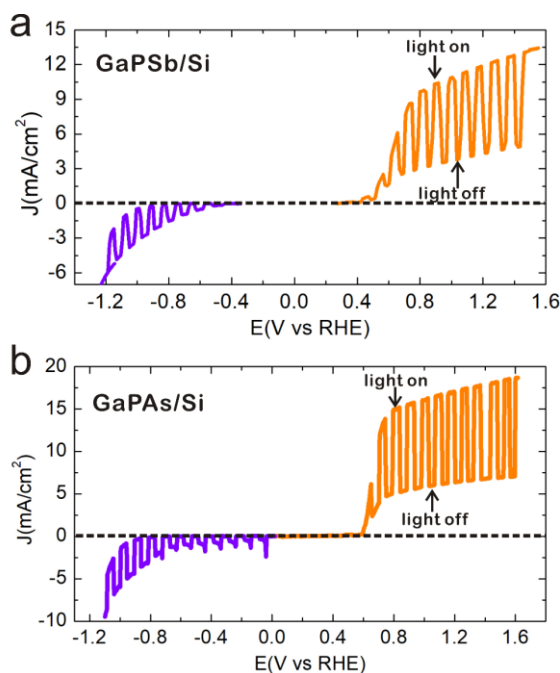


Figure 5.10 Chopped-light linear sweep voltammetry curves (scan rate = 50 mV/s) of GaPSb/Si (a) and GaPAs/Si (b) samples with emerging APBs.

The large and indirect bandgap of GaP leads to relatively low light absorption and consequently to small photocurrent (as shown in **Fig. 5.9a** and **Fig. 5.9b**). Nevertheless, with the addition of Sb or As, the bandgap and band type of GaP-based ternary alloys can be adjusted, which allows improvement of solar spectrum absorption and enable better PEC performances, as testified by the relatively high photocurrent for GaPSb/Si (around 30% Sb content & 1.7 eV bandgap) and GaPAs/Si (around 90% As content & 1.5 eV bandgap) samples. One bi-domain GaPSb sample on p-doped Si also shows photo-induced ambipolar characteristic (**Fig. 5.11**), indicating that the intrinsic ambipolar behavior does not depend on the Si substrate doping, but the Si substrate doping could be used to adjust the proportion between anodic and cathodic photocurrent, this will be

discussed at the end of this chapter.

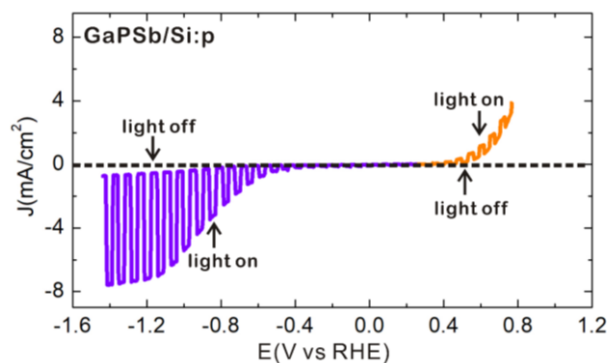


Figure 5.11 Voltammetry curve of GaPSb/Si:p sample with emerging APBs in 1.0M H₂SO₄ (pH=0.3) electrolyte under chopped simulated sunlight.

5.5.2 Incident photon-to-current efficiency (IPCE) spectra

Figure 5.12 shows the incident photon-to-current efficiency (IPCE) spectra of the GaP/Si:n sample and GaP:n wafer, recorded at 1.26 V (anodic region) and -0.74 V (cathodic region) versus RHE. Firstly, the integrated photocurrents derived from the IPCE curve ($0.2 \text{ mA}\cdot\text{cm}^{-2}$ for GaP/Si at -0.74 V; $1.0 \text{ mA}\cdot\text{cm}^{-2}$ for GaP/Si at 1.26 V; $0 \text{ mA}\cdot\text{cm}^{-2}$ for the GaP wafer at -0.74 V; $1.68 \text{ mA}\cdot\text{cm}^{-2}$ for the GaP wafer at 1.26 V) show good consistencies with those extracted from the voltammetry curves (**Fig. 5.9**), which validate the accuracy of the measurements. Secondly, the GaP/Si sample shows IPCE signal on both anodic and cathodic regions, which further confirms the ambipolar characteristic of the GaP/Si sample. Thirdly, the IPCE of GaP/Si mainly increases around 550nm, similarly to the GaP wafer, which corresponds well to the bandgap of the GaP semiconductor, indicating the carriers are mainly created by the absorption within the GaP matrix. This is an important point as it already confirms that carriers are photogenerated in bulk-like domains, and then transferred to APBs which ensure the transport, and that the absorption of the underlying Si substrate is not interfering in the PEC response.

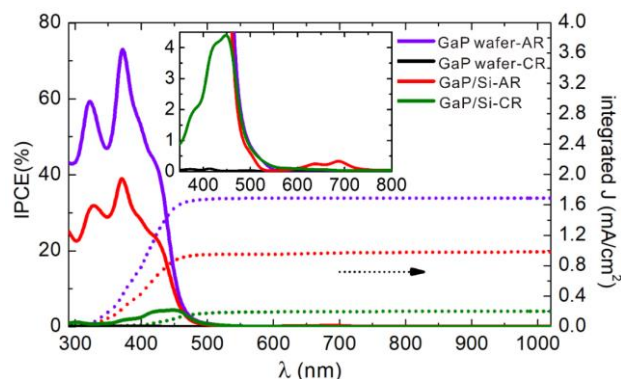


Figure 5.12 IPCE spectra recorded at -0.74 V vs RHE (cathodic region (CR)-green and black lines) and 1.26 V vs RHE (anodic region (AR)-red and purple lines) for the GaP/Si (red and green lines) and GaP wafer (purple and black lines). The dotted lines correspond to integrated photocurrent and the inset are the enlarged IPCE spectra around 350-800nm.

5.5.3 Electrochemical impedance spectroscopy (EIS)

Additionally, electrochemical impedance spectroscopy (EIS) measurements were performed for the n-doped GaP wafer and the GaP/Si sample. Nyquist plots (imaginary part $-Z_{im}$ vs. real part Z_{re} of the total impedance) of the GaP/Si sample measured in the dark and under illumination in the frequency range of 100kHz-1Hz at different potentials (open circuit potential (OCP), anodic region, and cathodic region) are shown in **Fig. 5.13**. It suggests that the charge-transfer resistance (R_{ct}) (correlated with the diameters of the semi-circles measured) [244] strongly decreased under illumination and that the relatively small semi-circles were obtained in both anodic and cathodic regimes, echoing with the ambipolar behavior.

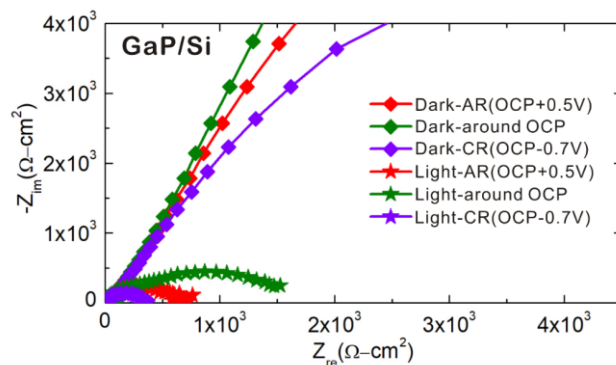


Figure 5.13 Nyquist plots (between 100 kHz and 1 Hz) of the GaP/Si sample in the dark and under illumination at different applied potentials (OCP point, anodic region (AR), cathodic region (CR)).

5.5.4 Mott-Schottky (MS) plots

Figure 5.14a shows the Mott-Schottky (MS) plots recorded at 500 Hz for the GaP wafer, which demonstrates the typical positive slope of the reciprocal of the square of the capacitance versus the applied potential expected for an n-doped semiconductor. From the slope, the donor density is evaluated to $2 \times 10^{17} \text{ cm}^{-3}$, in good agreement with the GaP wafer specifications. The MS plot for the GaP/Si sample recorded at 1 kHz is displayed in **Fig. 5.14b**, and reveals both the positive and negative slopes, echoing with the previously discussed ambipolar behavior and suggesting attractive simultaneous n- and p-type-like electronic nature of III-V/Si materials [245-247].

From all these PEC characterizations, we can therefore draw the following picture: the III-V/Si materials with emerging APBs allow (i) photogeneration of carriers in bulk monodomain semiconducting grains, (ii) carrier separation and extraction from the bulk phase to the APB singularities, (iii) ambipolar vertical transport and (iv) efficient charge transfer at the solid/liquid interface.

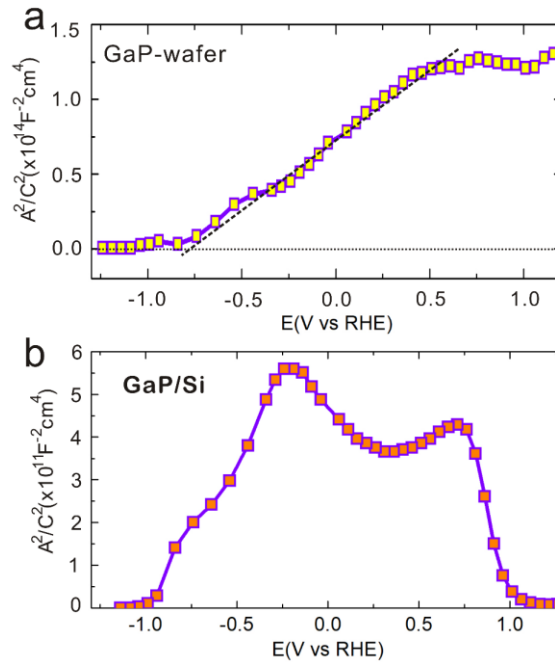


Figure 5.14 Mott-Schottky plot for the GaP-wafer (a) and bi-domain GaP/Si sample (b) in the dark.

5.6 DFT calculations for non-stoichiometric APB structures

In order to better understand the original electronic and PEC properties of the APB singularities buried into III-V semiconductors, theoretical calculations are performed for III-V-based non-stoichiometric APB structures.

5.6.1 Construction of non-stoichiometric APB supercells

As discussed in the **Chapter 3**, the stoichiometric APB structure belong to Pnm space group. The symmetry is different for non-stoichiometric APB structures, which belong to Pmma space group. Both structures present an inversion symmetry (which is absent in the bulk III-V zinc-blende lattice), but the atomic motifs are different. First-principle calculations were performed for non-stoichiometric Pmma APB structures with GaP, GaAs and GaSb semiconductors. In order to investigate separately the III-III and V-V APB singularities, slab structures are constructed by adding vacuum on both sides and the surfaces were passivated with fictitious hydrogen atoms to avoid localized surface states, as shown in **Fig.5.15b,c** (called hereafter III-III and V-V APB structures). For comparison, the corresponding calculations were also done for the reference III-V slab structures without APB mimicking the bulk material (called hereafter zinc-blende slab structures) (**Fig. 5.15a**). Besides, relatively long APB structures (**Fig.5.16**) were also considered, in order to determine the charge distribution and Fermi levels more clearly and accurately. Around 20 Å and 30 Å vacuum were added on the short and long structures, respectively, which are thick enough to avoid any interaction between slab surfaces.

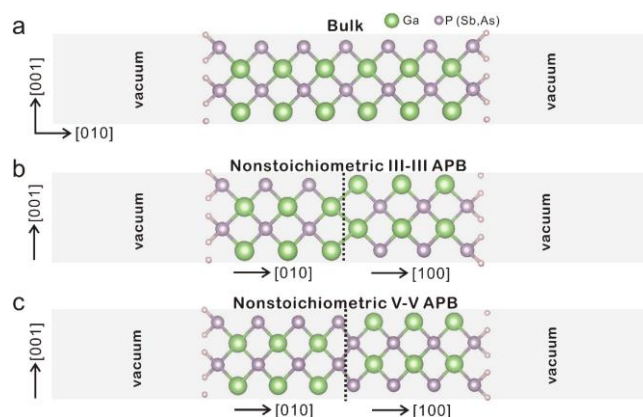


Figure 5.15 Zinc-blende (a), III-III APB (b) and V-V APB (c) slab structures with Pmma space group for theoretical calculations.

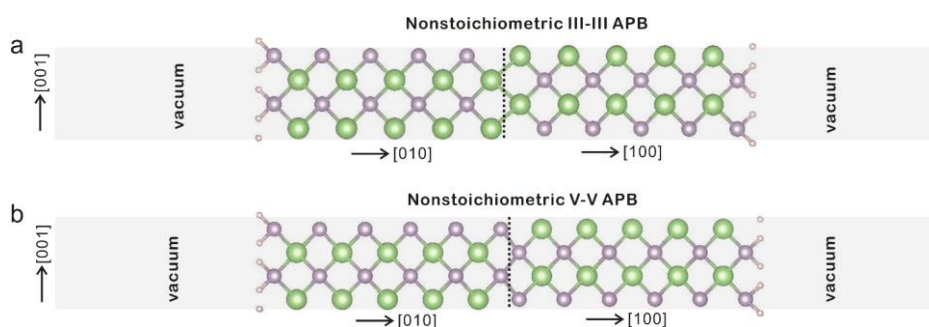


Figure 5.16 Longer III-III (a) and V-V (b) APB slab structures.

5.6.2 Band structure and charge density distribution of non-stoichiometric APBs

Electronic band structure calculations were performed using Density Functional Theory (DFT) along $X(0.5,0,0)-\Gamma(0,0,0)-X(-0.5,0,0)$ k-path, where the axes x, y, z of the reciprocal space correspond to the $[101], [10-1], [010]$ crystallographic directions, based on Heyd–Scuseria–Ernzerhof (HSE) hybrid functional. The band structure plots of the III-III and V-V APB structures for GaP, GaAs and GaSb are shown in **Fig. 5.18b,c,e,f,h,i** where the color scale indicates the spatial localization of the electronic state in the APB plane. Note that the common k-paths chosen in all the cases for the sake of comparison

correspond to APB in-plane directions (**Fig. 5.15b,c**) to illustrate the effects of the 2D electronic dispersion. **Figure 5.18a,d,g** show the band structure of the respective reference III-V zinc-blende slab structures for GaP (**Fig. 5.18a**), GaAs (**Fig. 5.18d**) and GaSb (**Fig. 5.18g**), respectively. Compared to the normal bulk structures (unit cell with 2 atoms) with a zinc-blende lattice (**Fig. 5.17**), the slab structures used to mimic bulk properties, exhibit slightly larger bandgaps due to quantum effect, and exhibit more bands resulting from band folding effect. The Fermi energy levels are determined by DFT calculations using dense k point meshes and a metaGGA (TB-mBJ) functional [128], which possesses similar accuracy than computationally more expensive functionals, such as HSE, or even many-body calculations at the GW level [130] (see the next section). Compared to the reference III-V slab structures, all the III-III and V-V APB structures introduce localized metallic states on the APB atoms in the gap, which indicates that they are a direct consequence of the specific 2D topology of the APB.

Additionally, **Fig. 5.19a,b** show the planar averages of the charge densities integrated parallel to the APB plane. The charge density increases on III-III APB and drops on V-V APB, revealing that more electrons (holes) are localized on the III-III (V-V) APB planes, and suggesting that the non-stoichiometric APB singularities behave as charged domain walls.

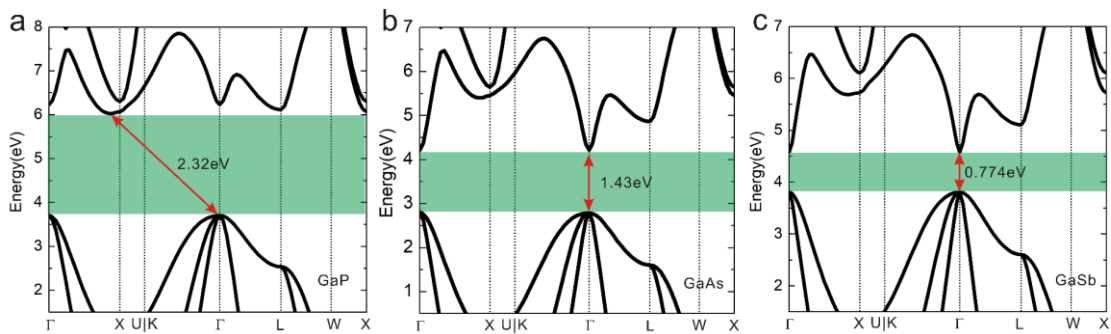


Figure 5.17 DFT band structures based on HSE potential for zinc-blende unit cell of GaP (a), GaAs (b) and GaSb (c).

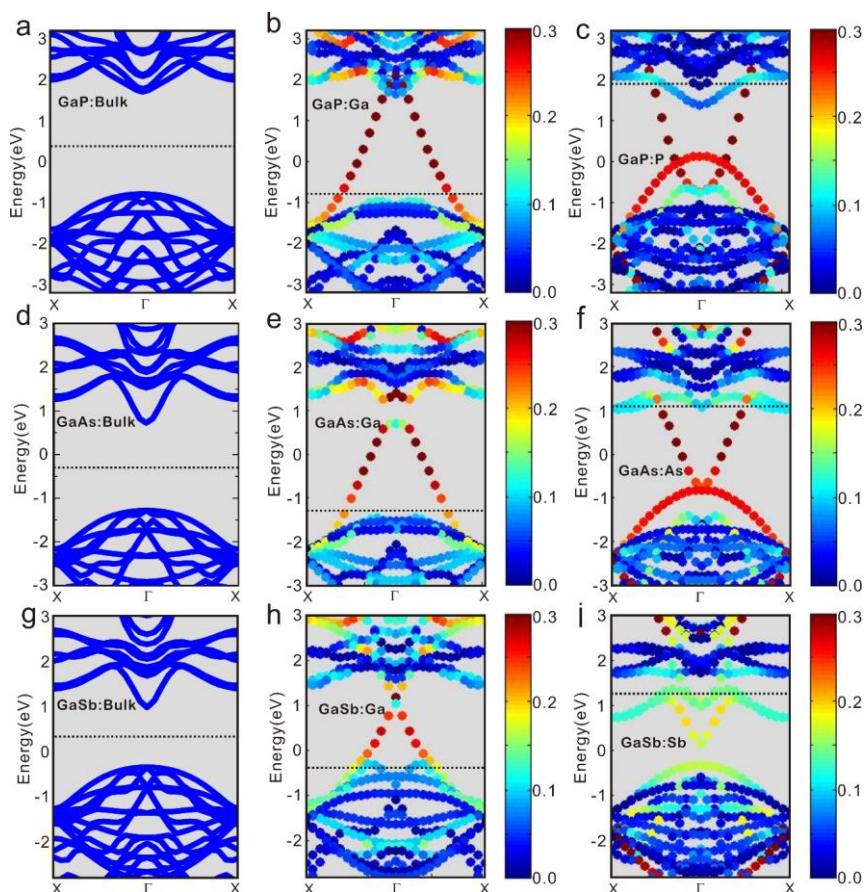


Figure 5.18 Calculated electronic band structures of zinc-blende, III-III APB and V-V APB structures for GaP (a-c), GaAs (d-f) and GaSb (g-i). The APB band structures (b,c,e,f,h,i) are weighted by the spatial localization of the states at the APB interface and the color map from blue to red underlines the increase of localization effect of the states at the APB.

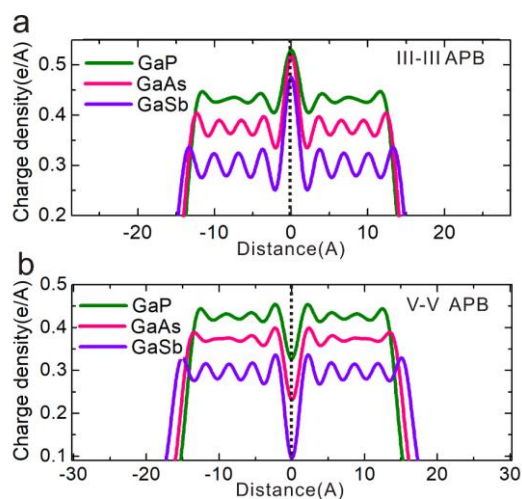


Figure 5.19 Charge density of III-III APB (a) and V-V APB (b) structures, integrated in the planes parallel to APBs.

5.6.3 3D band structure and density of states

To further explore the intrinsic semimetal nature of these APB structures, first-principle tight-binding models were constructed by projecting the electronic states on to Wannier orbitals [248]. This analysis was performed on top of state of the art DFT calculations at the HSE level to have a precise insight into the topological properties of APBs [145]. The band structures along the X- Γ -X k-path of III-III and V-V APB structures for GaP, GaAs and GaSb were extracted, as shown in **Fig. 5.20**, with a very good correspondence to the initial DFT calculations (**Fig. 5.18**).

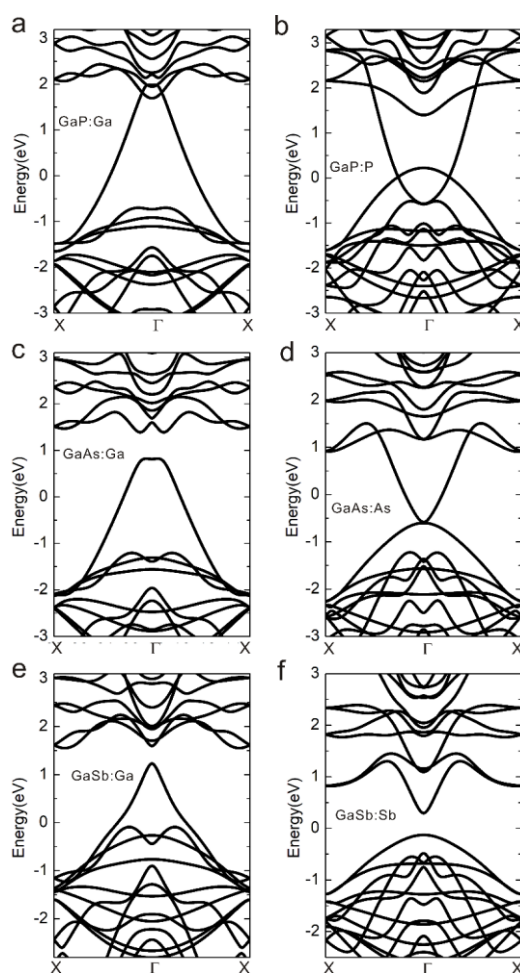


Figure 5.20 Band structures associated to III-III and V-V APBs along X- Γ -X based on first-principle tight-binding model for GaP (a,b) GaAs (c,d) and GaSb (e,f).

The total density of states (unit: states/eV) of the slab structures were extracted, as shown in **Fig.5.21**, which corresponds essentially to the superposition of a 2D electronic density of states with 3D-like CB (Conduction Band) and VB (Valence Band) densities of states. In order to better capture the effect of this superposition in real heterostructures, it is necessary to consider that the experimental linear density of APBs is in fact smaller than the effective ones considered for the simulation due to the limited size of the supercells.

In the realistic material, the linear density of APB is $10.47 \mu\text{m}^{-1}$, which can be roughly extracted from SEM images, i.e. around 1 APB each 100 nm of bulk. While, the linear density of APB of the supercell for calculation, taking III-III APB slab structure for example, is 0.5826 nm^{-1} i.e. around 1 APB each 1.7163 nm of bulk. Therefore, the APB part of the total density states of III-III APB supercell (**Fig.5.21a**) keep unchanged (i.e. is multiplied by 1) and the bulk part needs to be multiplied by 58.26 ($100 \text{ nm}/1.71631 \text{ nm}$) to get the real total density states. Finally, the total density of states is divided by the volume and we can get the real density of states with a $\text{states/eV}/\mu\text{m}^3$ unit for the III-III APB structure in realistic materials, as shown in **Fig.5.22b**. In the same way, the density states for the other III-III and V-V APB structures can be obtained, as shown in **Fig.5.22**.

The DOS representation confirms the semimetallic nature of both III-III and V-V APBs and a large ratio of at least 10^3 between the number of states available at a given energy in the bulk region and the number of states localized in the APBs indicates that any charge transfer from the bulk semiconductor domains to the 2D APB singularities drastically changes the filling of the APBs states and thus easily shifts its Fermi level.

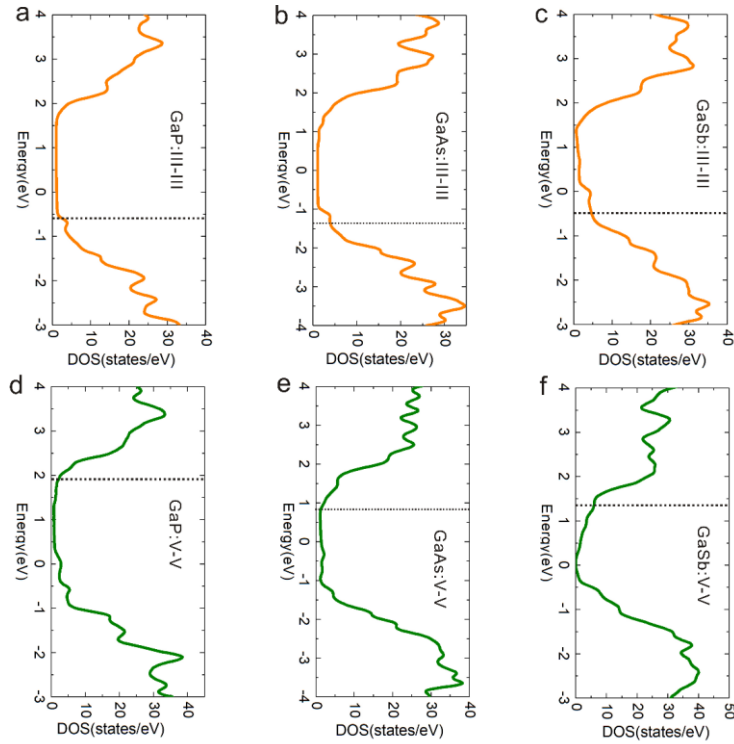


Figure 5.21 Total density states of the III-III and V-V APB slab structures for GaP (a,d), GaAs (b,e) and GaSb (c,f) based on first-principle tight-binding model.

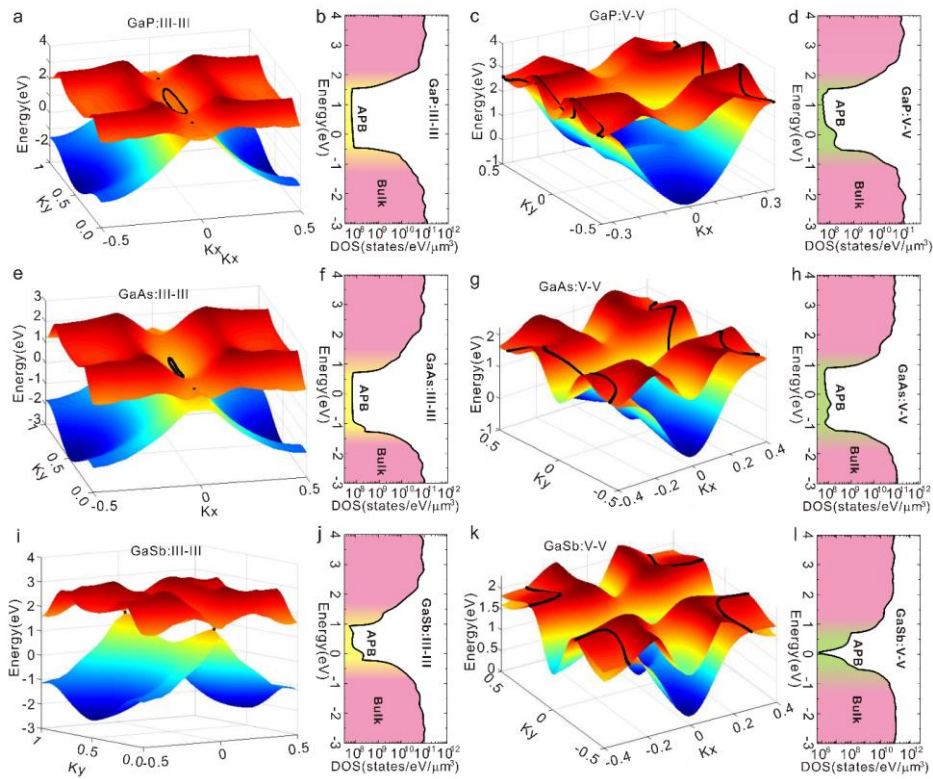


Figure 5.22 3D plot of CBM and VBM of the III-III and V-V APB slab structures, extracted based on first-principle tight-binding model (a,c,e,g,i,k) and realistic density of states in log scale for the III-III and V-V APB structures (b,d,f,h,j,l).

Moreover, 3D plot of the VBM (Valence Band Maximum) and CBM (Conduction Band Minimum) for III-III and V-V APB structures corresponding to $k_z=0$ planes for GaP, GaAs and GaSb are plotted in **Fig. 5.22a,c,e,g,i,k**. The crossing points are marked by black dots. We can observe that for the III-III APB structures, one pair of Weyl points [249] and one closed nodal ring [136] around the high symmetry Y point exist. The pair of Weyl points is always observed for all the III-V materials with APBs. While the nodal ring varies from a large one (GaP) to small one (GaAs) and even disappears for GaSb, which may be related to the differences of their bandgaps. On the other hand, non-closed snakelike nodal lines [136] are evidenced for the V-V APB structures. The crossing points are further confirmed by DFT enlarged band structure calculations based on metaGGA (TB-mBJ) potential combined with band symmetry analysis (the detailed analysis will be given in the following part). The pairs of topological Weyl points observed for III-III APB structures are characterized by a Berry phase equals to π , along a close k path in $k_z=0$ plane (as shown in **Fig. 5.23**). The band crossings are protected by a combination of the time-reversal symmetry preserved in the III-V lattice and the spatial inversion symmetry restored at the APB [136,250,251]. Therefore, such topological features are predicted to be fingerprints of the intrinsic symmetry properties of charged APB planes [252]. Deeper investigations are however needed to further explore the experimental implications of such topological predictions, but non-stoichiometric and charged III-V APBs presented here appear as leading to a first practical device realization based on these concepts.

5.6.4 Enlarged band structure and Fermi energy calculations

As demonstrated above, the 3D bandstructures of nonstoichiometric APB structures determined from first-principle tight-binding model (**Fig. 5.22**) show that the crossing points exist in the form of pairs of discrete points (called Weyl point) and along special lines creating either closed rings (called nodal ring) or non-closed lines (called nodal line) in momentum space. In order to further confirm the crossing points, DFT electronic band calculations were conducted for nonstoichiometric GaP APB structures based on the

metaGGA (TB-mBJ) potential along multiple k paths with dense k points together with band symmetry analysis.

Fig. 5.23 displays the selected k -paths in the $k_z=0$ plane for electronic band calculations of the III-III APB structure centering around Γ and Y points. The corresponding band structures and enlarged band structures centering around Γ points are shown in **Fig. 5.24** and **Fig. 5.25**, where the irreducible representations (IRs) of the CBM and VBM are indicated. We can observe the bands open gaps around 40-60 meV (**Fig. 5.25**) due to the hybridization of the same irreducible representation of the CBM and VBM [136]. The band structures and enlarged band structures around crossing point centering around Y points are shown in **Fig. 5.26** and **Fig. 5.27**, together with the irreducible representations (IRs) of the CBM and VBM around crossing points. The different irreducible representations (IRs) of the CBM and VBM avoid hybridization effects and protect the crossing points, which are evidenced by the enlarged band structures (**Fig. 5.27**). The crossing points are marked by green dots in the k -path illustration (**Fig. 5.23**), which form one pair of Weyl points and one nodal ring centering around Y point, showing good agreement with the 3D band plot based on first-principle tight-binding model (**Fig. 5.22**).

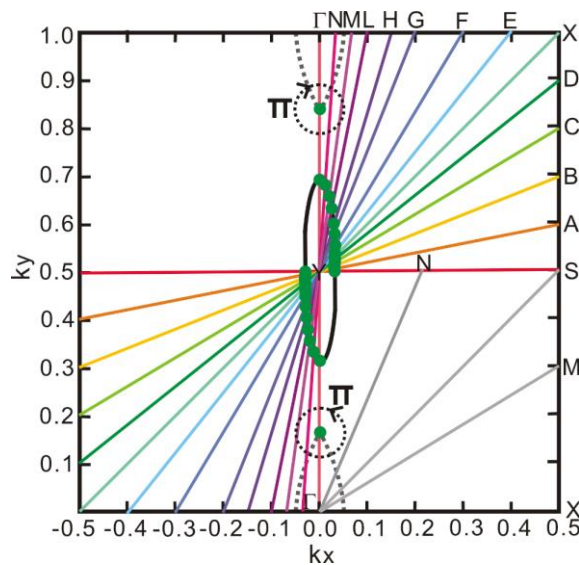


Figure 5.23 Illustration of selected k -paths in the $k_z=0$ plane for electronic band calculations based on III-III APB structure and the crossing points marked by green dots.

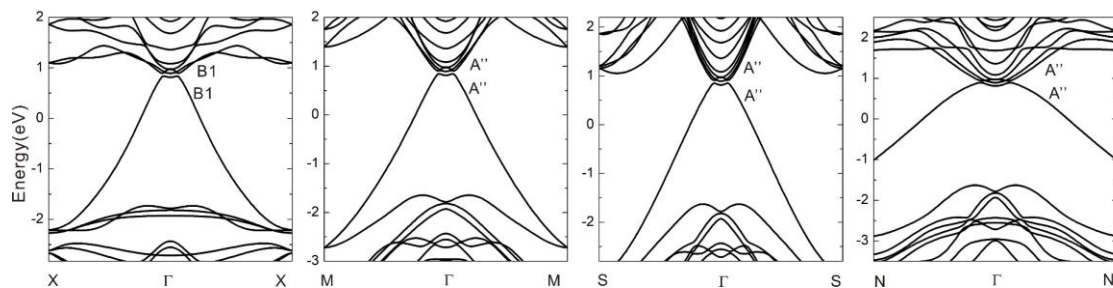


Figure 5.24 Electronic bands with band symmetry information of III-III APB structure along k-path X- Γ -X, M- Γ -M, S- Γ -S and N- Γ -N.

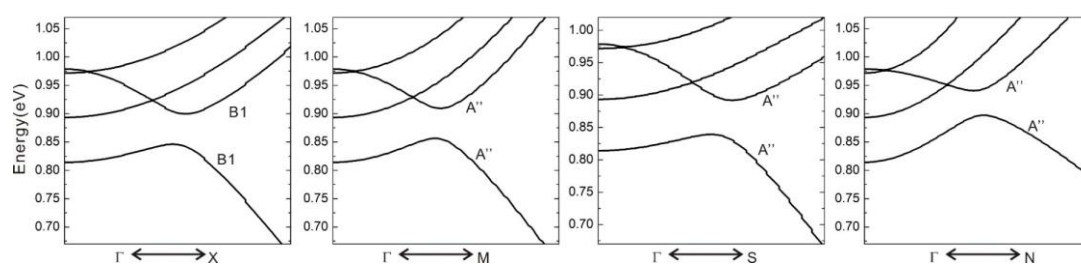


Figure 5.25 Enlarged band structures corresponding to **Fig. 5.24**.

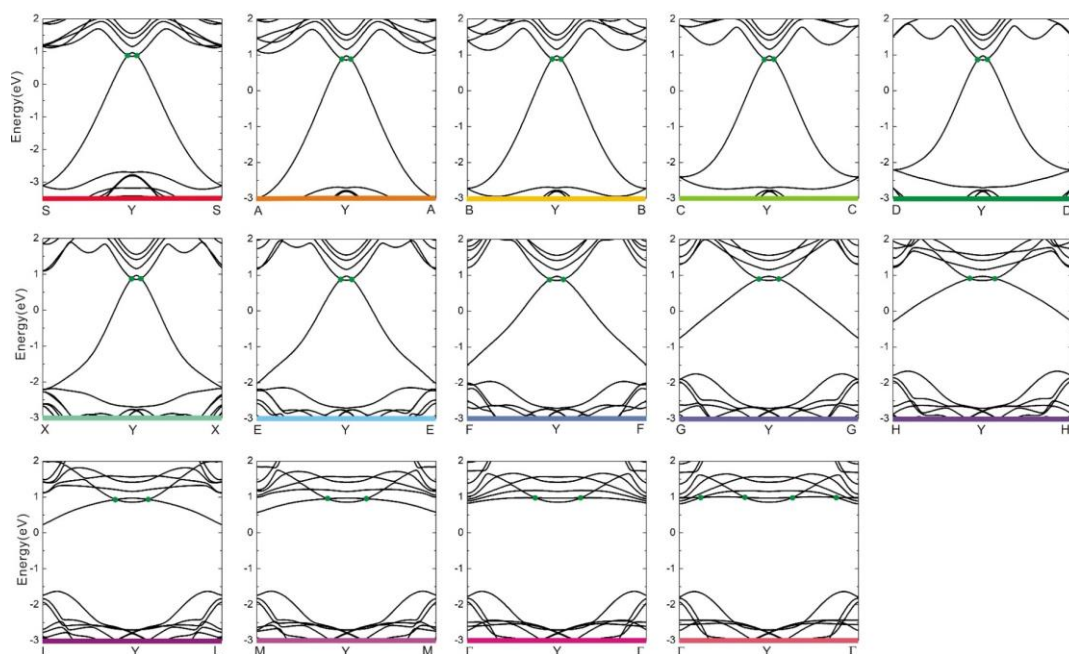


Figure 5.26 Electronic bands with band symmetry information of III-III APB structure along the different k-paths centering Y high symmetry k point.

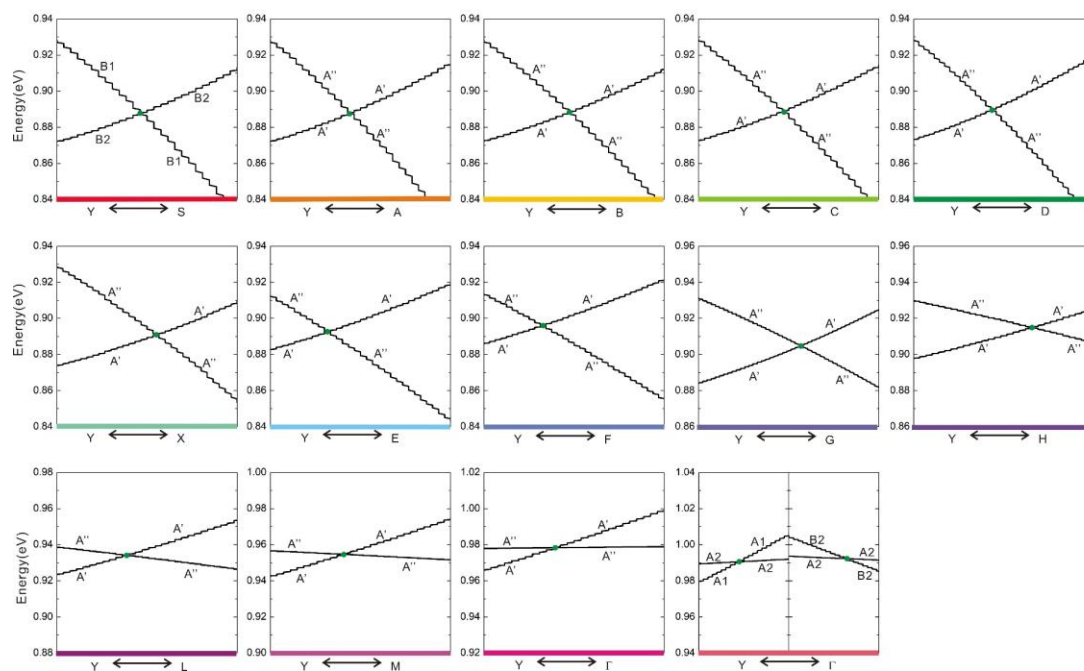


Figure 5.27 Enlarged band structures corresponding to **Fig. 5.26**.

In the same way, the electronic band calculations for the V-V APB structure of GaP are also performed along multiple k paths at $k_z=0$ plane (as shown in **Fig. 5.28**). The band structures together with irreducible representations (IRs) of the CBM and VBM around crossing points are shown in **Fig. 5.29** and **Fig. 5.30**, which indicate the existence of band crossing. The crossing points marked in **Fig. 5.28** as purple dots form two snake-like nodal lines, in good agreement with the **Fig. 5.22**.

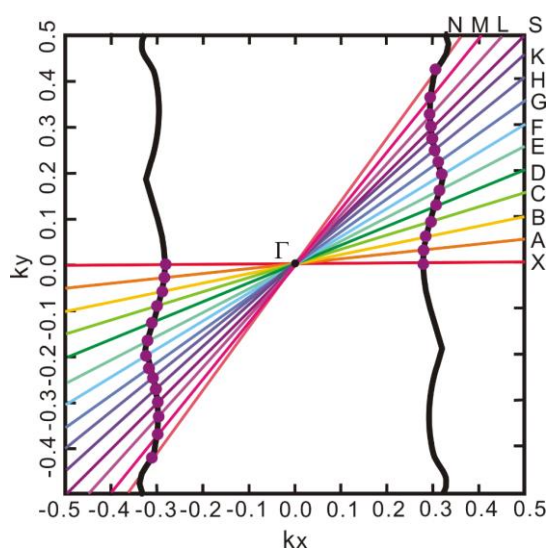


Figure 5.28 Illustration of selected k -paths in the $k_z=0$ plane for electronic band calculations based on V-V APB structure and the crossing points marked by purple dots.

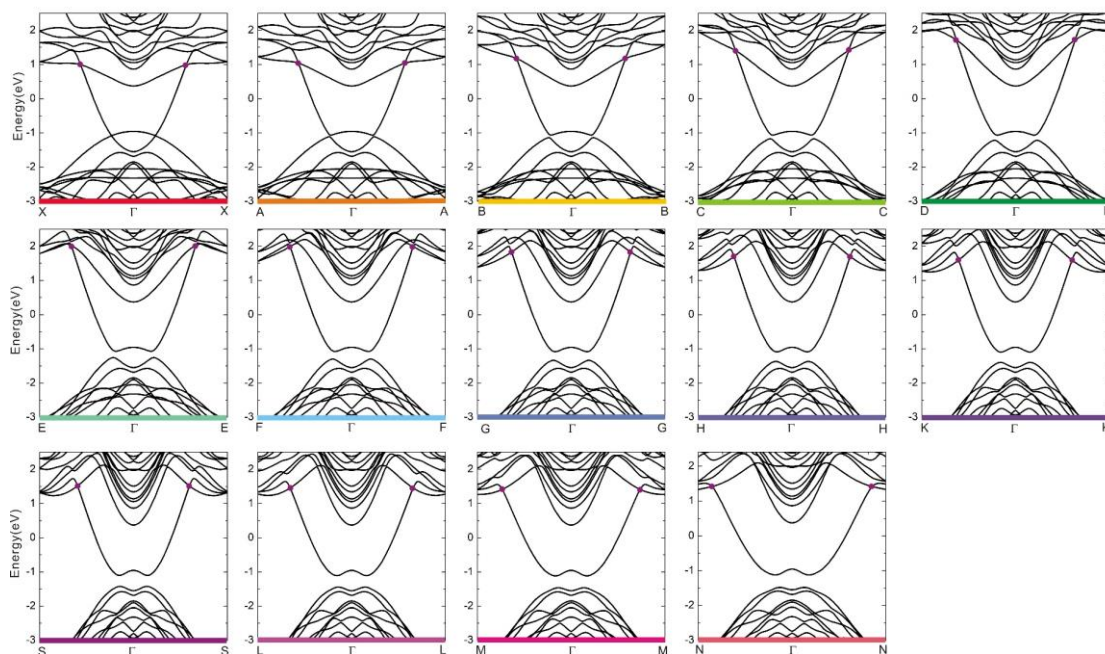


Figure 5.29 Electronic band with band symmetry information of V-V APB structure along the different k-paths centering Γ high symmetry k point.

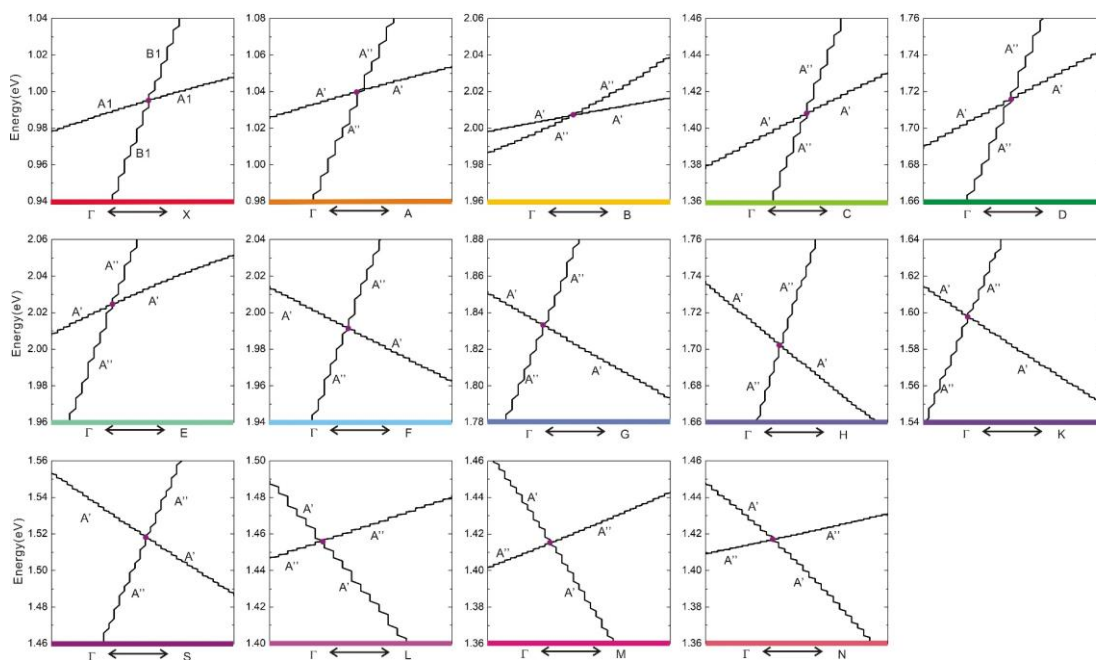


Figure 5.30 Enlarged band structures corresponding to Fig. 5.29.

From the present analysis and experimental study, it is already clear that epitaxial bi-domain III-V/Si materials are hybrid structures, composed of bulk semiconductors, with 2D semi metallic vertical inclusions, enabling simultaneously photo-activity, charge separation and ambipolar transport. In order to have a better hint of the promising

functionalities afforded by this new class of heterostructures for photonic, computing, or energy harvesting devices, a general overview of the related energy diagrams is necessary. Fermi energy levels of reference zinc blende, III-III and V-V APB structures were carefully determined by DFT calculations using a metaGGA functional with dense k point meshes. The Fermi energy lineups after careful calibration of the vacuum energy, as well as energetic positions of the deep energy levels and bulk energy states, are shown in **Fig. 5.31**, together with the VBM and CBM of zinc blende III-V bulk materials and the energy levels of Si. The VBM and CBM of Si were aligned with the ones of bulk III-Vs based on ref. [207], and the fluctuations of the Fermi level of n-doped and p-doped Si corresponds to the range of the doping concentration of Si substrates experimentally used in this study. All the energy levels are shifted by setting the energy of vacuum equal to 0eV. We can find that compared to the bulk Fermi levels, the V-V APB structures have quite high Fermi levels and the III-III APB structures have much lower Fermi levels, close to the CBM and VBM of the bulk, respectively.

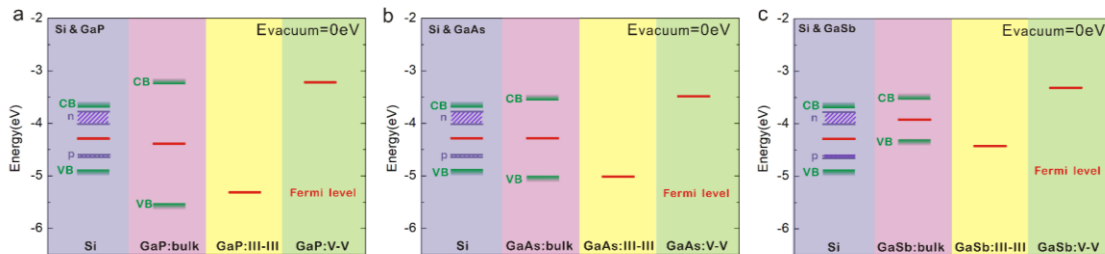


Figure 5.31 Fermi energy alignments of III-V zinc-blende, III-III and V-V APB structures with n-doped and p-doped Si corresponding to GaP/Si (a), GaAs/Si (b) and GaSb/Si (c). All the energy levels are shifted with the energy of vacuum set to 0 eV.

The Fermi energy calculations indicate that the two different $\sigma^{+/-}$ APBs are expected to behave as highly n-doped and p-doped semiconductors, which should dominate the ambipolar PEC properties and shed light on the MS plot with positive and negative slopes observed [245-247]. We will see hereafter that this result is very important for the understanding of III-V/Si photoelectrodes operation.

5.7 Band structure of stoichiometric APB in GaP and GaSb

In order to check the contribution of the stoichiometric APB to the PEC properties, DFT band structure calculations based on HSE functionals were performed for GaP and GaSb in the same way as in **Chapter 3** for InP. The results are shown in **Fig. 5.32**, where the white dotted lines are the CBM and VBM of the corresponding bulk supercell. We can find that, similarly to the InP case, the stoichiometric APB structures of GaP and GaSb also introduce several localized states on the top of valence bands, shifting VBM upward and reducing the band gap (around 0.5 eV for GaP and 0.3 eV for GaSb). The IPCE data shows a weak signal in the 550 nm-750 nm range for GaP/Si sample (**Fig. 5.12**), which might correspond to the absorption of stoichiometric APB structures. These stoichiometric APBs may also contribute to the transport through strong electron-phonon coupling related processes (as discussed in **Chapter 3**), while it is not considered to be the main origin of the efficient ambipolar transport properties observed here.

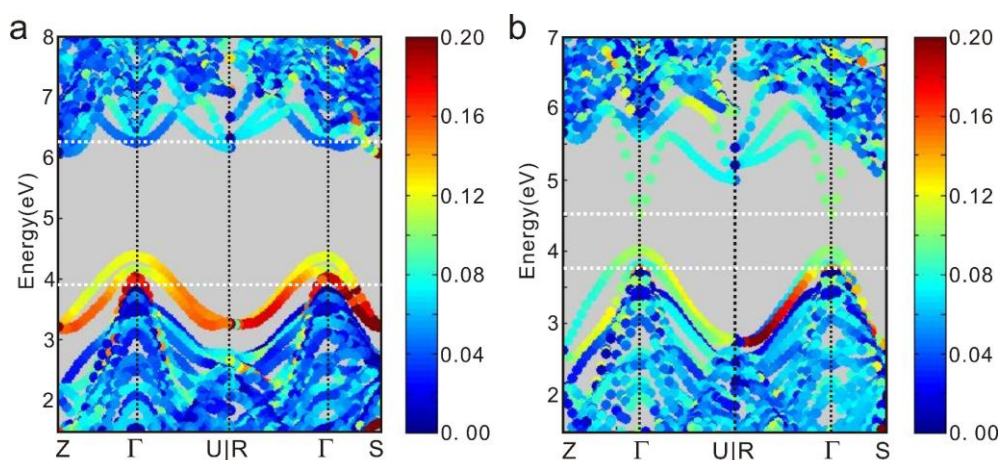


Figure 5.32 Electronic band structures of the stoichiometric APB structures of GaP (a) and GaSb (b). The white dotted lines corresponding to the CBM and VBM of the bulk supercell.

5.8 General description of III-V/Si photoelectrodes operation

5.8.1 General picture for the ambipolar III-V/Si photoelectrode

To describe the ambipolar PEC operation of the hybrid semimetal/semiconductor

bidomain III-V/Si material, from the carrier photo-generation to the interfacial Faradaic reactions (represented in this scheme as OER and HER, although photocorrosion certainly takes place), we propose the mechanism depicted in terms of band lineups for GaP (**Fig.5.33a-c**), together with its spatial representation (**Fig.5.33d,e**). As described above, the Fermi levels of V-V APBs and III-III APBs are respectively close to the CBM and VBM of the bulk (**Fig.5.31a-c**). When the III-III and V-V APBs couple together with bulk materials, charge redistribution occurs and align the Fermi levels to reach equilibrium state. Especially, V-V APB structures are expected to lose electrons, to lower the V-V Fermi level. Meanwhile, III-III APB structures on the contrary will tend to capture electrons, with an associated increase of their Fermi level. Indeed, even though the APBs introduce metallic states, the states are much less numerous than the bulk part as shown previously by the DOS calculation (**Fig.5.22b,d,f,h,g,l**), which indicates that the Fermi level of the APB structures can easily be shifted by accepting or donating electrons without significant change of the bulk III-V Fermi level. As a consequence, the bands of the bulk III-V will bend downward at the vicinity of V-V APB and bend upward at the vicinity of III-III APB (as shown in **Fig.5.33d,e**), and lead to more holes in V-V APB and more electrons in III-III APB structures and forming strong in plane built-in electric field with a direction from V-V APB pointing to III-III APB structures (white arrows in **Fig. 5.33d,e**). We note that this situation is very different from the one encountered with conventional inorganic semiconductors stacked structures, where the separation of photogenerated carriers is usually made vertically, with the help of the so-called p-n architecture.

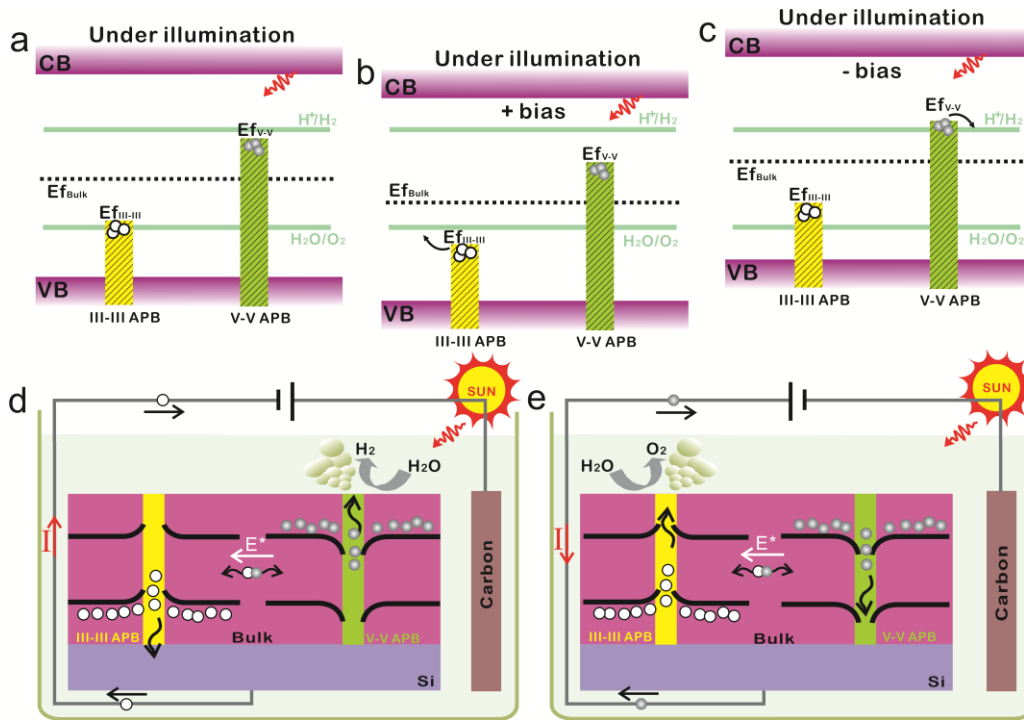


Figure 5.33: Ambipolar water splitting with bidomain III-V/Si materials. a-c, Fermi energy band diagram of III-V bulk, III-III APB, V-V APB and electrolyte for GaP in three cases: (a) under illumination, (b) under illumination and positive bias and (c) under illumination and negative bias. The yellow and green strips correspond to the occupied states of III-III and V-V APBs. d,e, Spatial schematic diagram of the ambipolar water splitting mechanism as a photocathode (d) and as a photoanode (e) based on V-V and III-III APB singularities, respectively. The yellow and green rectangles represent the III-III and V-V APB singularities, respectively, and the black lines correspond to the CBM and VBM of bulk III-V semiconductor. The black arrows represent the directions of carriers (electrons or holes) movement, and the red arrows represent the directions of current.

Under light illumination, the electrons and holes photogenerated in the bulk III-V matrix will then migrate to V-V and III-III APB singularities, respectively, thanks to the in-plane built-in electric field (as shown in Fig.5.33d,e). The built-in electric field provides here the driving force for efficient photogenerated charge carriers separation. In addition, photogenerated carriers are rapidly captured by APBs due to very short distance (<100 nm), reducing the recombination-related losses, which shed light on the strong decrease of the charge-transfer resistance after illumination (Fig.5.13) [253-254]. With the electrons (holes) reinjected in V-V (III-III) APBs, the Fermi energy level of V-V (III-III) increases (decreases) again, as shown in Fig.5.33a. The induced photo-potential between these two quasi-Fermi levels can be large due to the small DOS of metallic states.

Finally, under negative bias applied vertically, the electrons in V-V APB will be driven to the surface to generate H_2 and holes in III-III will be transferred to Si and further feed the counter-electrode (**Fig.5.33d**). Under positive bias applied vertically, the holes in III-III will move to the surface to generate O_2 and the electrons in V-V will transfer to Si and feed the counter-electrode (**Fig.5.33e**), through conductive APB paths. This process also implies that the electrical resistance of the APBs is large enough to be able to apply a potential drop vertically along the APB. From the energy band point of view, under positive and negative bias, the Fermi energy levels of III-V APBs and bulk will shift down (**Fig.5.33b**) and up (**Fig.5.33c**), respectively, promoting the oxygen evolution (**Fig.5.33b**) and hydrogen evolution (**Fig.5.33c**) reactions respectively. Overall, the proposed mechanism allows us to explain why the bidomain III-V/Si material allows achieving efficient ambipolar water splitting.

5.8.2 Influence of Si substrate doping on PEC performances

Besides, the III-V samples grown on a n-doped Si substrate show an anodic photocurrent higher than the cathodic one (**Fig. 5.9a** and **Fig. 5.10**) while the opposite situation is encountered for the sample grown on p-doped Si with higher cathodic photocurrent (**Fig. 5.11**). This indicates that the local band bendings of Si with III-III and V-V APBs at the III-V/Si interfaces play an important role in the process.

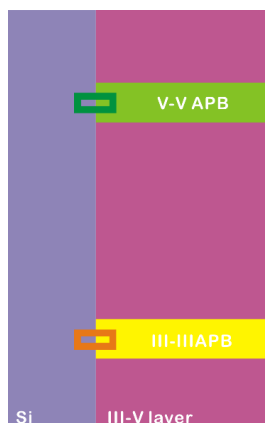


Figure 5.34 Schematic diagram of bi-domain III-V/Si sample with III-III and V-V APBs. The

interfaces of Si with V-V APB and Si with III-III APB are marked by the green and orange boxes, respectively.

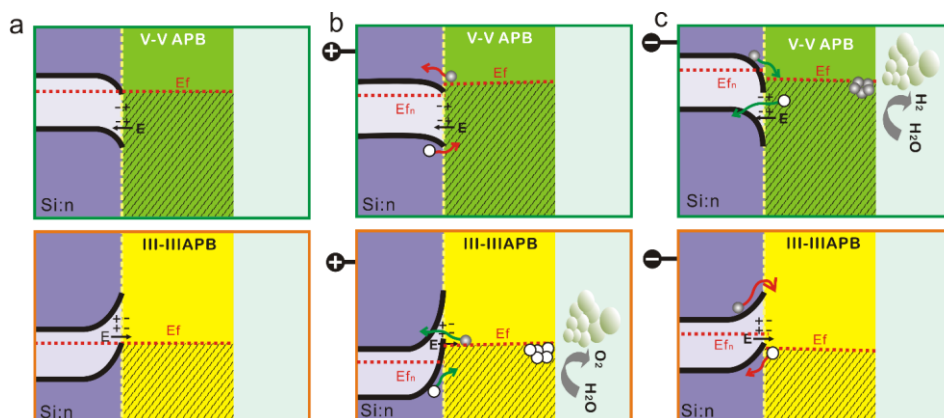


Figure 5.35 Local band bendings between Si with III-III and V-V APBs of the GaP/Si:n samples in three conditions: without bias (a), under positive bias (b) and under negative bias (c), proposed to explain the higher anodic photocurrent and lower cathodic photocurrent as shown in the voltammetry curve (**Fig. 5.9a**). The small subgraphs with green and orange enclosed boxes correspond to the interfaces of Si with V-V APB and Si with III-III APB, respectively.

Schematic band bending drawings are displayed in **Fig.5.35** for the GaP/Si:n samples and **Fig.5.36** for the GaPSb/Si:p sample, where the small subgraphs with green and orange enclosed boxes correspond to the interfaces of Si with III-III APB and Si with V-V APB, respectively (**Fig.5.34**). **Fig.5.35a** shows the band bendings between n-doped Si with III-III APB and V-V APB without applied bias. Based on Fermi level alignments (**Fig.5.31**), we know that the Fermi level of n-doped Si lies between the V-V and III-III Fermi levels of the GaP/Si:n, which causes the bands of Si to bend downwards and upwards the V-V and III-III APB structures, respectively. It must be noticed that due to the fact that Fermi energy level of n-doped Si is closer to the one of V-V APB, the band bending between Si and V-V APB is weaker than the band bending between Si and III-III APB. When positive voltage is added on Si, the strong band bending between Si and III-III APB facilitates the carrier transport, as illustrated by the green arrows in **Fig.5.35b**, and the weak band bending between Si and III-III APB becomes a small barrier for carrier transfer (illustrated by the red arrows in **Fig.5.35b**), which can disappear easily with increasing of the voltage, leading to relatively large anodic photocurrent. At the opposite,

when negative voltage is applied on Si, the relatively strong band bending between Si and III-III APB becomes a barrier for carrier transfer (illustrated by the red arrows in **Fig.5.35c**), which causes relatively small cathodic photocurrent.

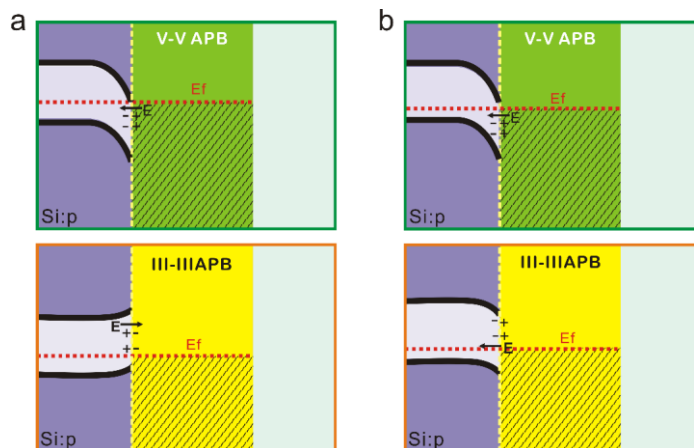


Figure 5.36 Local band bendings between Si with III-III and V-V APBs of the GaPSb/Si:p sample, proposed to explain the higher cathodic photocurrent and lower anodic photocurrent as shown in the voltammetry curve (**Fig. 5.11**). The Fermi level of Si is either between the Fermi levels of III-III and V-V APBs and closer to the III-III's one (a) or even below both III-III and V-V Fermi energies (b). The small subgraphs with green and orange enclosed boxes correspond to the interfaces of Si with V-V APB and Si with III-III APB, respectively.

For the III-V sample on p-doped Si substrate (GaPSb/Si:p sample), the situation is reversed. The Fermi energy level of p-doped Si is closer to the one of III-III APB (**Fig.5.36a**) or even below the Fermi level of III-III APB (**Fig.5.36b**) based on the Fermi calculation results (**Fig.5.31**). This situation results in a stronger band bending between Si and V-V APB, which acts as a large barrier for carrier transport under positive voltage on Si, giving rise to relatively low anodic photocurrent. When the Fermi level of Si is below both III-III and V-V Fermi levels (**Fig.5.36b**), both the band bendings between Si and III-III and Si and V-V will facilitate cathodic photocurrent and impede anodic photocurrent, leading to a larger difference between cathodic and anodic photocurrent. Besides, in this case, the PEC response of the Si substrate can be activated.

5.8.3 Contribution of the Si substrate to the PEC response

Based on the description of local band bendings of Si with III-III and V-V APBs at the interfaces, we can also make a discussion explaining why the absorption of the n-doped Si substrate doesn't provide a contribution to PEC response for the GaP/Si:n sample (almost no IPCE signal below 750 nm in **Fig.5.12**). As discussed above, in this situation, the Fermi level of n-doped Si lies between the Fermi levels of III-III and V-V APB structures. Therefore, the bands of Si bend downward and upward with V-V and III-III APB structures, respectively. In this situation, under an incident light in the 750 nm–1100 nm wavelength range, the Si substrate will absorb the light and generate electron/hole pairs. Due to the inverted band bendings between Si/V-V and Si/III-III, the photo-generated electrons close to the Si/V-V interface will easily access to the GaP layer through V-V APB leaving the holes in Si. The photo-generated holes close to the Si/III-III interface will easily flow to the GaP layer through III-III APB structure leaving the electrons in Si. This will lead to electrons/holes recombinations, as shown in **Fig.5.37a**. Therefore, the light absorption of n-doped Si (of the GaP/Si:n sample) doesn't lead to an obvious PEC response.

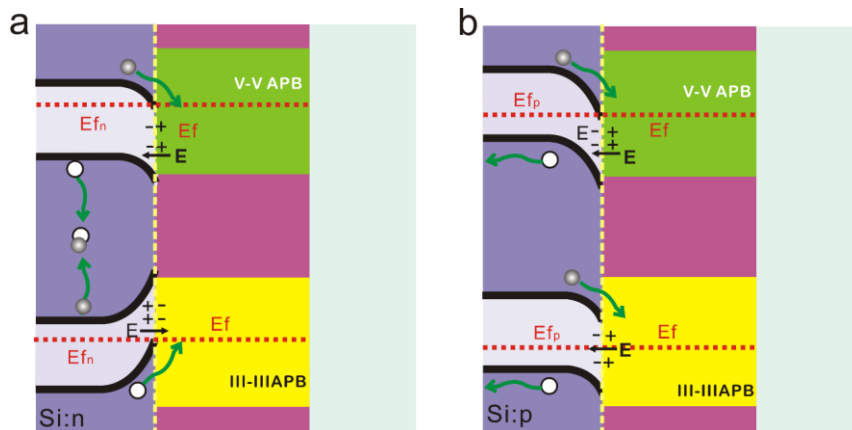


Figure 5.37 Scheme explaining the light-absorption contribution of the different Si substrates to the PEC response for the III-V sample (a) with n-doped Si substrate (i.e. the Si Fermi level lies between the Fermi levels of III-III and V-V APB structures) and (b) with a p-doped Si substrate (where the Si Fermi level lies below both the III-III and V-V Fermi levels).

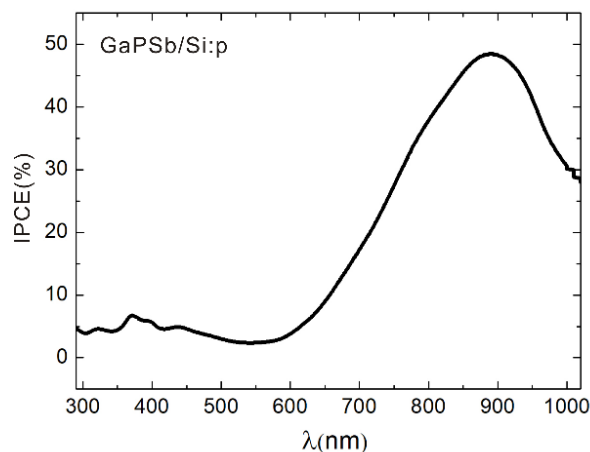


Figure 5.38 IPCE spectrum recorded at -0.74 V (cathodic region) for the bi-domain GaPSb/Si:p sample, which shows a large signal between 600 and 1000 nm (corresponding to Si absorption).

On the other hand, if the Fermi energy of Si is below or above the Fermi levels of both III-III and V-V APB structures, then the same band bendings between Si and V-V APB or Si and III-III APB will occur. For example, this configuration is achieved for GaSb or GaSb-based alloys grown on Si:p substrates (the Fermi level can be lower than both III-III and V-V APB structures). In this situation, the band of Si will bend downward with both V-V and III-III APB structures (**Fig.5.37b**). The photo-generated electrons in Si will flow to III-V layer and the holes will stay in Si, leading to charge separation and contribute to the IPCE response, as shown in **Fig.5.37b**. This was evidenced by the IPCE spectrum of the GaPSb/Si:p sample, which shows a large IPCE signal in the 600-1000 nm wavelength range (mainly corresponding to Si absorption), as shown in **Fig.5.38**.

The local band bendings between Si with III-III and V-V APBs at the III-V/Si interfaces provides degrees of improvements to optimize charge carriers transfers, or even by making the Si substrate photoactive for improving PEC performance, with a careful optimization of Fermi energy levels alignments through both III-V alloys composition or Si substrate doping.

5.8.4 Synthetic view

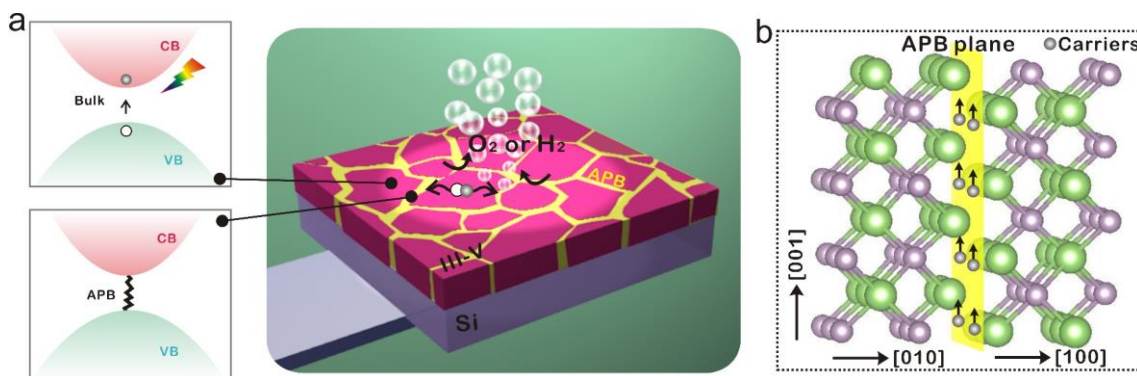


Figure 5.39 a. General illustration of the bi-domain III-V/Si material composed of bulk photoactive semiconductors with 2D APB semi metallic inclusions, realizing ambipolar PEC water splitting. b. Schematic plot of carriers' transport along the 2D APB planes at the atomic scale.

Therefore, epitaxial III-V/Si materials with hybrid 2D semimetal/semiconductor properties (**Fig. 5.39**) enable not only photo-generation through optical absorption and good vertical ambipolar transport, but also efficient in-plane charge carrier separation and efficient charge transfers between bulk semiconducting domains and 2D semimetal singularities. The Fermi level and bandgap engineering capabilities offered by the control of III-V ternary and quaternary alloys with today's epitaxial setups or the choice of Si substrate doping, and the possibility to tune the vertical or lateral APB distribution in III-V/Si samples [3,83], is promising for the development of novel multifunctional photoelectric devices using epitaxial III-V/Si materials with non-stoichiometric APBs.

5.9 Summary

In this chapter, we demonstrated experimentally and theoretically that epitaxial bi-domain III-V/Si materials with non-stoichiometric APBs are hybrid structures, composed of bulk semiconductors enabling photo-activity, and antiphase boundaries that are 2D topological semi metallic inclusions with ambipolar transport properties. The demonstration of operating ambipolar III-V/Si photoelectrodes is completed by dedicated theoretical and experimental studies. It shows that the epitaxial bi-domain III-V/Si

materials are indeed able within the same layer to absorb light efficiently, separate laterally the photo-generated carriers, transfer them to semimetal singularities, and extract both electrons and holes vertically. These very specific and multifunctional properties obtained within the same layer provide new paradigms for energy harvesting, photonics, electronics or computing applications and may also expand a new route for the exploration of novel topological materials.

Conclusions and perspectives

In **Chapter 1**, the advantages of III-V/Si co-integration, as well as the general interest of III-V/Si materials for integrated photonics and energy harvesting applications have been clarified. Then the III-V/Si monolithic integration methods and corresponding issues and strategies have been presented. Finally, focusing on antiphase boundaries, their generation, propagation, burying mechanisms and properties were reviewed.

In **Chapter 2**, the experimental and theoretical supports of this work have been presented. The related mechanisms, techniques and parameters settings of different structural, optical and photo-electro-chemical characterizations used in this thesis have been described. Besides, after a brief introduction to the basic concepts of the DFT, the calculation steps and parameters settings of DFT calculations for band structures, phonons and electron-phonon coupling have been presented.

In **Chapter 3**, antiphase boundaries in InGaP were found to enhance In incorporation around the APBs in the sample, thus behaving as 2D In-rich vertical homovalent singularities. Based on Raman, PL experiments and DFT calculations, simultaneous confinement of charge carriers and phonons at the vicinity of the 2D homovalent singularity (In-rich stoichiometric APB) has been evidenced. This situation led to a strong enhancement of the electron-phonon coupling, which has been indicated by a large experimental Huang-Rhys factor and discussed in the framework of the optical deformation potential.

In **Chapter 4**, a novel III-V/Si (GaPSb/Si) tandem materials association was investigated for solar water splitting applications. The band evolution of the GaPSb alloy has been determined over the whole Sb range by absorption measurements and tight-binding calculations. The indirect (X-band) to direct (Γ -band) cross-over was found to occur at 30% Sb content. Especially, at a Sb content of 32%, the $\text{GaP}_{1-x}\text{Sb}_x$ alloy reached the desired 1.7 eV direct bandgap, enabling efficient sunlight absorption. Besides, the

band alignment of $\text{GaP}_{1-x}\text{Sb}_x/\text{Si}$ with respect to water redox potential levels has been analyzed, which shows the 1.7eV/1.1eV GaPSb/Si association is an interesting combination both for the hydrogen and oxygen evolution reactions. Finally, a $\text{GaP}_{0.67}\text{Sb}_{0.33}/\text{Si}$ photoanode with a very close to the optimal bandgap combination (1.7eV/1.1eV) was investigated for photoelectrochemical (PEC) characterizations and it shows promising PEC performances due to the high light absorption but the transport mechanism in these photoelectrodes is questioned.

In **Chapter 5**, we proved that the two kinds of III-III and V-V non-stoichiometric APBs in the III-V layers are 2D semi-metallic inclusions by combining structural, transport characterizations with first-principle calculations. Besides, The III-III and V-V non-stoichiometric APBs have been evidenced to have quite high and low Fermi energy levels, respectively, which introduces a strong built-in electric field in nano-scale regions when they couple together with the bulk III-V. On this basis, we demonstrate ambipolar operation of various III-V/Si photoelectrodes (GaP/, GaAsP/ and GaPSb/ on silicon). The built-in electric field provides efficient driving force for efficient photogenerated charge carriers separation. Overall, we demonstrate that the hybrid bidomain III-V/Si materials are able within the same layer to absorb light efficiently, separate laterally the photo-generated carriers, transfer them to semimetal singularities, and extract both electrons and holes vertically, leading to efficient carrier collection and ambipolar performances.

Perspectives

In this thesis, we clarified for the first time the unusual physical properties of antiphase boundaries, which fully explain why APBs cannot be used in standard p-n architectures for photonics (e.g. lasers) or for energy harvesting (e.g. photovoltaic solar cells). But these new clarified physical properties also open many prospects to design novel devices for photonics, electronics, computing or energy harvesting. Even if a first device demonstration was performed with the development of operating photoanodes with these 2D nano-objects, many different devices architectures could be imagined from these findings.

More specifically, from the water splitting point of view, this work only gave the first demonstrations of operating photoanodes, and the PEC experiments were performed in acid and alkaline electrolytes with only two pH values. Systematic research of the influence of pH on band alignment between III-V and water levels could be done. The efficiency and spectral dependency of PEC performances should also be considered in the future. Besides, as demonstrated in **Chapter 4** and **5**, a careful optimization of Fermi levels lineups through both III-V alloys composition or Si substrate doping can optimize charge carriers transfers and activate the Si substrate PEC response. Therefore, more III-V/Si MBE samples with different composition or doping would surely be of great interest to reach high-efficiency water splitting. Finally, with these materials, a whole PEC cell combining a photo-anode and a photo-cathode should rapidly be developed, in order to demonstrate autonomous operation of the system.

Finally, in **Chapter 5**, we demonstrated preliminary results on the topological properties of the non-stoichiometric APB structures. These investigations are of high interest, as it could lead to a new topological nano-material to be studied experimentally and theoretically in fundamental physics with expected non-trivial topology-induced transport properties.

Appendices

Molecular beam epitaxy and ultra-high vacuum chemical vapor deposition

III-V on Si epitaxial growth is realized in an Ultra-High-Vacuum Chemical Vapor Deposition (UHVCVD) - Molecular Beam Epitaxy (MBE) cluster equipment, which was developed and installed in FOTON-OHM/INSA laboratory in 2010. The Riber UHVCVD reactor dedicated to group-IV elements growth is connected to the Riber compact 21 solid source MBE chamber devoted to III-V compound growth by an ultra-high vacuum (UHV) tunnel kept at 10^{-9} Torr thanks to ionic pumps, as shown in **Figure A.1**. MBE growth method needs very high vacuum environment, which can enable long mean-free path of atoms or molecules. Like this, the evaporated atoms can avoid interacting with each other or vacuum-chamber gases until they reach the substrate. This is why we call it “beam”. In order to monitor the growth in-situ, a Reflection High-Energy Electron Diffraction (RHEED) system consisting of a RHEED Gun and a fluorescent screen are equipped on both the chambers, operating at 30 keV for UHVCVD and 12 keV for MBE. A computer is used to control the temperature of the substrate and evaporation sources, allowing precise control of the thickness and composition of samples.

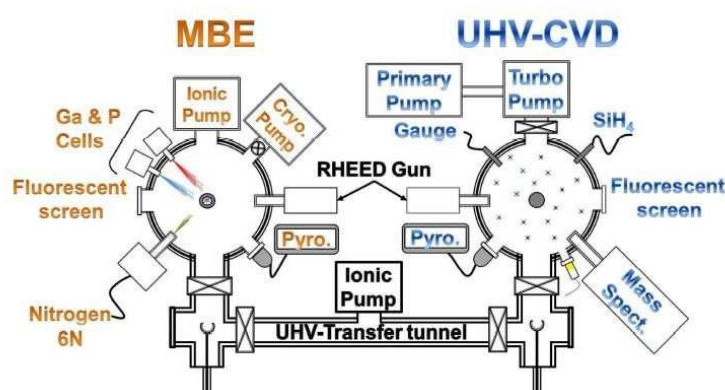


Figure A.1 Schematic representation of the UHVCVD-MBE growth cluster. The UHVCVD reactor for group IV growth is linked to the MBE reactor for group III-V growth by a UHV transfer tunnel maintained at 10^{-9} Torr [201].

For III-V samples grown directly on Si, freshly prepared Si substrates are loaded into the MBE chamber, heated at 800°C during several minutes for dehydrogenation and cooled down to III-V layer growth temperature. For samples with Si buffer layer prior to III-V layer growth, the substrates after chemical preparation are introduced to the UHVCVD chamber and heated to 800°C (heater on the sample holder) under a residual atmosphere of silane at about 10^{-6} torr. The homoepitaxial Si layer is deposited using silane (SiH_4) injected through a mass flow/Baratron flux/pressure controller and the pressure is fixed at 6.10^{-3} Torr, with 10 min annealing before cooling down. The homoepitaxial Si/Si sample is then transferred under UHV to the MBE growth chamber for III-V layer overgrowth.

Group-III elements (Ga, In, Al) are generated from conventional Knudsen effusion cells containing pure metal solid sources. The group-V elements (P, As, Sb) are provided via a thermal effusion cell where heated solid sources of these elements (released as tetramer such as P_4 and As_4) are cracked (by the valved-cracker cell) in P_2 and As_2 molecules.

There are two growth modes (as shown in **Fig.A2**). One is the traditional Molecular Beam Epitaxy (MBE) growth where the Group-III elements and the Group-V elements are supplied at the same time and the growth rate is controlled by the flux of Group-III elements. The other mode is called Migration Enhanced Epitaxy (MEE) including alternated deposition of Group-III elements and Group-V elements. The growth rate expressed by monolayer (ML) per second and the amount of group-III elements per cycle are two important parameters for the MEE growth mode. For III-V/Si samples, they can be grown by two-step growth process. It contains low-temperature MEE growth, which allows having a very smooth surface at the early stage of growth, then followed by the conventional molecular beam epitaxy (MBE) growth mode, as shown in **Fig.A2**. If you want to get more information about the sample growth of III-V/Si, please see the paper of Quinci *et al.* [201], where all the technical details are given.

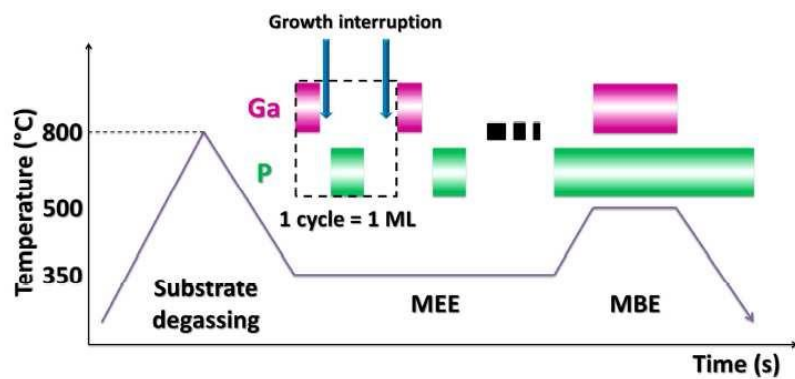


Figure. A2 Two steps III-V on Si growth process: Silicon substrate degassing followed by MEE and MBE two growth modes [255].

List of publications/conferences

a)-Publications and proceedings Publications

-**L. Chen**, Y. Léger, G. loget, M. Piriyeve, I. Jadli, S. Tricot, T. Rohel, R. Bernard, A. Beck, J. Le-Pouliquen, P. Turban, P. Schieffer, C. Levallois, B. Fabre, L. Pedesseau, J. Even, N. Bertru and C. Cornet. *Epitaxial III-V/Si vertical heterostructures with hybrid 2D-semimetal/semiconductor ambipolar and photoactive properties*, submitted.

-**L. Chen**, M. Alqahtani, C. Levallois, A. Létoublon, J. Stervinou, R. Piron, S. Boyer-Richard, J.-M. Jancu, T. Rohel, R. Bernard, Y. Léger, N. Bertru, J. Wu, I. P. Parkin and C. Cornet. *Assessment of GaPSb/Si tandem material association properties for photoelectrochemical cells[J]*. *Solar Energy Materials and Solar Cells*, 2021, 221: 110888.

-**L. Chen**, O. Skibitzki, L. Pedesseau, A. Létoublon, J. Stervinou, R. Bernard, C. Levallois, R. Piron, M. Perrin, M. A. Schubert, A. Moréac, O. Durand, T. Schroeder, N. Bertru, J. Even, Y. Léger, and C. Cornet. *Strong Electron–Phonon Interaction in 2D Vertical Homovalent III–V Singularities[J]*. *ACS nano*, 2020, 14(10): 13127-13136.

-C. Cornet, S. Charbonnier, I. Lucci, **L. Chen**, A. Létoublon, A. Alvarez, K. Tavernier, T. Rohel, R. Bernard, J.-B. Rodriguez, L. Cerutti, E. Tournié, Y. Léger, M. Bahri, G. Patriarche, L. Largeau, A. Ponchet, P. Turban, and N. Bertru. *Zinc-blende group III-V/group IV epitaxy: Importance of the miscut[J]*. *Physical Review Materials*, 2020, 4(5): 053401.

-M. Alqahtani, S. Sathasivam, **L. Chen**, P. Jurczak, R. Piron, C. Levallois, A. Létoublon, Y. Léger, S. Boyer-Richard, N. Bertru, J.-M. Jancu, C. Cornet, J. Wu and I. P. Parkin. *Photoelectrochemical water oxidation of GaP_{1-x}Sb_x with a direct band gap of 1.65 eV for full spectrum solar energy harvesting[J]*. *Sustainable Energy & Fuels*, 2019, 3(7): 1720-1729.

-B. Fan, F. Li, **L. Chen**, B. Fan, F. Li, L. Chen, L. Shi, W. Yan, Y. Zhang, S. Li, X. Wang, X. Wang, and H. Chen. *Photovoltaic manipulation of water microdroplets on a hydrophobic LiNbO₃ substrate[J]*. *Physical Review Applied*, 2017, 7(6): 064010.

-S. Li, G. Liang, Z. Zan, L. Shi, W. Yan, C. Liang, F. Li, **L. Chen**, B. Fan, X. Wang, X. Jiang and H. Chen. *Impact of the crystal orientation of Fe-doped lithium niobate on photo-assisted proton exchange and chemical etching[J]*. *Scientific Reports*, 2017, 7(1): 1-11.

-**L. Chen**, B. Fan, W. Yan, S. Li, L. Shi, and H. Chen. *Photo-assisted splitting of dielectric microdroplets in a LN-based sandwich structure[J]*. *Optics letters*, 2016, 41(19): 4558-4561.

-**L. Chen**, S. Li, B. Fan, W. Yan, D. Wang, L. Shi, H. Chen, D. Ban and S. Sun *Dielectrophoretic behaviours of microdroplet sandwiched between LN substrates[J]*. *Scientific reports*, 2016, 6:

29166.

b)-Patents

-L. Chen, S. Li, B. Fan et al. *A new real-time controllable device and method for separation of micro-droplets based on lithium niobate wafer sandwich structure (CN105413767A).*

-L. Chen, S. Li, B. Fan et al. *A new method for transporting micro-droplets based on Y-cut lithium niobate wafer (CN105510615A).*

c)-Invited talks

-C. Cornet, L. Chen, A. Ruiz, I. Lucci, A. Beck, L. Pedesseau and Y. Léger. “*Monolithic integration of III-V semiconductors on silicon for photonics and solar hydrogen production*”, Invited talk at SPb Photonic, Optoelectronic, & Electronic Materials (SPb-POEM), April 24-27, 2019, Saint-Petersburg, Russia.

-C. Cornet, L. Chen, I. Lucci, A. Ruiz, A. Beck, L. Pedesseau, and Y. Léger. “*GaP-based materials for photonics and energy*”, Invited talk at SNAIA 2018 - Smart Nanomaterials Conference, December 10-13, 2018, Ecole normale supérieure de Chimie- Paris.

d)-Communications with international audience

-L. Chen, O. Skibitzki, Y. Léger, C. Levallois, R. Piron, T. Rohel, J. Stervinou, A. Letoublon, T. Schroeder and C. Cornet. *Photoluminescence of 2D-vertical In-rich APBs embedded in InGaP/SiGe/Si. Poster at 20th International Conference on Molecular-Beam Epitaxy (ICMBE 2018), September 02-07, 2018, Shanghai, China.*

-L. Chen, O. Skibitzki, Y. Léger, C. Levallois, R., T. Rohel, J. Le Pouliquen, A. Letoublon, T. Schröder and C. Cornet. *Excitons bounded around In-rich antiphase boundaries. Poster at 34th International Conference on the Physics of Semiconductors (ICPS 2018), July 29 to August 3, 2018, Montpellier, France.*

-L. Chen, O. Skibitzki, R. Piron, J. Stervinou, A. Letoublon, R. Tremblay, T. Rohel, R. Bernard, C. Levallois, Y. Léger, T. Schroeder, G. Capellini and C. Cornet. *Antiphase boundaries in InGaP/SiGe/Si: structural and optical properties. Poster at European Materials Research Society- Spring Meeting 2018 (E-MRS 2018 Spring Meeting), June 18-22, 2018, Strasbourg, France.*

e)-Communications with national audience

-L. Chen, M. Alqahtani, C. Levallois, A. Létoublon, J. Le Pouliquen, R. Piron, S. Boyer-Richard, L. Pedesseau, T. Rohel, R. Bernard, Y. Léger, G. Loget, J. Wu, I. P. Parkin, B. Fabre, N. Bertru and C. Cornet. *GaPSb/Si tandem material with APBs for efficient overall water splitting*, Talk at journée nano-matériaux de Rennes, January 14, 2020, Rennes, France.

-L. Chen, O. Skibitzki, Y. Léger, R. Piron, J. Stervinou, A. Letoublon, R. Tremblay, T. Rohel, R. Bernard, C. Levallois, L. Pedesseau, T. Schroeder, A. Moréac and C. Cornet. *Strong electron-phonon coupling in 2D-vertical In-rich APB structures*, Poser at journée nano-matériaux de Rennes, January 14, 2020, Rennes, France.

-L. Chen, R. Piron, O. Skibitzki, Y. Léger, C. Levallois, T. Rohel, L. Pédésseau, R. Bernard, J. Stervinou, A. Letoublon, T. Schroeder and C. Cornet. *Electron-phonon interactions around antiphase boundaries in InGaP/SiGe/Si: structural and optical characterizations*, Poster at 20th Anniversary of LPQM-Institut d'Alembert, ENS - Paris/Saclay, Cachan 2019, April 12, 2019, Paris, France.

-L. Chen, M. Alqahtani, C. Levallois, A. Létoublon, J. Stervinou, R. Piron, S. Boyer-Richard, J.-M. Jancu, T. Rohel, R. Bernard, Y. Léger, L. Pédésseau, N. Bertru, J. Wu, I. P. Parkin and C. Cornet. *GaPSb/Si electrodes for Solar Fuel Production*, Poster at European COST action on Solar Energy, April 10-12, 2019, Bulgaria.

-L. Chen, O. Skibitzki, Y. Léger, R. Piron, C. Levallois, A. Letoublon, J. Stervinou, R. Tremblay, T. Rohel, R. Bernard, T. Schroeder, G. Capellini and C. Cornet. *study on structural and optical properties of InGap/SiGe/Si*, Poster at 3M doctor day, October 29, 2018, Rennes, France.

f)-Selected seminars

-L. Chen, Y. Léger, L. Pedesseau, J. Even, C. Cornet, *Oral presentation for a reunion about calculations about topological properties*, September 18, 2020, Rennes.

-L. Chen, R. Piron, C. Levallois, Y. Léger, C. Cornet, *Oral presentation for a video reunion about PHD works in front of members of three FOTON labs*, June 16, 2019, Rennes.

-L. Chen, R. Piron, C. Levallois, Y. Léger, C. Cornet, *Oral presentation for a reunion about PL experiment results of III-V/Si materials*, May 18, 2018, Rennes.

-L. Chen, R. Piron, C. Levallois, C. Cornet. *Oral presentation about PHD thesis in front of members of FOTON-OHM*, February 22, 2018, Rennes.

Bibliography

- [1] Fan, S. et al. Current-Matched III–V/Si Epitaxial Tandem Solar Cells with 25.0% Efficiency. *Cell Rep. Phys. Sci.* 1, 100208 (2020).
- [2] Tang, M. et al. Integration of III-V lasers on Si for Si photonics. *Prog. Quantum Electron.* 66, 1–18 (2019).
- [3] Lucci, I. et al. Universal description of III-V/Si epitaxial growth processes. *Phys. Rev. Mater.* 2, 060401 (2018).
- [4] Cornet, C. et al. Zinc-blende group III-V/group IV epitaxy: Importance of the miscut. *Phys. Rev. Mater.* 4, 053401 (2020).
- [5] Thomson, T. A system of chemistry: in four volumes. vol. 4 (Abraham Small, 1818).
- [6] Berzelius, M. XLII. On the mode of obtaining silicium, and on the characters and properties of that substance. *Philos. Mag.* 65, 254–267 (1825).
- [7] Silicon and Germanium. <http://hyperphysics.phy-astr.gsu.edu/hbase/Solids/sili2.html>.
- [8] Liang, D. & Bowers, J. E. Recent progress in lasers on silicon. *Nat. Photonics* 4, 511–517 (2010).
- [9] Holt, D. B. & Yacobi, B. G. *Extended Defects in Semiconductors: Electronic Properties, Device Effects and Structures.* (Cambridge University Press, 2007).
- [10] Structures of Element and Compound Semiconductors. Chemistry LibreTexts <https://chem.libretexts.org> (2016).
- [11] Tanabe, K. A Review of Ultrahigh Efficiency III-V Semiconductor Compound Solar Cells: Multijunction Tandem, Lower Dimensional, Photonic Up/Down Conversion and Plasmonic Nanometallic Structures. *Energies* 2, 504–530 (2009).
- [12] Why GaAs and III-Vs Probably Won't Replace Silicon | by Tapabrata Ghosh | Medium. <https://medium.com/@sixsamuraisoldier/why-gaas-and-iii-vs-probably-wont-replace-silicon-568b4701901d>.
- [13] Band-gap engineering. Wikipedia (2020).
- [14] Bayo, C. & Ángel, M. *Theory of elasticity and electric polarization effects in the group-III nitrides.* (University College Cork, 2013).
- [15] Kour, R. et al. Review—Recent Advances and Challenges in Indium Gallium Nitride ($\text{In}_x\text{Ga}_{1-x}\text{N}$) Materials for Solid State Lighting. *ECS J. Solid State Sci. Technol.* 9, 015011 (2019).
- [16] Vegard, L. Die Konstitution der Mischkristalle und die Raumbfüllung der Atome. *Z. Für Phys.* 5, 17–26 (1921).
- [17] Mahala, P., Behura, S. K., Ray, A., Dhanavantri, C. & Jani, O. p-GaN/i- $\text{In}_x\text{Ga}_{1-x}\text{N}$ /n-GaN solar cell with indium compositional grading. *Opt. Quantum Electron.* 47, 1117–1126 (2015).
- [18] Vurgaftman, I., Meyer, J. R. & Ram-Mohan, L. R. Band parameters for III–V compound semiconductors and their alloys. *J. Appl. Phys.* 89, 5815–5875 (2001).
- [19] Vurgaftman, I. & Meyer, J. R. Band parameters for nitrogen-containing semiconductors. *J. Appl. Phys.* 94, 3675–3696 (2003).
- [20] Thompson, S. E. & Parthasarathy, S. Moore's law: the future of Si microelectronics. *Mater.*

- Today 9, 20–25 (2006).
- [21] Park, J.-S., Tang, M., Chen, S. & Liu, H. Heteroepitaxial Growth of III-V Semiconductors on Silicon. *Crystals* 10, 1163 (2020).
- [22] What is Integrated Photonics? | Knowledge and Innovation for Manufacturing Initiative. <https://aimphotonics.academy/about/what-integrated-photonics>.
- [23] Rong, H. et al. A continuous-wave Raman silicon laser. *Nature* 433, 725–728 (2005).
- [24] Ng, W. L. et al. An efficient room-temperature silicon-based light-emitting diode. *Nature* 410, 192–194 (2001).
- [25] Pillai, S. et al. Enhanced emission from Si-based light-emitting diodes using surface plasmons. *Appl. Phys. Lett.* 88, 161102 (2006).
- [26] Integrated Photonics Laboratory. <http://www.bu.edu/ipl/research.html>.
- [27] Jain, N. & Hudait, M. K. III–V Multijunction Solar Cell Integration with Silicon: Present Status, Challenges and Future Outlook. *Energy Harvest. Syst.* 1, 121–145 (2014).
- [28] Data Cite Search. <https://search.datacite.org/works/10.4229/28theupvsec2013-1ap.1.1> (2013).
- [29] Shah, A., Torres, P., Tscherner, R., Wyrsh, N. & Keppner, H. Photovoltaic Technology: The Case for Thin-Film Solar Cells. *Science* 285, 692–698 (1999).
- [30] Tsai, H. et al. High-efficiency two-dimensional Ruddlesden–Popper perovskite solar cells. *Nature* 536, 312–316 (2016).
- [31] Bard, A. J. & Fox, M. A. Artificial photosynthesis: solar splitting of water to hydrogen and oxygen. *Acc. Chem. Res.* 28, 141–145 (1995).
- [32] Lewis, N. S. & Nocera, D. G. Powering the planet: Chemical challenges in solar energy utilization. *Proc. Natl. Acad. Sci.* 103, 15729–15735 (2006).
- [33] Alqahtani, M. et al. Photoelectrochemical water oxidation of GaP_{1-x}Sb_x with a direct band gap of 1.65 eV for full spectrum solar energy harvesting. *Sustain. Energy Fuels* 3, 1720–1729 (2019).
- [34] Kumar, P. et al. Quantum dot activated indium gallium nitride on silicon as photoanode for solar hydrogen generation. *Commun. Chem.* 2, 1–7 (2019).
- [35] Maeda, K. Photocatalytic water splitting using semiconductor particles: History and recent developments. *J. Photochem. Photobiol. C Photochem. Rev.* 12, 237–268 (2011).
- [36] Yamaguchi, M., Nishioka, T. & Sugo, M. Analysis of strained-layer superlattice effects on dislocation density reduction in GaAs on Si substrates. *Appl. Phys. Lett.* 54, 24–26 (1989).
- [37] Lucci, I. Surface and interface contributions to III-V/Si hetero-epitaxial growth: Theory and Experiments. (INSA de Rennes, 2019).
- [38] Kostrzewa, M. et al. InP dies transferred onto silicon substrate for optical interconnects application. *Sens. Actuators Phys.* 125, 411–414 (2006).
- [39] Molecular Beam Epitaxy | London Nano. <https://www.london-nano.com/research/techniques/molecular-beam-epitaxy>.
- [40] Luxmoore, I. J. et al. III–V quantum light source and cavity-QED on Silicon. *Sci. Rep.* 3, 1239 (2013).
- [41] Huang, S. H., Balakrishnan, G., Khoshakhlagh, A., Dawson, L. R. & Huffaker, D. L. Simultaneous interfacial misfit array formation and antiphase domain suppression on miscut silicon substrate. *Appl. Phys. Lett.* 93, 071102 (2008).
- [42] Jallipalli, A. et al. Atomistic modeling of strain distribution in self-assembled interfacial

- misfit dislocation (IMF) arrays in highly mismatched III–V semiconductor materials. *J. Cryst. Growth* 303, 449–455 (2007).
- [43] Kim, Y. H. et al. Growth mode and structural characterization of GaSb on Si (001) substrate: A transmission electron microscopy study. *Appl. Phys. Lett.* 88, 241907 (2006).
- [44] Akahane, K., Yamamoto, N., Gozu, S., Ueta, A. & Ohtani, N. Initial growth stage of GaSb on Si(001) substrates with AlSb initiation layers. *J. Cryst. Growth* 283, 297–302 (2005).
- [45] Reboul, J. R., Cerutti, L., Rodriguez, J. B., Grech, P. & Tournié, E. Continuous-wave operation above room temperature of GaSb-based laser diodes grown on Si. *Appl. Phys. Lett.* 99, 121113 (2011).
- [46] Monge-Bartolome, L. et al. Etched-cavity GaSb laser diodes on a MOVPE GaSb-on-Si template. *Opt. Express* 28, 20785–20793 (2020).
- [47] Tournet, J. et al. GaSb-based solar cells for multi-junction integration on Si substrates. *Sol. Energy Mater. Sol. Cells* 191, 444–450 (2019).
- [48] Tournié, E. et al. Antimonide-based optoelectronic devices grown on Si substrates (Conference Presentation). in *Silicon Photonics XIV* vol. 10923 109230C (International Society for Optics and Photonics, 2019).
- [49] Tournie, E., Rodriguez, J., Cerutti, L., Teissier, R. & Baranov, A. Epitaxial Integration of GaSb-based mid-IR devices on Silicon. in *Light Conference 2019* (2019).
- [50] Samonji, K. et al. Reduction of threading dislocation density in InP-on-Si heteroepitaxy with strained short-period superlattices. *Appl. Phys. Lett.* 69, 100–102 (1996).
- [51] Fitzgerald, E. A. et al. Totally relaxed $\text{Ge}_x\text{Si}_{1-x}$ layers with low threading dislocation densities grown on Si substrates. *Appl. Phys. Lett.* 59, 811–813 (1991).
- [52] Andre, C. L. et al. Investigations of high-performance GaAs solar cells grown on Ge-Si/sub 1-x/Ge/sub x/-Si substrates. *IEEE Trans. Electron Devices* 52, 1055–1060 (2005).
- [53] Groenert, M. E. et al. Monolithic integration of room-temperature cw GaAs/AlGaAs lasers on Si substrates via relaxed graded GeSi buffer layers. *J. Appl. Phys.* 93, 362–367 (2002).
- [54] Geisz, J. F., Olson, J. M., Romero, M. J., Jiang, C. S. & Norman, A. G. Lattice-mismatched GaAsP Solar Cells Grown on Silicon by OMVPE. in *2006 IEEE 4th World Conference on Photovoltaic Energy Conference* vol. 1 772–775 (2006).
- [55] Svensson, C. P. T. et al. Monolithic GaAs/InGaP nanowire light emitting diodes on silicon. *Nanotechnology* 19, 305201 (2008).
- [56] Koblmüller, G. & Abstreiter, G. Growth and properties of InGaAs nanowires on silicon. *Phys. Status Solidi RRL – Rapid Res. Lett.* 8, 11–30 (2014).
- [57] Mårtensson, T. et al. Epitaxial III–V Nanowires on Silicon. *Nano Lett.* 4, 1987–1990 (2004).
- [58] Ping Wang, Y. et al. Abrupt GaP/Si hetero-interface using birstepped Si buffer. *Appl. Phys. Lett.* 107, 191603 (2015).
- [59] Ping Wang, Y. et al. Quantitative evaluation of microtwins and antiphase defects in GaP/Si nanolayers for a III–V photonics platform on silicon using a laboratory X-ray diffraction setup. *J. Appl. Crystallogr.* 48, 702–710 (2015).
- [60] Takagi, Y., Yonezu, H., Samonji, K., Tsuji, T. & Ohshima, N. Generation and suppression process of crystalline defects in GaP layers grown on misoriented Si(100) substrates. *J. Cryst. Growth* 187, 42–50 (1998).
- [61] Volz, K. et al. GaP-nucleation on exact Si (001) substrates for III/V device integration. *J. Cryst. Growth* 315, 37–47 (2011).

- [62] Grassman, T. J. et al. Control and elimination of nucleation-related defects in GaP/Si(001) heteroepitaxy. *Appl. Phys. Lett.* 94, 232106 (2009).
- [63] Liebich, S. et al. Laser operation of Ga(NAsP) lattice-matched to (001) silicon substrate. *Appl. Phys. Lett.* 99, 071109 (2011).
- [64] Cornet, C., Da Silva, M., Levallois, C. & Durand, O. Chapter 28 - GaP/Si-Based Photovoltaic Devices Grown by Molecular Beam Epitaxy. in *Molecular Beam Epitaxy (Second Edition)* (ed. Henini, M.) 637–648 (Elsevier, 2018).
- [65] Saleem-Urothodi, R. et al. Loss assessment in random crystal polarity gallium phosphide microdisks grown on silicon. *Opt. Lett.* 45, 4646–4649 (2020).
- [66] Ayers, J. E., Kujofsa, T., Rago, P. & Raphael, J. *Heteroepitaxy of Semiconductors: Theory, Growth, and Characterization*, Second Edition. (CRC Press, 2016).
- [67] Soga, T., Jimbo, T. & Umeno, M. Dislocation generation mechanisms for GaP on Si grown by metalorganic chemical vapor deposition. *Appl. Phys. Lett.* 63, 2543–2545 (1993).
- [68] Takagi, Y., Furukawa, Y., Wakahara, A. & Kan, H. Lattice relaxation process and crystallographic tilt in GaP layers grown on misoriented Si(001) substrates by metalorganic vapor phase epitaxy. *J. Appl. Phys.* 107, 063506 (2010).
- [69] Skibitzki, O. et al. GaP collector development for SiGe heterojunction bipolar transistor performance increase: A heterostructure growth study. *J. Appl. Phys.* 111, 073515 (2012).
- [70] Pohl, U. W. *Epitaxy of Semiconductors: Introduction to Physical Principles*. (Springer-Verlag, 2013).
- [71] Matthews, J. W. & Blakeslee, A. E. Defects in epitaxial multilayers: I. Misfit dislocations. *J. Cryst. Growth* 27, 118–125 (1974).
- [72] Németh, I. Transmission electron microscopic investigations of heteroepitaxial III/V semiconductor thin layer and quantum well structures. (2008).
- [73] Kroemer, H. Polar-on-nonpolar epitaxy. *J. Cryst. Growth* 81, 193–204 (1987).
- [74] Aminoff, G. & Broomé, B. Strukturtheoretische Studien über Zwillinge. I. *Z. Für Krist. - Cryst. Mater.* 80, 355–376 (1931).
- [75] Rubel, O. & Baranovskii, S. D. Formation Energies of Antiphase Boundaries in GaAs and GaP: An ab Initio Study. *Int. J. Mol. Sci.* 10, 5104–5114 (2009).
- [76] Calvo, M. R. Épitaxie de GaSb sur substrat Si(100) “on-axis” pour l’optoélectronique intégrée. <http://www.theses.fr/http://www.theses.fr/s188558> (2020).
- [77] Kawabe, M. & Ueda, T. Self-Annihilation of Antiphase Boundary in GaAs on Si(100) Grown by Molecular Beam Epitaxy. *Jpn. J. Appl. Phys.* 26, L944 (1987).
- [78] Lin, A. C., Fejer, M. M. & Harris, J. S. Antiphase domain annihilation during growth of GaP on Si by molecular beam epitaxy. *J. Cryst. Growth* 363, 258–263 (2013).
- [79] Ponchet, A., Patriarche, G., Rodriguez, J. B., Cerutti, L. & Tournié, E. Interface energy analysis of III–V islands on Si (001) in the Volmer-Weber growth mode. *Appl. Phys. Lett.* 113, 191601 (2018).
- [80] Ernst, F. & Pirouz, P. Formation of planar defects in the epitaxial growth of GaP on Si substrate by metal organic chemical-vapor deposition. *J. Appl. Phys.* 64, 4526–4530 (1988).
- [81] Petroff, P. M. Nucleation and growth of GaAs on Ge and the structure of antiphase boundaries. *J. Vac. Sci. Technol. B Microelectron. Process. Phenom.* 4, 874–877 (1986).
- [82] Hull, R. & Fischer-Colbrie, A. Nucleation of GaAs on Si: Experimental evidence for a three-dimensional critical transition. *Appl. Phys. Lett.* 50, 851–853 (1987).

- [83] Guillemé, P. et al. Antiphase domain tailoring for combination of modal and 4^- -quasi-phase matching in gallium phosphide microdisks. *Opt. Express* 24, 14608–14617 (2016).
- [84] Galiana, B. et al. Characterization of antiphase domains on GaAs grown on Ge substrates by conductive atomic force microscopy for photovoltaic applications. *Sol. Energy Mater. Sol. Cells* 95, 1949–1954 (2011).
- [85] Paladugu, M. et al. Site Selective Integration of III–V Materials on Si for Nanoscale Logic and Photonic Devices. *Cryst. Growth Des.* 12, 4696–4702 (2012).
- [86] Tea, E. et al. Theoretical study of optical properties of anti phase domains in GaP. *J. Appl. Phys.* 115, 063502 (2014).
- [87] Quinci, T. Composant photovoltaïque innovant à base d'hétérojonction GaP/Si. (Rennes, INSA, 2015).
- [88] Nguyen, T. T. Silicon photonics based on monolithic integration of III-V nanostructures on silicon. (INSA de Rennes, 2013).
- [89] Conductive AFM. <https://parksystems.com/park-spm-modes/94-electrical-properties/233-conductive-afm>.
- [90] Chapter 3 - Methods for Assessing Surface Cleanliness. in *Developments in Surface Contamination and Cleaning*, Volume 12 (eds. Kohli, R. & Mittal, K. L.) 23–105 (Elsevier, 2019).
- [91] X-Ray diffraction (XRD): Anton Paar Wiki. <https://wiki.anton-paar.com/hu-hu/roentgendiffrakcio-xrd/>.
- [92] Nguyen Thanh, T. et al. Structural and optical analyses of GaP/Si and (GaAsPN/GaPN)/GaP/Si nanolayers for integrated photonics on silicon. *J. Appl. Phys.* 112, 053521 (2012).
- [93] Nellist, P. D. Scanning Transmission Electron Microscopy. in *Springer Handbook of Microscopy* (eds. Hawkes, P. W. & Spence, J. C. H.) 49–99 (Springer International Publishing, 2019).
- [94] Chemical-mechanical polishing. Wikipedia (2020).
- [95] Introduction to Microelectronic Fabrication processes. https://nptel.ac.in/content/storage2/courses/103106075/Courses/4_3_1.html.
- [96] Vuong, P. Optical spectroscopy of boron nitride heterostructures. (Université Montpellier, 2018).
- [97] Almosni, S. Growth, structural and electro-optical properties of GaP/Si and GaAsPN/ GaP single junctions for lattice-matched tandem solar cells on silicon. (INSA de Rennes, 2015).
- [98] Raman spectroscopy. Wikipedia (2021).
- [99] Aspnes, D. E. Spectroscopic ellipsometry—A perspective. *J. Vac. Sci. Technol. A* 31, 058502 (2013).
- [100] Garcia-Caurel, E., Martino, A. D., Gaston, J.-P. & Yan, L. Application of Spectroscopic Ellipsometry and Mueller Ellipsometry to Optical Characterization. *Appl. Spectrosc.* 67, 1–21 (2013).
- [101] Kang, D. et al. Electrochemical Synthesis of Photoelectrodes and Catalysts for Use in Solar Water Splitting. *Chem. Rev.* 115, 12839–12887 (2015).
- [102] Nahir, T. M., Clark, R. A. & Bowden, E. F. Linear-Sweep Voltammetry of Irreversible Electron Transfer in Surface-Confined Species Using the Marcus Theory. *Anal. Chem.* 66, 2595–2598 (1994).

- [103] Song, A. et al. Cu:NiO as a hole-selective back contact to improve the photoelectrochemical performance of CuBi_2O_4 thin film photocathodes. *J. Mater. Chem. A* 7, 9183–9194 (2019).
- [104] Pedroni, M., Chiarello, G. L., Vassallo, E. & Selli, E. Multilayer $\text{WO}_3/\text{BiVO}_4$ Photoanodes for Solar-Driven Water Splitting Prepared by RF-Plasma Sputtering. *Surfaces* 3, 105–115 (2020).
- [105] Chen, Z. et al. Incident Photon-to-Current Efficiency and Photocurrent Spectroscopy. in *Photoelectrochemical Water Splitting: Standards, Experimental Methods, and Protocols* (eds. Chen, Z., Dinh, H. N. & Miller, E.) 87–97 (Springer, 2013).
- [106] Oh, K. et al. Elucidating the performance and unexpected stability of partially coated water-splitting silicon photoanodes. *Energy Environ. Sci.* 11, 2590–2599 (2018).
- [107] Barsoukov, E. & Macdonald, J. R. *Impedance Spectroscopy: Theory, Experiment, and Applications*. (John Wiley & Sons, 2018).
- [108] Choi, W., Shin, H.-C., Kim, J. M., Choi, J.-Y. & Yoon, W.-S. Modeling and Applications of Electrochemical Impedance Spectroscopy (EIS) for Lithium-ion Batteries. *J. Electrochem. Sci. Technol.* 11, 1–13 (2020).
- [109] Koushik, D. et al. Plasma-assisted atomic layer deposition of nickel oxide as hole transport layer for hybrid perovskite solar cells. *J. Mater. Chem. C* 7, 12532–12543 (2019).
- [110] Hankin, A., Bedoya-Lora, F. E., Alexander, J. C., Regoutz, A. & Kelsall, G. H. Flat band potential determination: avoiding the pitfalls. *J. Mater. Chem. A* 7, 26162–26176 (2019).
- [111] Argaman, N. & Makov, G. Density functional theory: An introduction. *Am. J. Phys.* 68, 69–79 (1999).
- [112] Hartree, D. R. The wave mechanics of an atom with a non-Coulomb central field. Part I. Theory and methods. in *Mathematical Proceedings of the Cambridge Philosophical Society* vol. 24 111–132 (Cambridge University Press, 1928).
- [113] Hartree, D. R. The wave mechanics of an atom with a non-coulomb central field. Part II. Some results and discussion. in *Mathematical Proceedings of the Cambridge Philosophical Society* vol. 24 111–132 (Cambridge University Press, 1928).
- [114] Slater, J. C. Note on Hartree's Method. *Phys. Rev.* 35, 210–211 (1930).
- [115] Fock, V. Näherungsmethode zur Lösung des quantenmechanischen Mehrkörperproblems. *Z. Für Phys.* 61, 126–148 (1930).
- [116] Slater, J. C. The Theory of Complex Spectra. *Phys. Rev.* 34, 1293–1322 (1929).
- [117] Thomas, L. H. The calculation of atomic fields. *Math. Proc. Camb. Philos. Soc.* 23, 542–548 (1927).
- [118] Fermi, E. Statistical method to determine some properties of atoms. *Rend Accad Naz Lincei* 6, 5 (1927).
- [119] Dirac, P. a. M. Note on Exchange Phenomena in the Thomas Atom. *Math. Proc. Camb. Philos. Soc.* 26, 376–385 (1930).
- [120] Hohenberg, P. & Kohn, W. Inhomogeneous Electron Gas. *Phys. Rev.* 136, B864–B871 (1964).
- [121] Kohn, W. & Sham, L. J. Self-Consistent Equations Including Exchange and Correlation Effects. *Phys. Rev.* 140, A1133–A1138 (1965).
- [122] Lejaeghere, K. et al. Reproducibility in density functional theory calculations of solids. *Science* 351, (2016).
- [123] Perdew, J. P. et al. Prescription for the design and selection of density functional

- approximations: More constraint satisfaction with fewer fits. *J. Chem. Phys.* 123, 062201 (2005).
- [124] Perdew, J. P., Burke, K. & Ernzerhof, M. Generalized Gradient Approximation Made Simple. *Phys. Rev. Lett.* 77, 3865–3868 (1996).
- [125] Perdew, J. P., Burke, K. & Ernzerhof, M. Generalized Gradient Approximation Made Simple [*Phys. Rev. Lett.* 77, 3865 (1996)]. *Phys. Rev. Lett.* 78, 1396–1396 (1997).
- [126] Perdew, J. P. & Zunger, A. Self-interaction correction to density-functional approximations for many-electron systems. *Phys. Rev. B* 23, 5048–5079 (1981).
- [127] Heyd, J., Scuseria, G. E. & Ernzerhof, M. Hybrid functionals based on a screened Coulomb potential. *J. Chem. Phys.* 118, 8207–8215 (2003).
- [128] Tran, F. & Blaha, P. Accurate Band Gaps of Semiconductors and Insulators with a Semilocal Exchange-Correlation Potential. *Phys. Rev. Lett.* 102, 226401 (2009).
- [129] Becke, A. D., & Johnson, E. R. A simple effective potential for exchange. *J. Chem. Phys.* 124, 221101 (2006).
- [130] Becke, A. D. & Roussel, M. R. Exchange holes in inhomogeneous systems: A coordinate-space model. *Phys. Rev. A* 39, 3761 (1989).
- [131] Kresse, G. & Furthmüller, J. Efficiency of ab-initio total energy calculations for metals and semiconductors using a plane-wave basis set. *Comput. Mater. Sci.* 6, 15–50 (1996).
- [132] Blöchl, P. E. Projector augmented-wave method. *Phys. Rev. B* 50, 17953–17979 (1994).
- [133] Monkhorst, H. J. & Pack, J. D. Special points for Brillouin-zone integrations. *Phys. Rev. B* 13, 5188–5192 (1976).
- [134] Giannozzi, P. et al. QUANTUM ESPRESSO: a modular and open-source software project for quantum simulations of materials. *J. Phys. Condens. Matter* 21, 395502 (2009).
- [135] Jia, T.-T. et al. Dirac cone move and bandgap on/off switching of graphene superlattice. *Sci. Rep.* 6, 18869 (2016).
- [136] Yang, S.-Y. et al. Symmetry demanded topological nodal-line materials. *Adv. Phys. X* 3, 1414631 (2018).
- [137] Togo, A. & Tanaka, I. First principles phonon calculations in materials science. *Scr. Mater.* 108, 1–5 (2015).
- [138] Feynman, R. P. Forces in Molecules. *Phys. Rev.* 56, 340–343 (1939).
- [139] Giannozzi, S. P. An introduction to linear response and to phonon calculations. (2010).
- [140] Fröhlich, H. Electrons in lattice fields. *Adv. Phys.* 3, 325–361 (1954).
- [141] Giorgio. School on Electron-Phonon Physics from First Principles | (smr 3191) (19-23 March 2018). <http://indico.ictp.it/event/8301/other-view?view=ictp timetable>.
- [142] Verdi, C. & Giustino, F. Fröhlich Electron-Phonon Vertex from First Principles. *Phys. Rev. Lett.* 115, 176401 (2015).
- [143] Giustino, F. Electron-phonon interactions from first principles. *Rev. Mod. Phys.* 89, 015003 (2017).
- [144] Phonopy/Phono3py. (Phonopy, 2021).
- [145] Franchini, C. et al. Maximally localized Wannier functions in LaMnO₃ within PBE+ U, hybrid functionals and partially self-consistent GW: an efficient route to construct ab initio tight-binding parameters for eg perovskites. *Journal of Physics: Condensed Matter* 24, 235602 (2012).
- [146] Wu, Q. et al. WannierTools: An open-source software package for novel topological

- materials. *Computer Physics Communications* 224, 405–416 (2018).
- [147] Chen, L. et al. Strong Electron–Phonon Interaction in 2D Vertical Homovalent III–V Singularities. *ACS Nano* 14, 13127–13136 (2020).
- [148] Yu, S., Zhang, J., Tang, Y. & Ouyang, M. Engineering Acoustic Phonons and Electron–Phonon Coupling by the Nanoscale Interface. *Nano Lett.* 15, 6282–6288 (2015).
- [149] Jin, C. et al. Interlayer electron–phonon coupling in WSe₂/hBN heterostructures. *Nat. Phys.* 13, 127–131 (2017).
- [150] Czerniuk, T. et al. Lasing from active optomechanical resonators. *Nat. Commun.* 5, 4038 (2014).
- [151] Lanzara, A. et al. Evidence for ubiquitous strong electron–phonon coupling in high-temperature superconductors. *Nature* 412, 510–514 (2001).
- [152] Driza, N. et al. Long-range transfer of electron–phonon coupling in oxide superlattices. *Nat. Mater.* 11, 675–681 (2012).
- [153] Byrnes, S. J. F. 1 Basic theory and phenomenology of polarons. (2008).
- [154] Wang, Z. et al. Tailoring the nature and strength of electron–phonon interactions in the SrTiO₃ (001) 2D electron liquid. *Nat. Mater.* 15, 835–839 (2016).
- [155] Wright, A. D. et al. Electron–phonon coupling in hybrid lead halide perovskites. *Nat. Commun.* 7, 1–9 (2016).
- [156] Leung, C. H. & Song, K. S. On the luminescence quenching of F centres in alkali halides. *Solid State Commun.* 33, 907–910 (1980).
- [157] Bissiri, M. et al. Optical evidence of polaron interaction in InAs/GaAs quantum dots. *Phys. Rev. B* 62, 4642–4646 (2000).
- [158] Gindele, F., Hild, K., Langbein, W. & Woggon, U. Phonon interaction of single excitons and biexcitons. *Phys. Rev. B* 60, R2157–R2160 (1999).
- [159] Heitz, R., Mukhametzhanov, I., Stier, O., Madhukar, A. & Bimberg, D. Enhanced Polar Exciton-LO-Phonon Interaction in Quantum Dots. *Phys. Rev. Lett.* 83, 4654–4657 (1999).
- [160] Alkauskas, A., McCluskey, M. D. & Van de Walle, C. G. Tutorial: Defects in semiconductors—Combining experiment and theory. *J. Appl. Phys.* 119, 181101 (2016).
- [161] Fockele, M., Meyer, B. K., Spaeth, J. M., Heuken, M. & Heime, K. Arsenic antisite defects in Al_xGa_{1-x}As observed by luminescence-detected electron-spin resonance. *Phys. Rev. B* 40, 2001–2004 (1989).
- [162] Kang, M. et al. Holstein polaron in a valley-degenerate two-dimensional semiconductor. *Nat. Mater.* 17, 676–680 (2018).
- [163] Roulleau, P. et al. Coherent electron–phonon coupling in tailored quantum systems. *Nat. Commun.* 2, 239 (2011).
- [164] Brar, V. W. et al. Hybrid Surface-Phonon-Plasmon Polariton Modes in Graphene/Monolayer h-BN Heterostructures. *Nano Lett.* 14, 3876–3880 (2014).
- [165] Skibitzki, O. et al. Lattice-engineered Si_{1-x}Ge_x-buffer on Si(001) for GaP integration. *J. Appl. Phys.* 115, 103501 (2014).
- [166] Yuan, Q. et al. Interplay Effect of Temperature and Excitation Intensity on the Photoluminescence Characteristics of InGaAs/GaAs Surface Quantum Dots. *Nanoscale Res. Lett.* 13, 387 (2018).
- [167] Lindsay, L., Broido, D. A. & Reinecke, T. L. Ab initio thermal transport in compound semiconductors. *Phys. Rev. B* 87, 165201 (2013).

- [168] Haas, P., Tran, F., Blaha, P. & Schwarz, K. Construction of an optimal GGA functional for molecules and solids. *Phys. Rev. B* 83, 205117 (2011).
- [169] Ravoux, F. et al. Effect of rapid thermal annealing on crystallization and stress relaxation of SiGe nanoparticles deposited by ICP PECVD. *RSC Adv.* 7, 32087–32092 (2017).
- [170] Peternai, L. et al. Investigation of graded $\text{In}_x\text{Ga}_{1-x}\text{P}$ buffer by Raman scattering method. *Microelectron. J.* 37, 487–490 (2006).
- [171] Varshni, Y. P. Temperature dependence of the energy gap in semiconductors. *Physica* 34, 149–154 (1967).
- [172] Aspnes, D. E. & Studna, A. A. Dielectric functions and optical parameters of Si, Ge, GaP, GaAs, GaSb, InP, InAs, and InSb from 1.5 to 6.0 eV. *Phys. Rev. B* 27, 985–1009 (1983).
- [173] Zhang, Y. & Gu, Y. Al(Ga)InP-GaAs Photodiodes Tailored for Specific Wavelength Range. *Photodiodes - Fundam. Appl.* (2012).
- [174] Schmidt, T., Lischka, K. & Zulehner, W. Excitation-power dependence of the near-band-edge photoluminescence of semiconductors. *Phys. Rev. B* 45, 8989–8994 (1992).
- [175] Bimberg, D., Schairer, W., Sondergeld, M. & Yep, T. O. Bound exciton luminescence in epitaxial Sn-doped gallium-arsenide. *J. Lumin.* 3, 175–184 (1970).
- [176] Hellmann, R. et al. Low-temperature anti-Stokes luminescence mediated by disorder in semiconductor quantum-well structures. *Phys. Rev. B* 51, 18053–18056 (1995).
- [177] Lambkin, J. D. et al. Temperature dependence of the photoluminescence intensity of ordered and disordered $\text{In}_{0.48}\text{Ga}_{0.52}\text{P}$. *Appl. Phys. Lett.* 65, 73–75 (1994).
- [178] Mourad, D. et al. Determination of valence-band offset at cubic CdSe/ZnTe type-II heterojunctions: A combined experimental and theoretical approach. *Phys. Rev. B* 86, 195308 (2012).
- [179] Stoneham, A. M. *Theory of Defects in Solids: Electronic Structure of Defects in Insulators and Semiconductors.* (Clarendon Press, 2001).
- [180] Lax, M. The Franck-Condon Principle and Its Application to Crystals. *J. Chem. Phys.* 20, 1752–1760 (1952).
- [181] Malm, H. L. & Haering, R. R. Franck-Condon Effects in the Luminescence of CdS. *Can. J. Phys.* 49, 2970–2988 (1971).
- [182] Besombes, L., Kheng, K., Marsal, L. & Mariette, H. Acoustic phonon broadening mechanism in single quantum dot emission. *Phys. Rev. B* 63, 155307 (2001).
- [183] Paskov, P. P. et al. Phonon-Assisted Photoluminescence in InGaN/GaN Multiple Quantum Wells. *Phys. Status Solidi B* 234, 755–758 (2002).
- [184] Norris, D. J., Efros, A. L., Rosen, M. & Bawendi, M. G. Size dependence of exciton fine structure in CdSe quantum dots. *Phys. Rev. B* 53, 16347–16354 (1996).
- [185] Odnoblyudov, M. A., Yassievich, I. N. & Chao, K. A. Polaron Effects in Quantum Dots. *Phys. Rev. Lett.* 83, 4884–4887 (1999).
- [186] Lucci, I. et al. A Stress-Free and Textured GaP Template on Silicon for Solar Water Splitting. *Adv. Funct. Mater.* 28, 1801585 (2018).
- [187] Chen, L. et al. Assessment of GaPSb/Si tandem material association properties for photoelectrochemical cells. *Sol. Energy Mater. Sol. Cells* 221, 110888 (2021).
- [188] Van de Krol, R. & Grätzel, M. *Photoelectrochemical hydrogen production.* vol. 90 (Springer, 2012).
- [189] Rongé, J. et al. Monolithic cells for solar fuels. *Chem. Soc. Rev.* 43, 7963–7981 (2014).

- [190] Bae, D., Seger, B., Vesborg, P. C. K., Hansen, O. & Chorkendorff, I. Strategies for stable water splitting via protected photoelectrodes. *Chem. Soc. Rev.* 46, 1933–1954 (2017).
- [191] Hu, S., Xiang, C., Haussener, S., Berger, A. D. & Lewis, N. S. An analysis of the optimal band gaps of light absorbers in integrated tandem photoelectrochemical water-splitting systems. *Energy Environ. Sci.* 6, 2984–2993 (2013).
- [192] Young, J. L. et al. Direct solar-to-hydrogen conversion via inverted metamorphic multi-junction semiconductor architectures. *Nat. Energy* 2, 1–8 (2017).
- [193] Khaselev, O. & Turner, J. A. A Monolithic Photovoltaic-Photoelectrochemical Device for Hydrogen Production via Water Splitting. *Science* 280, 425–427 (1998).
- [194] May, M. M., Lewerenz, H.-J., Lackner, D., Dimroth, F. & Hannappel, T. Efficient direct solar-to-hydrogen conversion by in situ interface transformation of a tandem structure. *Nat. Commun.* 6, 8286 (2015).
- [195] Cheng, W.-H. et al. Monolithic Photoelectrochemical Device for Direct Water Splitting with 19% Efficiency. *ACS Energy Lett.* 3, 1795–1800 (2018).
- [196] Chen, S. et al. Electrically pumped continuous-wave III–V quantum dot lasers on silicon. *Nat. Photonics* 10, 307–311 (2016).
- [197] Licht, S. et al. Efficient Solar Water Splitting, Exemplified by RuO₂-Catalyzed AlGaAs/Si Photoelectrolysis. *J. Phys. Chem. B* 104, 8920–8924 (2000).
- [198] Döscher, H. et al. Epitaxial III–V Films and Surfaces for Photoelectrocatalysis. *ChemPhysChem* 13, 2899–2909 (2012).
- [199] Nguyen-Van, H. et al. Quantum cascade lasers grown on silicon. *Sci. Rep.* 8, 7206 (2018).
- [200] Martinez-Garcia, A. et al. Unassisted Water Splitting Using a GaSb_xP_(1-x) Photoanode. *Adv. Energy Mater.* 8, 1703247 (2018).
- [201] Quinci, T. et al. Defects limitation in epitaxial GaP on birstepped Si surface using UHVCVD–MBE growth cluster. *J. Cryst. Growth* 380, 157–162 (2013).
- [202] Adachi, S. Optical dispersion relations for GaP, GaAs, GaSb, InP, InAs, InSb, Al_xGa_{1-x}As, and In_{1-x}Ga_xAs_yP_{1-y}. *J. Appl. Phys.* 66, 6030–6040 (1989).
- [203] Loualiche, S. et al. GaPSb: A new ternary material for Schottky diode fabrication on InP. *Appl. Phys. Lett.* 59, 423–424 (1991).
- [204] Jancu, J.-M., Scholz, R., Beltram, F. & Bassani, F. Empirical spds* tight-binding calculation for cubic semiconductors: General method and material parameters. *Phys. Rev. B* 57, 6493–6507 (1998).
- [205] Panish, M. B. & Casey, H. C. Temperature Dependence of the Energy Gap in GaAs and GaP. *J. Appl. Phys.* 40, 163–167 (1969).
- [206] Wu, M. & Chen, C. Photoluminescence of high-quality GaSb grown from Ga- and Sb-rich solutions by liquid-phase epitaxy. *J. Appl. Phys.* 72, 4275–4280 (1992).
- [207] Van de Walle, C. G. & Neugebauer, J. Universal alignment of hydrogen levels in semiconductors, insulators and solutions. *Nature* 423, 626–628 (2003).
- [208] Borg, B. M. & Wernersson, L.-E. Synthesis and properties of antimonide nanowires. *Nanotechnology* 24, 202001 (2013).
- [209] Jing, D. et al. Efficient solar hydrogen production by photocatalytic water splitting: From fundamental study to pilot demonstration. *Int. J. Hydrog. Energy* 35, 7087–7097 (2010).
- [210] Kudo, A. & Miseki, Y. Heterogeneous photocatalyst materials for water splitting. *Chem. Soc. Rev.* 38, 253–278 (2009).

- [211] Chu, S. et al. Roadmap on solar water splitting: current status and future prospects. *Nano Futur.* 1, 022001 (2017).
- [212] Hu, S. et al. Amorphous TiO₂ coatings stabilize Si, GaAs, and GaP photoanodes for efficient water oxidation. *Science* 344, 1005–1009 (2014).
- [213] Robert, C. et al. Room temperature operation of GaAsP(N)/GaP(N) quantum well based light-emitting diodes: Effect of the incorporation of nitrogen. *Appl. Phys. Lett.* 98, 251110 (2011).
- [214] Robert, C. et al. Electronic, optical, and structural properties of (In,Ga)As/GaP quantum dots. *Phys. Rev. B* 86, 205316 (2012).
- [215] Standing, A. et al. Efficient water reduction with gallium phosphide nanowires. *Nat. Commun.* 6, 7824 (2015).
- [216] Strandwitz, N. C. et al. Photoelectrochemical Behavior of Planar and Microwire-Array Si|GaP Electrodes. *Adv. Energy Mater.* 2, 1109–1116 (2012).
- [217] Kargar, A. et al. GaP/GaNP Heterojunctions for Efficient Solar-Driven Water Oxidation. *Small* 13, 1603574 (2017).
- [218] McKone, J. R., Lewis, N. S. & Gray, H. B. Will Solar-Driven Water-Splitting Devices See the Light of Day? *Chem. Mater.* 26, 407–414 (2014).
- [219] Liang, Y. et al. Co₃O₄ nanocrystals on graphene as a synergistic catalyst for oxygen reduction reaction. *Nat. Mater.* 10, 780–786 (2011).
- [220] Li, L. et al. Assembling a lasing hybrid material with supramolecular polymers and nanocrystals. *Nat. Mater.* 2, 689–694 (2003).
- [221] Zhou, W. et al. Seebeck-driven transverse thermoelectric generation. *Nat. Mater.* 1–5 (2021).
- [222] Allain, A., Han, Z. & Bouchiat, V. Electrical control of the superconducting-to-insulating transition in graphene–metal hybrids. *Nat. Mater.* 11, 590–594 (2012).
- [223] Yu, P. & Cardona, M. *Fundamentals of Semiconductors: Physics and Materials Properties.* (Springer Science & Business Media, 2010).
- [224] Vandewal, K., Tvingstedt, K., Gadisa, A., Inganäs, O. & Manca, J. V. On the origin of the open-circuit voltage of polymer–fullerene solar cells. *Nat. Mater.* 8, 904–909 (2009).
- [225] Li, X. et al. Graphene-On-Silicon Schottky Junction Solar Cells. *Adv. Mater.* 22, 2743–2748 (2010).
- [226] Wang, Z. et al. The ambipolar transport behavior of WSe₂ transistors and its analogue circuits. *NPG Asia Mater.* 10, 703–712 (2018).
- [227] Zhou, Y., Han, S.-T., Sonar, P. & Roy, V. a. L. Nonvolatile multilevel data storage memory device from controlled ambipolar charge trapping mechanism. *Sci. Rep.* 3, 2319 (2013).
- [228] Chen, X. et al. Polyoxometalates-Modulated Reduced Graphene Oxide Flash Memory with Ambipolar Trapping as Bidirectional Artificial Synapse. *Adv. Electron. Mater.* 4, 1800444 (2018).
- [229] Kwon, H. et al. Gate-tunable gas sensing behaviors in air-stable ambipolar organic thin-film transistors. *RSC Adv.* 10, 1910–1916 (2020).
- [230] Zaumseil, J., Friend, R. H. & Sirringhaus, H. Spatial control of the recombination zone in an ambipolar light-emitting organic transistor. *Nat. Mater.* 5, 69–74 (2006).
- [231] An, M.-H. et al. Well-Balanced Ambipolar Organic Single Crystals toward Highly Efficient Light-Emitting Devices. *Adv. Funct. Mater.* 30, 2002422 (2020).

- [232] Zhang, M. et al. Synergistic Cascade Carrier Extraction via Dual Interfacial Positioning of Ambipolar Black Phosphorene for High-Efficiency Perovskite Solar Cells. *Adv. Mater.* 32, 2000999 (2020).
- [233] Bourée, W. S. et al. Robust Hierarchically Structured Biphasic Ambipolar Oxide Photoelectrodes for Light-Driven Chemical Regulation and Switchable Logic Applications. *Adv. Mater.* 28, 9308–9312 (2016).
- [234] Feifel, M. et al. MOVPE Grown Gallium Phosphide–Silicon Heterojunction Solar Cells. *IEEE J. Photovolt.* 7, 502–507 (2017).
- [235] Beyer, A. et al. Atomic structure of (110) anti-phase boundaries in GaP on Si(001). *Appl. Phys. Lett.* 103, 032107 (2013).
- [236] Wright, S. L., Kroemer, H. & Inada, M. Molecular beam epitaxial growth of GaP on Si. *J. Appl. Phys.* 55, 2916–2927 (1984).
- [237] Kao, Y. C. & Eknayan, O. Electron and hole carrier mobilities for liquid phase epitaxially grown GaP in the temperature range 200–550 K. *J. Appl. Phys.* 54, 2468–2471 (1983).
- [238] Alberding, B. G., Thurber, W. R. & Heilweil, E. J. Direct comparison of time-resolved terahertz spectroscopy and Hall Van der Pauw methods for measurement of carrier conductivity and mobility in bulk semiconductors. *JOSA B* 34, 1392–1406 (2017).
- [239] Jacoboni, C., Canali, C., Ottaviani, G. & Alberigi Quaranta, A. A review of some charge transport properties of silicon. *Solid-State Electron.* 20, 77–89 (1977).
- [240] Butler, M. A. & Ginley, D. S. P-Type GaP as a Semiconducting Photoelectrode. *J. Electrochem. Soc.* 127, 1273 (1980).
- [241] Malizia, M., Seger, B., Chorkendorff, I. & Vesborg, P. C. K. Formation of a p–n heterojunction on GaP photocathodes for H₂ production providing an open-circuit voltage of 710 mV. *J. Mater. Chem. A* 2, 6847–6853 (2014).
- [242] Pishgar, S. et al. Investigation of the photocorrosion of n-GaP photoanodes in acid with in situ UV-Vis spectroscopy. *J. Mater. Chem. A* 7, 25377–25388 (2019).
- [243] Alqahtani, M. et al. Gallium Phosphide photoanode coated with TiO₂ and CoO_x for stable photoelectrochemical water oxidation. *Opt. Express* 27, A364–A371 (2019).
- [244] Randviir, E. P. & Banks, C. E. Electrochemical impedance spectroscopy: an overview of bioanalytical applications. *Anal. Methods* 5, 1098–1115 (2013).
- [245] Meng, F., Li, J., Cushing, S. K., Zhi, M. & Wu, N. Solar Hydrogen Generation by Nanoscale p–n Junction of p-type Molybdenum Disulfide/n-type Nitrogen-Doped Reduced Graphene Oxide. *J. Am. Chem. Soc.* 135, 10286–10289 (2013).
- [246] Li, J. et al. Photoelectrochemical performance enhanced by a nickel oxide–hematite p–n junction photoanode. *Chem. Commun.* 48, 8213–8215 (2012).
- [247] Zhu, L. et al. Synthesis of the 0D/3D CuO/ZnO Heterojunction with Enhanced Photocatalytic Activity. *J. Phys. Chem. C* 122, 9531–9539 (2018).
- [248] Marzari, N. et al. Maximally localized Wannier functions: Theory and applications. *Reviews of Modern Physics* 84, 1419 (2012).
- [249] Yan, B. & Felser, C. Topological Materials: Weyl Semimetals. *Annu. Rev. Condens. Matter Phys.* 8, 337–354 (2017).
- [250] Huang, H., Liu, J., Vanderbilt, D. & Duan, W. Topological nodal-line semimetals in alkaline-earth stannides, germanides, and silicides. *Phys. Rev. B* 93, 201114 (2016).
- [251] Weng, H. et al. Topological node-line semimetal in three-dimensional graphene networks.

- Phys. Rev. B 92, 045108 (2015).
- [252] Sekine, A. & Nagaosa, N. Tunable charged domain wall from topological confinement in nodal-line semimetals. Phys. Rev. B 101, 081102 (2020).
- [253] Sacco, A. Electrochemical impedance spectroscopy as a tool to investigate the electroreduction of carbon dioxide: A short review. J. CO2 Util. 27, 22–31 (2018).
- [254] Shaislamov, U. et al. Growth of CuO/ZnO Nanobranched Photoelectrode with Enhanced Stability for Solar Hydrogen Generation. J. Nanosci. Nanotechnol. 16, 10541–10547 (2016).
- [255] Yanping, W. Structural analyses by advanced X-ray scattering on GaP layers epitaxially grown on silicon for integrated photonic applications. (INSA de Rennes, 2016).

Titre : Propriétés optoélectroniques, vibrationnelles et de transport de parois d'antiphase III-V/Si pour la photonique et la récupération d'énergie solaire

Mots clés : Semi-conducteurs III-V/Si, parois d'antiphase, matériaux 2D, singularités verticales homovalentes, propriétés optoélectroniques

Résumé : L'objectif de cette thèse est d'étudier les propriétés optoélectroniques spécifiques des parois d'antiphase (APBs) III-V/Si et leur utilisation pour des dispositifs de récupération d'énergie solaire, de manière théorique et expérimentale. Un fort couplage électron-phonon autour des APBs stœchiométriques est d'abord démontré en raison du confinement simultané des porteurs de charge et des phonons dans la même région, sur la base de caractérisations structurales et optiques et de calculs de théorie de la fonctionnelle de la densité (DFT). D'autre part, une nouvelle association tandem de matériaux GaPSb/Si pour le craquage de l'eau à partir de l'énergie solaire est étudiée. En combinant des mesures d'ellipsométrie et les calculs de liaisons fortes, la bande interdite des alliages GaPSb pour toutes les concentrations en Sb et les alignements de bande de GaPSb/Si avec les niveaux de l'eau sont obtenus, et montrent le potentiel de ces matériaux pour

les réactions d'évolution de l'hydrogène et de l'oxygène. Ensuite, une photoanode GaP_{0.67}Sb_{0.33}/Si avec une combinaison de bandes interdites très proche de l'optimum (1.7eV/1.1eV) a été étudiée pour le craquage de l'eau photoélectrochimique (PEC) et montre des propriétés prometteuses du fait de leur bonne absorption solaire. Le transport et les propriétés PEC des couches III-V/Si avec des APBs verticales non-stœchiométriques sont étudiés sur la base de caractérisations expérimentales et de calculs DFT. Nous démontrons que les matériaux III-V/Si épitaxiés contenant des APBs verticales non stœchiométriques sont des structures hybrides, composées de semi-conducteurs photo-actifs massifs avec des inclusions verticales semi-métalliques topologiques 2D, permettant simultanément une bonne photo-activité, un transport et une séparation efficaces des charges, et des propriétés ambipolaires intéressantes.

Title : Optoelectronic, vibrational and transport properties of III-V/Si antiphase boundaries for photonics and solar energy harvesting

Keywords : III-V/Si semiconductors, antiphase boundaries, 2D materials, vertical homovalent singularities, optoelectronic properties

Abstract : This thesis aims to investigate the specific optoelectronic properties of III-V/Si Anti-Phase Boundaries (APBs) and its use for energy harvesting devices theoretically and experimentally. Strong electron-phonon coupling around stoichiometric APBs are first demonstrated due to simultaneous confinement of charge carriers and phonons in the same region, based on structural and optical characterizations and density functional theory calculations. The GaPSb/Si tandem materials association for solar water splitting is then studied. Combining ellipsometry measurements and tight binding calculations, the bandgap of GaPSb alloys in the whole Sb range and band lineups of GaPSb/Si with water redox levels are obtained, which shows the potential of the GaPSb/Si association for the hydrogen evolution and oxygen evolution reactions.

Then a GaP_{0.67}Sb_{0.33}/Si photoanode with an almost optimal bandgap combination (1.7eV/1.1eV) was investigated for photoelectrochemical (PEC) water splitting with promising performances related to efficient sunlight spectrum absorption. Finally, the transport and PEC properties of III-V/Si with vertical non-stoichiometric APBs are investigated from experimental characterizations and first-principle calculations. We demonstrate that epitaxial III-V/Si materials with vertical non-stoichiometric APBs are hybrid structures, composed of bulk photo-active semiconductors with 2D topological semi metallic vertical inclusions, enabling simultaneously good photo-activity, efficient charge transport and separation, and interesting ambipolar properties.